

SIMULATION AND DESIGN OF PASSIVE DECAY HEAT REMOVAL SYSTEM FOR ADVANCED HEAVY WATER REACTOR

By

**NITIN MINOCHA
ENGG01201104018**

Homi Bhabha National Institute, Mumbai

*A thesis submitted to the
Board of Studies in Engineering Sciences*

*In partial fulfillment of requirements
for the Degree of*

DOCTOR OF PHILOSOPHY

of

HOMI BHABHA NATIONAL INSTITUTE

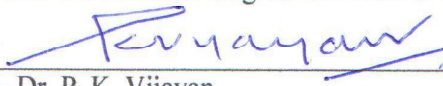


April, 2016

Homi Bhabha National Institute

Recommendations of the Viva Voce Committee

As members of the Viva Voce Committee, we certify that we have read the dissertation prepared by Mr. Nitin Minocha entitled "Simulation and Design of Passive Decay Heat Removal System for Advanced Heavy Water Reactor" and recommend that it may be accepted as fulfilling the thesis requirement for the award of Degree of Doctor of Philosophy.



Chairman – Dr. P. K. Vijayan
Date: 2/9/16


Guide / Convener – Prof. J. B. Joshi
Date: 2/9/16


Co-guide - Dr. A. K. Nayak
Date: 2-9-16


Examiner – Prof. Shankar Narasimhan
Date: 02/09/16


Member 1- Dr. K. Velusamy
Date: 2/9/2016


Member 2- Prof. Atul Sharma
Date: 2/9/16

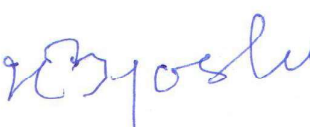
Final approval and acceptance of this thesis is contingent upon the candidate's submission of the final copies of the thesis to HBNI.

I/We hereby certify that I/we have read this thesis prepared under my/our direction and recommend that it may be accepted as fulfilling the thesis requirement.

Date: 2/9/16

Place: MUMBAI


Co-guide


Guide

STATEMENT BY AUTHOR

This dissertation has been submitted in partial fulfillment of requirements for an advanced degree at Homi Bhabha National Institute (HBNI) and is deposited in the Library to be made available to borrowers under rules of the HBNI.

Brief quotations from this dissertation are allowable without special permission, provided that accurate acknowledgement of source is made. Requests for permission for extended quotation from or reproduction of this manuscript in whole or in part may be granted by the Competent Authority of HBNI when in his or her judgment the proposed use of the material is in the interests of scholarship. In all other instances, however, permission must be obtained from the author.

Nitin Minocha

DECLARATION

I, hereby declare that the investigation presented in the thesis has been carried out by me. The work is original and has not been submitted earlier as a whole or in part for a degree / diploma at this or any other Institution / University.

Nitin Minocha

ACKNOWLEDGEMENTS

First and foremost, I wish to dedicate this work to my parents for their support and encouragement throughout my PhD.

I am very much grateful to Prof. J. B. Joshi, for giving me an opportunity to work in his research group. On the very first day of joining PhD, he told me that you will get PhD for sure but the main thing is you must enjoy this period to be a better person and have enough confidence to face any problem in life. I always remember his words “Keep smiling in all circumstances”. His suggestions helped me a lot to overcome all the difficulties in my PhD work. Apart from the PhD work, he also taught me the real problems faces by our country and how easily we can overcome these problems. The best thing which I like and respect the most about him is his infinite passion for understanding turbulence. I am very much grateful to him to transfer this passion in me also.

I would like to thank Dr. A.K. Nayak for being very supportive. He always encourages my ideas (specially, effect of inclination) and gave me a freedom to explore these ideas. I remember his words “PhD is your baby, take very good care of it”. I am very much grateful to him for the timely review of my work and giving important advices.

I would like to thank my senior Dr. Mayur Gandhi for guiding me and helping me in understanding the problem of thermal stratification. I am very much grateful to him to listen all my queries and answering them very sincerely.

I would like to thank my colleagues and friends Eshita, Ankur and Vishal. I am very much grateful to all of them for making the journey of PhD smooth and enjoyable. Vishal taught me the basic fluid dynamics and transport phenomena. Eshita was the first person in our group who learns Gmsh by herself and then taught all of us how to use this software for geometry and grid generation. She always pushes me to finish my work on time and helped me a lot in my PhD journey. Ankur is the coolest person in our group. I don't remember the last time when I saw him in a tense situation. He always brings positive energy in our lab.

I would like to thank all my seniors Ram, Zoheb, Chinmay and Varsha for being a part of this wonderful journey.

I am grateful to HBNI/BARC for providing me the scholarship to pursue my PhD work. I am also thankful to the HBNI admin staff for helping me in the administrative work.

CONTENTS

	Page No.
Title	i
Contents	vi
Synopsis	xi
List of Figures	xxiii
List of Tables	xxx

CHAPTERS

1. Introduction	1-6
1.1 Motivation	1
1.2 Importance of Passive Safety Systems	2
1.3 Natural Convection	3
1.4 Critical Issues in the Design of PDHRS	3
1.5 Objectives	4
1.6 Design Methodology	5
1.7 Outline of report	5
2. CFD code validation	8-36
2.1 Assessment of turbulence models	8
2.1.1 Introduction	8
2.1.2 Literature Survey	10
2.1.3 Buoyancy Models	12
2.1.3.1 Full Buoyancy Model	12
2.1.3.2 Buoyancy Model with Boussinesq Approximation	12
2.1.3.3 Limitations of Boussinesq approximation	14
2.1.4 Turbulence Models	14
2.1.4.1 Standard k- ϵ model	14
2.1.4.2 Low Re k - ϵ model	17
2.1.4.3 SST k- ω model	17
2.1.4.4 Elliptic Relaxation (v2f) model	18
2.1.4.5 Reynolds Stress Model (RSM)	18
2.1.5 Numerical Procedure	21

2.1.5.1 Geometry	21
2.1.5.2 Governing equations	22
2.1.5.3 Model Assumptions	23
2.1.5.4 Method of Solution	23
2.1.5.5 Grid Independence	23
2.1.5.6 Time Independence	24
2.1.6 Results and Discussions	24
2.1.6.1 Velocity and Temperature Profiles	25
2.1.6.2 Average Heat Transfer Coefficient	28
2.2 CFD model capability to study thermal stratification inside small and large water pools	30
2.2.1 Gandhi et al., (2013)	30
2.2.2 Aszodi et al., (2000)	33
2.2.3 Krepper et al., (2002)	35
2.3 Closure	36
3. Numerical investigation of three-dimensional natural circulation phenomenon in Passive Safety Systems for decay heat removal in large pools	37-86
3.1 Introduction	37
3.2 System description	37
3.3 Literature survey	40
3.4 Numerical Procedure	46
3.4.1 Governing equations	46
3.4.2 Model Assumptions	48
3.4.3 Geometry	52
3.4.4 Mesh construction algorithm	54
3.4.5 Boundary condition	57
3.4.6 Method of solution	61
3.4.7 Grid independence	62
3.4.8 Time independence	64
3.5 Results and discussions	66
3.5.1 Single Heat Source (IC1)	67
3.5.1.1 Velocity and Temperature profiles	67
3.5.1.2 Turbulent kinetic energy (k) and turbulent viscosity (ν_t) profiles	72

3.5.1.3 Quantification of Stratification and Extent of mixing	72
3.5.2 Effect of distribution of heat sources inside GDWP	76
3.5.3 Effect of Submergence of Isolation Condenser	77
3.5.4 Effect of Submergence and distribution of heat sources inside GDWP	78
3.5.5 Effect of Draft tubes	80
3.5.5.1 Transient Heat Transfer	83
3.5.5.2 Onset of Secondary Flow (Longitudinal Vortices)	84
3.6 Closure	86
4. Design of an optimized IC and study on the effect of inclination of condenser tube on natural convection and stratification in PDHRS	88-123
4.1 Introduction	88
4.2 Literature survey	88
4.3 Numerical Procedure	92
4.4 Results and discussions	92
4.4.1 Effect of inclination of IC tube for pilot scale GDWP	93
4.4.1.1 Geometry and Boundary conditions	93
4.4.1.2 Grid independence and assessment of turbulence models	95
4.4.1.3 Temperature contours and Flow distribution	101
4.4.1.4 Azimuthal Heat Transfer	101
4.4.1.5 Transition from primary to secondary flow	103
4.4.1.6 Fluid flow near the upward and downward face of the heated tube	105
4.4.1.7 Turbulent kinetic energy (k) contour	106
4.4.1.8 Transient heat transfer	107
4.4.1.9 Quantification of Stratification and Extent of mixing	110
4.4.2 Natural convection and heat transfer for new design of IC for real size GDWP	111
4.4.2.1 Geometry and Boundary conditions	111
4.4.2.2 Laminar-turbulent natural convection and heat transfer	114
4.4.2.3 Temperature Contours and Flow distribution	118
4.4.2.4 Transient heat transfer and Thermal Stratification	121
4.5 Closure	123
5. 3D CFD Simulation to study pressure and flow distribution in isolation condenser	125-141
5.1 Introduction	125

5.2 Numerical procedure	126
5.2.1 Flow geometry considered for present study	126
5.2.2 Governing equations	126
5.2.3 Simulation details	127
5.2.4 Model Assumptions	127
5.2.5 Method of solution	127
5.3 Results and discussions	128
5.3.1 Conventional design of isolation condenser(IC)	129
5.3.2 Effect of tube pitch	131
5.3.3 Effect of header shape	132
5.3.4 Effect of inlet tube diameter	134
5.3.5 Effect of number of tubes	136
5.3.6 Effect of header diameter	136
5.3.7 Effect of perforated baffle	138
5.4 Closure	141
6. 3D CFD Simulation of passive decay heat removal system under boiling conditions: role of bubble sliding motion on inclined heated tubes	142-196
6.1 Introduction	142
6.2 Literature survey	142
6.3 Numerical procedure	147
6.3.1 State of art in the code for multiphase flow	147
6.3.1.1 Euler-Euler approach	148
6.3.1.1.1 Volume of Fluid (VOF) Model	148
6.3.1.1.2 Mixture Model	150
6.3.1.1.3 Eulerian Model	156
6.3.1.2 Limitations of RPI model at low pressures or large void-fractions	158
6.3.1.2.1 Mean bubble diameter	159
6.3.1.2.2 Wall heat flux partitioning	159
6.3.1.2.3 Bubble departure diameter and frequency	161
6.3.1.3 Euler-Lagrange approach	161
6.3.2 Governing equations	162

6.3.3 Model Assumptions	163
6.3.4 Method of solution	163
6.3.5 Model Validation	164
6.4 Results and discussions	167
6.4.1 Effect of inclination of IC tube for pilot scale GDWP	167
6.4.1.1 Geometry and Boundary conditions	167
6.4.1.2 Grid independence	168
6.4.1.3 Azimuthal Variation of Temperature and Vapor fraction	171
6.4.1.4 Flow patterns associated with bubble sliding motion	175
6.4.1.5 Transient bubble formation over inclined tube	176
6.4.1.6 Fluid flow near the upward and downward face of the heated tube	178
6.4.1.7 Turbulent kinetic energy (k) contour	180
6.4.1.8 Transient heat transfer	180
6.4.1.9 Quantification of Thermal Stratification	183
6.4.2 Condensation heat transfer over inclined tube	184
6.4.2.1 Analytical Model	184
6.4.2.2 Literature Survey on condensation inside inclined tubes	187
6.4.3 Natural convection and heat transfer for new design of IC for real size GDWP	189
6.4.3.1 Geometry and Boundary conditions	189
6.4.3.2 Vapor fraction Contours and Flow distribution	192
6.4.3.3 Interaction between the tubes	192
6.4.3.4 Transient heat transfer	194
6.5 Closure	196
7. Conclusions and recommendations for future work	197-199
7.1 Conclusions	197
7.2 Recommendations for future work	199
Nomenclature	201
References	208
List of publications	



Homi Bhabha National Institute

SYNOPSIS REPORT

1. **Name of the Student:** Nitin Minocha
2. **Name of the Constituent Institution:** Homi Bhabha National Institute
3. **Enrollment No.:** ENGG01201104018
4. **Title of the Thesis:** Simulation and design of Passive decay heat removal system (PDHRS) of Advanced heavy water reactor (AHWR)
5. **Board of Studies:** Engineering Science

In the core of nuclear reactors, when a shutdown occurs, the fission chain reaction is stopped. However, because of decay heat (approximately 6% of operating power at shutdown) released by fuel, the heat generation continues at considerable levels for a long time. If effective removal of the decay heat is not assured, the reactor core may get damaged and may result in release of fission products and radionuclides. In order to avoid the occurrence of a severe accident, many advanced nuclear reactors such as Advanced Heavy Water Reactor (AHWR) have adopted a methodology of providing a passive safety system to remove the decay heat during accidental conditions. The use of passive safety systems eliminate the costs associated with the installation, maintenance and operation of active safety systems that require multiple pumps with independent and redundant electric power supplies. In AHWR, to remove the decay heat passively, a passive decay heat removal system (PDHRS) employs a combination of multiple isolation condensers (ICs). The decay heat generated from the core is removed by natural circulation (boiling light water at 285⁰C and 7 MPa pressure) circulating in the primary system. The heat from the core is transferred to the PDHRS through isolation condensers (ICs) submerged in a large pool of water called the Gravity Driven Water Pool (GDWP) which is considered as a near infinite heat sink.

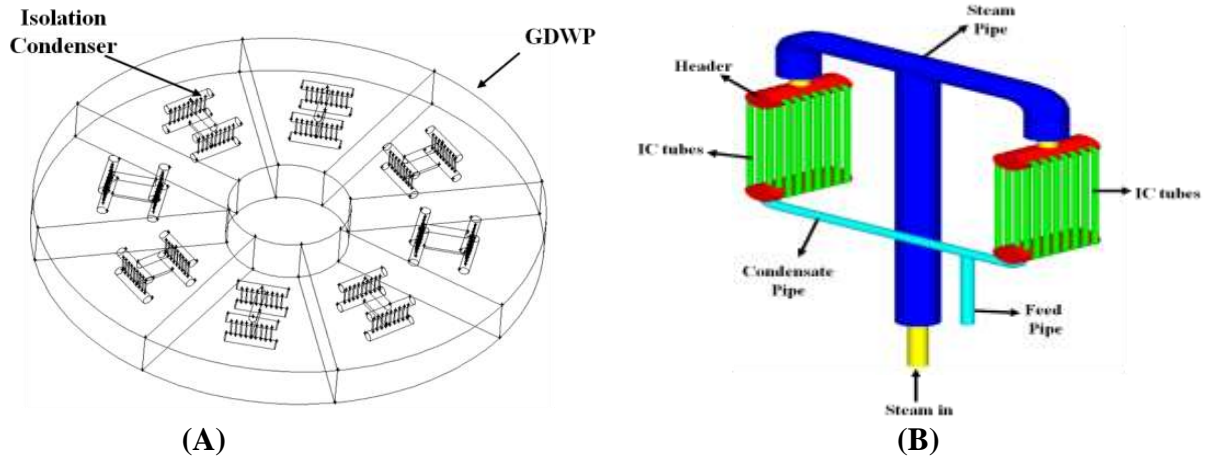


Fig 1: Schematic of (A) GDWP tank (B) Isolation condenser (IC)

The GDWP tank ($\sim 9247 \text{ m}^3$) shown in Fig 1A having dimensions ($R_o = 25\text{m}$, $R_i = 6\text{m}$, $H_T = 5\text{m}$) is divided into 8 compartments and one IC is located in each compartment. The IC consists of a bundle of vertical IC tubes Fig 1B. In the passive decay heat removal system, the heat transfer from the isolation condenser (IC) may be concentrated in a limited zone of a large water pool (GDWP) in terms of GDWP volume and hence results into multi dimensional flow and temperature fields. The non-uniform temperature distribution can result in thermal stratification. The heat removal rate from the ICs can get seriously affected by such temperature stratifications and the rate is also governed by the flow field in the vicinity of IC. Under strong temperature stratification conditions, the fluid at the top of the pool reaches the saturation temperature much earlier as compared to the case of homogeneous temperature distribution. In addition, the stratification is not desired because of the limitation imposed by the GDWP concrete walls (i.e. the temperature should not exceed beyond 65°C at any location). Hence, it is necessary to optimize the design of isolation condenser (a) to reduce thermal stratification (b) to enhance heat transfer and (c) to prevent early water evaporation so as to avoid over-pressurization of containment. An extensive literature survey on above aspects indicates:

- Since the flow field around the IC is multi-dimensional, one needs to use a 3D CFD model to understand the natural convection phenomena inside GDWP. However, there are almost no

studies to evaluate the capability of the CFD model to simulate multi dimensional natural convection and thermal stratification phenomenon inside large water pool such as GDWP

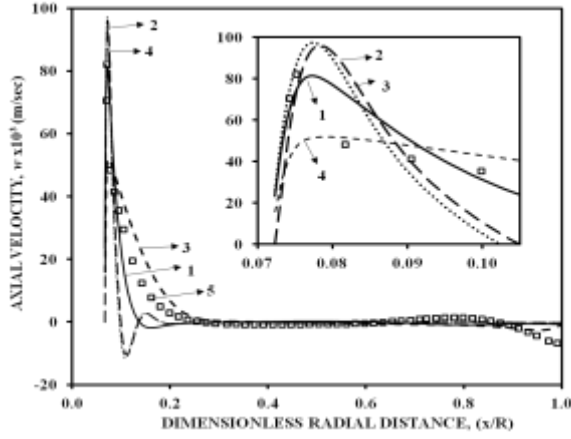
- Very limited studies have been performed related to the design modification of IC to remove decay heat effectively
- None of earlier studies have established relationship between inclination angle of condenser tube and thermal stratification
- Since the steam is entering at one point inside IC header and there are multiple tubes. So, it may happen that some of the tubes get excess of steam and some of the tubes get starved of fluid. Therefore, it is necessary to study steam mal-distribution in IC header and tube assembly and its effect on heat transfer inside GDWP
- Due to high temperature (285°C) of steam inside the IC tubes, local boiling may occur inside the GDWP. The effect of boiling on thermal stratification phenomenon inside GDWP needs to be studied.

In view of above, the objective of this thesis is to design an efficient isolation condenser (IC) for the PDHRS of AHWR. The main objective has been recast into following sub objectives:

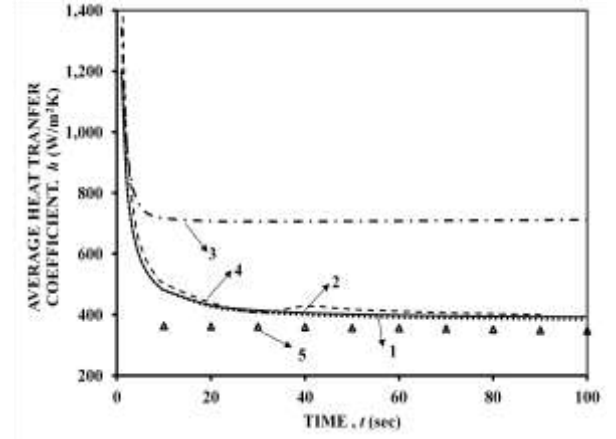
1. Establish the capability of the CFD model to simulate thermal stratification inside large water pool such as GDWP
2. Study of multi dimensional natural convection and flow fields inside GDWP in the presence of IC. Further, the effect of these fields on thermal stratification inside GDWP.
3. Optimize the design of IC to maximize heat transfer and reduced thermal stratification by changing the geometry of the IC tubes such as heat source distribution, submergence depth of IC, inclination of IC tubes, etc. A new concept of passive draft tube around the IC has been proposed to guide the flow inside GDWP and to reduce thermal stratification.

4. Study of steam mal-distribution in IC header and tube assembly of IC and its effect on heat transfer inside GDWP. Optimize the design of IC to achieve uniform steam distribution amongst the IC tubes.
5. Effect of local boiling in the water pool (GDWP) on heat transfer and thermal stratification.

In natural convective flows, turbulence is mainly concentrated in the thin region close to wall (heat source) and it is almost absent in the core. The velocity and temperature gradients are also very high in this region. Hence, most of the heat transfer occurs in this region. In order to accurately predict the near wall heat transfer, efficient modeling of this region is required. Based on this framework, the performance of various turbulence models has been investigated to study turbulent natural convection and near wall heat transfer. Four turbulence models such as SST $k-\omega$, standard $k-\varepsilon$, elliptic relaxation ($v2-f$) and low Reynolds $k-\varepsilon$ model by Launder and Sharma have been selected and their results have been compared with the experimental data of Gandhi et al., (2011). It was found that standard $k-\varepsilon$ model (with wall functions) was unable to capture the large velocity gradients (Fig 2A) near the heat source ($y^+ < 20$). The velocity gradients were under predicted (40%) near the heat source ($y^+ < 20$) and over predicted (15%) away from the heat source and results in 100% more heat transfer coefficient (HTC) as compared to experimental values (Fig 2B). The low Reynolds $k-\varepsilon$ model uses special damping functions to solve k and ε equation near the wall. As a result the turbulence was damped near the heat source. The low Reynolds $k-\varepsilon$ model and $v2f$ model over predict (20%) the velocity gradients (Fig 2A) near the heat source ($y^+ < 20$) and consequently over predict (10%) the HTC (Fig 2B). The SST $k-\omega$ model accurately (error of 5%) predicts the velocity gradients near the heat source and hence able to predict the transient HTC (Fig 2B) with an accuracy of 10%.



(A)



(B)

Fig 2: Comparison of turbulence models to study (A) radial distribution of Axial velocity and (B) transient volumetric average heat transfer coefficient (h),
(1) SST $k-\omega$ (2) low Re $k-\epsilon$ model (3) standard $k-\epsilon$ (4) $v2-f$ (5) experiment

Even though SST $k-\omega$ was found to be most adequate to simulate turbulent natural convection and near wall heat transfer in the small water pool [Gandhi et al., (2011)], the applicability of this model needs to be established for larger pools considering the geometry of GDWP of AHWR. For this purpose, experimental data from the literature [Aszodi et al., (2000) and Krepper et al., (2002)] have been used for validating the current CFD model. Single phase transient CFD simulations using SST $k-\omega$ turbulence model have been performed for all the cases. The transient temperature profiles predicted by CFD simulations in Fig 3 show that the maximum temperature and velocity gradient prevails in the vicinity of heat source and it becomes weak with an increase in the distance from the heat source. The overall result is that the total energy supplied to the system gets accumulated near the heat source and near the free surface region. The major portion of fluid in the bulk was not involved in the heat transfer process. Further, it results in non-uniform temperature distribution and hence thermal stratification. It was found that transient temperature profiles predicted by CFD simulations were in close agreement (7%) with experimental values and clearly indicates the stratified condition inside the tank and no bulk mixing. The benchmark studies indicated that CFD model is capable of predicting accurately the non-uniform temperature distribution and thermal stratification inside large water pool such as GDWP.

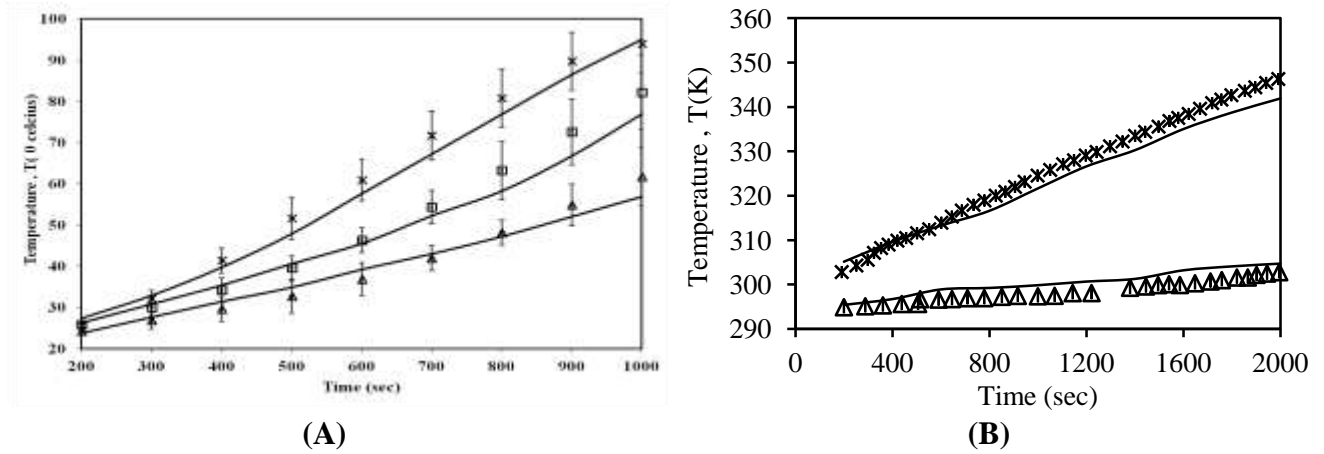


Fig 3: Comparison of present CFD model and experimental data for the temperature distribution for the geometry of (A) Aszodi et al., (2000); (B) Krepper et al., (2002).

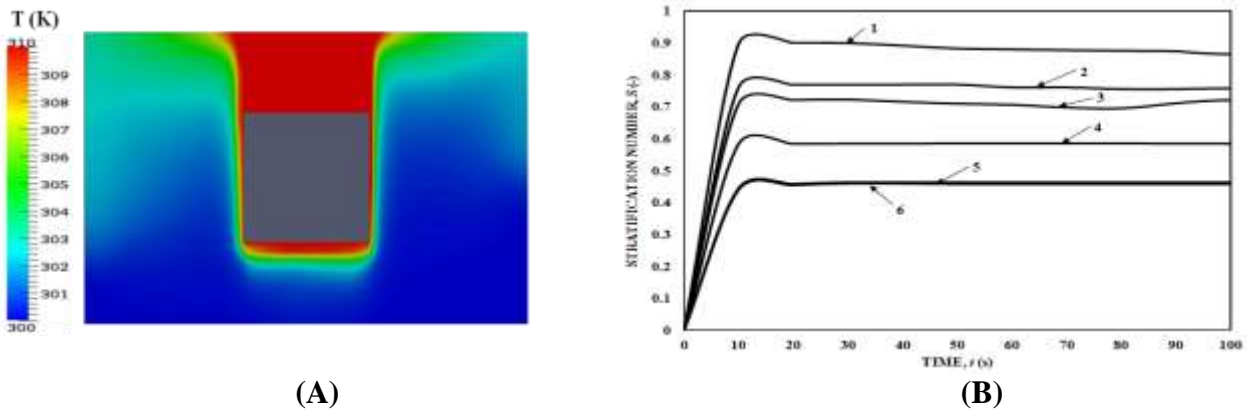


Fig 4: (A) Temperature contours for single heat source (IC1) at centre of GDWP (B) Effect of various designs on stratification number (S) with time (1) $IC1$; (2) $IC2$; (3) $IC2s0.1$; (4) $ICMs0.1$; (5) $DF1$; (6) $BDF3$;

Fig 4A shows typical temperature contours around the single IC tube inside GDWP. Due to concentrated heat source ($IC1$) at centre of GDWP, heat transfer was also concentrated in a very small volume near the IC. The liquid velocities were also very high near the heat source and it becomes weak away from the heat source. As the time progressed, the hot water gets accumulated near the top free surface. The non uniform temperature distribution results into thermal stratification which was quantified in terms of stratification number (S). The value of S varies from zero to one with zero representing no stratification (complete mixing) and one representing complete stratification. The value of S was found to be 0.87 for the $IC1$ [case (1) in Fig 4B] which indicates

highly stratified flow and poor mixing. In order to reduce S , it was thought desirable to have a distribution of heat sources inside GDWP in comparison of a single IC at centre. The distance between the two ICs was selected in such a way that the convective flow becomes very intense in this region which results in enhanced mixing and reduction in S . The heat source distribution ($IC2$) results in an enhancement in the average circulation velocity by 35% and reduction in S by 12% as compared to $IC1$ [case (2) in Fig 4B]. In the next step, the effect of vertical confinement has been studied by varying the submergence (s) depth of IC inside the GDWP ($IC2s0.1$). It was observed that higher submergence results in enhanced heat transfer and lowering of stratification. The submergence of IC results in 13% rise in average circulation velocity and reduction in S by 17% [case (3) in Fig 4B]. By combining the benefits of (1) distribution and (2) submergence of ICs, a new geometry (3) $ICMs0.1$ was considered which consists of 36 ICs placed at a distance of 0.1m from bottom of the tank. The presence of multiple ICs results into formation of multiple convective cells. The length of natural circulation loop (and hence the mixing length) gets reduced because of the multiplicity of convective cells. Thus the combination was found to result in 33% reduction in S for $ICMs0.1$ [case (4) in Fig 4B].

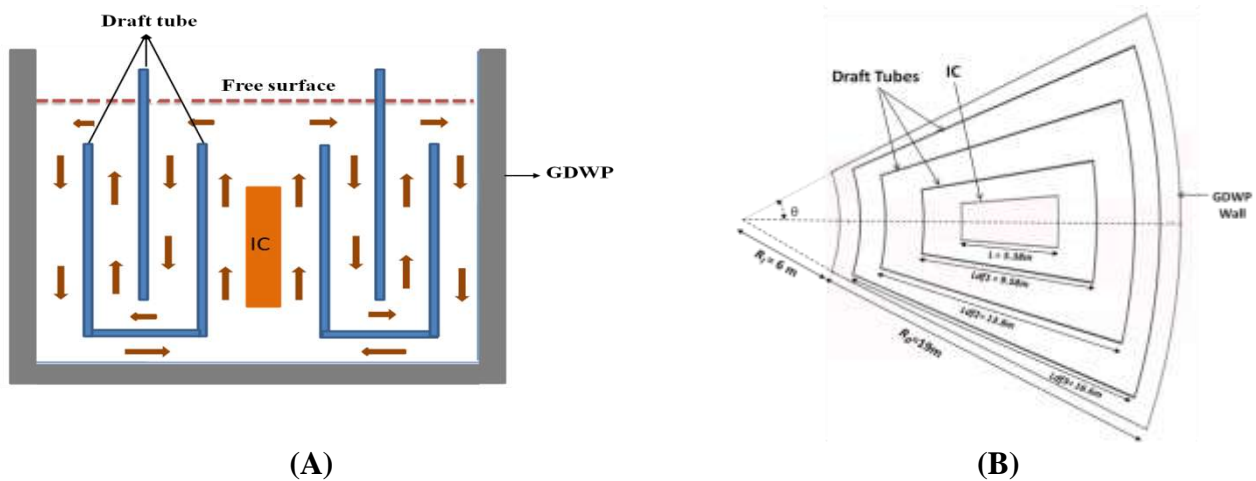


Fig 5: Schematic diagram of three draft tubes inside GDWP (A) Front View (B) Top view

In addition to the above two parameters (distribution and submergence), a new concept of employing draft tubes (Fig 5) around the IC tubes has been investigated. The draft tubes (Fig 5A)

provide multiple natural circulation loops around the IC tubes, thereby facilitating mixing of hot and cold fluid which further results in suppression of thermal stratification. For this purpose, two designs '*DF1*' and '*BDF3*' were considered. The *DF1* design consists of a single draft tube around the IC whereas the *BDF3* design consists of three draft tubes along with a baffle at the top. The fluid inside the draft tube is in direct contact with the heat source and hence it is at higher temperature and become lighter as compared to the fluid outside the draft tube. The temperature difference results into density difference. As a result, the lighter hot fluid rises inside the draft tube and descends in the annular region between the wall and the draft tube. The distance between the first draft tube and the IC is the most crucial parameter in the design of draft tube. In order to avoid the formation of recirculation cells within the draft tube, it is deliberately kept closer to the IC. Presence of draft tube (*DF1*) gives directional motion from bottom to top (or top to bottom) and improves mixing in the liquid phase and reduces S by 46% [case (5) in Fig 4B]. In addition, the combination of three draft tubes and baffle (*BDF3*) prevents the accumulation of hot fluid at the top by providing a flow path to it and results in 40% reduction in stratification [case (6) in Fig 4B].

In all the above cases, vertical IC tubes were considered. The phenomenon of thermal stratification was more pronounced in the presence of vertical heat source (IC). As the hot fluid rises upwards along the length of IC, temperature difference (ΔT) between the IC and the nearby fluid decreases which further results in a decrease in heat transfer rate. The effect of inclination ($\alpha = 0^\circ, 15^\circ, 30^\circ, 45^\circ, 60^\circ, 75^\circ, 90^\circ$) of condenser tube on single phase natural convection and heat transfer was investigated. As the angle of inclination ($\alpha > 15^\circ$) of IC tube increases, the primary flow (along the tube length due to pressure gradient) decreases and the secondary flow (along vertical direction due to buoyancy forces) become stronger. Further, it enhances the liquid convection at the tube bottom and prevents the liquid convection at the top of the tube. The enhanced liquid convection results in enhanced heat transfer and a decrease in the fluid temperature at the tube bottom. The thermal stratification was found to be minimum for $\alpha = 90^\circ$ and maximum for $\alpha = 15^\circ$. For the horizontal

heated tube ($\alpha = 90^\circ$), there was no primary flow and the secondary flow due to buoyancy forces acts completely perpendicular to the tube. Hence, results in enhanced heat transfer and reduction in stratification.

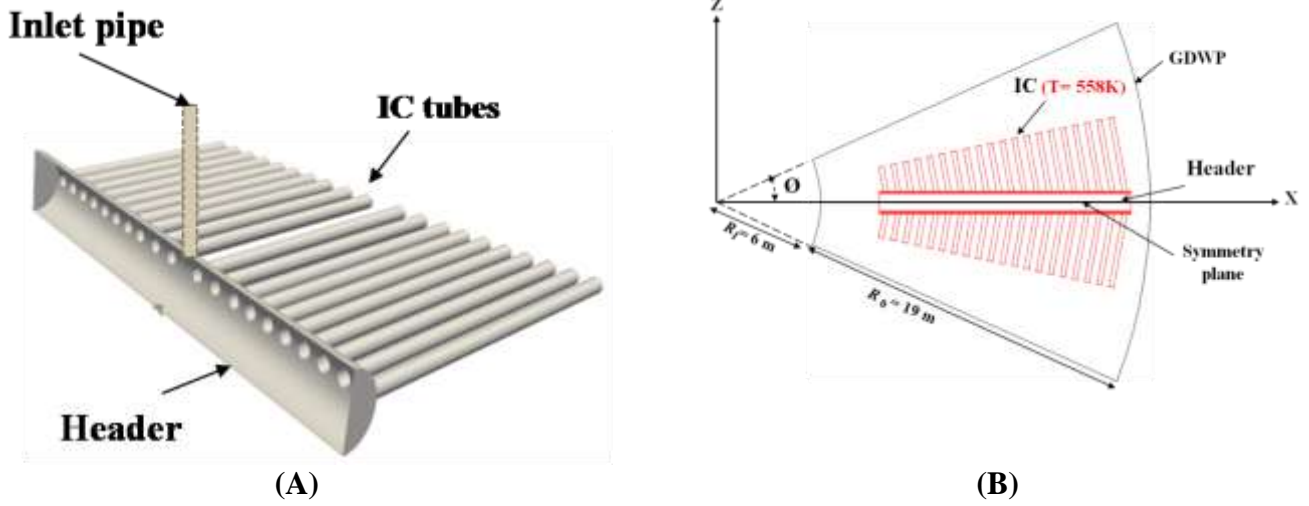


Fig 6: (A) Schematic of the new design of IC with inclined IC tubes and (B) top view of the IC inside GDWP

The steam distribution in header and tubes assembly of IC (Fig 6) consisting of inclined IC tubes were investigated. Non-uniform steam distribution lowers the decay heat removal efficiency of the IC because some portion of the IC becomes ineffective. The effects of design parameters (tube pitch, tube diameter, inlet tube diameter, perforated plate inside header) on the extent of non-uniformity (ENU) have been investigated over a wide range. The ENU was very high, when the tube 1 was placed near the inlet tube. Fig 7A shows the vortex formation inside the header and a dead zone was formed for the reverse flow, thus fluid is distributed very non uniformly in axial direction. It was found that ENU decrease with increase in the distance between the inlet tube and tube 1. The ENU was around 30% when the tube 1 is placed at 2m away from the inlet tube. In order to further decrease the ENU, tube diameter has been changed ($0.1 < d_t < 0.4\text{m}$). The increase in tube diameter results in increase in pressure recovery and decrease in frictional losses. The ENU decreases with increase in tube diameter from 0.1m to 0.2m. The ENU was 10% for tube diameter 0.2m. Further

increase in tube diameter results in increase in ENU. Hence, the optimum tube diameter (d_i) is 0.2m. The next step is to study the effect of inlet tube diameter on ENU. The increase in inlet tube diameter results in further decrease in ENU. The effect of perforated plate inside the header has also been studied. The perforated plate consists of small size holes (4mm) at center part and large size holes (20mm) near the tubes. The vortex in front of the perforated plate vanishes compared to that of conventional header with no plate. Hence, the fluid was distributed more uniformly.

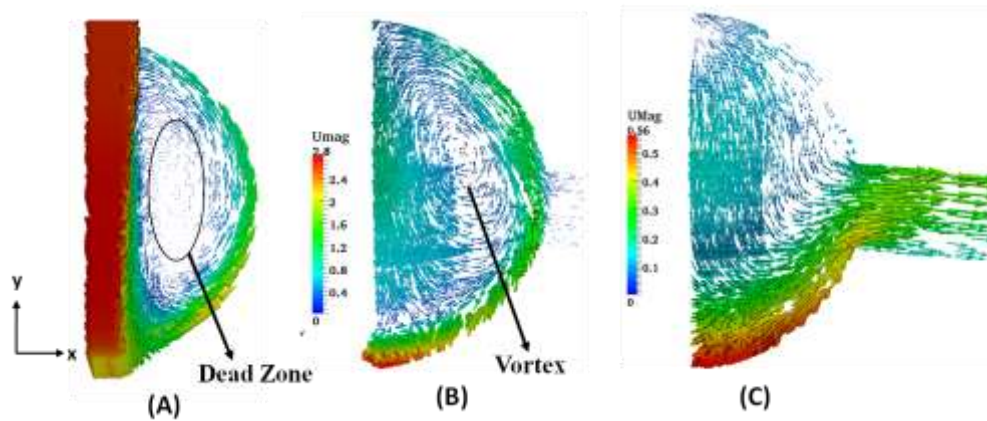


Fig 7: Flow distribution inside header of spider shaped IC at different cross sections
(A) $z = 0$ (at centre); (B) $z = 0.5\text{m}$; (C) $z = 2.5\text{m}$.

Since the decay steam is at very high temperature (285°C , 7MPa) inside the condenser tubes, sub-cooled nucleate boiling occurs on the tube surfaces. The mechanism of sub cooled nucleate boiling results in enhanced heat transfer due to evaporation. The heat transfer can be enhanced further when the bubble slides over the tube surface. In addition to the enhanced heat transfer, the bubble sliding motion also results in improved thermal mixing inside the tank and hence a reduction in the thermal stratification. The effect of inclination of condenser tube on sliding bubble dynamics and associated heat transfer has been studied for seven tube inclination angles (α) (in the range $0^\circ \leq \alpha \leq 90^\circ$). The major heat transfer mechanism was found to be the liquid agitation caused by sliding bubbles on the tube surface. The heat transfer contribution due to evaporation was found to be very small because of highly sub-cooled ($\Delta T_{sub} = 70\text{K}$) liquid inside the GDWP. The bubble sliding length (Fig 8) at the tube top was found to decrease and at the tube bottom was found to increase with increase in

inclination angle (α). The increase in angle of inclination (α) of IC tubes results in enhanced heat transfer and reduction in thermal stratification. The heat transfer was found to be maximum for $\alpha = 75^\circ$ and minimum for $\alpha = 30^\circ$. The enhanced transfer at $\alpha = 75^\circ$ ensures excellent thermal mixing and hence results in reduction in thermal stratification. The stratification number (S) was found to be 0.35 for $\alpha = 75^\circ$.

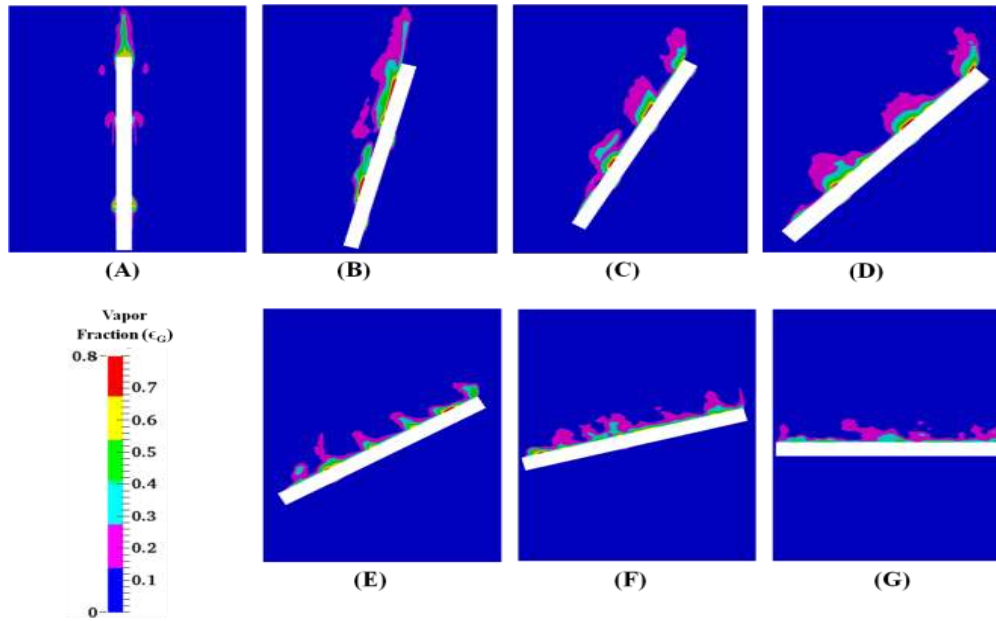


Fig 8: Vapor Fraction Contours for different inclination angles at $t=10s$ along symmetry plane:

(A) $\alpha=0^\circ$; (B) $\alpha=15^\circ$; (C) $\alpha=30^\circ$; (D) $\alpha=45^\circ$; (E) $\alpha=60^\circ$; (F) $\alpha=75^\circ$; (G) $\alpha=90^\circ$

Based on the above findings, an improved design of IC (Fig 6B) has been proposed which consists of a steam header ($D=0.6m$) and a bundle of 40 inclined ($\alpha=75^\circ$) tubes uniformly distributed inside GDWP and submerged towards the tank bottom to prevent non-uniform temperature distribution and hence thermal stratification. The effect of two phase flow (boiling) on natural convection and heat transfer has been studied for a new design of IC. It was found that the new design of IC condenser is able to remove more than 50 per cent of decay heat in 100s.

The conclusions of the thesis are as follows:

1. The assessment of various turbulence models implies that SST $k-\omega$ model is capable of accurately predicting the near wall fluid flow and heat transfer. Hence, SST $k-\omega$ model was used to study turbulent natural convection inside GDWP.

2. The detailed CFD analysis of 3D temperature and flow distribution indicates GDWP indicates thermal stratification and poor mixing. The optimization in the design of IC by distribution and submergence of heat source results in enhanced mixing and reduction in stratification number by 33%.
3. A new concept of employing multiple draft tubes around IC is proposed in this thesis. Presence of appropriate size of draft tube at an optimum distance from the IC tubes results in additional driving force apart from buoyancy and results in reduction in stratification number by 46% and 40% for single and three draft tube design. In addition to this, it also reduces the size of hot dead zones near the top free surface.
4. The effect of inclination of condenser tubes on single phase natural convection and heat transfer has been studied. The relationship between inclination angle and thermal stratification phenomenon inside the GDWP has been established. The thermal stratification phenomenon was found to be maximum at $\alpha = 15^0$ and minimum at $\alpha = 90^0$.
5. The steam mass distribution inside IC header and tube assembly was investigated. The uniform steam distribution inside the IC tube bundles has been achieved and the maximum extent of non uniformity (ENU) was found to be 10 %.
6. The effect of local boiling on heat transfer inside GDWP for inclined IC tubes was studied. The major heat transfer mechanism was found to be liquid agitation caused by bubble sliding motion. The heat transfer coefficient was found to be maximum at $\alpha = 75^0$ and minimum at $\alpha = 30^0$.
7. A new and improved design of IC is proposed which ensure efficient decay heat removal and mitigation of thermal stratification.

LIST OF FIGURES

No.	Title	Page No.
Figure 2.1	(A) Schematic of the experimental set up consists of a water tank fitted with a centrally heated tube (B) top view of the set up along with heated tube, tank wall and symmetry planes	22
Figure 2.2	Temperature Contours for different turbulence models at $t=100s$ for symmetry plane (S1): (A) standard $k-\varepsilon$ (B) SST $k-\omega$ (C) low Re $k-\varepsilon$ model (D) $v2-f$ (E) RSM	25
Figure 2.3	Comparison of turbulence models to study distribution of axial velocity at $z/H=0.5$ at $t=100s$, (1) SST $k-\omega$ (2) low Re $k-\varepsilon$ model (3) standard $k-\varepsilon$ (4) $v2-f$ (5) RSM (6) Experimental data	26
Figure 2.4	Comparison of turbulence models to study radial distribution of turbulent kinetic energy (k) at $z/H=0.5$ at $t=100s$, (1) SST $k-\omega$ (2) low Re $k-\varepsilon$ model (3) standard $k-\varepsilon$ (4) $v2-f$ (5) RSM	28
Figure 2.5	Comparison of turbulence models to study transient volumetric average heat transfer coefficient (h), (1) SST $k-\omega$ (2) low Re $k-\varepsilon$ model (3) standard $k-\varepsilon$ (3) $v2f$ (5) RSM (6) Experimental data	29
Figure 2.6	Schematic of the experimental set up of Gandhi et al. (2013)	31
Figure 2.7	Comparison of present CFD model and experimental data for the temperature distribution for the geometry of Gandhi et al., (2013); (1) $x/W=0.01$, experiment (\square), OpenFOAM-1.6 (—); (2) $x/W=0.1$, experiment (Δ), OpenFOAM-2.2 (—)	32
Figure 2.8	Schematic of the (A) experimental facility of Aszodi et al. (2000) along with (B) Grid generation	32
Figure 2.9	Comparison between CFD predictions and experimental data of Aszodi et al., (2010); for the transient temperature distribution at 1mm away from wall at different vertical positions	33
Figure 2.10	Schematic of the experimental test facility of Krepper et al. (2002)	34
Figure 2.11	Schematic of the water tank along with thermocouples locations	34
Figure 2.12	Schematic of Grid used for CFD calculation	34
Figure 2.13	Comparison of present CFD model and experimental data for the temperature distribution for the geometry of Krepper et al., (2002); Experimental value (x) at $y=1.4m$, (Δ) at $y=1.04m$, CFD (—)	35

Figure 3.1	Schematic of Passive decay heat removal system	38
Figure 3.2	Schematic of GDWP pool with Isolation condensers (ICs)	38
Figure 3.3	Schematic of Isolation Condenser (IC)	39
Figure 3.4	Schematic diagram (Top view) for various designs of ICs (A) ' <i>IC1c1.4</i> ' (B) ' <i>IC2c0.5</i> '	49
Figure 3.5	Schematic diagram for <i>ICMc0.1</i> design (A) Isometric view (B) Top view	50
Figure 3.6	Schematic diagram of three draft tube with baffle (BDF3) inside GDWP (A) Front view ; (B) Top view	53
Figure 3.7	Mesh generation algorithm	55
Figure 3.8	Schematic of Boundary conditions for ' <i>IC1</i> ' design.	57
Figure 3.9	Effect of symmetry boundary condition on flow distribution at $t=100s$ at IC top $z = 2.31$ m (A) 1/16th sector of GDWP with symmetry boundary condition (B) 1/8th sector of GDWP	59
Figure 3.10	Effect of symmetry boundary condition on radial (r) distribution of axial velocity at $t=100s$ at $z = 2.31$ m (1) 1/16th sector of GDWP with symmetry boundary condition (2) 1/8th sector of GDWP	60
Figure 3.11	Schematic of grid size for ' <i>DF1</i> ' design	62
Figure 3.12	Effect of grid size for ' <i>DF1</i> ' design: Variation in axial velocity at $t=40s$ for symmetry plane ($\theta = 0^\circ$) with dimensionless radial distance at $z/H=0.6$; for different grid sizes (1) 2M (2) 4M (3) 5M (4) 6M.	63
Figure 3.13	(A) Time step independent studies at four different time steps for ' <i>DF1</i> ' design (1) $10^{-6}s$ (2) $10^{-5}s$ (3) $5 \times 10^{-5}s$ (4) $10^{-4}s$; (B) Time varying temperature profiles for symmetry plane ($\theta = 0^\circ$) with dimensionless radial distance at $z/H=0.5$; (1) 1s (2) 4s (3) 8s (4) 10s (3) 30s (4) 50s.	65
Figure 3.14	Temperature Contours at three different tangential directions at $t=100s$ (A) ' <i>IC1c1.4</i> , (B) ' <i>IC2 c1.4</i> ; (1) $\theta = 00$; (2) $\theta = 11.250$; (3) $\theta = 21.50$	66
Figure 3.15	Temperature Contours at $t=100s$ at symmetry plane and $\theta = 00$. (A) ' <i>IC1c1.4</i> , (B) ' <i>IC2c1.4</i> , (C) ' <i>IC1c0.6</i> , (D) ' <i>IC2c0.6</i> ,	68
Figure 3.16	Temperature Contours and (B) Flow distribution at symmetry plane ($\theta = 0^\circ$) at $t=100s$ (1) ' <i>IC1C1.4</i> ', (2) ' <i>IC2C1.4</i> '.	68
Figure 3.17	Variation in temperature with dimensionless radial distance at $t=100s$ for symmetry plane ($\theta = 0^\circ$) (A) ' <i>IC1c1.4</i> ', (B) ' <i>IC2c1.4</i> '; (1) $z/H = 0.04$; (2) $z/H = 0.26$; (3) $z/H = 0.5$; (4) $z/H = 0.74$; (5) $z/H = 0.92$;	69

Figure 3.18	Variation in axial velocity with dimensionless radial distance at $t=100s$ for symmetry plane ($\theta = 0^0$) (A) 'IC1c1.4', (B) 'IC2c1.4'; (1) $z/H = 0.04$; (2) $z/H = 0.26$; (3) $z/H = 0.5$; (4) $z/H = 0.74$; (5) $z/H = 0.92$;	70
Figure 3.19	Variation in (A) Turbulent kinetic energy (k) (B) Ratio of turbulent and kinematic viscosity (ν_t / ν) with dimensionless radial distance for 'IC1c1.4' at $z/H = 0.5$ and $\theta = 0^0$ at $t=100s$	71
Figure 3.20	Variation in (A) Turbulent kinetic energy (k) (B) Ratio of turbulent and kinematic viscosity (ν_t / ν) with dimensionless tangential distance (θ/θ_t) for 'IC1c1.4' at $z/H=0.5$ and $r/R=0.5$ at $t=100s$	73
Figure 3.21	Temperature Contours for 'IC1c1.4' at $t=100s$ for symmetry plane ($\theta = 0^0$). Calculation of stratification number (S).	75
Figure 3.22	Effect of various designs on stratification number (S) with time (1) IC1c1.4; (2) IC1c0.6; (3) IC2c1.4; (4) IC2c0.6; (5) IC2c0.1; (6) ICMc0.1; (7) DF0; (8) DF1; (9) BDF3;	78
Figure 3.23	Temperature Contours for 'ICMc0.1' design. (A) $t=100s$, (B) $t=300s$, (1) $z/H = 0.90$; (2) $z/H = 0.44$; (3) $z/H = 0.02$.	79
Figure 3.24	Variation in axial velocity with dimensionless radial distance for 'ICMc0.1' at $t=100s$ for symmetry plane ($\theta = 0^0$). (1) $z/H = 0.01$; (2) $z/H = 0.24$; (3) $z/H = 0.48$; (4) $z/H = 0.62$; (5) $z/H = 0.96$;	79
Figure 3.25	Temperature contours for different draft tube designs at $t = 50s$ at symmetry plane ($\theta = 00$) (1) DF0; (2) DF1; (3) BDF3	81
Figure 3.26	Flow distribution for different draft tube designs at $t = 50s$ at symmetry plane ($\theta= 0^0$) (1) DF0; (2) DF1; (3) BDF3	82
Figure 3.27	Variation of average heat transfer coefficient (h) with time (1) DF0 (2) DF1	83
Figure 3.28	Temperature Contours at $z/H=0.562$ for $t=10s, 20s, 30s, 40s, 50s, 60s$. (A) DF0; (B) DF1	85
Figure 4.1	(A) Schematic of pilot scale GDWP with single inclined IC tube and (B) Grid generation	94
Figure 4.2	Effect of first node distance from wall on non dimensional velocity for inclined heat source ($\alpha = 45^0$) at $t=50s$ for different grid sizes and turbulence models (1) 0.6mm, $k-\varepsilon$; (2) 0.3mm, $k-\varepsilon$; (3) 0.15mm, $k-\varepsilon$; (4) 0.15mm, LRR; (5) 0.15mm, SST $k-\omega$	95
Figure 4.3	Effect of first node distance from wall on (A) turbulent kinetic energy (k) and	97

	(B) dissipation rate (ε) for inclined heat source ($\alpha = 45^\circ$) at $t = 50$ s for different grid sizes and turbulence models (1) 0.6mm, $k-\varepsilon$; (2) 0.3mm, $k-\varepsilon$; (3) 0.15mm, $k-\varepsilon$; (4) 0.15mm, LRR; (5) 0.15mm, SST $k-\omega$	
Figure 4.4	Effect of grid size for inclined heat source ($\alpha = 45^\circ$): Variation in (A) Axial temperature and (B) Axial velocity at 2mm away from the IC tube ($\theta = 180^\circ$): at $t = 50$ s for different grid sizes (1) 0.3M; (2) 0.6M; (3) 0.8M.	98
Figure 4.5	Temperature Contours at different inclination angles at $t = 100$ s along plane (P): (A) $\alpha = 0^\circ$; (B) $\alpha = 15^\circ$; (C) $\alpha = 30^\circ$; (D) $\alpha = 45^\circ$; (E) $\alpha = 60^\circ$; (F) $\alpha = 75^\circ$; (F) $\alpha = 90^\circ$	100
Figure 4.6	Flow distribution at different inclination angles at $t = 100$ s along plane (P): (A) $\alpha = 0^\circ$; (B) $\alpha = 15^\circ$; (C) $\alpha = 30^\circ$; (D) $\alpha = 45^\circ$; (E) $\alpha = 60^\circ$; (F) $\alpha = 75^\circ$; (F) $\alpha = 90^\circ$	100
Figure 4.7	Effect of inclination of IC tube on azimuthal heat transfer coefficient at $t = 100$ s; (1) $\alpha = 0^\circ$; (2) $\alpha = 15^\circ$; (3) $\alpha = 30^\circ$; (4) $\alpha = 45^\circ$; (5) $\alpha = 60^\circ$; (6) $\alpha = 75^\circ$; (7) $\alpha = 90^\circ$	102
Figure 4.8	Effect of inclination of IC tube on (A) Axial temperature and (B) Axial velocity at $t = 100$ s and 1mm away from the tube for different inclination angles; (1) $\alpha = 0^\circ$; (2) $\alpha = 15^\circ$; (3) $\alpha = 30^\circ$; (4) $\alpha = 45^\circ$; (5) $\alpha = 60^\circ$; (6) $\alpha = 75^\circ$; (7) $\alpha = 90^\circ$	104
Figure 4.9	Isotherms at different inclination angles at $t = 100$ s along plane (P): (a) $\alpha = 0^\circ$; (b) $\alpha = 15^\circ$; (c) $\alpha = 30^\circ$; (d) $\alpha = 45^\circ$; (e) $\alpha = 60^\circ$; (f) $\alpha = 75^\circ$	105
Figure 4.10	Turbulent kinetic energy Contours at different inclination angles at $t = 100$ s along plane (P): (A) $\alpha = 0^\circ$; (B) $\alpha = 15^\circ$; (C) $\alpha = 30^\circ$; (D) $\alpha = 45^\circ$; (E) $\alpha = 60^\circ$; (F) $\alpha = 75^\circ$; (F) $\alpha = 90^\circ$	106
Figure 4.11	Transient Variation of (A) Average heat transfer coefficient (h_{avg}) and (B) Average Turbulent kinetic energy for different inclination angles; (1) $\alpha = 0^\circ$; (2) $\alpha = 15^\circ$; (3) $\alpha = 30^\circ$; (4) $\alpha = 45^\circ$; (5) $\alpha = 60^\circ$; (6) $\alpha = 75^\circ$; (7) $\alpha = 90^\circ$	108
Figure 4.12	Effect of inclination of IC tube on thermal stratification (S) for small scale GDWP	110
Figure 4.13	(A) Schematic of the (A) Plan view of $1/8^{\text{th}}$ section of real size GDWP and (B) Isolation condenser with inclined ($\alpha = 75^\circ$) IC tubes	112
Figure 4.14	(A) Schematic of the (A) $1/16^{\text{th}}$ of real size GDWP with IC and (B) Grid generation along Plane 1	113
Figure 4.15	Azumithal variation of (A) Temperature and (B) Turbulent kinetic energy (k)	115

for new design of IC at 2mm away from the IC tubes at $t = 90s$

Figure 4.16	Radial distribution of (A) Temperature and (B) Axial velocity at $z/H=0.2$ along plane 1 at $t = 50s$ for New design of IC	117
Figure 4.17	Transient variation of isotherms for new design of IC along Plane 1: (a) $t = 10s$; (b) $t = 20s$; (c) $t = 30s$; (d) $t = 40s$; (e) $t = 50s$	118
Figure 4.18	Transient variation of Flow distribution for new design of IC along Plane 1: (a) $t = 10s$; (b) $t = 20s$; (c) $t = 30s$; (d) $t = 40s$	119
Figure 4.19	(A) Flow distribution and (B) Temperature Contours for new design of IC along Plane 2	120
Figure 4.20	Transient variation of (A) average heat transfer coefficient (h_{avg}) and (B) Stratification number (S) for real size of GDWP	122
Figure 5.1	Schematic diagram of conventional design of IC	126
Figure 5.2	Flow distribution inside header for conventional IC at different cross sections (A) $z = 0$ (at centre); (B) $z = 0.5m$; (C) $z = 2.5m$.	130
Figure 5.3	Extent of non-uniformity for conventional header	131
Figure 5.4	Effect of 1 st tube pitch (D_{pt1}) on extent of non-uniformity (ENU): (1) $D_{pt1} = 1m$; (2) $D_{pt1} = 1.3m$; (3) $D_{pt1} = 1.5m$; (4) $D_{pt1} = 1.7m$; (5) $D_{pt1} = 2m$	131
Figure 5.5	Schematic diagram of (A) Converging header (H1) (B) Cylindrical header (C) Converging header (H2)	132
Figure 5.6	Effect of header shape on (A) Extent of non-uniformity (ENU) and (B) Pressure distribution (1) Converging header (H1); (2) Cylindrical header; (3) Converging header (H2)	134
Figure 5.7	Effect of inlet tube diameter (d_{in}) on (A) Extent of non-uniformity (ENU) and (B) Pressure distribution; (1) $d_{in} = 0.15m$; (2) $d_{in} = 0.2m$; (3) $d_{in} = 0.25m$;	135
Figure 5.8	Effect of number of tubes on Extent of non-uniformity (ENU); (1) 40 tubes; (2) 54 tubes; (3) 60 tubes;	136
Figure 5.9	Effect of header diameter (d_h) on (A) Extent of non-uniformity (ENU) and (B) Pressure distribution; (1) $d_h = 0.4m$; (2) $d_h = 0.6m$; (3) $d_h = 0.8m$;	137
Figure 5.10	Schematic diagram of IC along with perforated baffle inside the header	138
Figure 5.11	Comparison of flow distribution inside header (A) Conventional header (B) Header with perforated baffle at different cross sections; (1) $z = 0$ (at centre); (2) $z = 0.5m$; (3) $z = 2.5m$.	139
Figure 5.12	Effect of header configuration on (A) Extent of non-uniformity (ENU) and (B)	140

	Pressure distribution (1) Conventional header; (2) Cylindrical header along with perforated baffle	
Figure 6.1	Comparison of CFD model and experimental data for azimuthal (θ) variation of average heat transfer coefficient for Kang, 2013; Experimental value (\square) and CFD (—)	165
Figure 6.2	Comparison of present CFD model and experimental data of Ganguli et al. (2010) to study transient heat flux distribution. Experimental value (1) Natural Convection (\blacksquare); (2) Quenching (\blacktriangle); (3) Evaporation (\bullet), CFD (—)	165
Figure 6.3	(A) Schematic of pilot scale GDWP with single inclined IC tube and (B) Grid generation	166
Figure 6.4	Effect of grid size for inclined heat source ($\alpha = 45^\circ$): Variation in (A) Axial temperature and (B) Axial velocity at 1mm away from the heat source at $t=8s$ for different grid sizes (1) 0.3M; (2) 0.6M; (3) 0.8M.	170
Figure 6.5	Azimuthal variation of fluid temperature at 1mm away from the tube at $t=10s$ for different inclination angle (1) $\alpha=0^\circ$; (2) $\alpha=15^\circ$; (3) $\alpha=30^\circ$; (4) $\alpha=45^\circ$; (5) $\alpha=60^\circ$; (6) $\alpha=75^\circ$; (7) $\alpha=90^\circ$	171
Figure 6.6	Vapor Fraction Contours for different inclination angles at $t=10s$ along symmetry plane: (A) $\alpha=0^\circ$; (B) $\alpha=15^\circ$; (C) $\alpha=30^\circ$; (D) $\alpha=45^\circ$; (E) $\alpha=60^\circ$; (F) $\alpha=75^\circ$; (F) $\alpha=90^\circ$	172
Figure 6.7	Effect of inclination of IC tube on (A) and (B) Axial temperature and (C) and (D) Axial velocity at $t=10s$ and 1mm away from the tube for different inclination angles; (1) $\alpha=0^\circ$; (2) $\alpha=15^\circ$; (3) $\alpha=30^\circ$; (4) $\alpha=45^\circ$; (5) $\alpha=60^\circ$; (6) $\alpha=75^\circ$; (7) $\alpha=90^\circ$	174
Figure 6.8	Transient vapor fraction contour and fluid flow perpendicular to the tube for inclined ($\alpha = 60^\circ$) tube	177
Figure 6.9	Transient vapor formation along the tube length for inclined ($\alpha = 60^\circ$) tube at symmetry plane	178
Figure 6.10	Turbulent kinetic energy contours for different inclination angles at $t=10s$ along symmetry plane : (A) $\alpha=0^\circ$; (B) $\alpha=15^\circ$; (C) $\alpha=30^\circ$; (D) $\alpha=45^\circ$; (E) $\alpha=60^\circ$; (F) $\alpha=75^\circ$; (F) $\alpha=90^\circ$	179
Figure 6.11	Transient variation of (A) Total heat transfer coefficient (h_{avg}) (B) Evaporation heat transfer coefficient (h_{eva}) with time for different inclination angles;	182

(1) $\alpha = 0^0$; (2) $\alpha = 15^0$; (3) $\alpha = 30^0$; (4) $\alpha = 45^0$; (5) $\alpha = 60^0$; (6) $\alpha = 75^0$; (7) $\alpha = 90^0$

Figure 6.12	Effect of inclination of IC tube on thermal stratification (S) at $t = 10s$	184
Figure 6.13	Modelling: (A) differential control volume of the condensate film inside the tube, (B) distribution of condensate inside the tube and (C) condensate layer at lowermost point of tube	186
Figure 6.14	(A) Schematic of the (A) top view of large scale GDWP and (B) Isolation condenser with inclined ($\alpha = 75^0$) IC tubes	188
Figure 6.15	Distribution of condensate inside IC header for new IC design	189
Figure 6.16	Transient variation of Vapor Fraction for spider shape IC along Plane 1: (a) $t = 40s$; (b) $t = 60s$; (c) $t = 80s$; (d) $t = 100s$	191
Figure 6.17	Radial distribution of Axial velocity at different axial locations (1) $z/H = 0.24$, (2) $z/H = 0.4$; (3) $z/H = 0.6$; (4) $z/H = 0.8$ at $t = 60s$ along plane 1 for new design of IC;	193
Figure 6.18	Transient variation of (A) Total heat transfer coefficient (h_{avg}) (B) Enthalpy decay for new design of IC	195

LIST OF TABLES

Table 2.1	Governing equations for full buoyancy model	13
Table 2.2	Governing equations with Boussinesq approximation	13
Table 2.3	Details of boundary conditions	21
Table 2.4	Governing equations for single phase CFD simulations	23
Table 2.5	Details of experimental situations of various authors	30
Table 3.1	Summary of literature survey	43
Table 3.2	Physical properties of fluid used for CFD simulations	47
Table 3.3	Governing equations for single phase CFD simulations	47
Table 3.4	Design details of different designs of Isolation Condensers and Draft Tubes	51
Table 3.5	Details of the boundary conditions	58
Table 3.6	Circulation flow rate and mixing time	74
Table 4.1	Design details of pilot scale and large scale GDWP and Isolation condenser (ICs)	93
Table 4.2	Details of the boundary conditions for pilot scale GDWP	93
Table 4.3	Details of the boundary conditions for large scale GDWP	114
Table 5.1	Details of the boundary conditions for conventional design of IC	127
Table 6.1	Governing Equations for two phase CFD simulations using Mixture model	151
Table 6.2	Modeling heat flux at the tube wall for two phase CFD simulations (boiling phenomenon)	157
Table 6.3	Physical properties of fluid used for CFD simulations	162
Table 6.4	Details of experimental situations of various authors	163
Table 6.5	Design details of pilot scale and large scale GDWP and Isolation condenser (ICs)	167
Table 6.6	Details of the boundary conditions for pilot scale GDWP	168
Table 6.7	Summary of Literature survey on condensation heat transfer inside inclined tubes	187
Table 6.8	Comparison of new IC design and conventional IC design	190
Table 6.9	Details of the boundary conditions for large scale GDWP	191

CHAPTER 1

INTRODUCTION

1.1. Motivation

Energy availability has been universally recognized as one of the most important factors affecting economic growth and human development. There is a strong relationship between economic development and energy consumption (India core, 2015). Growth and global competitiveness of an economy hinges on the availability of cost effective and sustainable energy sources. More than 35% of global electricity consumption is in the form of electricity; and this number for a given region correlates strongly with the standard of living in that region. Irrespective of the source, it takes a significant amount of energy to make electricity. Further, a significant amount of energy is lost in the electricity generation process. For example, a new turbine powered by coal or nuclear (which produces about 55% of global electricity) is, at most 40% efficient, while natural gas plants have a peak efficiency of 60%. Further, as much as 15% of electricity produced is lost in transmission to the end-users.

In recent years, energy demand increases drastically and it is mainly due to increase in the population and the standard of living. At present most of the energy (specifically electrical) demand is fulfilled by use of fossil fuels (coal, liquid and natural gas). However, the uses of fossil fuels have concerns over global warming and pollutions. Therefore, it is important to see new and alternate energy source. One such an alternate energy source is nuclear energy for electricity generation. However, the current available technologies and reactors may not meet the required demand. In addition, there are lot of concerns related to plant safety, radioactive waste disposal, and nuclear material proliferation. Moreover, the explosions at Japan's Fukushima Daiichi nuclear power plant in

aftermath of the March 2011 earthquake and tsunami could have long implications for the use of nuclear energy.

1.2 Importance of Passive Safety Systems

In the core of nuclear reactors, when a shutdown occurs, the fission chain reaction is stopped. However, because of decay heat (approximately 6% of operating power at shutdown) release by fuel, the thermal power generation continues at considerable levels for a long time. If effective removal of the decay heat is not assured, the reactor core may get damaged and may result in release of fission products and radionuclides. In order to avoid the occurrence of a severe accident, many advanced nuclear reactors adopt a methodology of providing a passive safety system to remove the decay heat during accidental conditions. The use of passive safety systems eliminate the costs associated with the installation, maintenance and operation of active safety systems that require multiple pumps with independent and redundant electric power supplies. As a result, passive safety systems are being considered for many advanced reactors. During passive decay heat removal system (PDHRS) operation, the decay heat generated from the core is removed by coolant (subcooled water initially at a temperature of 258°C and 7 MPa pressure) circulating in the primary system. In the process of heat transfer, the coolant is converted into two phase mixture which is then separated into steam and water inside a steam drum. The steam thus formed is injected into and condensed in the PDHRS heat exchangers called Isolation condensers (ICs) submerged in a large pool of water called the Gravity Driven Water Pool (GDWP) which is considered as a near infinite heat sink. The condensing heat is transferred to the GDWP, the heat of which is removed by a heating and evaporation of the stored inventory. Considering the weak driving forces of passive systems based on natural circulation, careful design of heat exchanger is necessary to facilitate the efficient decay heat removal. Such a PDHRS also cools the core to the desired temperature with a continuous reduction in saturation temperature with respect to time.

1.3 Natural Convection

Natural convection based systems are getting importance due to its high reliability, low maintenance cost and absence of moving parts. In natural convection, a flow is arising naturally due to the effect of a density difference in a body force field (e.g. gravity). The density difference may arise due to a temperature gradient or due to heterogeneous multiphase flow. The presence of an adequate amount of heat flux in an enclosed region causes the hot fluid to rise due to set up of natural convection currents and, in time, the hotter (lighter) fluid forms a layer over the colder (heavier) fluid. This situation is known as thermal stratification. Thermal stratification is undesirable in many practical instances like storage of liquid hydrogen, cooking and heat dissipation in water reservoirs (like passive decay heat removal systems in nuclear power plants, etc.). This is because, in the thermally stratified systems, heat transfer rate decreases (Ganguli et al., 2010). For instance, in a cooker heated from the sides (by steam), thermal convection currents are suppressed and may cause food in the central of wider vessel to remain uncooked (Joshi et al., 2012). Another example is that of passive decay heat removal systems.

1.4 Critical Issues in the Design of PDHRS

(1) In a PDHRS, the heat transfer from the isolation condenser (ICs) is concentrated in a limited zone of a large water pool (GDWP) in terms of volume and results into the three dimensional flow and temperature fields. The non-uniform temperature distribution results in thermal stratification due to accumulation of hot (lighter) fluid at the top and cold (heavier) fluid at the bottom. The heat transfer rate can get compromised by such temperature stratifications.

(2) Under strong temperature stratification conditions, the fluid at the top of the pool reaches the saturation temperature much earlier as compared to the case of homogeneous temperature distribution. The early water evaporation at the tank top results in over-pressurization of containment building.

(3)The stratification is also not desirable because of the limitation imposed by the GDWP cement walls (i.e. the temperature should not exceed beyond 65⁰C at any location).

(4) The heat transfer through the surface of condenser tubes depends upon the steam flow distribution inside the tube. The non-uniform steam distribution inside the condenser tubes (a) lower the decay heat removal efficiency of the IC because some portion of the IC becomes ineffective (b) results in creation of dead zones and hot spots inside the IC header.

Hence, it is necessary to optimize the design of Isolation condenser (a) to reduce thermal stratification (b) to ensure efficient decay heat removal in a stipulated time (50% decay in 100s) (c) to prevent early water evaporation in the GDWP so as to avoid over-pressurization of containment building (d) to avoid formation of hot spots or dead zones inside the IC header.

1.5 Objectives

The objective of this thesis is to design an efficient Isolation condenser (IC) for the Passive Decay Heat Removal System (PDHRS) of AHWR. The main objective has been recast into following sub objectives:

- Establish the capability of the CFD model to simulate natural convection and thermal stratification inside large water pool (GDWP).
- Study of multi dimensional natural convection and flow fields inside GDWP in the presence of IC. Further, investigate the effect of these fields on mixing and thermal stratification inside GDWP.
- Optimize the design of IC to maximize heat transfer and reduction in thermal stratification.
- Study the effect of inclination of condenser tubes on heat transfer and thermal stratification.
- Study the effect of steam distribution in header and tube assembly of IC and design optimization.
- Study the effect of local boiling in the water pool (GDWP) on the performance of PDHRS.

1.6 Design Methodology

The objective of the thesis is to design an efficient isolation condenser (IC) for the PDHRS of AHWR. In order to design an efficient IC, the following five step methodology is adopted.

Step 1. The 3D temperature and flow distribution inside GDWP has been studied in the presence of conventional design of IC. The detailed CFD analysis shows the presence of non-uniform temperature distribution and hence thermal stratification inside GDWP.

Step 2. The design parameters affecting the performance of conventional IC design have been identified. The main design parameters are: (a) non-uniform distribution of enthalpy inside GDWP; (b) higher submergence of IC tubes; (c) vertical orientation of IC tubes; (d) non-uniform distribution of steam inside IC header and tube assembly.

Step 3. The effect of design parameters such as distribution of IC tubes; submergence depth of IC tubes; passive multiple shrouds around the IC tubes; inclination of IC tubes; IC header shape and diameter; number and diameter of IC tubes; tube pitch has been studied and optimum design parameters have been obtained.

Step 4. A new design of IC has been proposed based on the optimization studies in Step 3.

Step 5. The performance of a new design of IC is compared with the conventional design of IC.

1.7 Outline of report

The aforementioned objectives are discussed in greater detail as separate chapters.

Outline of the report is as follows:

Chapter 2 deals with the development of the CFD model using open source CFD code [OpenFOAM-2.2.0] to simulate thermal stratification inside large water pool (GDWP). The performance of various turbulence models has been investigated to study turbulent natural convection and near wall heat transfer. The turbulence models selected for the studies are eddy viscosity models [SST $k-\omega$, standard $k-\varepsilon$, elliptic relaxation ($v2-f$) and low Reynolds $k-\varepsilon$ model] and Reynolds Stress Model

(RSM) have been selected. The CFD results were compared with the experimental data in the literature.

Chapter 3 deals with the investigation of multidimensional natural circulation phenomenon in GDWP. Single phase CFD simulations have been performed for the real size GDWP of volume 9247 m³. In order to reduce the thermal stratification, various modifications in the IC design have been incorporated, such as (1) distributing the heat transfer area of IC among two and multiple ICs (2) variation in the submergence of ICs (3) combined effect of distribution and submergence (4) provision of passive elements such as draft tube (shrouds) around a heat source (5) combination of multiple draft tubes (shrouds) and baffle at the top.

Chapter 4 focuses on the effects of angle of inclination (α) of condenser tube on buoyancy-driven flows inside a pilot scale (10 l) GDWP. In order to reduce the thermal stratification, fluid flow and heat transfer has been studied for different tube inclination angles (α w.r.t vertical) in the range 0° to 90° ($\alpha = 0^\circ, 15^\circ, 30^\circ, 45^\circ, 60^\circ, 75^\circ, 90^\circ$). The objective is to find out the optimum inclination angle (α) for a condenser tube at which heat transfer is maximum and thermal stratification is minimum. The natural convection and heat transfer in the regime of laminar-turbulent transition has been studied in the presence of longitudinal vortices.

Chapter 5 deals with the study of steam distribution in header and tubes assembly of IC. The objective is to optimize the design of isolation condenser to attain uniform steam distribution in all condenser tubes. In order to attain uniform steam distribution through the IC tubes, the effects of various design parameters such as: tube pitch ($0.1 < D_{pt} < 1.5m$), inlet tube diameter ($0.1 < d_{in} < 0.3m$), header diameter ($0.5 < D_h < 0.9m$), number of tubes ($20 < n_t < 50$), mass flow rate (0.05-5kg/sec) and baffle plate; have been investigated on fluid flow and pressure distribution inside the condenser tubes.

Chapter 6 focuses on the effect of inclination (α) of condenser tube on sliding bubble dynamics and associated heat transfer has been studied for seven angles of tube inclination α (with respect to

vertical direction), in the range $0^0 \leq \alpha \leq 90^0$. For this purpose, two phase transient 3D CFD simulations using mixture model (based on Euler-Euler approach) have been performed. The model considers different mechanisms such as single phase natural convection, latent heat transfer due to evaporation, transient conduction due to disruption of thermal boundary layer and enhanced liquid convection due to bubble sliding motion (quenching).

The overall conclusions from the present work are presented in Chapter 7. This chapter also gives recommendations for future work.

CHAPTER 2

CFD CODE VALIDATION

2.1 Assessment of turbulence models

2.1.1 Introduction

The working of passive safety systems such as PDHRS of advanced heavy water reactor (AHWR) is based completely on natural forces such as gravity. In PDHRS, the decay heat generated from a reactor is transferred by natural circulation into large pool of water (GDWP). In natural convective flows, turbulence is mainly concentrated in the thin region close to wall (IC) and it is almost absent in the core (Henkes et al., 1991). The velocity and temperature gradients are also very high in this region. Hence, most of the heat transfer occurs in this region. In order to design an efficient and economical IC, accurate prediction of near wall heat transfer is essential. In natural convective flows, the validation of turbulence models is very difficult due to the lack of precise and accurate experimental data near the wall. It is very difficult to accurately measure the near wall turbulent heat fluxes and the low fluid flow (few mm/s). Apart from the lack of accurate experimental data, the other challenges in CFD modeling of near wall heat transfer are: (1) very few attempts have been made to extend the flow patterns knowledge obtained from different turbulent models to heat transfer (2) the accuracy of modeling the energy dissipation (ε) equation is limited which can directly affect the flow quantities and thereby heat transfer (3) the selection of the turbulent Prandtl number (Pr_t) is also very difficult (4) no suitable near wall second moment closure for scalar flux (turbulent heat flux) transport.

In view of the importance of accurate prediction of the near wall heat transfer, various attempts have been made to employ computational fluid dynamics (CFD) for the accurate prediction of turbulent parameters (k, ε, ν_t) as well as temperature and velocity profiles. These efforts can be classified as (a) eddy viscosity models, (b) Reynolds-stress model (RSM), (c) large eddy simulation

(LES), and (d) direct numerical simulation (DNS). The widely used eddy viscosity models are standard $k-\varepsilon$, low Re $k-\varepsilon$, SST $k-\omega$ and elliptic relaxation model (v_2f). The two common approaches for the near-wall treatment of these models are: (i) the wall function approach (Launder and Spalding, 1972) and (ii) low-Reynolds-number modeling. In industrial CFD simulations, the most widely used turbulence model is standard $k-\varepsilon$ model with logarithmic wall functions. The wall function approach allows the use of much coarser near-wall grids and hence results in reduced computation requirement. The wall functions are based on the local equilibrium logarithmic velocity and temperature assumptions, which were originally derived for forced convective flows and do not hold for the natural convective flows. The standard $k-\varepsilon$ model also predicts excessive turbulent viscosity near the wall as evidenced by Heindel et al. (1994). Hence, it becomes essential to find other options in place of logarithmic wall functions to solve k and ε equations directly up to the wall. In order to overcome these limitations, some of the available solutions are: (1) derive special wall functions for natural convective flows (2) solve flow equations upto the wall directly without using any wall functions (3) use damping functions in k and ε equation, to damp the turbulence in the viscous region close to the wall (4) use DNS or LES. The special wall functions for the natural convective flows are not available in a current state of art of turbulence modeling. Another more promising approach is low-Reynolds-number modeling. The low Reynolds $k-\varepsilon$ model use special damping functions to solve k and ε equations near the wall. As a result, the turbulence was damped near the wall in comparison to standard $k-\varepsilon$ model. Fairly complete reviews of the development of such two equation near-wall turbulence closures have been provided by Patel et al. (1984). It is well known that the low Re models do not work well in the adverse pressure gradient region. The other way to avoid the deficiency of wall function method is to use the one equation model (Chen and Patel, 1988) near the wall instead of wall functions. Medic and Durban (2002) developed an elliptic relaxation (v_2f) model which does not use any wall functions or damping functions to solve turbulent equations near the wall. Instead of turbulent kinetic energy k , the model uses a velocity

scale $\overline{v^2}$ (hence the name *v2-f model*) for the evaluation of the eddy viscosity, where $\overline{v^2}$ represents the velocity fluctuations normal to the streamlines. It can perhaps provide the right scaling for the representation of the damping of turbulent transport close to the wall. In addition to this, it also incorporates some near-wall turbulence anisotropy as well as non-local pressure-strain effects. Choi et al. (2004) applied this model to the computation of natural convection in a rectangular cavity and showed that this model outperforms the conventional $k-\varepsilon$ models. The other turbulence model currently used by many authors is the shear stress transport (SST $k-\omega$) model by Menter (1994). The SST $k-\omega$ is a modified version of the standard $k-\varepsilon$ model with a capability of better prediction of near wall heat transfer. The SST $k-\omega$ model uses the turbulence frequency $\omega = \varepsilon/k$ as the second variable to solve turbulent length scale near the wall. This model behaves as $k-\omega$ model in the near wall region and as the $k-\varepsilon$ model in the fully turbulent region away from the wall. The SST $k-\omega$ model consists of limiters which limits the eddy viscosity to give improved performance in flows with adverse pressure gradients and wake regions. Also, the turbulent kinetic energy is limited to prevent the buildup of turbulence in the stagnation region. The most complex classical turbulence model is the Reynolds stress equation model (RSM). The RSM model does not rely on the turbulent viscosity concept, but instead incorporate transport equations for second order velocity and temperature correlations. Launder et al. (1989) provides a comprehensive discussion of these models. The assessment of various two equation turbulence models and their modifications for near wall heat transfer has been done in the literature. A brief summary of previous work has been given in Literature survey (Section 2.1.2).

2.1.2 Literature Survey

Henkes et al. (1989, 1991) have compared the performance of different turbulence models to study natural convection boundary layer for air along a heated vertical plate. The algebraic Cebeci-Smith model (1974), the standard $k-\varepsilon$ model with logarithmic wall functions and three low-Reynolds number $k-\varepsilon$ models were tested. The Cebeci-Smith model under-predicts the heat transfer by 21%.

The standard k - ε model with wall functions over-predicts the heat transfer by 31% but the velocity and temperature profiles agree reasonably with experiments. Accurate wall-heat transfer results require the use of low-Reynolds number k - ε models; the models of Lam and Bremhorst (1981), Chien (1980), and Jones and Launder (1972) perform best up to a Grashof number of 10^{11} . For larger Grashof numbers the Jones and Launder (1972) model perform best amongst other models.

Thakre and Joshi (2000) have investigated turbulent heat transfer for pipe flows using twelve versions of low Reynolds number k - ε models and two low Reynolds number Reynolds stress turbulence models (RSM) for heat transfer. The model by Lai and So (1990a, 1990b) from the k - ε group predicts the heat transfer very well. The Lai and So model gives better prediction of mean axial velocity profiles and other turbulence parameters (k , ε and eddy diffusivity). Hence, results in better prediction of heat transfer. Even though the Reynolds stress models neglect the assumptions of isotropy and constancy of the turbulent Prandtl number(Pr_t), their applicability for heat transfer needs reconsideration. It may be attributed to the fact that heat flux transport is more complicated than momentum transport and is more likely to be influenced by two or more time scales instead of one. A second reason might be due to inappropriate near-wall modeling of the dissipation and pressure scrambling terms.

He et al. (2008) evaluate the performance of various low-Re turbulence models to predict mixed convection heat transfer for fluids at supercritical pressure. The authors have also studied the effect of flow acceleration due to buoyancy on turbulent field. Most of the turbulence models were not able to predict turbulent heat flux. Hence, wrongly predict the heat transfer. The $v2f$ model was found to perform best amongst all models.

Choi and Kim (2012) have performed the assessment of four turbulence models (two-layer k - ε model, the shear stress transport (SST) model, the elliptic-relaxation ($v2f$) model and the elliptic-blending second-moment closure (EBM)) to study natural convection in enclosure (square and

rectangular). The two-layer model predicts well the vertical turbulent heat flux near the hot wall region and the peak regions are skewed to the hot wall. The EBM model predicts the horizontal turbulent heat flux very well but under predicts the vertical turbulent heat flux.

From the literature review, it is clear that many attempts have been made by various authors to understand the near wall turbulent flow and heat transfer using low Re turbulence models. However, the performance of the turbulence models is very much dependent on the flow conditions and geometry of the system. Therefore, in the present work, a systematic analysis of the interaction between near wall fluid flow and heat transfer has been performed using different turbulence models: (1) shear stress transport SST $k-\omega$ (Menter, 1994) (2) standard $k-\varepsilon$ (3) low Reynolds number $k-\varepsilon$ model (Launder, 2007) (4) elliptic relaxation model (v_2-f) (Medic and Durbin, 2012) (5) Reynolds stress models (Launder et al. 1974)

2.1.3 Buoyancy models

2.1.3.1 Full Buoyancy Model

The governing equations for the full buoyancy model [Gray and Giorgini (1976)] given in Table 2.1

2.1.3.2 Buoyancy Model with Boussinesq Approximation

In buoyancy driven flows, the exact governing equations are intractable. Some approximation is needed, and the simplest one which admits buoyancy is the Boussinesq approximation. This approximation consists of following assumptions:

- (i). Variations of all other fluid properties other than the density with temperature are ignored completely
- (ii). Density variations result mainly from temperature variations
- (iii). The density variations are taken to have a small effect on the inertial mass of the fluid but a significant effect on the fluid motion through the effect of gravity
- (iv). Viscous dissipation is assumed negligible

Table 2.1: Governing equations for full buoyancy model

Continuity	$\frac{\partial \rho}{\partial t} + \frac{\partial}{\partial x_j} (\rho \bar{u}_j) + \rho \frac{\partial \bar{u}_j}{\partial x_j} = 0$
Momentum	$\frac{\partial \rho \bar{u}_i}{\partial t} + \frac{\partial}{\partial x_j} (\rho \bar{u}_j \bar{u}_i) - \frac{\partial \tau_{ij}}{\partial x_j} = -\frac{\partial \bar{P}}{\partial x_i} - \rho g_i$
Energy	$\frac{\partial \bar{T}}{\partial t} + \frac{\partial}{\partial x_j} (\bar{T} \bar{u}_j) = \frac{\partial}{\partial x_j} \left[\left(\frac{\nu_t}{Pr_t} + \frac{\nu_0}{Pr} \right) \frac{\partial \bar{T}}{\partial x_k} \right] + \frac{1}{\rho C_p} \frac{\partial \bar{K}}{\partial x_k} \frac{\partial \bar{T}}{\partial x_k} + \frac{\beta \bar{T}}{\rho C_p} \frac{\partial \rho}{\partial t} + \frac{\nu}{\rho C_p} \tau_{ij} \left(\frac{\partial \bar{u}_i}{\partial x_j} + \frac{\partial \bar{u}_j}{\partial x_i} \right)$

According to Gray and Giorgini (1976), the Boussinesq approximation is valid if following three conditions are satisfied:

$$\frac{\beta g L}{C_p} \left(\frac{Pr}{Ra} \right)^{0.5} \leq 0.1 \frac{1}{(Pr Ra)^{0.5}} \quad (2.1)$$

$$\frac{\beta g L}{C_p} \frac{T_0}{\Delta T} \leq 0.1 \quad (2.2)$$

$$\left(\frac{1}{\mu} \frac{\partial \mu}{\partial T} \right) \leq 0.1 \quad (2.3)$$

In PDHRS, all above conditions are satisfied. Hence, the Boussinesq approximation can be used in this system. The governing equations for the buoyancy model with Boussinesq approximation are given in Table 2.2.

Table 2.2: Governing equations with Boussinesq approximation

Continuity	$\frac{\partial \bar{u}_j}{\partial x_j} = 0$
Momentum	$\frac{\partial \bar{u}_i}{\partial t} + \frac{\partial}{\partial x_j} (\bar{u}_j \bar{u}_i) - \frac{\partial}{\partial x_j} \left\{ \nu_{eff} \left[\left(\frac{\partial \bar{u}_i}{\partial x_j} + \frac{\partial \bar{u}_j}{\partial x_i} \right) - \frac{2}{3} \left(\frac{\partial \bar{u}_k}{\partial x_k} \right) \delta_{ij} \right] \right\} = -\frac{\partial \bar{p}}{\partial x_i} + S_M$
Energy	$\frac{\partial \bar{T}}{\partial t} + \frac{\partial}{\partial x_j} (\bar{T} \bar{u}_j) = \frac{\partial}{\partial x_j} \left[\left(\frac{\nu_t}{Pr_t} + \frac{\nu_0}{Pr} \right) \frac{\partial \bar{T}}{\partial x_k} \right]$

In natural convection system, the density variation is only due to temperature variations. According to Boussinesq approximation, the buoyancy effect is modeled in the momentum equation [Table 2.2] by the inclusion of a source term as follows:

$$S_M = -\rho_{ref} \beta g_i (T - T_{ref})$$

where β is the thermal expansivity $\beta = -(1/\rho) \cdot \partial\rho/\partial T|_P$

2.1.3.3 Limitations of Boussinesq approximation

According to Boussinesq approximation, the flow acceleration due to thermal expansion of heated fluid is zero because divergence of velocity is zero. In reality, a divergence free flow field is non-physical, especially for non-isothermal flow fields. As a fluid changes its position in a flow field, the volume of the fluid particle may change due to addition of enthalpy from the heat source. The change in volume results in work done on the surrounding fluid. In full buoyancy model, the flow acceleration due to thermal expansion or contraction is taken into account as follows:

$$\Delta \cdot \vec{u} = \frac{1}{\rho} \frac{\partial \rho}{\partial t} = \frac{1}{V} \frac{\partial V}{\partial t} \quad (2.4)$$

The combined effect of buoyancy and thermal expansion results in flow acceleration and enhanced turbulence production. Further, it results in enhanced heat transfer and reduction in thermal stratification.

2.1.4 Turbulence Models

2.1.4.1 Standard k - ε model

The transport equation of turbulent kinetic energy (k) and dissipation rate (ε) are as follows:

$$\frac{\partial k}{\partial t} + U_i \frac{\partial k}{\partial x_j} = \nu_t \left(\frac{\partial U_i}{\partial x_j} + \frac{\partial U_j}{\partial x_i} \right) \frac{\partial U_i}{\partial x_j} - \varepsilon + \frac{\partial}{\partial x_j} \left[\left(\nu + \frac{\nu_t}{\sigma_k} \right) \frac{\partial k}{\partial x_j} \right] \quad (2.5)$$

$$\frac{\partial \varepsilon}{\partial t} + U_j \frac{\partial \varepsilon}{\partial x_j} = C_1 \frac{\varepsilon}{k} \nu_t \left(\frac{\partial U_i}{\partial x_j} + \frac{\partial U_j}{\partial x_i} \right) \frac{\partial U_i}{\partial x_j} + \frac{\partial}{\partial x_j} \left[\left(\nu + \frac{\nu_t}{\sigma_\varepsilon} \right) \frac{\partial \varepsilon}{\partial x_j} \right] + C_2 \frac{\varepsilon^2}{k} \quad (2.6)$$

The values of constants are as follows:

$$C_u = 0.09, C_1 = 1.44, C_2 = 1.92, \sigma_k = 1.0, \sigma_\varepsilon = 1.3 \quad (2.7)$$

In the case of standard k - ε model, ν_t is estimated using turbulent kinetic energy (k) and rate of dissipation of turbulent kinetic energy (ε).

$$\nu_t = C_\mu \frac{k^2}{\varepsilon} \quad (2.8)$$

The values of k and ε are obtained by solving their transport equations (Launder and Spalding, 1974). However, the exact k and ε equations cannot be solved directly, as they contain triple correlations of fluctuating velocity, or ensemble-averaging of gradients of fluctuating velocities. These terms cannot be estimated directly and need modeling. The standard way to approximate turbulent transport of scalar quantities is to use the gradient-diffusion hypothesis. As a result

$$\frac{1}{2} \langle u'_i u'_i u'_j \rangle + \frac{1}{\rho} \langle u'_j p' \rangle = - \frac{\nu_t}{\sigma_k} \frac{\partial k}{\partial x_j} \quad (2.9)$$

The production term $\left[-\langle u'_i u'_j \rangle \left(\partial U_i / \partial x_j \right) \right]$ is modeled using the turbulent viscosity hypotheses introduced by Boussinesq in 1977 and is analogous to the stress-rate-of-strain relation for a Newtonian fluid. According to the hypotheses the relationship is

$$u'_i u'_j = \nu_t \left(\frac{\partial U_i}{\partial x_j} + \frac{\partial U_j}{\partial x_i} \right) - \frac{2}{3} k \delta_{ij} \quad (2.10)$$

The Reynolds stress; which is an essential part of the production term, has six components is assumed to be proportional to the mean rate of strain with the same constant of proportionality, ν_t for all the components.

The turbulent transport correlation term is the sum of the Reynolds stress transport term and the pressure velocity correlation. The RANS models approach treats the turbulent transport terms as symmetric i.e. the reordering of the terms does not change its effect on the flow. The assumption of symmetry is only valid if there is a valid justification for the neglect of the pressure term. The k - ε model falters because of the complete neglect of the stress terms and the assumption of isotropy. The ε equation is modeled in an analogous way to k equation and using dimensional analysis. The production term in the exact dissipation equation is modeled as:

$$-2\mu \left(\left\langle \frac{\partial u'_i}{\partial x_j} \frac{\partial u'_k}{\partial x_j} \right\rangle + \left\langle \frac{\partial u'_j}{\partial x_i} \frac{\partial u'_j}{\partial x_k} \right\rangle \right) \frac{\partial U_i}{\partial x_k} - 2\mu \left\langle u'_k \frac{\partial u'_i}{\partial x_j} \right\rangle \frac{\partial^2 U_i}{\partial x_k \partial x_j} - 2\mu \left\langle \frac{\partial u'_i}{\partial x_k} \frac{\partial u'_i}{\partial x_m} \frac{\partial u'_k}{\partial x_m} \right\rangle \quad (2.11)$$

$$\begin{aligned}
&\approx \mu \frac{u^2}{L^2} \frac{\partial U_i}{\partial x_j} \approx \frac{u}{L} \mu \frac{u}{L} \frac{\partial U_i}{\partial x_j} \approx \frac{u}{L} \tau_{ij} \frac{\partial U_i}{\partial x_j} \\
&\approx \frac{u^2}{t_s} \frac{1}{u^2} \tau_{ij} \frac{\partial U_i}{\partial x_j} \approx \frac{\varepsilon}{k} \tau_{ij} \frac{\partial U_i}{\partial x_j} \approx C_{\varepsilon 1} \frac{\varepsilon}{k} \tau_{ij} \frac{\partial U_i}{\partial x_j}
\end{aligned} \tag{2.12}$$

Further the modeling of dissipation term is given by:

$$-2\mu v \left\langle \frac{\partial^2 u'_i}{\partial x_k \partial x_m} \frac{\partial^2 u'_i}{\partial x_k \partial x_m} \right\rangle \approx -\rho v^2 \frac{u^2}{L^4} \approx -\rho \frac{L^4}{t_s^2} \frac{u^2}{L^4} \approx -C_{\varepsilon 2} \rho \frac{\varepsilon^2}{k} \tag{2.13}$$

The above mentioned modeling of k and ε equations result into five turbulence parameters $C_\mu, C_1, C_2, \sigma_k$ and σ_ε . These parameters have been estimated from studies in simple flows. In the log-law region of the boundary layer, experimentally it has been found that the turbulence production and the dissipation terms are much larger than the other terms. Turbulence in this region is considered to be in local equilibrium. Neglecting transport and production in this flow, the value of C_μ works out to be 0.09. For the value of C_2 , experiments have been carried out in decaying grid turbulence. Turbulence is generated when free flow goes through a grid which generates mean flow gradients and in turn via the production term generates turbulence. Sufficiently far downstream, the velocity gradients are zero and hence the production and dissipation terms are zero in contrast to log-law region in the boundary layer. The turbulent diffusion term is also negligible. The balance of turbulence convection and dissipation gives $C_2=1.92$. The constant C_1 is obtained by looking at the dissipation rate equation in the log-region of boundary layer. The turbulent diffusion is not negligible in this case unlike k equation. The simplifications of ε equation using velocity profiles in log law region and the numerical solution of these equations give $C_1=1.44$, σ_k and $\sigma_\varepsilon=1.0$ and 1.3 respectively.

The standard k - ε model has performed satisfactorily in many flows, but the applicability of this model is limited due to uncertainties involved in the modeling of turbulence production, turbulent transport and the assumptions in modeling dissipation rate equation. Further, the modeling

of transport equations for k and ε pose difficulties to account for streamline curvature, rotational strains, and the other body-force effects.

2.1.3.2. Low Re k - ε model (Launder, 2007)

The standard k - ε model only holds if the local turbulence Re number is large. Close to the wall, e.g. this is not the case, and a modification of the model should be applied. Low Re number effects are modelled by the introduction of the function f_μ, f_1, f_2, D and E

$$\frac{\partial k}{\partial t} + U_i \frac{\partial k}{\partial x_j} = \nu_t \left(\frac{\partial U_i}{\partial x_j} + \frac{\partial U_j}{\partial x_i} \right) \frac{\partial U_i}{\partial x_j} - \varepsilon + \frac{\partial}{\partial x_j} \left[\left(\nu + \frac{\nu_t}{\sigma_k} \right) \frac{\partial k}{\partial x_j} \right] + 2\nu \left(\frac{\partial \sqrt{k}}{\partial y} \right)^2 \quad (2.14)$$

$$\frac{\partial \varepsilon}{\partial t} + U_j \frac{\partial \varepsilon}{\partial x_j} = C_{\varepsilon 1} f_1 \nu_t \left(\frac{\partial U_i}{\partial x_j} + \frac{\partial U_j}{\partial x_i} \right) \frac{\partial U_i}{\partial x_j} + \frac{\partial}{\partial x_j} \left[\left(\nu + \frac{\nu_t}{\sigma_\varepsilon} \right) \frac{\partial \varepsilon}{\partial x_j} \right] + C_{\varepsilon 2} f_2 \frac{\varepsilon^2}{k} + 2\nu \nu_t \left(\frac{\partial^2 y}{\partial y^2} \right)^2 \quad (2.15)$$

Where, $\nu_t = \frac{C_\mu f_\mu k^2}{\varepsilon}$, $f_\mu = \exp \frac{-3.4}{(1+R_t/50)^2}$, $C_u = 0.09$, $C_{\varepsilon 1} = 1.44$, $C_{\varepsilon 2} = 1.92$, $\sigma_k = 1.0$, $\sigma_\varepsilon = 1.3$

2.1.4.3. SST k - ω model (Menter, 1994)

Turbulent kinetic energy (k) transport equation:

$$\frac{\partial k}{\partial t} + U_j \frac{\partial k}{\partial x_j} = P_k - \beta^* k \omega + \frac{\partial}{\partial x_j} \left[\left(\nu + \sigma_k \nu_t \right) \frac{\partial k}{\partial x_j} \right] \quad (2.16)$$

$$\text{where,} \quad P_k = \min \left(\tau_{ij} \frac{\partial U_i}{\partial x_j}, 10\beta^* k \omega \right) \quad (2.17)$$

Turbulent dissipation rate (ε) transport equation:

$$\frac{\partial \omega}{\partial t} + \bar{u}_j \frac{\partial \omega}{\partial x_j} = \alpha S^2 - \beta \omega^2 + \frac{\partial}{\partial x_j} \left[\left(\nu + \sigma_\omega \nu_T \right) \frac{\partial \omega}{\partial x_j} \right] + 2(1 - F_1) \sigma_{\omega 2} \frac{1}{\omega} \frac{\partial k}{\partial x_i} \frac{\partial \omega}{\partial x_i} \quad (2.18)$$

The eddy viscosity is modeled as follows:

$$\nu_t = \frac{a_1 k}{\max(a_1, \omega, SF_2)} \quad (2.19)$$

Each of the constants is a blend of an inner (1) and outer (2) constant, blended via:

$$\phi = \phi_1 F_1 + \phi_2 (1 - F_1) \quad (2.20)$$

where ϕ_1 represents constant 1 and ϕ_2 represents constant 2. Additional functions blended via:

$$F_1 = \tanh \left\{ \left\{ \min \left[\max \left(\frac{\sqrt{k}}{\beta^* y \omega}, \frac{500\nu}{y^2 \omega} \right), \frac{4\sigma_{\omega 2} k}{CD_{k\omega} y^2} \right] \right\}^4 \right\} \quad (2.21)$$

$$F_2 = \tanh \left[\left[\max \left(\frac{2\sqrt{k}}{\beta^* y \omega}, \frac{500\nu}{y^2 \omega} \right) \right]^2 \right] \quad (2.22)$$

where $CD_{k\omega} = \max \left(2\rho\sigma_{\omega 2} \frac{1}{\omega} \frac{\partial k}{\partial x_i} \frac{\partial \omega}{\partial x_i}, 10^{-10} \right)$, y is the distance from the field point to the nearest

wall and S is an invariant measure of the strain rate. The model constants are given as follows:

$$\alpha_1 = \frac{5}{9}, \alpha_2 = 0.44, \beta_1 = \frac{3}{40}, \beta_2 = 0.0828, \beta^* = \frac{9}{100}, \sigma_{k1} = 0.85, \sigma_{k2} = 1, \sigma_{\omega 1} = 0.5, \sigma_{\omega 2} = 0.856.$$

2.1.4.4 Elliptic Relaxation ($\nu 2f$) model (Medic and Durbin, 2012)

In the elliptic relaxation model, the governing equations for k and ε are the same as the $k - \varepsilon$ model except the expressions of the turbulent eddy viscosity and the time scale. The following two additional governing equations are solved to determine the velocity scale:

$$\frac{\partial \vartheta^2}{\partial t} + U_i \frac{\partial \vartheta^2}{\partial x_j} = kf - \frac{\vartheta^2 \varepsilon}{k} + \frac{\partial}{\partial x_j} \left[\left(\nu + \frac{\nu_t}{\sigma_{\vartheta^2}} \right) \frac{\partial \vartheta^2}{\partial x_j} \right] \quad (2.23)$$

$$L_s^2 \frac{\partial^2 f}{\partial x_j \partial x_j} - f = \frac{1}{T} \left\{ (C_1 - 1) \left(\frac{2}{3} - \frac{\vartheta^2}{k} \right) \right\} + C_2 \frac{P_k + G_k}{k} \quad (2.24)$$

The time and length scale in the above equations are given by

$$T = \min \left\{ \max \left[\frac{k}{\varepsilon}, C_T \left(\frac{\nu}{\varepsilon} \right)^{1/2} \right], \frac{\alpha k}{\sqrt{6} \vartheta^2 C_u |S|} \right\} \quad (2.25)$$

$$L_s = C_L \max \left\{ \min \left[\frac{k^{3/2}}{\varepsilon}, \frac{k^{3/2}}{\sqrt{6} \vartheta^2 C_u |S|} \right], C_\eta \left(\frac{\nu^3}{\varepsilon} \right)^{1/4} \right\} \quad (2.26)$$

Where, $\nu_t = C_\mu \vartheta^2 T$, $C_u = 0.22$, $C_1 = 1.4$, $C_2' = \sigma_{\vartheta^2} = 1.2$, $\sigma_\varepsilon = 1.3$

2.1.4.5 Reynolds Stress Model (RSM) (Launder et al. 1974)

It is clear that the standard $k - \varepsilon$ model inherently fails to predict properly the anisotropic flow situations (Reynolds, 1987, Launder 1989, Hanjalic 1994). Further, the modeling of transport equations for k and ε clearly brings out the difficulties to account for streamline curvature, rotational strains, and the other body-force effects. Reynolds stress model, in theory, can circumvent all the above mentioned deficiencies and also it has an ability to predict more accurately each individual

stress. A Reynolds stress model solves six equations for the Reynolds stress tensor and another equation for the dissipation rate. The equation of turbulent stresses contains the terms, namely pressure strain rate (which contains fluctuating pressure velocity gradients) and the flux of Reynolds stresses. In addition to the modeling of the terms in the turbulent energy dissipation rate equation, these terms need to be modeled accurately. Therefore, though RSM takes into consideration the transport of turbulent stresses, its parameters are not universal (i.e. model needs to be calibrated for different types of flows). Further, the extended system often has difficulties to produce converged solutions and thus it is computationally expensive.

The governing equation for the Reynolds stresses is, given as:

$$\begin{aligned} \frac{\partial \tau_{ij}}{\partial t} + \langle u_k \rangle \frac{\partial \tau_{ij}}{\partial x_k} = & - \left(\tau_{ik} \frac{\partial \langle u_j \rangle}{\partial x_k} + \tau_{jk} \frac{\partial \langle u_i \rangle}{\partial x_k} \right) + \left\langle \frac{p'}{\rho} \left[\frac{\partial u_j'}{\partial x_i} + \frac{\partial u_i'}{\partial x_j} \right] \right\rangle - 2\nu \left\langle \frac{\partial u_i'}{\partial x_k} \frac{\partial u_i'}{\partial x_k} \right\rangle \\ & + \nu \nabla^2 \tau_{ij} - \left[\frac{\partial \langle u_i' u_j' u_k' \rangle}{\partial x_k} + \frac{1}{\rho} \frac{\partial}{\partial x_k} \left(\langle p' u_i' \rangle \delta_{jk} + \langle p' u_j' \rangle \delta_{ik} \right) \right] \end{aligned} \quad (2.27)$$

$$\frac{\partial \tau_{ij}}{\partial t} + \langle u_k \rangle \frac{\partial \tau_{ij}}{\partial x_k} = - \left(\tau_{ik} \frac{\partial \langle u_j \rangle}{\partial x_k} + \tau_{jk} \frac{\partial \langle u_i \rangle}{\partial x_k} \right) + \Pi_{ij} - \varepsilon_{ij} + \nu \nabla^2 \tau_{ij} - \frac{\partial}{\partial x_k} C_{ijk} \quad (2.28)$$

The terms C_{ijk} , Π_{ij} and ε_{ij} are given as,

$$\Pi_{ij} = \left\langle \frac{p'}{\rho} \left[\frac{\partial u_j'}{\partial x_i} + \frac{\partial u_i'}{\partial x_j} \right] \right\rangle = \text{Pressure-strain correlation}$$

$$\varepsilon_{ij} = 2\nu \left\langle \frac{\partial u_i'}{\partial x_k} \frac{\partial u_j'}{\partial x_k} \right\rangle = \text{Dissipation rate correlation}$$

$$C_{ijk} = \langle u_i' u_j' u_k' \rangle + \frac{1}{\rho} \left(\langle p' u_i' \rangle \delta_{jk} + \langle p' u_j' \rangle \delta_{ik} \right) = \text{Third-order diffusion correlation}$$

where P , D , Π , and ε respectively denote the production, diffusion, pressure-strain correlation, and dissipation. Out of these, P_{ij} (production), D_{ij}^l (molecular diffusion) do not require modeling. However, The turbulent diffusion, D_{ij}^t , pressure strain, Π_{ij} , and dissipation rate tensor ε_{ij} need to be modeled to close the set of the governing equations.

The turbulent transport term is the sum of the Reynolds stress transport term $\langle u'_i u'_j u'_k \rangle$ and the pressure velocity fluctuation term $\langle P' u'_i \rangle \delta_{jk}$. The former is symmetric (i.e. the value remains unchanged by any reordering of the terms), where as the pressure velocity correlation is not. Hence to capture the symmetric nature, the pressure velocity fluctuating term is assumed to be zero. The remaining terms are modeled analogously to the molecular diffusion transport phenomena, where the rate of the transport of Reynolds stress by diffusion is directly proportional to the gradients of Reynolds stress, i.e.

$$C_{ijk} = \left\{ C_\mu \left(\frac{k^2}{\varepsilon} \frac{\partial \tau_{ij}}{\partial x_k} \right) \right\} \approx \left\{ \left(\frac{\mu_t}{\sigma_k} \frac{\partial \tau_{ij}}{\partial x_k} \right) \right\} \quad (2.29)$$

It is obvious that the highly anisotropic flow due to the jet impinging on the tank bottom and subsequent interaction between the strong jet and the bulk flow suggests that the production term and the pressure strain correlation play a significant role in the prediction of turbulent stresses. The quadratic pressure strain model proposed by Speziale and Xu (1996), which is known to improve the accuracy of flow field with streamline curvature, is used to model the pressure-strain term of the Reynolds-stress model.

The pressure-strain correlation term is modeled by decomposing it two terms, the slow and fast contributions, represented as Π_{ij} . The pressure -strain correlation term is the most important and most difficult to model accurately. The pressure-velocity correlation is responsible for the redistribution of energy between normal components of Reynolds stress so as to make them more isotropic.

$$\Pi_{ij} = \left\langle p' \left[\frac{\partial u'_j}{\partial x_i} + \frac{\partial u'_i}{\partial x_j} \right] \right\rangle = \Pi_{ij,slow} + \Pi_{ij,rapid} \quad (2.30)$$

The slow component, $\Pi_{ij,slow}$ plays the role in the creation, maintenance and destruction of the anisotropy of turbulence. It is natural to insist that it depends on the measure of the anisotropy which is a function of the Reynolds stress.

$$\Pi_{ij,slow} = C_1 \frac{\varepsilon}{k} \left(\langle u_i' u_j' \rangle - \frac{2}{3} k \delta_{ij} \right) \quad (2.31)$$

where $C_1 = 1.8$. The rapid component, $\Pi_{ij,rapid}$, is the isotropization of production model proposed by Naot et al. (1970). The rate of the rapid processes is assumed to be proportional to the production process responsible for the generation of anisotropy.

$$\Pi_{ij,rapid} = C_2 \frac{\varepsilon}{k} \left(P_{ij} - \frac{2}{3} P \delta_{ij} \right) \quad (2.32)$$

with $C_2 = 0.6$ and P_{ij} is the production term. The equation for dissipation rate of turbulent kinetic energy treated in a similar manner as the k- ε model's equation for dissipation rate.

2.1.5 Numerical Procedure

2.1.5.1 Geometry

The experimental set up used by Gandhi et al., (2011) has been shown in Fig 2.1A consists of an open cylindrical tank ($D = 0.3$ m and $H_T = 0.3$ m) fitted with a centrally heated tube ($d = 0.02$ m, $h = 0.3$ m) through which steam is passed. Due to the symmetry in tangential direction, a 5° wedge geometry (Fig 2.1B) of tank has been considered for CFD simulations. The details of the boundary conditions are as follows:

Table 2.3: Details of boundary conditions

Zone	Temperature	Velocity
Heated tube	Constant Temp = 413K	No slip ($U_r = U_\theta = U_z = 0$)
Top free surface	Adiabatic ($\partial T / \partial z = 0$)	Free slip $\left\{ \frac{\partial u_r}{\partial z} = \frac{\partial u_\theta}{\partial z} = 0, u_z = 0 \right\}$
Side tank walls	Adiabatic ($\partial T / \partial r = 0$)	No slip ($U_r = U_\theta = U_z = 0$)
Bottom tank wall	Adiabatic ($\partial T / \partial z = 0$)	
Symmetry	($\partial T / \partial \theta = 0$)	$\left\{ \frac{\partial u_r}{\partial \theta} = \frac{\partial u_\theta}{\partial \theta} = \frac{\partial u_z}{\partial \theta} = 0 \right\}$

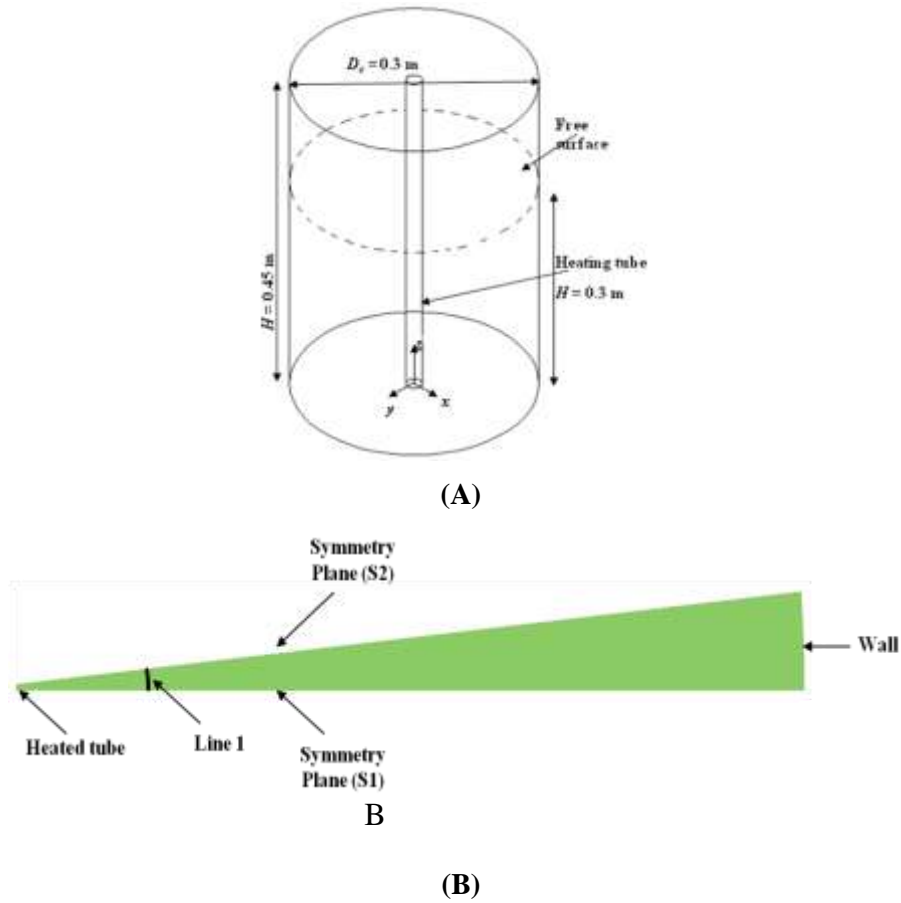


Fig 2.1: (A) Schematic of the experimental set up consists of a water tank fitted with a centrally heated tube
 (B) top view of the set up along with heated tube, tank wall and symmetry planes

2.1.5.2 Governing equations

In order to model the unsteady single phase natural convection, the governing equations (continuity, momentum, and energy) with the appropriate Reynolds stress closure need to be solved with the boundary conditions. In the present CFD simulations, the tube wall (heat exchanger) was kept at constant temperature ($T_w = 413 \text{ K}$). The Rayleigh number is the ratio of a buoyancy velocity ($\beta g \Delta T l^2 / \nu$) to a diffusion velocity (α / l). For the present case of $\beta = 8 \times 10^{-4} (\text{K}^{-1})$, $\Delta T = 113 \text{ K}$, the value of Ra works out to be 7×10^{12} . The flow was considered to be turbulent on the basis of general criteria of Rayleigh number ($Ra > 10^9$). The value of turbulent kinetic energy is $3.75 \times 10^{-5} \text{ m}^2/\text{s}^2$. In addition, the ratio of eddy to molecular viscosity was found to be in the range of 1000 to 5000. These

values justify the use of turbulent flow model. In the present case, the following assumptions have been made:

2.1.5.3 Model Assumptions

1. Condensation occurring inside the tube is film condensation and hence the tube is at a constant saturation temperature and $\Delta T = 113$ K.
2. The fluid is Newtonian and incompressible.
3. Boussinesq approximation is assumed to be valid.
4. Fluid properties are constant except in the formulation of buoyancy term.
5. The boiling phenomenon has been neglected.

Table 2.3: Governing equations for single phase CFD simulations

Continuity	$\frac{\partial \bar{u}_j}{\partial x_j} = 0$
Momentum	$\frac{\partial \bar{u}_i}{\partial t} + \frac{\partial}{\partial x_j} (\bar{u}_j \bar{u}_i) - \frac{\partial}{\partial x_j} \left\{ \nu_{eff} \left[\left(\frac{\partial \bar{u}_i}{\partial x_j} + \frac{\partial \bar{u}_j}{\partial x_i} \right) - \frac{2}{3} \left(\frac{\partial \bar{u}_k}{\partial x_k} \right) \delta_{ij} \right] \right\}$ $= -\frac{\partial \bar{p}}{\partial x_i} + g_i [1 - \beta(\bar{T} - T_0)]$
Energy	$\frac{\partial \bar{T}}{\partial t} + \frac{\partial}{\partial x_j} (\bar{T} \bar{u}_j) = \frac{\partial}{\partial x_j} \left[\left(\frac{\nu_t}{Pr_t} + \frac{\nu_0}{Pr} \right) \frac{\partial \bar{T}}{\partial x_k} \right]$

2.1.5.4 Method of Solution

The first order implicit scheme was used for the time discretization of all unsteady terms. QUICK spatial discretization scheme was used for modeling the convective terms and central differencing scheme for diffusive terms. All the discretized equations were solved in a segregated manner with the PISO (Pressure Implicit with Splitting of Operators) algorithm. Further, the solutions were considered to be fully converged when the sum of scaled residuals was below 10^{-5} .

2.1.5.5 Grid Independence

In order to make the final solution grid independent, the grid independence study was investigated for four different grids: (1) 0.05M (2) 0.1M (3) 0.2M and (4) 0.4M. In natural convection systems, higher gradient of velocity as well as temperature are present near the heat source region. Hence,

most of the heat transfer occurs in this region. In order to accurately predict the near wall heat transfer, efficient modeling of this region is required. A great care was taken by providing at-least three nodes in the viscous sub layer and several nodes in the buffer and turbulent zones. The mesh was adjusted in such a way to ensure that the near wall flow features were properly resolved and the y^+ value at the first node of the mesh was always less than 0.5. Grid independence study has been executed by comparing the mean axial velocity and temperature profiles for each of the four grid densities. All the chosen grids predict mean flow and temperature patterns effectively. Minor differences have been observed between 0.2M and 0.4M cells. However, the velocities were found to be within 2% average error although the grid size difference was 20%. Therefore, for all the simulations in the present work 0.2M cells have been used.

2.1.5.6 Time Independence

After finalizing the grid size, in the next step time step independence study was performed at four different time steps $1 \times 10^{-4}s$, $1 \times 10^{-5}s$, $5 \times 10^{-5}s$, $1 \times 10^{-6}s$. The axial temperature profiles clearly indicates that there was nominal variation (less than 5%) in the temperature for case and $1 \times 10^{-5}s$. Hence, time step in between these two $5 \times 10^{-6}s$ was selected for all the models.

2.1.6 Results and Discussions

The overall objective of the present work is to study the performance of different turbulence models to predict near wall turbulence and heat transfer inside a cylindrical water tank fitted with a centrally heated tube. The effect of turbulence models on temperature, velocity, turbulent kinetic energy profiles and heat transfer has been studied.

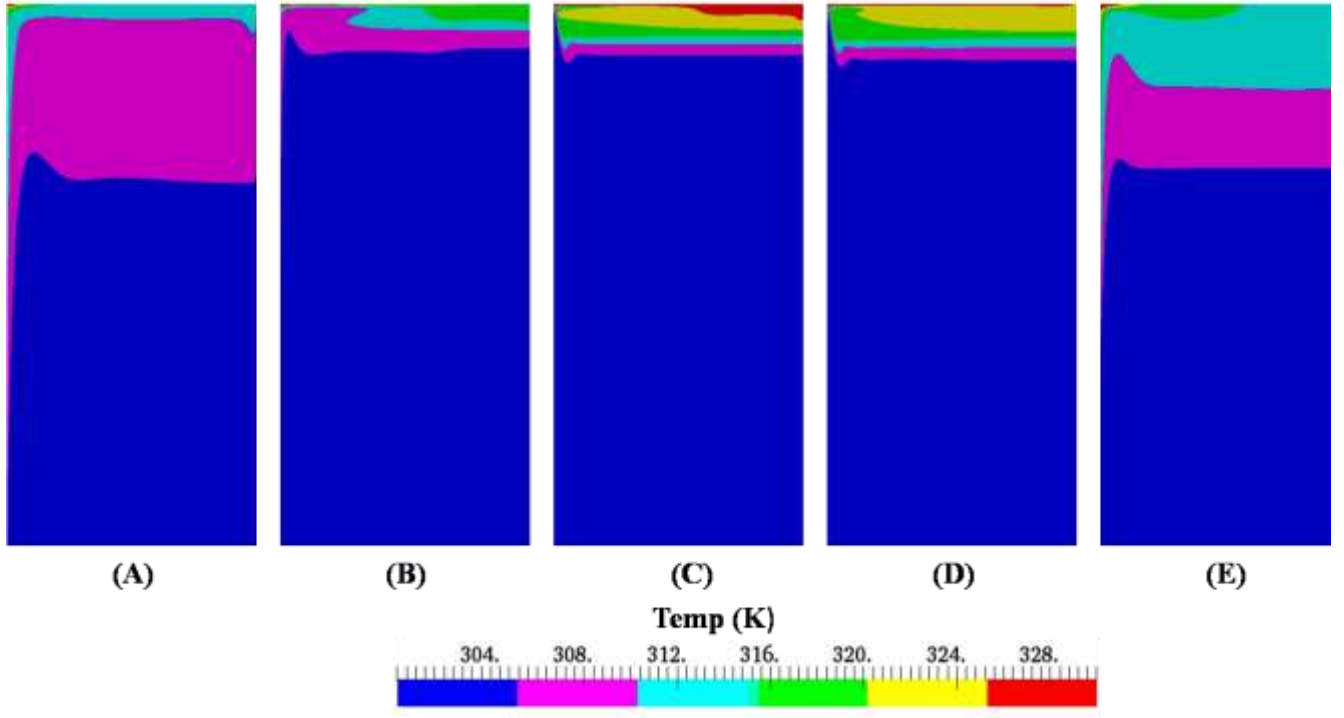


Fig 2.2: Temperature Contours for different turbulence models at $t=100s$ for symmetry plane (S1): (A) standard $k-\varepsilon$ (B) SST $k-\omega$ (C) low Re $k-\varepsilon$ model (D) $v2-f$ (E) RSM

2.1.6.1 Velocity and Temperature Profiles

The temperature contours obtained from the CFD simulations at symmetry plane at $t = 100s$ for various turbulence models are shown in Fig 2.2. In natural convection system, maximum temperature gradient prevails in the vicinity of heated tube and it becomes weak with an increase in the distance from the heat source. As a result, the fluid adjacent to the heat source gets heated, becomes light and rises. Consequently, the heavier fluid (cold water) from the neighboring areas rushes in to take the place of the rising fluid. The axial velocity shown in Fig 2.3 was very high near the heat source and it decreases as we move away from the heat source in radial direction. In fact, in the bulk of water pool, the liquid velocities are feeble. As the hot fluid reaches the free surface at the top, it flows in radially outward direction. When the fluid reaches the tank wall, it again gets diverted in the downward direction. As a result, circulation patterns get established in the water pool. The temperature and velocity increases with an increase in distance in the axial direction ($0 \leq z/H_T \leq 1$).

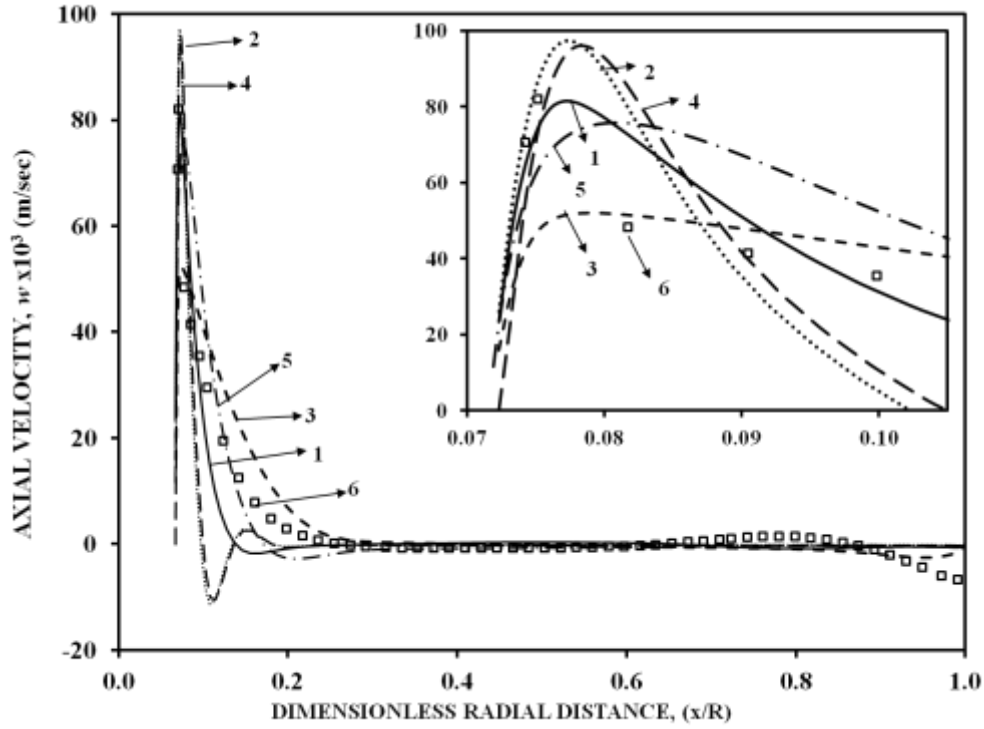


Fig 2.3: Comparison of turbulence models to study distribution of axial velocity at $z/H=0.5$ at $t=100s$, (1) SST $k-\omega$ (2) low Re $k-\epsilon$ model (3) standard $k-\epsilon$ (4) $v2-f$ (5) RSM (6) Experimental data

This is due to the continuous addition of enthalpy from the heat source. As the time progresses, the hot water layer near free surface region gets extended downwards. The overall result is that the total energy supplied to the system gets accumulated near the heat source and near the free surface region at top. The standard $k-\epsilon$ model [case (3) in Fig 2.3] under predict (40%) the velocity peaks near the heat source and over predict (15%) it away from the heat source. Further, it over predicts the heat transfer by 100% in comparison to the experimental values. This has been explained by the k vs y^+ plot [case (3) in Fig 2.4]. The standard $k-\epsilon$ model over predicted the turbulence [case (3) in Fig 2.4] near the heat source ($y^+ < 10$) which leads to enhanced heat transfer. The decay of turbulence away from the wall ($y^+ > 100$) was also very slow. This behaviour is attributed to the wall functions used by standard $k-\epsilon$ model to obtain boundary conditions for the k and ϵ equations up to the wall. These wall functions use $\epsilon = \frac{C_\mu^{3/4} k^{3/2}}{\kappa x}$ at the first node which results into higher values of ϵ when the first node

is taken very close to wall. These wall functions were originally derived for forced convection and do not hold for the natural convection. Hence, it is essential (a) to place first node at a distance greater than $y^+ > 10$ for using wall functions (b) find other options in place of logarithmic wall functions to solve k and ε equations directly up to the wall. The low Reynolds k - ε model by Launder uses special damping functions to solve k and ε equations near the wall. The low Reynolds k - ε model [case (2) in Fig 2.3] over predicts (20%) the velocity peaks near the heat source and under predict it away from the wall. The decay of turbulence [case (2) in Fig 2.4] was also very fast away from the heat source ($y^+ > 10$) which indicates no bulk flow and mixing away from the heat source. Further, the heat transfer coefficient (HTC) predicted by low Reynolds k - ε model [case (2) in Fig 2.5] was found out to be less as compared to standard k - ε model and agrees well (error of 10%) with the experimental data. The $\nu 2f$ model [case (4) in Fig 2.3] also over predicts (20%) the velocity peak near the heat source. Further, it over predicts (10%) the heat transfer [case (4) in Fig 2.5]. The SST k - ω model uses the turbulence frequency $\omega = \varepsilon/k$ as the second variable to solve turbulent length scale near the wall. This model behaves as k - ω model in the near wall region and as the k - ε model in the fully turbulent region away from the wall. The SST k - ω model consists of limiters which limits the eddy viscosity to give improved performance in flows with adverse pressure gradients and wake regions. Also, the turbulent kinetic energy is limited to prevent the buildup of turbulence in the stagnation region. The SST k - ω model [case (1) in Fig 2.3] accurately (error of 5%) predicts the velocity peak near the heat source. For $y^+ < 10$, the SST k - ω model predicts $u^+ = y^+$. Thus it is able to capture the viscous sub layer in the range of $y^+ < 10$. Thus the large velocity gradients near the wall are well captured. Away from the heat source ($y^+ > 30$), SST k - ω under predicts the velocity profile. The heat transfer coefficient by SST k - ω model was also found to be comparable (error of 10%) with the experimental data [case (1) in Fig 2.5]. The RSM model is the most complex model which does not rely on the turbulent viscosity concept, but instead incorporates transport equations for second order velocity and temperature correlations. The RSM model slightly under predicts [case (5) in Fig

2.3] the velocity profile by 5% in the viscous region ($y^+ < 10$), but accurately predict it in the turbulent regime ($y^+ > 30$). The RSM model gives the best overall prediction of velocity [case (5) in Fig 2.3] and turbulent kinetic energy profile [case (5) in Fig 2.4]. The near wall turbulence and velocity predictions by SST $k-\omega$ and RSM model were in good (5%) agreement. The RSM model requires large computation time as to solve additional six Reynolds stress equations. In order to save the computation time, the SST $k-\omega$ model has been used for further studies.

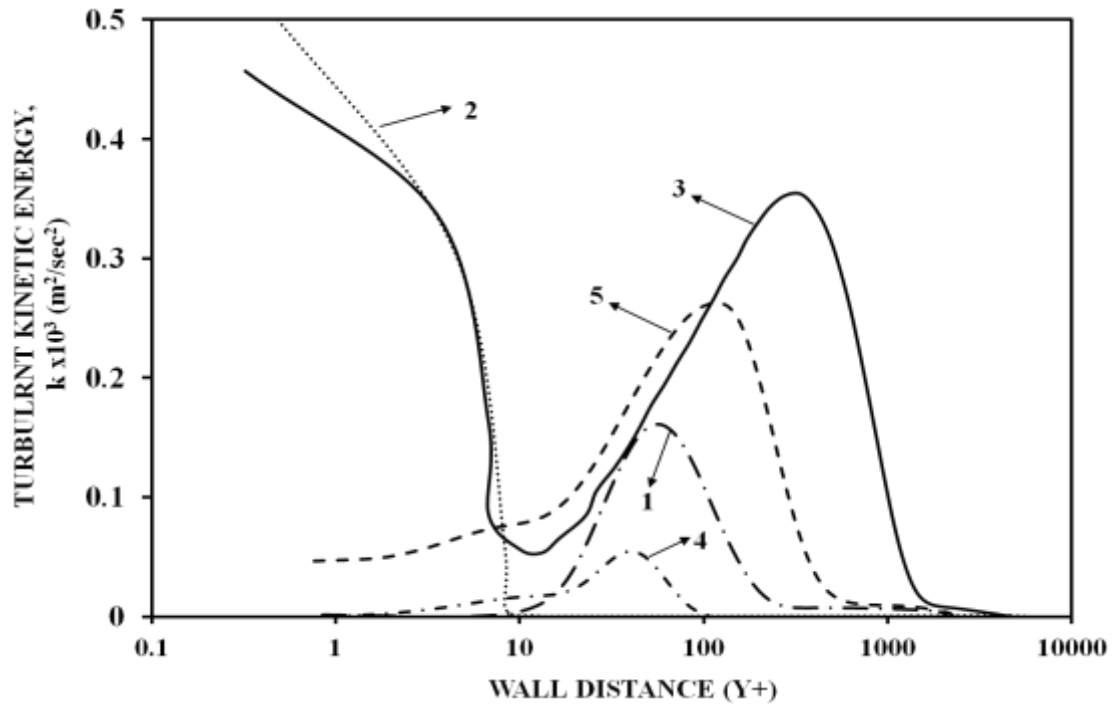


Fig 2.4: Comparison of turbulence models to study radial distribution of turbulent kinetic energy (k) at $z/H=0.5$ at $t=100s$, (1) SST $k-\omega$ (2) low Re $k-\epsilon$ model (3) standard $k-\epsilon$ (4) $v2-f$ (5) RSM

2.1.6.2 Average Heat Transfer Coefficient

The transient heat transfer behavior in Fig 2.5 indicates that heat transfer performance was maximum at the beginning ($t = 0s$) because of large $\Delta T = 113$ K and then it decreases very sharply for a few seconds until it reaches a constant value. The average heat transfer coefficient (h) was calculated as follows:

$$Q = mC_p \overline{\Delta T}_{w,t} = hA \overline{\Delta T}_{s,t} \quad (2.33)$$

$$\overline{\Delta T}_{w,t} = \overline{T}_{w,t} - T_{w,t=0} \quad (2.34)$$

$$\bar{T}_{w,t} = \frac{\iiint_{r,\theta,z}^{R,\theta,Z} T_{w,t} dr d\theta dz}{\iiint_{r,\theta,z}^{R,\theta,Z} dr d\theta dz} \quad (2.35)$$

$$\bar{\Delta T}_{s,t} = T_{s,t} - \bar{T}_{w,t} \quad (2.36)$$

$$\bar{T}_{s,t} = \frac{\int_{l,\theta}^{L,\theta} T_{s,t} dl d\theta}{\int_{l,\theta}^{L,\theta} dl d\theta} \quad (2.37)$$

$$h = \frac{mC_p \bar{\Delta T}_{w,t}}{A \bar{\Delta T}_{s,t}} \quad (2.38)$$

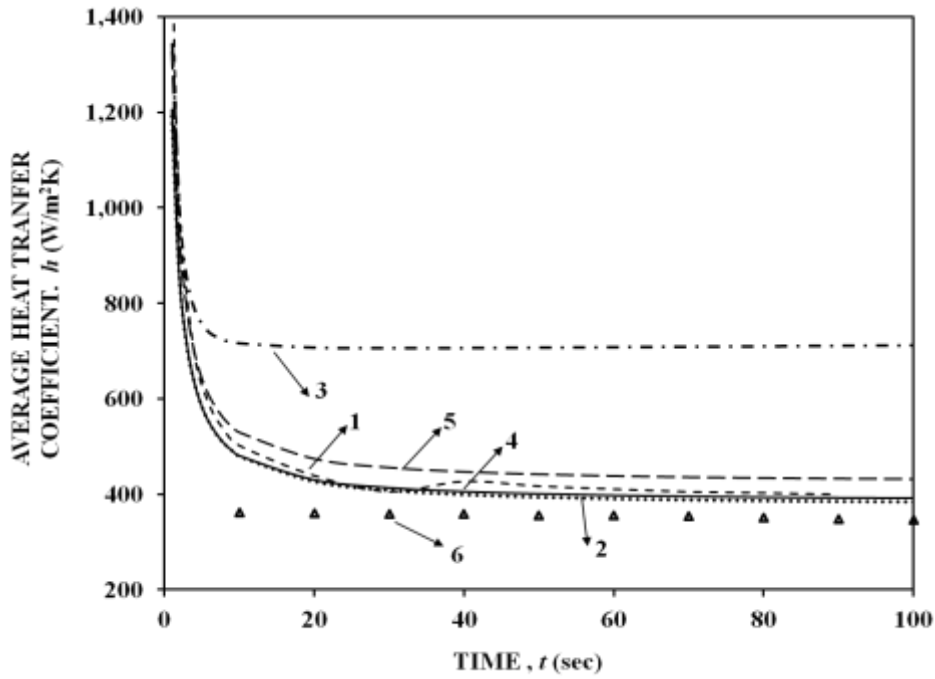


Fig 2.5: Comparison of turbulence models to study transient volumetric average heat transfer coefficient (h), (1) SST $k-\omega$ (2) low Re $k-\epsilon$ model (3) standard $k-\epsilon$ (3) v2f (5) RSM (6) Experimental data

The entire transient ($0 < t < 100s$) heat transfer behavior has been divided into three domains: conduction ($0 < t < 1s$), quasi-steady ($1s < t < 15s$) and fluctuating period ($15s < t < 100s$). Initially, the fluid is at rest. Hence, heat transfer occurs by conduction only. The decay in heat transfer coefficient (h) is very steep in the conduction period ($0 < t < 1s$). As time proceeds, the convective flow starts to develop near the heat source and heat transfer becomes increasingly dominated by convection. This period ($1s < t < 15s$) is referred to as quasi-steady and lasts until the circulating flow in the tank begins to disrupt the boundary layer near the heat source during the fluctuating

period. After ($t > 15s$) the convective flow near the heat source becomes very intense and results in perturbation in the boundary layer and increases heat transfer coefficient (h). This period is known as fluctuating period and characterized by intermittent disruption and growth of the boundary layer surrounding the heat source.

2.2 CFD model capability to study thermal stratification inside small and large water pools

In order to validate the present CFD model, to accurately predict the natural convection and heat transfer for small scale and large scale GDWP ($\sim 10000m^3$), experimental data from Gandhi et al. (2013); Aszodi et al. (2000) and Krepper et al. (2002) have been used. The details of these experimental set up are given in Table 2.4. Single phase CFD simulations have been performed under transient conditions. The SST $k-\omega$ turbulence model was used in all the cases to model turbulent natural convection and heat transfer.

Table 2.4: Details of experimental situations of various authors

Author	Tank Shape	Ra	Tank dimensions (m)	Tube dimensions (m)
Gandhi et al., (2013)	Vertical	10^{13}	$L = 0.8, W = 0.6, H = 0.6$	$d = 0.02, H = 0.5$
Aszodi et al., (2000)	Vertical	10^{10}	$D = 0.25m, H = 0.25m$	Side wall heating
Krepper et al., (2002)	Horizontal	10^9	$D = 2, L = 6m$	$d = 0.0445, L = 10$

2.2.1 Gandhi et al., (2013) Gandhi et al., (2013) have performed experiments to study thermal stratification phenomenon inside a rectangular tank ($0.25 m^3$) fitted with a centrally heated tube. A schematic of the experimental facility is shown in Fig 2.6. It consists of a rectangular tank filled with water up to a height of 0.5 m. The detailed dimensions of the experimental set up are given in Table 2.4. Fig 2.7 shows that high temperature gradient prevails in the vicinity of heat source (steam is passed from top to bottom of the central tube) and it becomes weak with an increase in the radial distance. The presence of vertical heat source was found to result in non-uniform temperature distribution in the tank which results in thermal stratification. The axial temperature profile (Fig 2.7)

clearly indicates the accumulation of hot fluid at top of the tank. The strong temperature stratification was also reflected in the CFD simulation. The temperature profiles in Fig 2.7 shows the axial (z) distribution of temperature at two different radial (x) locations. The temperature profiles at $x/W = 0.01$ shows the axial temperature distribution at 3 mm away from the IC tube whereas the temperature profiles at $x/W = 0.1$ shows the temperature at 3 cm away from the IC tube. Fig 2.7 shows the CFD predictions are in agreement with the experimental results near the IC tube ($x/W = 0.01$) whereas it under predicts the temperature distribution away from the IC tube near the top free surface ($0.8 \leq z/H \leq 1$). This behavior may be due to two reasons: (1) the mesh independence near the wall has been studied for different y^+ but mesh independence in the bulk has not been studied accurately (2) the CFD is unable to capture fluctuations in temperature and flow distribution at the top free surface due to approximate boundary conditions. We have used free slip boundary conditions for velocity and zero gradient boundary conditions for temperature at the top free surface. At the top free surface, there is an interaction between the air in the atmosphere and hot fluid at the top free surface.

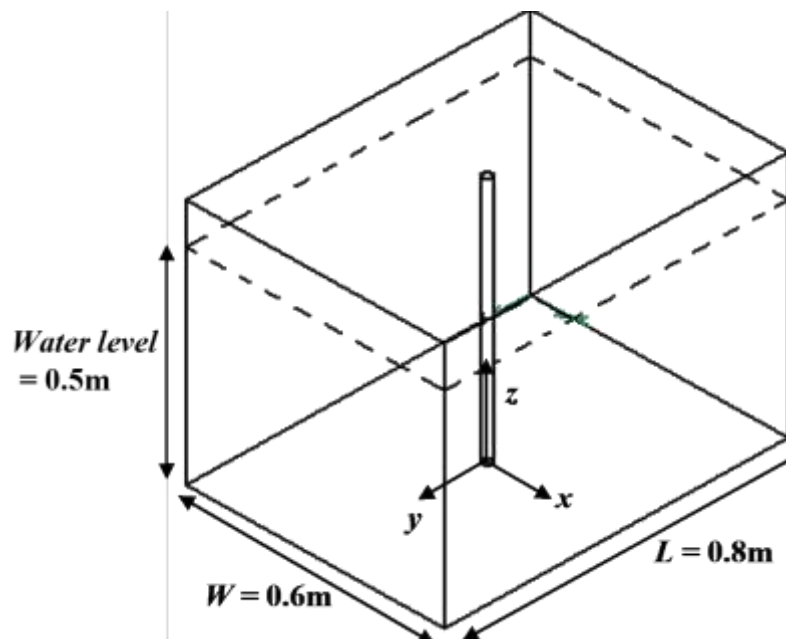


Fig 2.6: Schematic of the experimental set up of Gandhi et al. (2013)

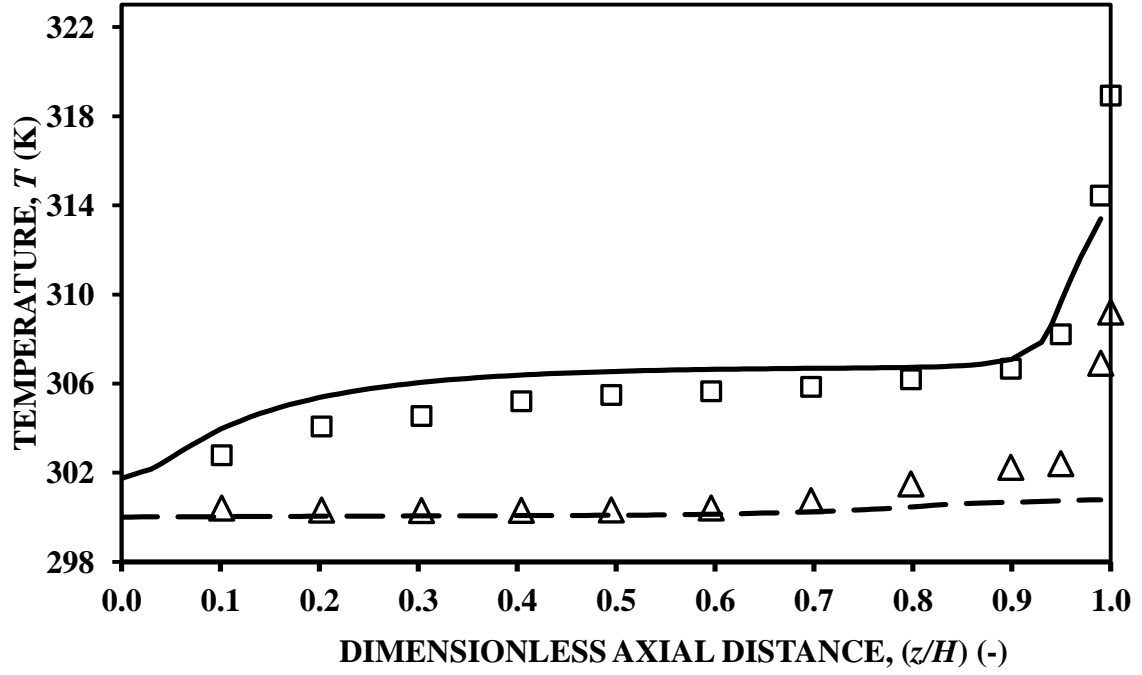


Fig 2.7: Comparison of present CFD model and experimental data for the temperature distribution for the geometry of Gandhi et al., (2013); (1) $x/W=0.01$, experiment (\square), OpenFOAM-1.6 (—); (2) $x/W=0.1$, experiment (Δ), OpenFOAM-2.2 (---)

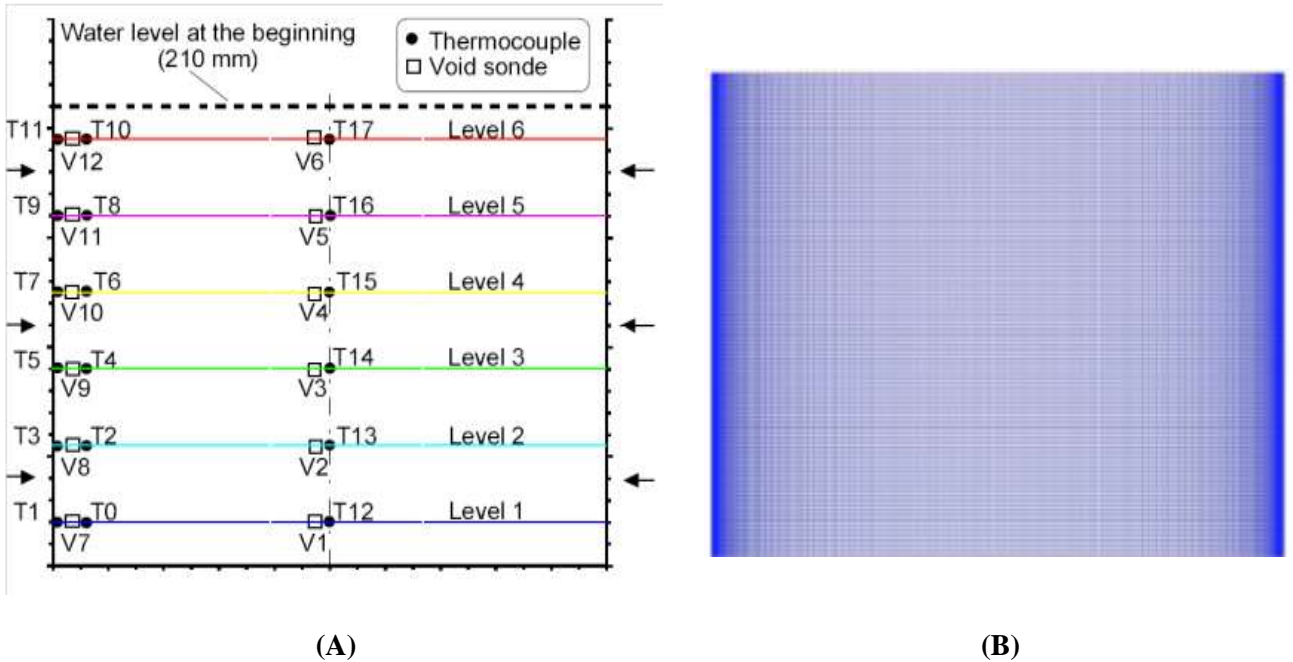


Fig 2.8: Schematic of the (A) experimental facility of Aszodi et al. (2000) along with (B) Grid generation

2.2.2 Aszodi et al., (2000) have performed experiments to study the effect of side wall heating on thermal stratification inside a water tank. The experimental test arrangement shown in Fig 2.8A consisted of a cylindrical tank with a diameter of 0.25 m and a height of 0.25 m. On the side walls, heating elements with an overall power of 4 kW are arranged, so that the heating power was equally distributed over the wall. During the tests, the tank was equipped with thermocouples and with conductivity probes for measuring the local void fractions at different locations. The transient temperature profiles at different heights from the tank bottom in Fig 2.9 shows that the side wall heating was found to result in non-uniform temperature distribution in the tank which results in thermal stratification. Due to side wall heating, the fluid adjacent to the heat source gets heated, becomes light and rises due to buoyancy. Consequently, the heavier fluid (cold water) from the neighboring areas rushes to take the place of the rising fluid. The temperature and velocity gradients are also concentrated near the heat source. In fact, in the bulk of water pool, the liquid velocities are feeble of the order of mm/s. As the rising fluid reaches the free water surface at the top, it flows in radially outward direction. When the fluid reaches the tank wall, it again gets diverted in the

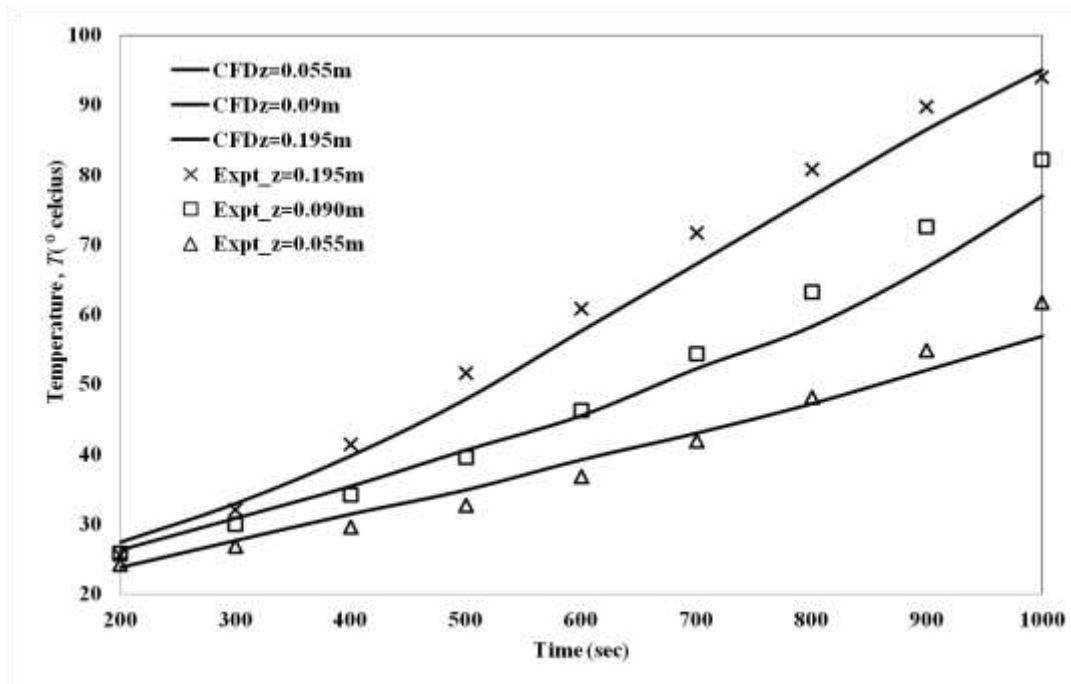


Fig 2.9: Comparison between CFD predictions and experimental data of Aszodi et al., (2010); for the transient temperature distribution at 1mm away from wall at different vertical positions

downward direction. As a result, circulation patterns get established in the water pool. As the time progresses, the hot liquid accumulate at the top free surface which results in increase in thermal stratification. The strong temperature stratification was also reflected in the CFD simulation. The time varying temperature profiles at three axial locations shown in Fig 2.9 clearly indicates that the CFD code is capable of predicting the non uniform temperature distribution in the tank to an accuracy of (1-7%). The error bar is very small (less than 4%) initially ($t < 500s$) and as the fluid temperature reaches saturation, CFD under predicts the temperature due to the absence of boiling model.

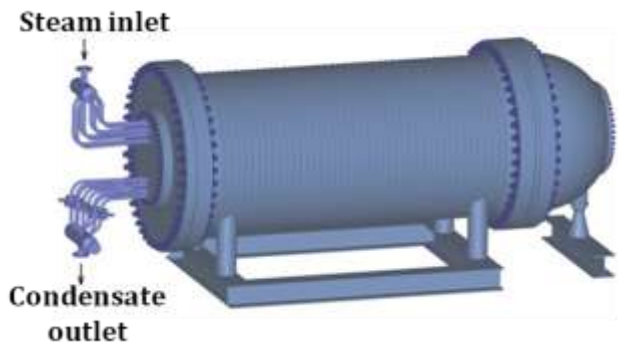


Fig 2.10: Schematic of the experimental test facility of Krepper et al. (2002)

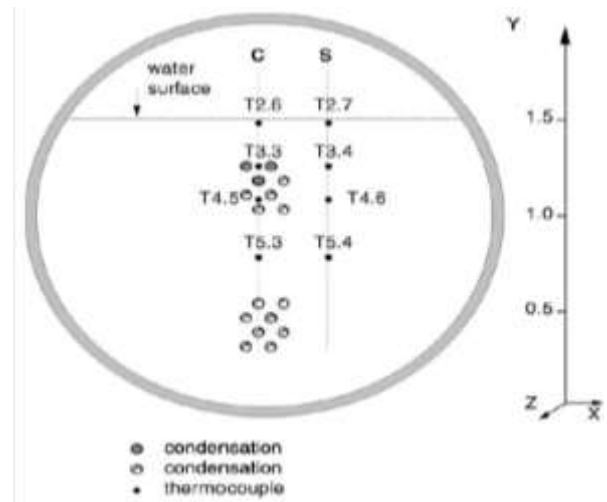


Fig 2.11: Schematic of the water tank along with thermocouples locations

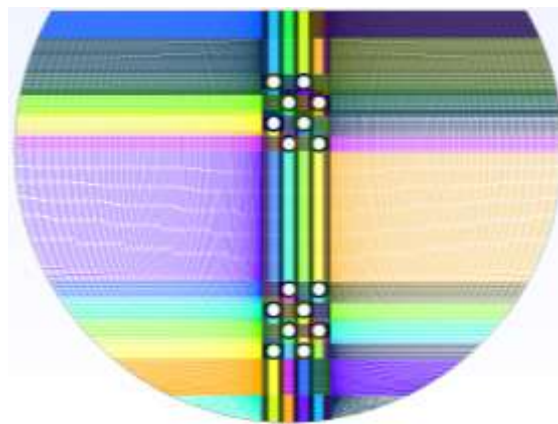


Figure 2.12: Schematic of Grid used for CFD calculation

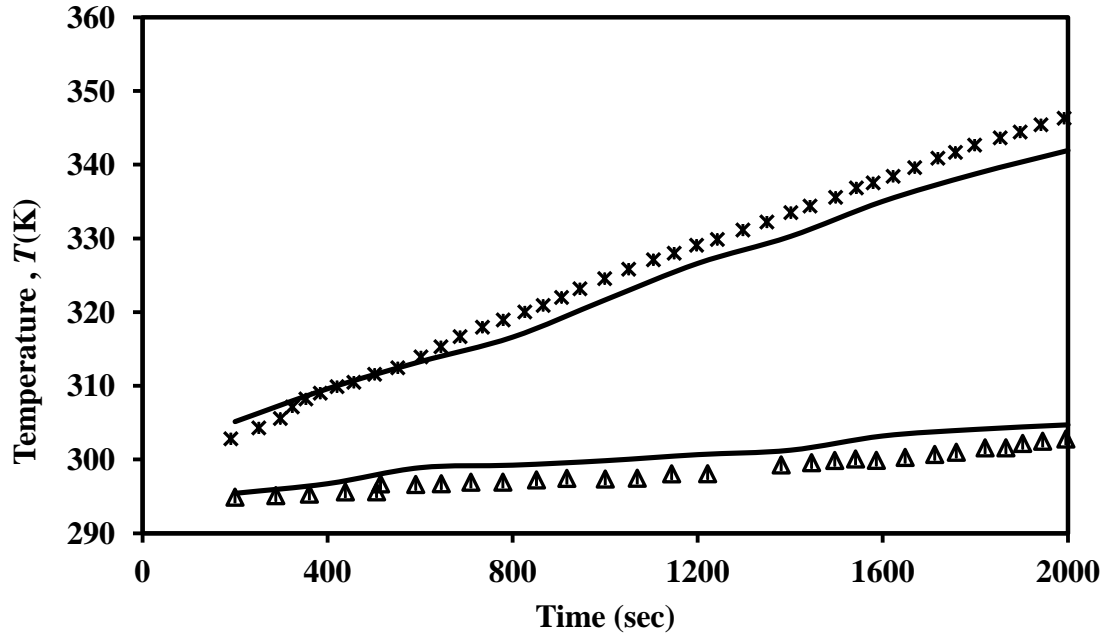


Fig 2.13: Comparison of present CFD model and experimental data for the temperature distribution for the geometry of Krepper et al., (2002); Experimental value (X) at $y=1.4\text{m}$, (Δ) at $y = 1.04\text{m}$, CFD (—)

2.2.3 Krepper et al., (2002) have studied the thermal stratification and heat transfer inside a horizontal water tank (18 m^3) consists of slightly inclined condenser tubes. A schematic of the experimental test facility of Krepper et al., (2002) is shown in Fig 2.10. The main components of the facility are the pressure vessel (height 12.6 m, diameter 0.448 m) and the laterally connected emergency condenser tube bundle. The tubes bundle consists of eight tubes having a length of 8.5–10 mm and an inner diameter of 44.5 mm. In the test facility, the steam is produced by an electrical heater with a maximum power of 4 MW. For simplification, the condenser was modelled only in two dimensions. A vertical cross-section was considered (see modelled plane in Figs 2.11 and 2.12).

The time varying temperature profiles at two axial locations shown in Fig 2.13 clearly indicates that the CFD simulation of the present case is capable of predicting the non uniform temperature distribution in the tank with an accuracy of (1-7%). In both experiments and CFD simulations, it was found that the hot water gets accumulated near the top surface and thus the system became thermally stratified. The major portion of fluid in the region below the tubes was not involved in the heating process. The comparison in Fig 2.13 clearly shows that the CFD code nominally over predict (4%)

the temperature distribution during the initial single phase period and under predict (7%) the two phase temperature distribution. This behavior is due to the fact that the CFD simulation is limited to single phase only.

2.3 Closure

The evaluation of five different turbulence models has been performed to study turbulent natural convection and heat transfer. The results show that the near wall turbulence and velocity predictions by SST $k-\omega$ and RSM model were in good (5%) agreement with the experiment. The RSM model requires large computation time to solve additional six Reynolds stress equations. In order to save the computation time, the SST $k-\omega$ model has been used for further studies. The benchmark studies performed above clearly indicates that CFD code OpenFOAM-2.2 is capable of predicting accurately the temperature and flow distribution inside the small (0.012 m^3 , 0.25 m^3) and large (18 m^3) water pool. Hence, the phenomenon of thermal stratification inside large water pool such as GDWP (9247 m^3) can be studied with good accuracy using OpenFOAM-2.2.

CHAPTER 3

Numerical investigation of three-dimensional natural circulation phenomenon in Passive Safety Systems for decay heat removal in large pools

3.1 Introduction

In a passive decay heat removal system, the heat transfer from the isolation condenser is concentrated in a limited zone of a large pool in terms of volume and results into the three dimensional flow and temperature fields. The non-uniform temperature distribution can be expressed in terms of extent of stratification. The heat transfer rate can get compromised by such temperature stratifications and the rate is also governed by the flow field in the vicinity of IC. Under strong temperature stratification conditions, the fluid at the top of the pool reaches the saturation temperature much earlier as compared to the case of homogeneous temperature distribution. In addition, the stratification is not desired because of the limitation imposed by the GDWP concrete walls (i.e. the temperature should not exceed beyond 65⁰C at any location). Hence, it is necessary to optimize the design of IC (a) to reduce thermal stratification (b) to attain the heat transfer rate in such a way that the heat gets decayed in a stipulated time (50% in 100s) and (c) to prevent early water evaporation so as to avoid over-pressurization of containment building.

3.2 System description

Passive decay heat removal system (PDHRS) is shown schematically in Fig 3.1. The PDHRS consists of Isolation condensers (ICs) (3) submerged in a Gravity Driven Water Pool (GDWP) (1). The GDWP is divided into 8 compartments (Fig 3.2) and one IC (3) is located in each compartment. The steam from four steam drums (4) flows through four pipes (5) which join into two (2) main steam lines. Four ICs are connected to each main steam line. The conventional design of isolation condenser (IC) shown in Fig 3.3 consists of vertical tubes, joined at both ends to a cylindrical header.

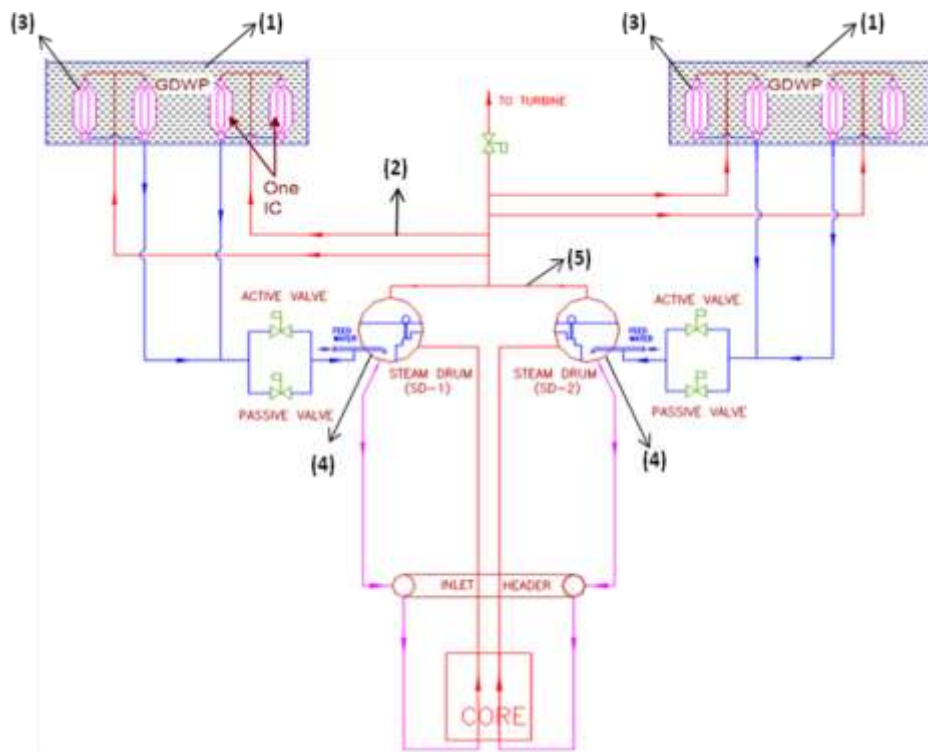


Fig 3.1: Schematic of Passive decay heat removal system

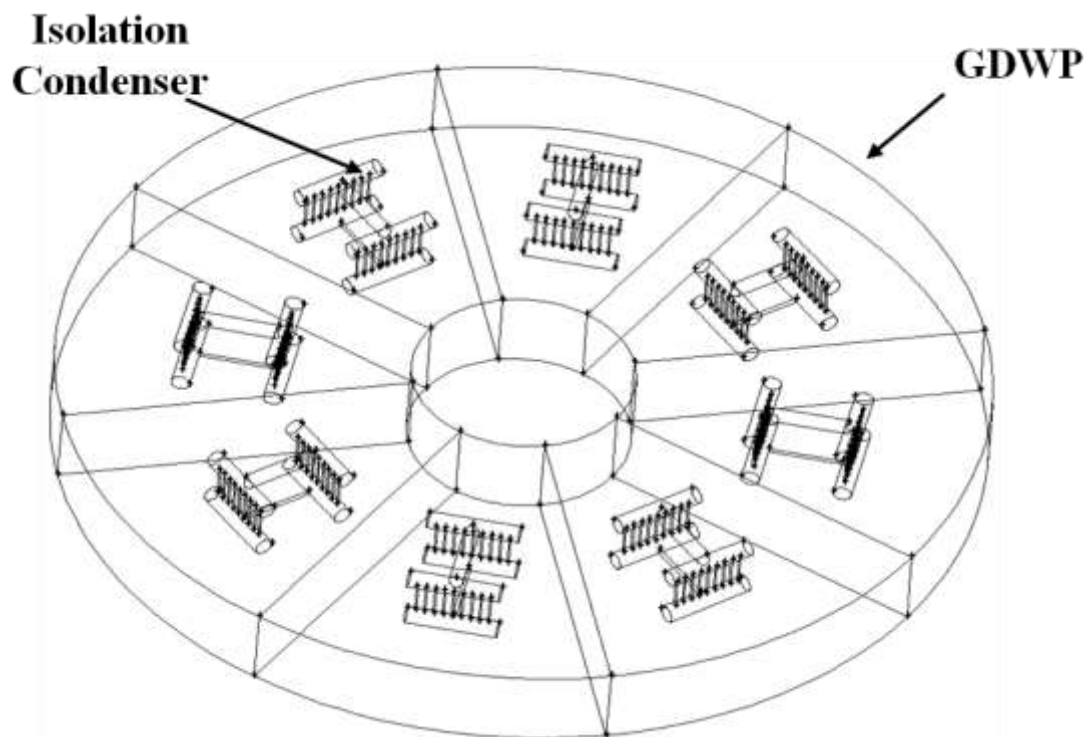


Fig 3.2: Schematic of GDWP pool with Isolation condensers (ICs)

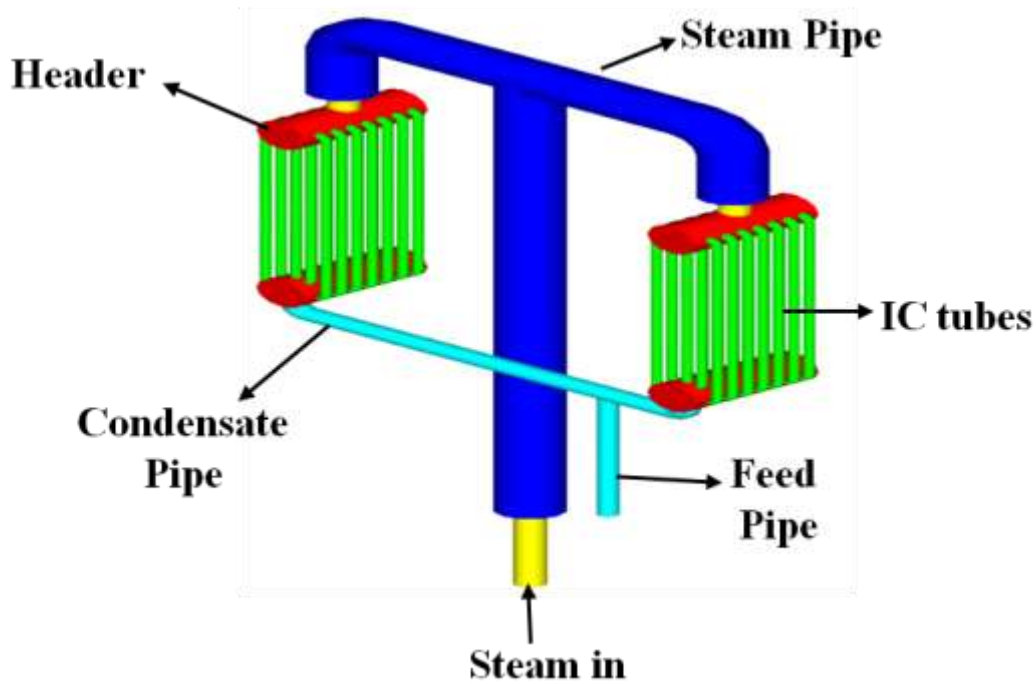


Fig 3.3: Schematic of isolation condenser (IC)

During normal reactor shut down, in case of unavailability of main condenser, decay heat in the form of steam enters from the steam drum into the ICs, condenses in the tubes, and the condensate returns by gravity to the steam drum. This condensation of steam enables to bring down the Main Heat Transport (MHT) system temperature from 285°C to 150°C. The GDWP inventory was decided on the basis of the following two criteria:

- (1) The water in GDWP must be able to accommodate decay heat for at least 7 days without operator intervention.
- (2) The temperature inside the GDWP should not exceed beyond 65°C at any location due to limitation imposed by the GDWP concrete walls

Initial Temperature of GDWP = 27°C

Estimated core decay heat (calculated from the decay heat curve) in 7 days

$$(Q) = 1417 \times 10^9 \text{ J}$$

Specific heat capacity of water $C_p = 4174 \text{ J/kg-}^\circ\text{C}$

The temperature limitation imposed by GDWP walls $\Delta T \leq (65^{\circ}\text{C} - 27^{\circ}\text{C}) = 38^{\circ}\text{C}$

$$Q = mC_p\Delta T$$

$$m = \frac{Q}{C_p\Delta T} = \frac{1417 \times 10^9}{4174 \times 38} = 8.93 \times 10^6 \text{ kg}$$

$$\text{Volume}(V) = \frac{m}{\rho} = \frac{8.93 \times 10^6 \text{ kg}}{1000 \text{ kg/m}^3} = 8930 \text{ m}^3$$

In view of the above estimates, the volume of GDWP is selected as 9247 m^3 .

3.3 Literature survey

Gandhi et al. (2013a, b) have reviewed the literature pertaining to the investigation of flow and temperature patterns in PDHRS. In their reviews, they included mostly laboratory scale investigations. The review of pilot and large scale installations and the systems exhibiting interesting phenomenon is given in the following subsection.

Kataoka et al. (1990) and Takamori et al. (1994) have investigated the effectiveness of baffle plate in mitigation of thermal stratification in the suppression pool of Passive Containment Cooling System (PCCS). Baffle plates results in 20% enhancement in heat transfer and reduction in thermal stratification. The major limitation of this work is that the study is limited to laminar flows. On the other hand, the flow in real passive safety systems is known to be turbulent because of large sizes of PDHRS as well as large temperature differences (Rayleigh number $= 10^{10} - 10^{16}$) between the heat source and the surrounding water pool.

Aszodi et al. (2000) have investigated the natural convection in a small cylindrical tank heated by the side wall. The side wall heating was found to result in non-uniform temperature distribution in the tank which results in thermal stratification. The authors have reported an interesting phenomenon of jumps in temperature field at various locations and at different time intervals. Immediately after these jumps (1300s), there was a quick transition from sub-cooled boiling to volumetric boiling and rapid saturation occurred in the entire fluid volume. As a consequence, the thermal stratification could be substantially reduced. Since the thermal

stratification needs the knowledge of the 3D temperature and flow fields, hence the 2D axis-symmetric assumption becomes restrictive in real life applications. Further, the study did not include any modification in the design of heated tube which could reduce the thermal stratification before the temperature jumps occurred.

Krepper et al. (2002) have investigated the phenomenon of natural convection and thermal stratification in a horizontal tank. Boiling at the upper surface of pool starts much earlier than expected due to thermal stratification. In order to reduce the stratification, the authors have numerically investigated the effect of two vertical guide plates to transport the lower cold fluid to replace the upper hot fluid. The guide plate arrangement resulted in an early onset of thermal stratification. Therefore, an optimization in the design of guide plates and the position of heat source was found to be necessary for efficient heat removal and also for the reduction of thermal stratification.

Natural circulation characteristics of an emergency condenser tank was investigated experimentally by Park et al. (2008). The thermal stratification phenomenon was reported which results in accumulation of hot fluid at the top. With progress in time, the high temperature region was found to penetrate below and the thermal mixing process was very slow in this region as the heat transfer was mainly due to conduction rather than a natural convection. This work, however did not suggest any modification in the hardware for reducing the thermal stratification.

Krepper et al. (2002) have performed experiments and CFD simulations to investigate the heat transfer capability of an emergency condenser. Thermal stratification was over-predicted in case of single phase simulation whereas the two phase simulations were found to be closer to the experimental observations. In the latter case, the maximum stratification was found to occur after about 1800s, which was then followed by a destruction of the stratification by increased steam production. Similar phenomena of establishment and destruction of temperature stratification have also been reported by Aszodi et al. (2000). Such a phenomenon is very useful for the overall

performance, however, it is very much system dependent (geometry, heat flux). Further, in actual nuclear reactors, (1) the system geometry is very large which can cause significant delay in the destruction of thermal stratification by uniform steam distribution. On contrast, such a time frame is not available in GDWP as the decay is expected to decrease sharply from 6% to 3% in about 100s.

Natural convection inside large water pool (GDWP) has been studied by Verma et al. (2013) using 1D code. In order to reduce the stratification, authors have proposed three shroud arrangement around the heat source which can result in reduction in thermal stratification. They have further found that, further increase in the number of shrouds increases stratification and reduction in mixing of hot and cold fluid. This work is very useful and needs confirmation by undertaking 3D simulations with appropriate turbulence models.

The foregoing discussion brings out the importance of design modifications in the IC design and the pool geometry on the stratification. Therefore, Gandhi et al. (2013a, b) investigated a large number of design modifications such as (a) IC submergence (b) diameter, height and number of draft tubes (c) attachment of fins to heat transfer tube. In this case, the size, number and their locations were varied over a wide range. In addition, the role of conducting versus non-conducting fins was investigated in detail. The effect of all these internals was studied in 25 litre circular tank (Gandhi et al., 2013a) and 210 litre rectangular tank (Gandhi et al., 2013b). Such a systematic investigation now needs to be extended to real size 9247m³ GDWP.

From the literature review [Table 3.1], it is clear that many successful attempts have been made by various authors to address the challenging problem of thermal stratification in the design of heated tubes submerged in water pool. Many modifications (draft tube, fins, insulation) in the design of heat exchangers have been proposed to improve the performance. However, the published work has a limitation that most of the work was restricted to small pools (less than one m³ in most of cases) and consisted of few heated tubes. The real pool is several hundreds of m³ volume and certain

able 3.1: Summary of literature survey

Author	System & experimental details	Methodology adopted	Conclusion	Limitation
Kataoka et al. (1990) and Takamori et al. (1994)	15 ⁰ Sector of tank, Working fluid = water. H=5.3m, W=1.25m. Baffle plate: L=3.1m and 0.7m away from heat source. $Ra = 10^{15}$.	3D code THERVIS Mesh size = $12 \times 5 \times 39$. Laminar flow model. Slip conditions on the wall.	Thermal stratification has been reduced and heat transfer is enhanced by 20% due to baffle plate.	Work was limited to laminar region. Slip conditions on the wall. Mesh size is very small. Quantification of thermal stratification has not been done.
Aszodi et al. (2000)	Cylindrical Tank $D = 0.25$ m, $H = 0.25$ m, $P = 4$ KW with side wall heating. $P/V = 3.3 \times 10^5$ W/m ³ Working fluid = water. Temperature measurements using thermocouples. Local void fractions using conductivity probes. $Ra = 10^{10}$	2D mathematical model Mass conservation for two phases and momentum and energy equations for fluid only Model is restricted to low gas densities Boussinesq approximation. Constant bubble rise velocity Constant turbulent viscosity	Thermal stratification due to non uniform temperature distribution. Temperature jumps at various locations at different time intervals. Quick transition from sub-cooled boiling to volumetric boiling and rapid saturation occurs in the entire fluid volume	Method to suppress the thermal stratification was not studied. Only 2D CFD simulation has been performed. Constant turbulent viscosity to incorporate turbulence.
Krepper et al. (2002)	Horizontal cylindrical pool $D = 2$ m and $L = 6$ m with 8 tube bundle assembly. $P = 0.6$ MW; $P/V = 3.2 \times 10^4$ W/m ³ , $Q = 1.68 \times 10^5$ W/m ² , Temperature measurements using thermocouples; Working fluid = Water Adiabatic guide plates = 0.25 m away for heat source $Ra = 10^9$	2D Navier-Stokes single phase simulations using commercial software CFX-4 Laminar flow inside tank volume. Boussinesq approximation.	Placements of guide plates are unable to enhance the natural circulation. Boiling at the upper surface of pool starts much earlier than expected due to thermal stratification.	Optimization in baffle design to reduce thermal stratification has not been studied. Placement of heated tubes near the top of the tank also results in early rise in temperature of fluid at top. 2D CFD simulation has been performed.

Park et al. (2008)	ECT tank of ID = 0.4m, H= 3.4m having 6 condensing tubes of L = 1.2m, OD = 15mm, P = 682 KW. Temperature measurements using K type thermocouples. Flow-meters for measuring flow rates.	1 D Navier-Stokes two phase simulations using thermal hydraulic system analysis code MARS.	Coolant above the upper plenum of PRHRS HX is mixed well but the coolant below the upper plenum of the PRHRS HX is stratified.	No modification in the heat exchanger design for ECT in order to avoid thermal stratification. Multidimensional natural convection inside tank has not been studied.
Krepper et al. (2010)	Horizontal cylindrical pool of volume 17.7m ³ . 8 tube bundle assembly having ID = 44 mm and L = 8 m. P = 4 MW; P/V= 2.3 x 10 ⁵ W/m ³ , Q = 2.32 x 10 ⁵ W/m ² . Temperature measurements using thermocouples. Working fluid = Water	2D Navier-Stokes two phase simulations using commercial software CFX-11. Wall boiling model is used to measure two phase. Boussinesq approximation. SST turbulence model.	Strong temperature stratification is observed. Thermal stratification is over-predicted by single phase CFD simulation. Two phase study shows max stratification after about 1800s, followed by destruction due to increased steam production.	Method to suppress the thermal stratification was not studied. Only 2D CFD simulation has been performed. Quantification of thermal stratification has not been done.
Gandhi et al. (2011)	Rectangular enclosure (0.8 × 0.6 × 0.6 m) Tube diameter = 0.02 m 10 Tube assembly Working fluid = Water Ra = 4.34 × 10 ¹¹ to 2.59 × 10 ¹⁴ Temperature measurement using thermocouples Flow measurements using PIV.	3D, single phase CFD simulations: OpenFOAM-1.6. two phase CFD simulations: FLUENT-6.3 Mesh size = 750,000 cells Simulation type = Transient. Film condensation inside tube is assumed. Boussinesq approximation.	For low Ra, deviation between single phase and two phase CFD simulations is less than 20% as amount of vapor generated is low. Bubbles are confined near the tube wall region. Increasing heat input the system becomes more thermally stratified. Mixing in the tank is poor even at very high Ra.	Method to suppress the thermal stratification was not studied.

Verma et al. (2013)	GDWP tank, H=5m, ID=12m, OD=50m. 8000m ³ 180 IC tubes, HT area=54m ² . Shrouds=3,5,7	1 D Navier-Stokes two phase simulations using thermal hydraulic system analysis code RELAP5/Mod 3.2.	Placement of shrouds results in reduction in thermal stratification. Oscillations in temperature and mass flow is observed. Three shroud arrangement is the best design because thermal stratification increases and mass flow rate decreases as the no. of shrouds increases.	Multidimensional natural convection inside GDWP tank has not been studied. Need of 3D CFD simulations to ensure the optimization in the design of shrouds arrangement.
Gandhi et al. (2013a)	Rectangular enclosure (0.8 × 0.6 × 0.6 m) d _t = 0.02 m, P =15KW Ra = 5.9 ×10 ¹¹ to 2.59 ×10 ¹⁴ . AR=1, 0.75 ,0.5 Draft tubes (H =0.4m,0.48m) (D =0.05m, 0.1m) Fins (Adiabatic and Conducting).	3D CFD simulations: Two phase simulation using FLUENT-6.3 Mesh size = 750,000 cells Film condensation inside tube is assumed. Boussinesq approximation.	Insulated region on the heating tube reduces the heat transfer area and hence energy input. Draft tubes increases temperature gradient and vapor generation rate near the vicinity of tube wall. Fins provide lateral motion to fluid which causes mixing of hot and cold fluid.	Need of scaling and optimization of the passive internals design for actual nuclear reactors to enhance heat transfer.

amount of energy has to be decayed in predetermined time. Therefore, the objective of this study is to investigate the three-dimensional natural circulation phenomenon in large water pools (GDWP) and hence see the possibilities of various passive internals to improve the efficiency of heat exchanger (IC). For this purpose, the validated open source CFD code [OpenFoam-2.2] has been used to study natural convection and thermal stratification in real size GDWP of 9247 m³.

3.4 Numerical Procedure

3.4.1 Governing equations

In order to simplify the problem of two phase flow inside the IC, it was assumed that the saturated steam enters the IC tube and undergoes only phase change due to condensation. The film condensation occurring inside the tube and hence the tube is at a constant saturation temperature ($T = 558$ K). Mukesh et al. (2013) performed 1D simulation of the PDHRS for a period of 10 days using system code RELAP. The authors have reported that for the initial transient period ($t < 1800$ s), there is only small change ($\Delta T < 10$ K) in the steam temperature inside the IC tubes. Since, the GDWP volume is of the order of (~ 10000 m³), the major focus is kept on understanding the fluid flow and temperature distribution inside the GDWP for the initial transient period ($t \leq 100$ s). Hence, a constant temperature boundary condition ($T = 558$ K) was used on the surface of IC tube for the initial transient period($t \leq 100$ s). In order to model the unsteady single phase thermal stratification, the governing equations (continuity, momentum, and energy) with the appropriate Reynolds stress closure need to be solved with the boundary conditions. In the present CFD simulations the tube wall (of isolation condenser) was kept at constant temperature ($T_w = 558$ K). This value corresponds to the saturation temperature of steam at 7 MPa pressure. The physical properties are given in Table 3.2. The Rayleigh number is the ratio of a buoyancy velocity ($g\beta\Delta T l^2 / \nu$) to a diffusion velocity(α / l). For the present case of $\beta = 8 \times 10^{-4}$ (K⁻¹), $\Delta T = 258$ K, the value of Ra works out to be 7×10^{13} .

Table 3.2: Physical properties of fluid used for CFD simulations

Characteristic length (l) (m)	2.2m
Thermal expansion coefficient (β) (K^{-1})	0.0008
Gravitational force (g) (m^2/s)	9.81
Fluid density (ρ) (kg/m^3)	980
Kinematic viscosity (ν) (m^2/s)	1.38×10^{-6}
Thermal diffusivity (α) (m^2/s)	2.3×10^{-7}
Operating temperature (T_o) (K)	300
Heat source wall temperature (T_w) (K)	558
Temperature driving force (ΔT) (K)	258
Rayleigh number $\left(Ra = \frac{g\beta\Delta T l^3}{\nu\alpha} \right)$	7×10^{13}

Table 3.3: Governing equations for single phase CFD simulations

Continuity	$\frac{\partial \bar{u}_j}{\partial x_j} = 0$
Momentum	$\frac{\partial \bar{u}_i}{\partial t} + \frac{\partial}{\partial x_j} (\bar{u}_j \bar{u}_i) - \frac{\partial}{\partial x_j} \left\{ \nu_{eff} \left[\left(\frac{\partial \bar{u}_i}{\partial x_j} + \frac{\partial \bar{u}_j}{\partial x_i} \right) - \frac{2}{3} \left(\frac{\partial \bar{u}_k}{\partial x_k} \right) \delta_{ij} \right] \right\}$ $= -\frac{\partial \bar{p}}{\partial x_i} + g_i [1 - \beta(\bar{T} - T_0)]$
Turbulent kinetic energy	$\frac{\partial k}{\partial t} + U_j \frac{\partial k}{\partial x_j} = P_k - \beta^* k \omega + \frac{\partial}{\partial x_j} \left[(\nu + \sigma_k \nu_T) \frac{\partial k}{\partial x_j} \right]$ $\nu_T = \frac{a_{1k}}{\max(a_{1\omega}, SF_2)}$
Energy dissipation rate equation	$\frac{\partial \omega}{\partial t} + U_j \frac{\partial \omega}{\partial x_j} = \alpha S^2 - \beta \omega^2 + \frac{\partial}{\partial x_j} \left[(\nu + \sigma_\omega \nu_T) \frac{\partial \omega}{\partial x_j} \right] + 2(1 - F_1) \sigma_{\omega 2}$
	$F_2 = \tanh \left[\left[\max \left(\frac{2\sqrt{k}}{\beta^* y \omega}, \frac{500\nu}{y^2 \omega} \right) \right]^2 \right]$
	$P_k = \min \left(\tau_{ij} \frac{\partial U_i}{\partial x_j}, 10\beta^* k \omega \right)$

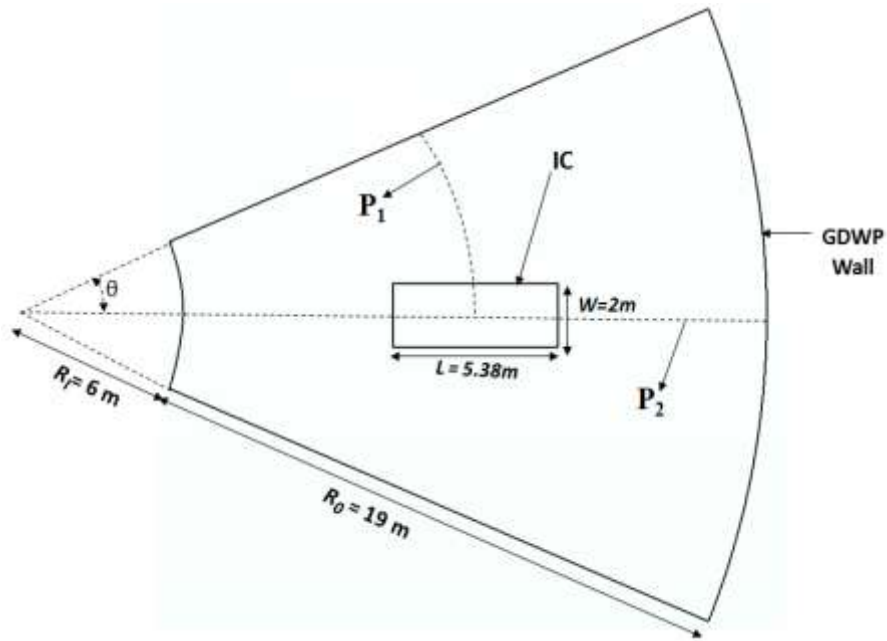
	$F_1 = \tanh \left\{ \left\{ \min \left[\max \left(\frac{\sqrt{k}}{\beta^* y \omega}, \frac{500 \nu}{y^2 \omega} \right), \frac{4 \sigma_{\omega 2} k}{C D_{k \omega} y^2} \right] \right\}^4 \right\}$
	$C D_{k \omega} = \max \left(2 \rho \sigma_{\omega 2} \frac{1}{\omega} \frac{\partial k}{\partial x_i} \frac{\partial \omega}{\partial x_i}, 10^{-10} \right)$
	$\phi = \phi_1 F_1 + \phi_2 (1 - F_1)$
	$\alpha_1 = \frac{5}{9}, \alpha_2 = 0.44$
	$\beta_1 = \frac{3}{40}, \beta_2 = 0.0828$
	$\beta^* = \frac{9}{100}$
	$\sigma_{k1} = 0.85, \sigma_{k2} = 1$
	$\sigma_{\omega 1} = 0.5, \sigma_{\omega 2} = 0.856$
Energy	$\frac{\partial \bar{T}}{\partial t} + \frac{\partial}{\partial x_j} (\bar{T} \bar{u}_j) = \frac{\partial}{\partial x_j} \left[\left(\frac{\nu_t}{Pr_t} + \frac{\nu_0}{Pr} \right) \frac{\partial \bar{T}}{\partial x_k} \right]$

In the present work, Shear Stress Transport (SST) $k - \omega$ turbulence model was used to study turbulent natural convection. The reason behind selection of this model has been explained in great detail in Chapter 2. The flow was considered to be turbulent on the basis of general criteria of Rayleigh number ($Ra > 10^9$). All the governing equations for the single-phase simulations of natural convection are given in Table 3.3. In the present case, the following assumptions have been made:

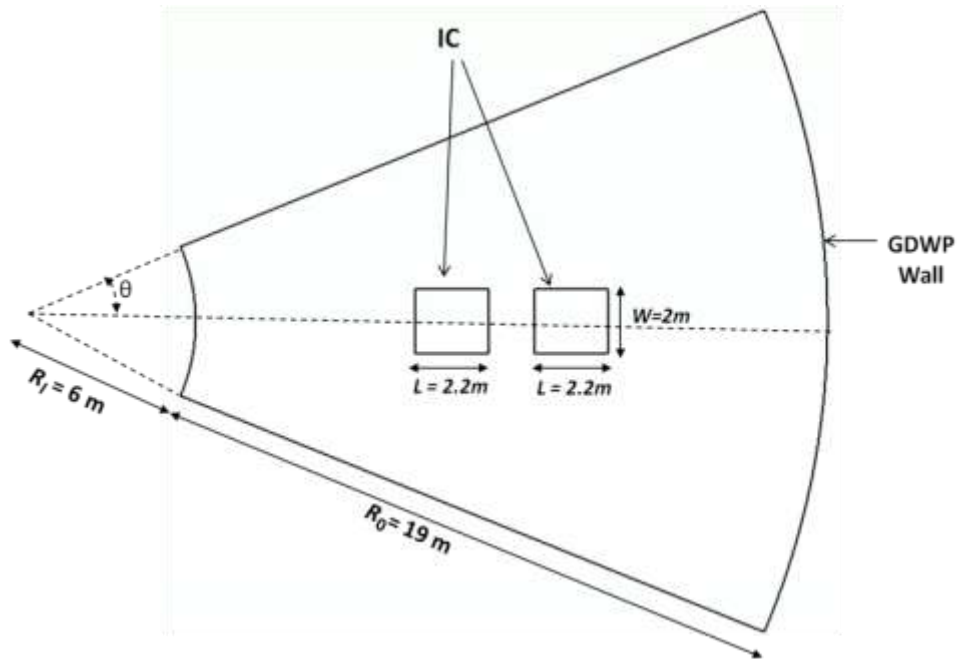
3.4.2 Model Assumptions

- (1) Condensation occurring inside the tube is film condensation and hence the tube is at a constant saturation temperature and $\Delta T = 258$ K.
- (2) Fluid is Newtonian and incompressible. However, boussinesq approximation has been assumed to be valid which means the temperature differences produced the force due to buoyancy.
- (3) Fluid properties are constant except in the formulation of buoyancy term.
- (4) The boiling phenomenon has been neglected.

- (5) In the case of perfectly non-conducting draft tubes, heat transfer does not take place from the surface of these baffles.



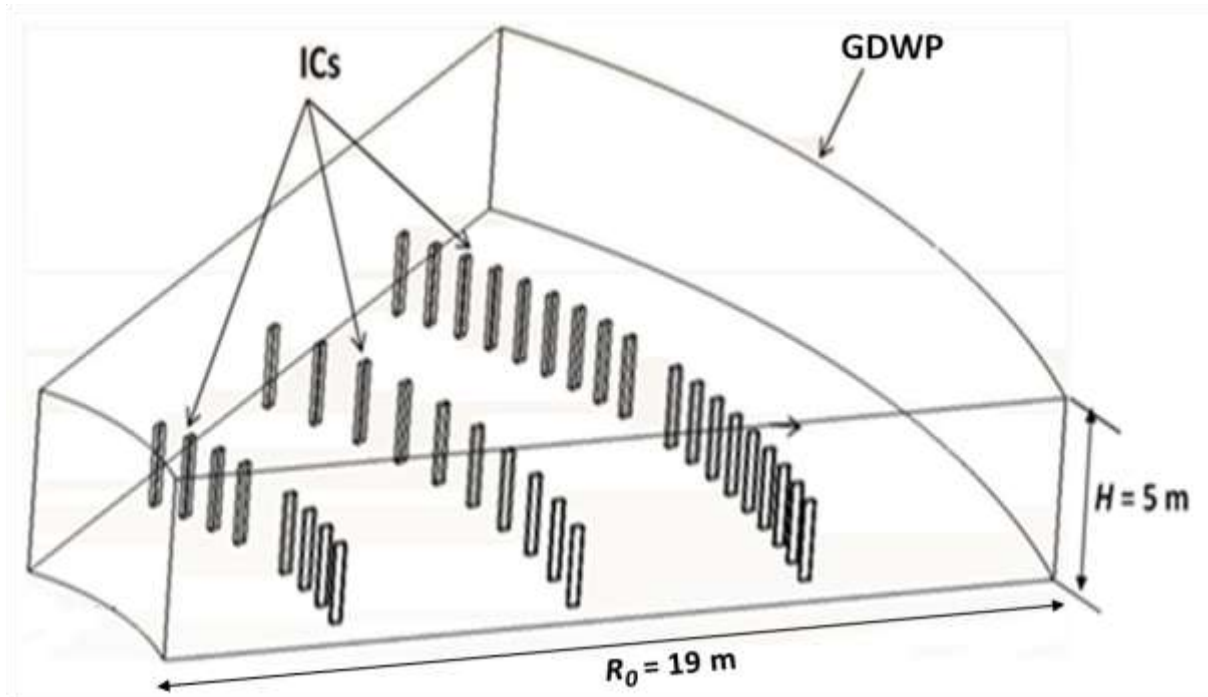
(A)



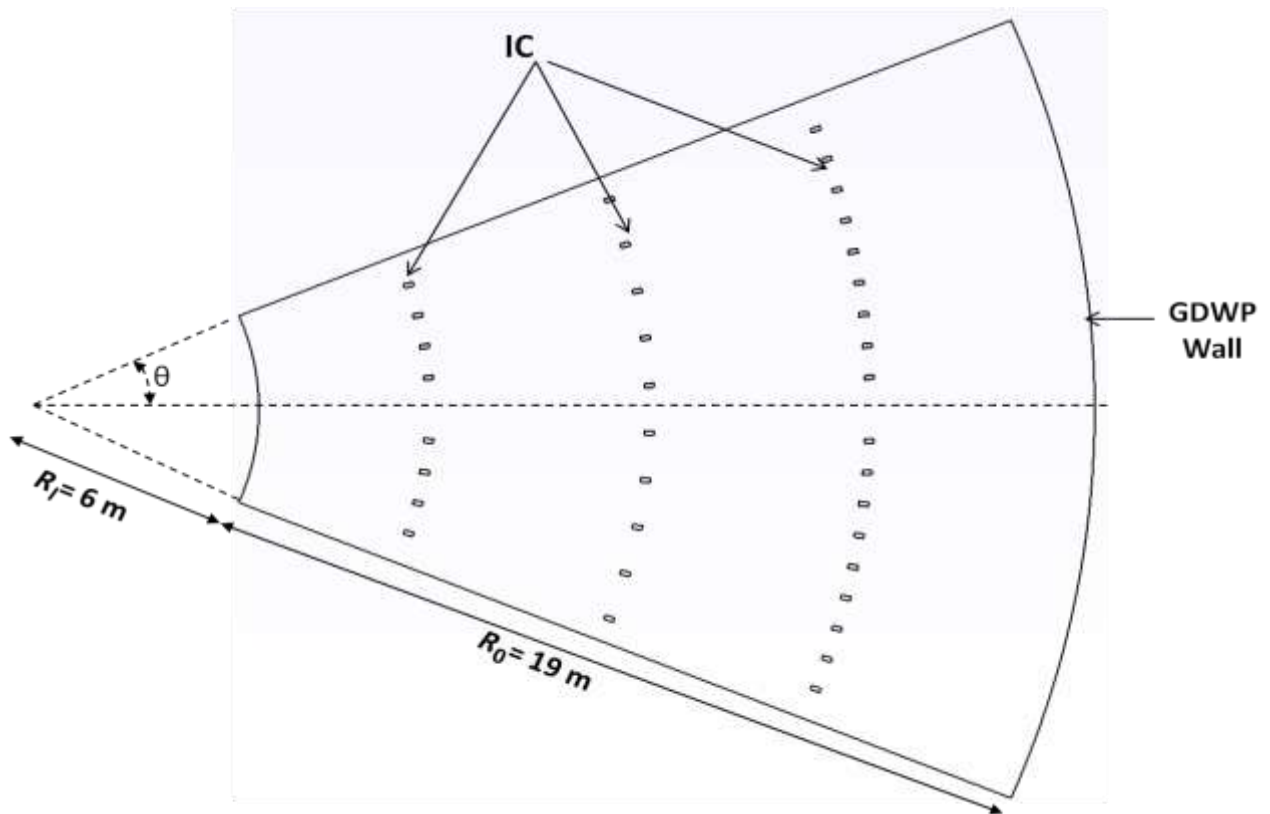
(B)

Fig 3.4: Schematic diagram (Top view) for various designs of ICs

(A) 'IC1c1.4' (B) 'IC2c0.5'



(A)



(B)

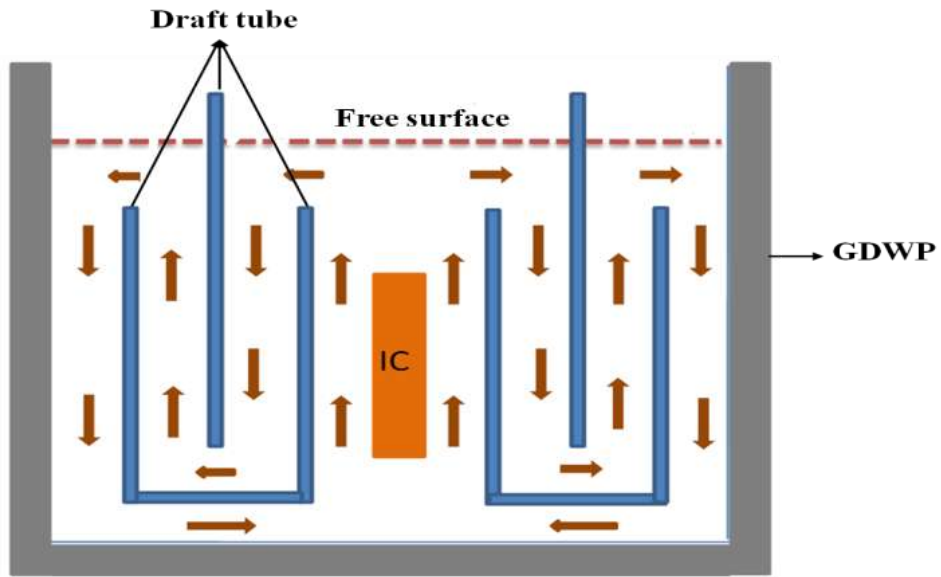
Fig 3.5: Schematic diagram for *ICMc0.1* design (A) Isometric view (B) Top view

Table 3.4: Design details of different designs of Isolation Condensers and Draft Tubes

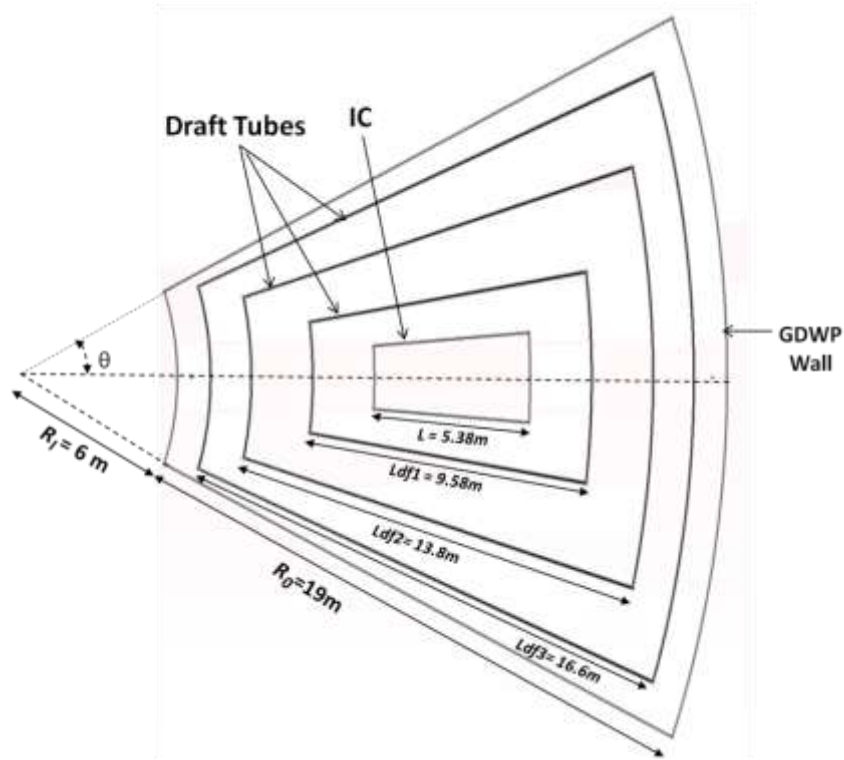
System	Design	Heat source dimensions (m)	Total Number (-)	Location (-)
Single heat source at centre	<i>IC1c1.4</i>	$H_{SI} = 5.381 \times 2 \times 2.2;$	1	H_{SI} @ r/R of 0.358 to 0.642 with $\Theta = 0^\circ$ at $z/H=0.28$ to 0.72
	<i>IC1c0.6</i>	$H_{SI} = 5.381 \times 2 \times 2.2;$ ($L \times W \times H$)		H_{SI} @ r/R of 0.358 to 0.642 with $\Theta = 0^\circ$ at $z/H=0.12$ to 0.56
Two heat sources at fixed radial location	<i>IC2c1.4</i>	$H_{SI} = 2.2 \times 2 \times 2.2;$	2	H_{SI} @ r/R of 0.347 to 0.463 and H_{S2} @ r/R of 0.536 to 0.652 with $\Theta = 0^\circ$ at $z/H=0.28$ to 0.72
	<i>IC2c0.6</i>	$H_{S2} = 2.2 \times 2 \times 2.2;$		$z/H=0.12$ to 0.56
	<i>IC2c0.1</i>	($L \times W \times H$)		$z/H=0.02$ to 0.46
Multiple heat sources at fixed radial location	<i>ICMs0.1</i>	$H_{SI} = 0.22 \times 0.11 \times 2.2;$	36	@ r/R of 0.764 to 0.836 with $\Theta = 11.25^\circ$ at $z/H=0.02$ to 0.46
Draft Tubes	<i>DF0</i>	$L=5.38\text{m}, h=2.2\text{m},$	0	$\theta_h = -3.8^0$ to 3.8^0 at $z/H=0.12$ to 0.56
	<i>DF1</i>	$L=5.38\text{m}, h=2.2\text{m},$ $t= 0.02\text{m}, L_{df1}=9.58\text{m},$ $H_{df1} = 4\text{m}, 0.2\text{m away}$	1	$\theta_h = -3.8^0$ to 3.8^0 at $z/H=0.12$ to 0.56 $\theta_{df1} = -7.9^0$ to 7.9^0 , at $z/H=0.12$ to 0.56
	<i>BDF3</i>	$L=5.38\text{m}, h=2.2\text{m},$ $t= 0.02\text{m}, H_{df1} = 4\text{m},$ $H_{df2} = 4\text{m}, H_{df3} = 4\text{m}$ $L_{df1}=9.58\text{m}, 0.2\text{m away}$ $L_{df2}=13.8\text{m}, 0.7\text{m away}$ $L_{df3}=16.6\text{m}, 1.2\text{m away}$	3	$\theta_h = -3.8^0$ to 3.8^0 at $z/H=0.12$ to 0.56 $\theta_{df1} = -7.9^0$ to 7.9^0 $\theta_{df2} = -14.4^0$ to 14.4^0 $\theta_{df3} = -18.8^0$ to 18.8^0

3.4.3 Geometry

In the present work, $1/8^{\text{th}}$ sector (1155 m^3) of GDWP tank having dimensions ($R_o = 25\text{m}$, $R_i = 6\text{m}$, $H_T = 5\text{m}$, $\theta_T = -22.5^\circ$ to 22.5°) has been used as an enclosure which is completely filled with water. The three dimensional natural convection has been studied inside GDWP pool in the presence of box type heat sources having three different heat transfer areas $IC1 = 54.6\text{m}^2$ ($5.381\text{m} \times 2\text{m} \times 2.2\text{m}$), $IC2 = 27.3\text{m}^2$ ($2.2\text{m} \times 2\text{m} \times 2.2\text{m}$), $ICM = 1.5\text{m}^2$ ($0.22\text{m} \times 0.11\text{m} \times 2.2\text{m}$). Heat source ($IC1c1.4$) (Fig 3.4A) was placed at the centre of the enclosure at $\theta = 0^\circ$ and having clearance (c) of 1.4m from the bottom of the tank. In order to reduce the stratification, the effects of various modifications in the design of IC (Table 3.4) have been examined. As a first simple modification (1) distribution of heat source was examined by distributing the HT area (54.6m^2) among two heat sources ($IC2c1.4$) (Fig 3.4B) of HT area 27.3m^2 each having clearance (c) of 1.4m from the bottom of the tank. The next modification was the (2) submergence of ($IC1$ and $IC2$) inside GDWP tank. The condensers were placed near the bottom (having clearance (c) of 0.6m and 0.1m away from bottom of the tank). Five cases were considered ' $IC1c1.4$ ', ' $IC1c0.6$ ', ' $IC2c1.4$ ', ' $IC2c0.6$ ' and ' $IC2c0.1$ '. Then the combined benefits of (1) heat source distribution and (2) submergence were incorporated in the $ICMc0.1$ design (Fig 3.5) which consisted of 36 box type heat sources having clearance (c) of 0.1m. Finally, the provision of draft tubes ($DF1$) and draft tube with baffle at the top ($BDF3$) around the single heat source has been examined (Fig 3.6). The shape of heat source was similar to GDWP tank having dimensions ($L=5.38\text{m}$, $H=5\text{m}$, $\theta_h = -3.8^\circ$ to 3.8°). The $DF1$ design consists of a single draft tube ($t=0.02\text{m}$, $L_{df1}=9.58\text{m}$, $\theta_{df1} = -7.9^\circ$ to 7.9° , $H_{df1}=4\text{m}$) placed at 2.1m away from heat source and having a geometry similar to heat source. On the other hand $BDF3$ (Fig 3.6) design consist of three draft tubes ($t= 0.02\text{m}$, $H_{df3} = 4\text{m}$). In ($BDF3$) design, the lateral span of the three draft tubes were: first ($\theta_{df1} = -7.9^\circ$ to 7.9°), second ($\theta_{df2} = -14.4^\circ$ to 14.4°), and third ($\theta_{df3} = -18.8^\circ$ to 18.8°). These three draft tubes were placed at 2.1m, 4.2m and 5.6m away from the heat source.



(A)



(B)

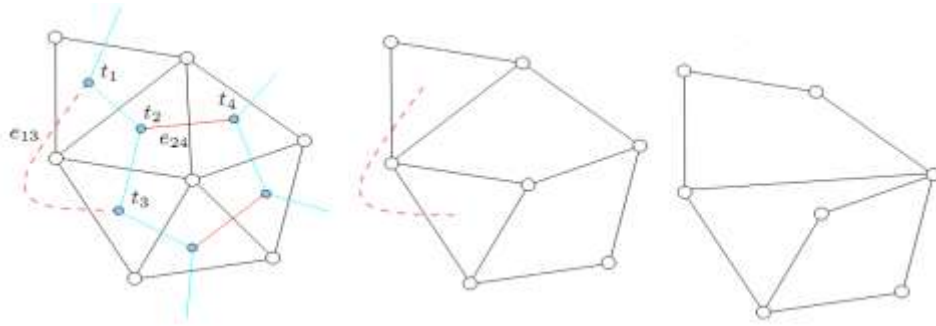
Fig 3.6: Schematic diagram of three draft tube with baffle (BDF3) inside GDWP

(A) Front view ; (B) Top view

3.4.4 Mesh construction algorithm

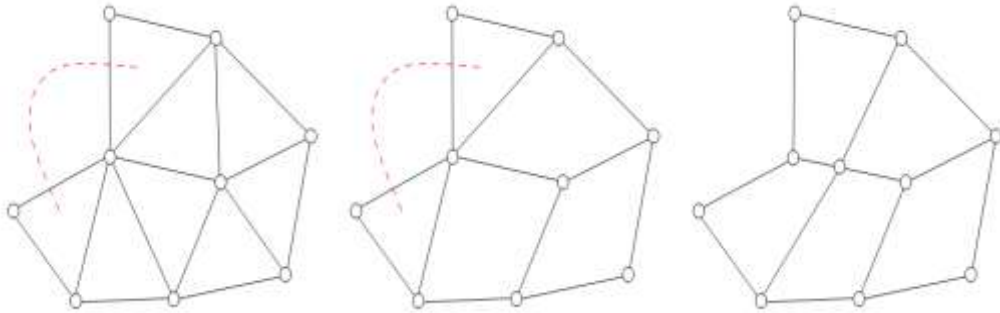
In the present work, an indirect way of producing all high quality quad surface meshes was used. The method takes advantage of a well known algorithm of the graph theory, namely the blossom algorithm (Remacle et al., 2010) that computes the minimum cost perfect matching in a graph in a polynomial time. In indirect methods, a triangular mesh is built first. These triangles are then recombined using triangle-merge procedure to form quadrangles. The mesh generation procedure was as per the following steps:

1. Starting from a solid geometry, mesh every model edge with an even number of mesh nodes on the boundary to have an even number of triangles in the initial triangular mesh. The even number of triangles is an initial requirement for the final mesh to be quadrilateral. Euler's formula for planar triangulations states that the number of triangles (n_t) in the mesh is defined by $n_t = 2(n_v - 1) - n_v^b$, where n_v^b is the number of mesh nodes on its boundary. So, the number of mesh points on the boundary n_v^b should be even.
2. Then mesh the model faces with a modified Frontal-Delaunay (Remacle et al., 2010) triangulation algorithm that allows building triangular meshes that are better suited for recombination into quadrangles. This is done by using the infinity norm to compute distances in the meshing process. The alignment of the elements in the frontal delaunay procedure is controlled by a cross field defined on the domain. Meshes generated in this way have their points aligned with the cross field directions and their triangles are almost right everywhere. Filling surface with right angle triangles requires 15% less vertices than conventional equilateral triangle and hence very useful.
3. From the produced mesh, a weighted graph $G(V, E, c)$ was made. Here, V is the set of n_v vertices, E is the set of n_E undirected edges and $c(E) = \sum c(e_{ij})$ is an edge based cost function, i.e., the sum



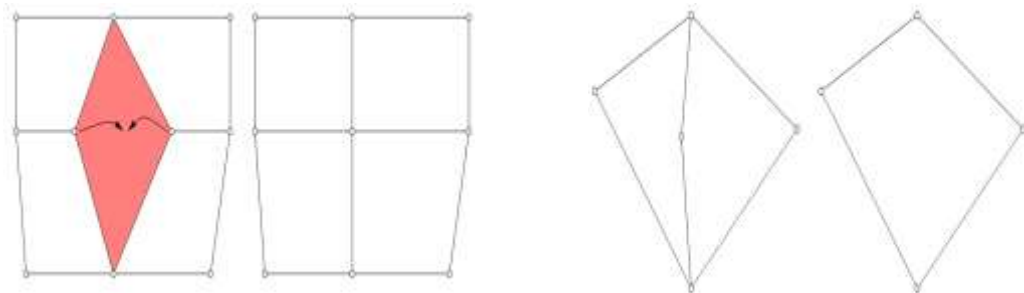
(A)

Edge swap algorithm for building an all-quad mesh when an extra edge such as e_{13} belongs to the matching

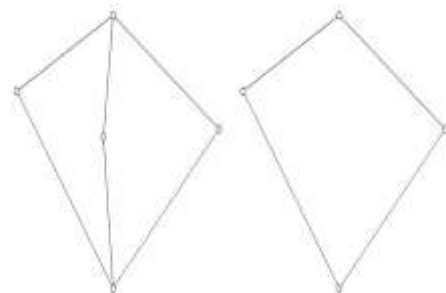


(B)

Vertex duplication algorithm for building an all-quad mesh when an extra-edge is in the matching



(C)



(D)

Illustration of (C) quad-vertex-merge and (D) doublet collapse optimization operation.

Fig 3.7: Mesh generation algorithm

of all weights associated to every edge $e_{ij} \in E$ of the graph. A cost function $c(e_{ij}) = 1 - \eta(q_{ij})$ is defined as the mesh quality of the quadrilateral q_{ij} .

4. The graph has been enriched with extra-edges if graph $G = (V, E)$ has no perfect matching. The added edges in the graph of the triangulation, maximizes the chance of existence of a perfect matching.
5. In a next step, the Blossom algorithm has been run to find the optimum perfect matching for the given graph. A matching is a subset $E' \subseteq E$ such that each node of V has at most one incident edge in E' . A matching is said to be perfect if each node of V has exactly one incident edge in E' . A matching is optimum if $c(E')$ is minimum among all possible perfect matching.
6. If the perfect matching contains no extra-edges, go to Step 7. If it contains some, apply the edge swap algorithm and the vertex duplication algorithm. The edge swap algorithm is essential when the extra edges connect two triangles t_1 and t_3 that surround one single triangle t_3 (Fig 3.7A). Edges that are colored in red in the graph belong to the perfect matching. If e_{13} belongs to the matching, then edge e_{24} belongs to the matching as well. It is therefore possible to swap the mesh edge that connects t_2 and t_4 and build an all-quad configuration. The vertex duplication algorithm (Fig 3.7B) is applied when the two triangles that are connected by the extra-edge are surrounded by more than one quad.
7. The resulting all-quad mesh has been optimized to enhance its quality. First, a standard vertex smoothing procedure is applied to the nodes of the mesh, taking into account the gradation of the size field. Next, two topological optimization operators were applied specially tailored for quadrilateral meshes. The topological optimization operators are local deletion operators: a quad-vertex-merge (Fig 3.7C) and the doublet collapse (Fig 3.7D) operation. Those operators allow to remove local mesh structures that have a bad topology. More precisely, the quad-vertex-merge operator replaces two mesh nodes that have 3 quadrilateral neighbors by one mesh node with 4 neighbors and the doublet collapse removes a vertex that has two neighbors.

8. Extrude the surface quad meshes and then recombine them to form hexahedral volume mesh.

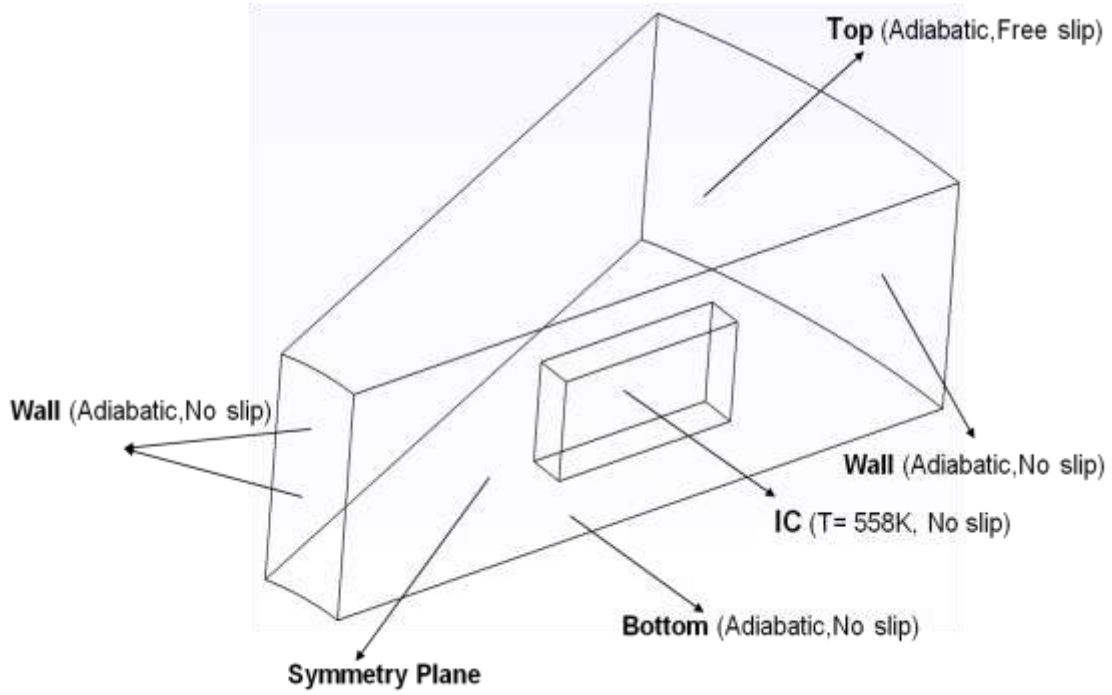


Fig 3.8: Schematic of Boundary conditions for ‘ICI’ design

3.4.5 Boundary condition

In the present work, due to the symmetry in tangential direction, a 22.5° wedge geometry of GDWP tank (Fig 3.8) has been considered for simulations. The sidewalls, the bottom of the tank, surfaces of the draft tube, were considered as adiabatic with no slip boundary condition. A constant temperature ($T_w = 558$ K) boundary condition was specified on the surfaces of all the heat sources. All the other boundary conditions are given in Table 3.5. Water in the open cylindrical tank can have motion in the radial as well as in tangential direction at the free water surface. However, water does not escape the surface. Therefore, the boundary conditions at the top liquid surface are as follow:

$$\frac{\partial u_r}{\partial z} = \frac{\partial u_\theta}{\partial z} = 0 \text{ and } u_z = 0 \quad (3.1)$$

At $\theta = 0^\circ$, symmetry Plane is considered having boundary conditions as follows:

$$\frac{\partial u_r}{\partial \theta} = \frac{\partial u_\theta}{\partial \theta} = \frac{\partial u_z}{\partial \theta} = 0 \quad (3.2)$$

Table 3.5: Details of the boundary conditions:

Zone	Boundary Conditions	
	Temperature	Velocity
Pipe	Constant Temp = 558K	No slip ($u_r = u_\theta = u_z = 0$)
Top	Adiabatic ($\partial T / \partial z = 0$)	Free slip ($\frac{\partial u_r}{\partial z} = \frac{\partial u_\theta}{\partial z} = 0, u_z = 0$)
Side walls	Adiabatic ($\partial T / \partial r = 0$)	No slip ($u_r = u_\theta = u_z = 0$)
Bottom wall	Adiabatic ($\partial T / \partial z = 0$)	
Symmetry	($\partial T / \partial \theta = 0$)	$\frac{\partial u_r}{\partial \theta} = \frac{\partial u_\theta}{\partial \theta} = \frac{\partial u_z}{\partial \theta} = 0$
Draft tubes	Adiabatic ($\frac{\partial T}{\partial r} = \frac{\partial T}{\partial \theta} = \frac{\partial T}{\partial z} = 0$)	No slip ($u_r = u_\theta = u_z = 0$)

All the three terms in Eq (3.2) represent symmetry and implemented in OpenFOAM 2.2 under the title of symmetry Plane boundary condition. Secondly, the condition of $u_z = 0$ at $z = 5\text{m}$ and at all r and θ permits the description of “no escape of water from the top surface”.

The additional boundary conditions are;

$$I_T = \text{turbulent intensity} = 5\%$$

$$k = \frac{3}{2} I_T^2 V_{avg}^2$$

V_{avg} is assumed to be 0.1m/sec.

$$k = \frac{3}{2} (0.05)^2 (0.1^2) = 3.75 \times 10^{-5} \text{ m}^2 \text{ s}^{-2}$$

$$\varepsilon = C_u^{3/4} \frac{k^{3/2}}{l}$$

Where $l = 10\%$ of characteristic length

$$\omega = \frac{\varepsilon}{k} = C_u^{3/4} \frac{k^{1/2}}{l} \quad \omega = \frac{(0.09)^{3/4} (3.75 \times 10^{-5})^{1/2}}{(0.1 \times 19)} = 5.29 \times 10^{-4} \text{ s}^{-1}$$

3.4.5.1 Method of solution

The effect of symmetry boundary condition has been studied for $ICI = 54.6\text{m}^2$ (5.381m x 2m x 2.2m) design having a single box type heat source placed at the centre of the enclosure at $\theta = 0^\circ$ and having clearance (c) of 0.1m from the bottom of the tank. Two geometries are considered (1) $1/16^{\text{th}}$ sector of GDWP tank having dimensions ($R_o = 25\text{m}$, $R_i = 6\text{m}$, $H_T = 5\text{m}$, $\theta_T = 0^\circ$ to 22.5°) with symmetry boundary condition (2) $1/8^{\text{th}}$ sector of GDWP tank having dimensions ($R_o = 25\text{m}$, $R_i = 6\text{m}$, $H_T = 5\text{m}$, $\theta_T = -22.5^\circ$ to 22.5°). Fig 3.9 and 3.10 shows the effect of symmetry boundary condition on the top ($z = 2.31\text{ m}$) of IC. The symmetry boundary condition results in 2% over prediction of velocity (Fig 3.9A) and temperature (Fig 3.9B) near the IC tube ($0.35 < r/L < 0.65$). Away from the IC tube, no difference in temperature has been observed. Hence, the symmetry boundary condition can be used for further studies.

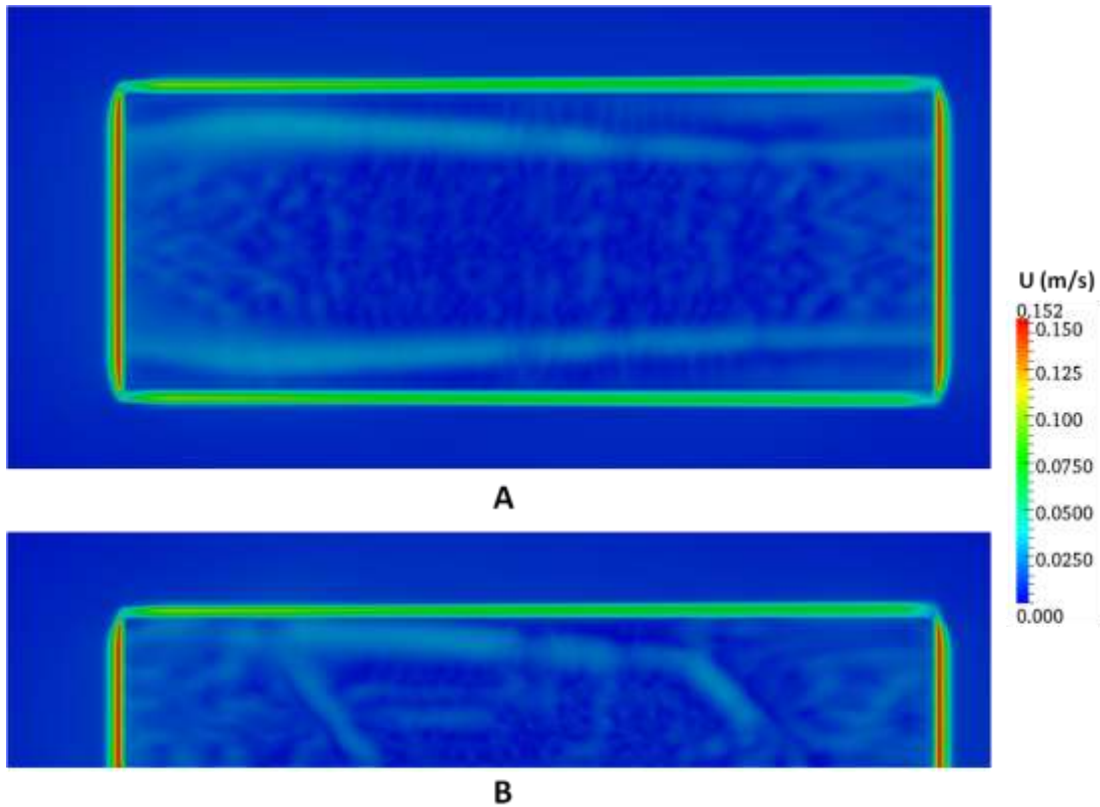


Fig 3.9: Effect of symmetry boundary condition on flow distribution at $t = 100\text{s}$ at IC top $z = 2.31\text{ m}$ (A) $1/16^{\text{th}}$ sector of GDWP with symmetry boundary condition (B) $1/8^{\text{th}}$ sector of GDWP

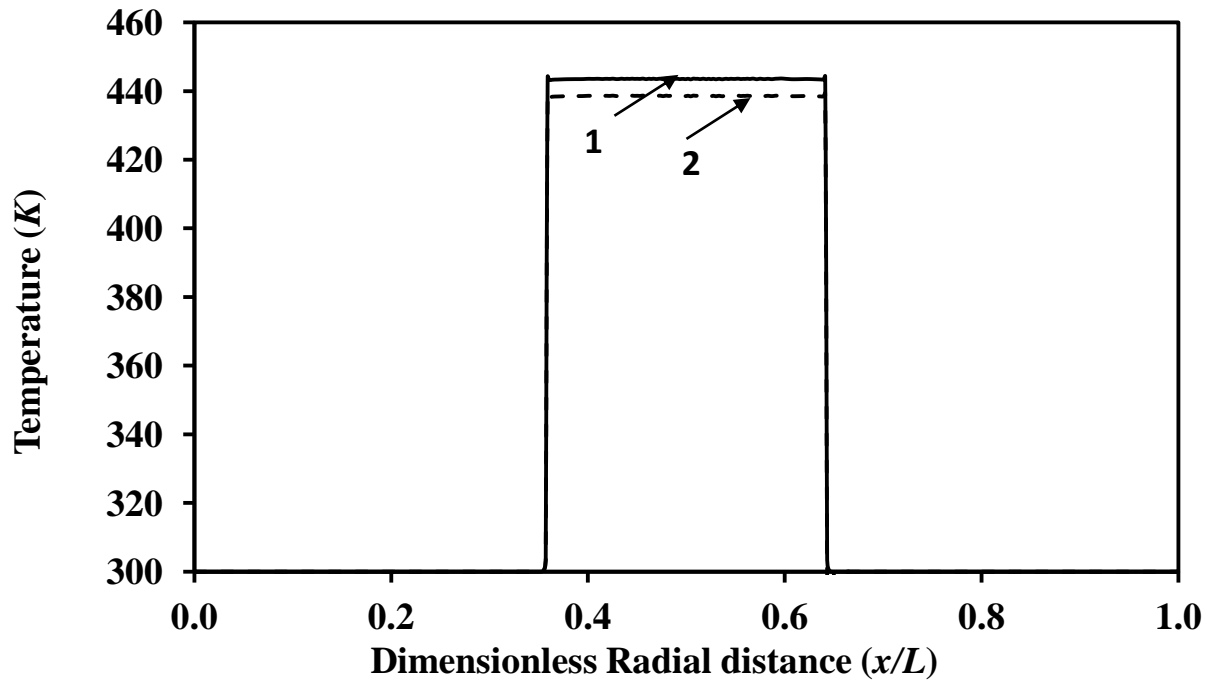
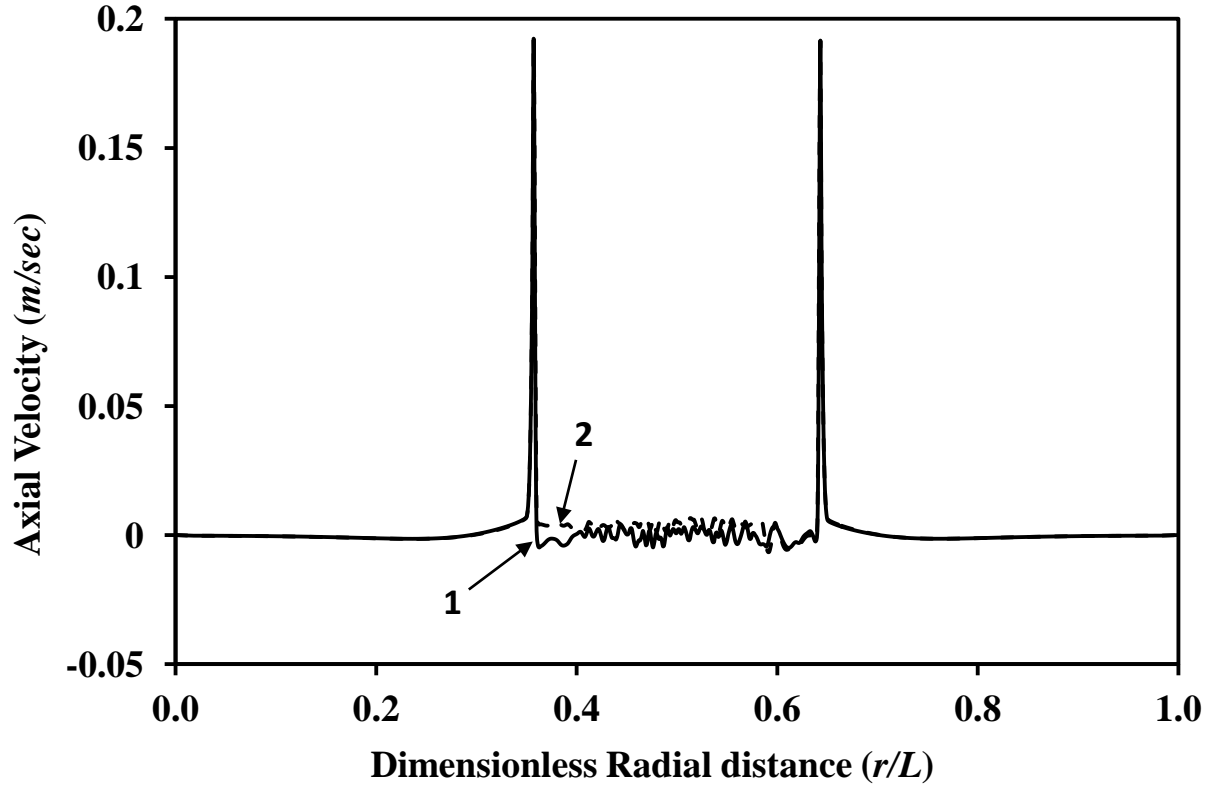


Fig 3.10: Effect of symmetry boundary condition on radial (r) distribution of axial velocity at $t=100s$ at $z = 2.31$ m (1) 1/16th sector of GDWP with symmetry boundary condition (2) 1/8th sector of GDWP

3.4.6 Method of solution

In the present work, simulations have been performed under unsteady conditions. All the computational work has been carried out using the CFD software OpenFOAM-2.2. The first order implicit scheme was used for the time discretization of all unsteady terms ($\partial T/\partial t, \partial u_i/\partial t, \partial k/\partial t, \partial v_i/\partial t, \partial \omega/\partial t$, where $i = r, \theta, z$) and the scheme is described as follows:

Consider an ODE given by

$$du/dt = R(u) \quad (3.3)$$

where u is a time (t) dependent variable like T, u_i, k, ω, v_i . The RHS of the (3.3) is a function of the solution u . If we know the solution at time level t and would like to get the solution at time level $(t+1)$, then we could have

$$du/dt = R(u^t) \quad (3.4)$$

or

$$du/dt = R(u^{t+1}) \quad (3.5)$$

There are two ways to do time discretization of the LHS (3.4) explicit procedure in which Euler backward differencing in time is used to solve (3.1) which give

$$\frac{(u^{t+1} - u^t)}{\Delta t} = R(u^t) \quad (3.6)$$

(b) on the other hand, for the same Euler discretisation if (3.5) had been employed then we would have

$$u^{t+1} - \Delta t \times R(u^{t+1}) = u^t \quad (3.7)$$

Note that u^{t+1} will be obtained after solving (3.7), and hence even when the functional relation for R is known the LHS remains unknown. It follows that an iterative procedure would become necessary for solving u^{t+1} . This is referred to as implicit procedure. Compared to explicit scheme, more computational effort would be required here, since an iterative solution is necessary. Explicit schemes are only conditionally stable because of the limitation on the maximum time step size which

can be used to solve unsteady problems. Though much easier to solve, the time step could be quite small, which means the code has to run for long before the converged solution is achieved. On the other hand, implicit schemes are unconditionally stable and therefore the time steps that can be taken are quite larger and this accelerates the convergence. Thus for convergence acceleration, implicit solvers play an important role. QUICK spatial discretization scheme was used for modeling the convective terms and central differencing scheme for diffusive terms. All the discretized equations were solved in a segregated manner with the PISO (Pressure Implicit with Splitting of Operators) algorithm. Further, the solutions were considered to be fully converged when the sum of scaled residuals was below 10^{-5} .

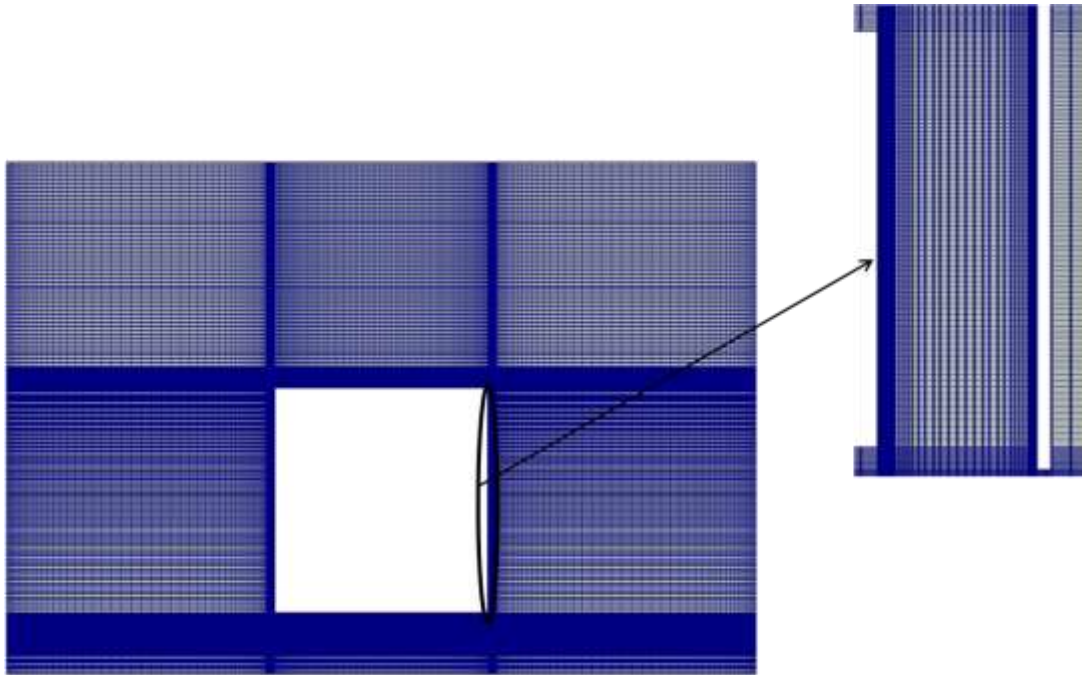


Fig 3.11: Schematic of Grid size for '*DF1*' design

3.4.7 Grid independence

In the present work, due to the symmetry in tangential direction, a 22.5° wedge geometry of GDWP tank (Fig 3.7) has been considered for simulations. The grid independence was investigated for few designs ('*DF0*', '*DF1*'). For instance, four different grids were selected: (1) 2M (2) 4M (3) 5M and (4) 6M for the case of single draft tube design ('*DF1*'). In natural convection systems, higher gradient of velocity as well as temperature are present near the heat source region. Therefore, it is

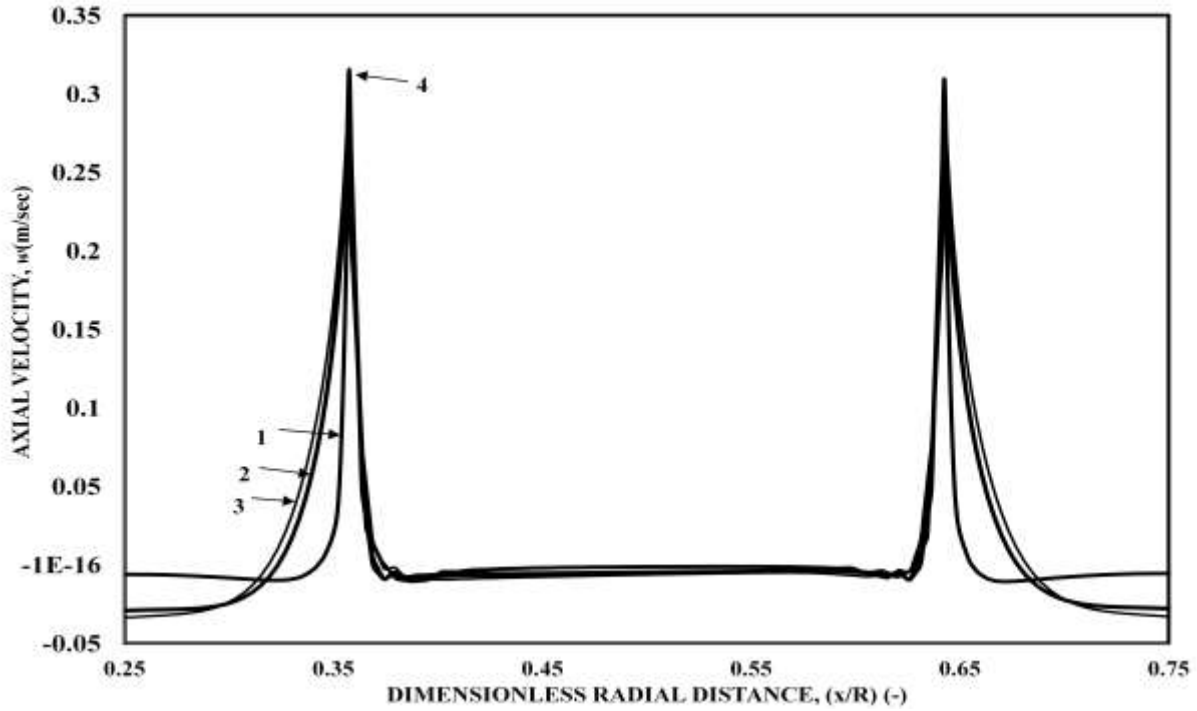


Fig 3.12: Effect of grid size for '*DFI*' design: Variation in axial velocity at $t=40s$ for symmetry plane ($\theta = 0^\circ$) with dimensionless radial distance $z/H=0.6$; at different grid sizes (1) 2M; (2) 4M; (3) 5M; (4) 6M.

important to provide dense meshing near the heat source region and gradually increase the mesh size as we move towards the tank wall. Accordingly, in the present work, a non-uniform hexahedral grid was employed which was finer near the tube wall region (Fig 3.11). Further, while generating grids for the different designs of draft tubes, care has been taken to generate dense meshing wherever sharp velocity gradients are expected. For instance, in the case of '*DFI*' design, dense meshing was provided near the heat source, draft tube and the region between heat source and draft tube because of large circulations expected due to chimney effect of draft tube. Therefore, approximately 70% of the nodes were located in the region between draft tube and heat source, and 30% were located in the region between draft tube and tank wall. Further, care was taken by providing five nodes in the viscous sublayer ($y^+ < 5$) and several nodes in the buffer and turbulent zones. Grid independence study has been executed by comparing the mean axial velocity at several positions for each of the four grid densities. Fig 3.12 shows the radial profiles of the axial velocity in the region between draft

tube and heat source ($z/H=0.6$, $0.25 \leq x/R \leq 0.75$). Two peaks in the axial velocity can be seen (at $x/R = 0.36, 0.64$) (Fig 3.12) near the heated tube wall due to development of natural convective flow, and negative velocity in the region ($0.25 \leq x/R \leq 0.32$, $0.68 \leq x/R \leq 0.75$). The lighter hot fluid rises inside the draft tube and descends in the annular region between the tank wall and the draft tube. All the chosen grids predict mean flow patterns effectively. Minor differences have been observed between 5M and 6M cells as shown in Fig 3.12 (lines 3 and 4). However, the velocities were found to be within 0.1% average error although the grid size difference was 20%. Therefore, for all the simulations in the present work 5M cells have been used.

3.4.8 Time independence

The time step independence study for 'DFI' case was done at four different time steps $1 \times 10^{-4} s, 1 \times 10^{-5} s, 5 \times 10^{-5} s, 1 \times 10^{-6} s$. The temperature profiles in the region between the draft tube and IC shown in Fig 3.13A clearly indicates that there was nominal variation (less than 1%) in the temperature for case $1 \times 10^{-6} s$ and $1 \times 10^{-5} s$. Hence, time step in between these two $5 \times 10^{-6} s$ was selected. It was observed that the values of residuals (R) for all unsteady terms at each time step, and if the residuals were found to be less than the convergence criteria ($R \leq 10^{-5}$), a very small increment in time step was introduced. In natural convection system, the flow initiates from rest ($u = 0$) at $t = 0s$. As time proceeds, the heat is transferred from IC to the water pool and hence the flow generates due to buoyancy. The velocity and temperature gradients are very high at the beginning ($t < 10s$) (Fig 3.13B). In order to capture these sharp gradients, very small time step ($dt = 5 \times 10^{-6} s$) was required. The convergence of implicit scheme is based on large number of iterations. Consider a linear set of equation e.g $Ax = b$. where A is the term of the order of $1/dt$ and appears in the diagonal of A . The convergence depends on the asymptotic condition number (i.e. the spectrum) of A . If dt is small, this term will be large and hence there is diagonal dominance. As dt increases, the matrix becomes less and less diagonally dominant and usually convergence slows down and eventually solution may

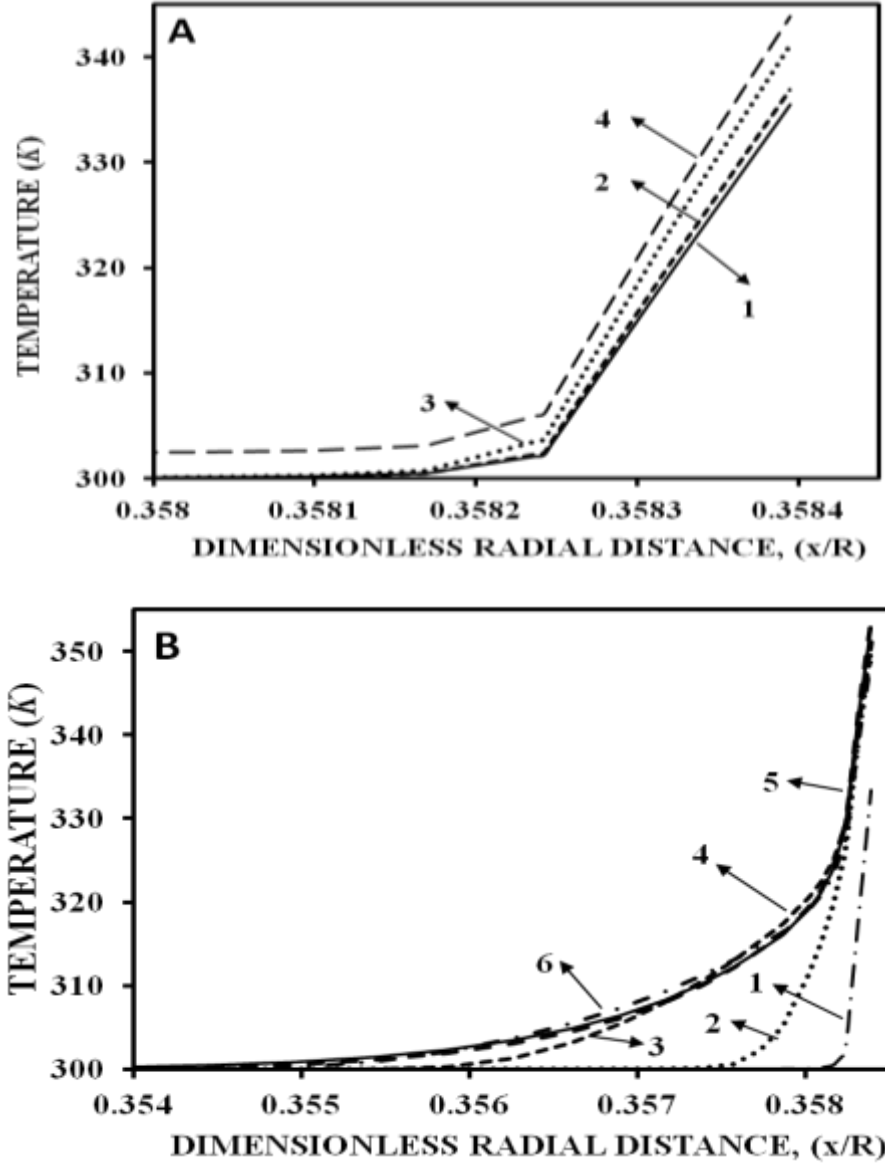


Fig 3.13: (A) Time step independent studies at four different time steps for ‘*DFI*’ design (1) 10^{-6} s (2) 10^{-5} s (3) 5×10^{-5} s (4) 10^{-4} s; (B) Time varying temperature profiles for symmetry plane ($\theta = 0^\circ$) with dimensionless radial distance at $z/H=0.5$; (1) 1s (2) 4s (3) 8s (4) 10s (3) 30s (4) 50s (5) 70s (6) 100s.

diverge. This is why implicit schemes cannot handle large time steps even though it is unconditionally stable. The small time step ($dt \leq 10^{-5}$ s) was required only at the beginning ($t < 10$ s). After ($t > 10$ s), the velocity and temperature gradients gradually reduce. Hence, the time step can also be incremented. However, the time step was kept ($dt \leq 10^{-4}$) even above 10s and upto 100s. As

mentioned above, time step was kept of $5 \times 10^{-6} s$, even though larger time step was permissible after the real time of 10s.

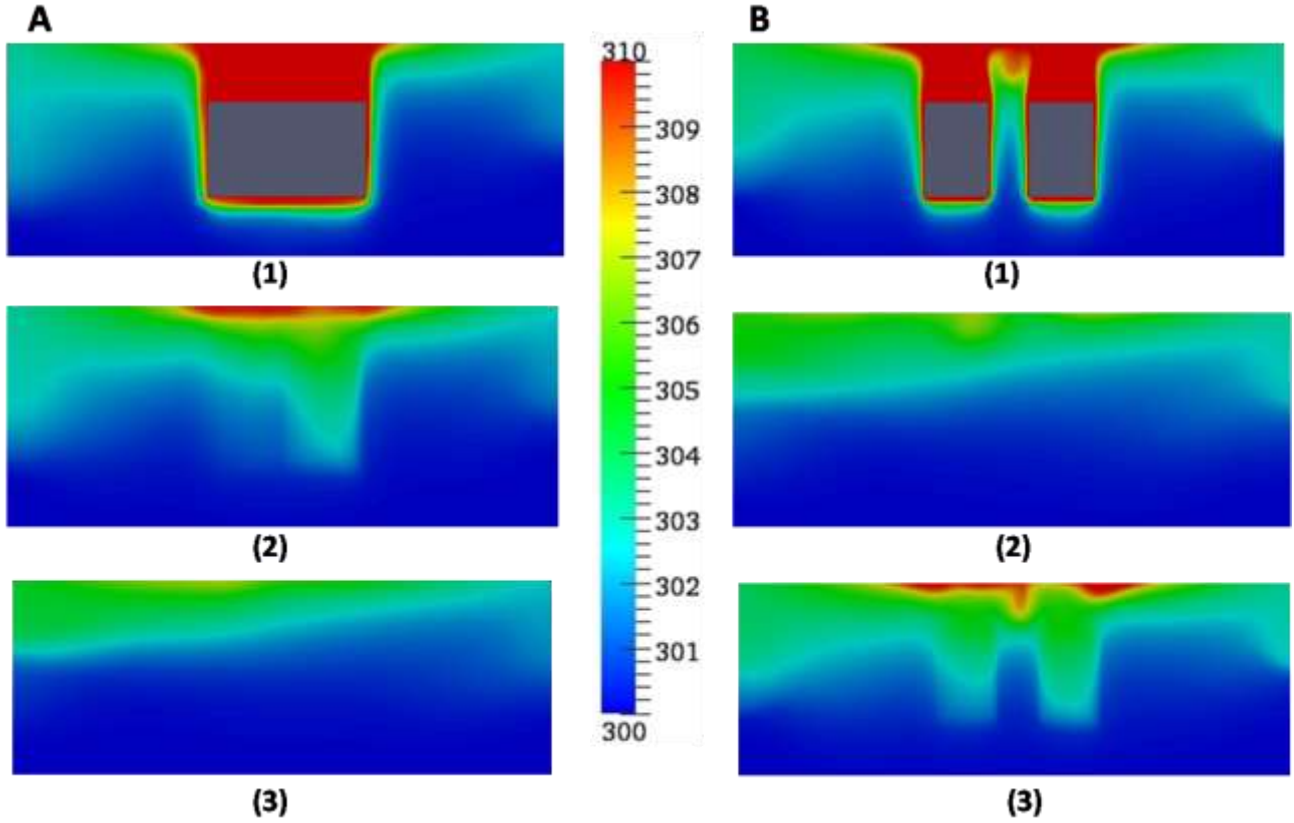


Fig 3.14. Temperature Contours at three different tangential directions at t=100s

(A) 'IC1 c1.4, (B) 'IC2 c1.4; (1) $\theta = 0^\circ$; (2) $\theta = 11.25^\circ$; (3) $\theta = 21.5^\circ$

3.5 Results and discussions

The overall objective of the present work is to investigate the mixing and stratification phenomena in single phase natural convection in the GDWP. Initially, 3D natural convection in the $1/8^{\text{th}}$ sector of GDWP pool (1155 m^3) has been examined in the presence of single heat source (HT area = 54.6 m^2). Thermal stratification phenomenon has been observed due to concentrated heat source (IC) at one location. In order to reduce the thermal stratification, parametric sensitivity has been investigated which includes (1) size and distribution of heat sources (2) submergence of heat source (3) provision of draft tubes, which can act as a chimney and possibly enhance the convection currents.

3.5.1 Single Heat Source (IC1)

3.5.1.1 Velocity and Temperature profiles

The temperature contours obtained from the CFD simulations at three different planes at $t = 100\text{s}$ for 'IC1c1.4' design are shown in Fig 3.14A. In natural convection system, maximum temperature gradient prevails in the vicinity of heat source and it becomes weak with an increase in the distance from the heat source. This can also be seen from radial temperature profiles plotted at z/H_T of 0.04, 0.26, 0.5, 0.74 and 0.96 (Fig 3.17A). As a result, the fluid adjacent to the heat source gets heated, becomes light and rises [case (1) Fig 3.16B]. Consequently, the heavier fluid (cold water) from the neighboring areas rushes to take the place of the rising fluid. This can also be seen from the axial velocity profiles plotted at z/H_T of 0.04, 0.26, 0.5, 0.74, 0.96 (Fig 3.18A), where a velocity peak is present near the heated surface and then the velocity decreases as we move away from the heat source in transverse directions. In fact, in the bulk of water pool, the liquid velocities are feeble of the order of mm/s. As the rising fluid reaches the free water surface at the top, it flows in radially outward direction. When the fluid reaches the tank wall, it again gets diverted in the downward direction. As a result, circulation patterns [case (1) in Fig 3.16B] get established in the water pool. It can be seen that the axial velocity (Fig 3.18A) increases with an increase in distance in the axial direction ($0 \leq z/H_T \leq 1$). This is due to the continuous addition of enthalpy. Further, it can be seen that the temperature distribution is not symmetric (in radial and axial directions) around the heat source. Temperature (Fig 3.17A) is high on the left side (r/R of 0 to 0.358) of heat source as compared to the right side (r/R_o of 0.642 to 1.0) which is due to the presence of lesser fluid volume on the left side of heat source as compared to the right side. As the time progresses, the accumulated hot water layer near free surface region gets extended downwards. However, the temperature near the tank wall is always low (Fig 3.17A). This is mainly due to feeble liquid velocity in the enclosure. The overall result is that the total energy supplied to the system gets accumulated near the wall of heat source and near the free surface region.

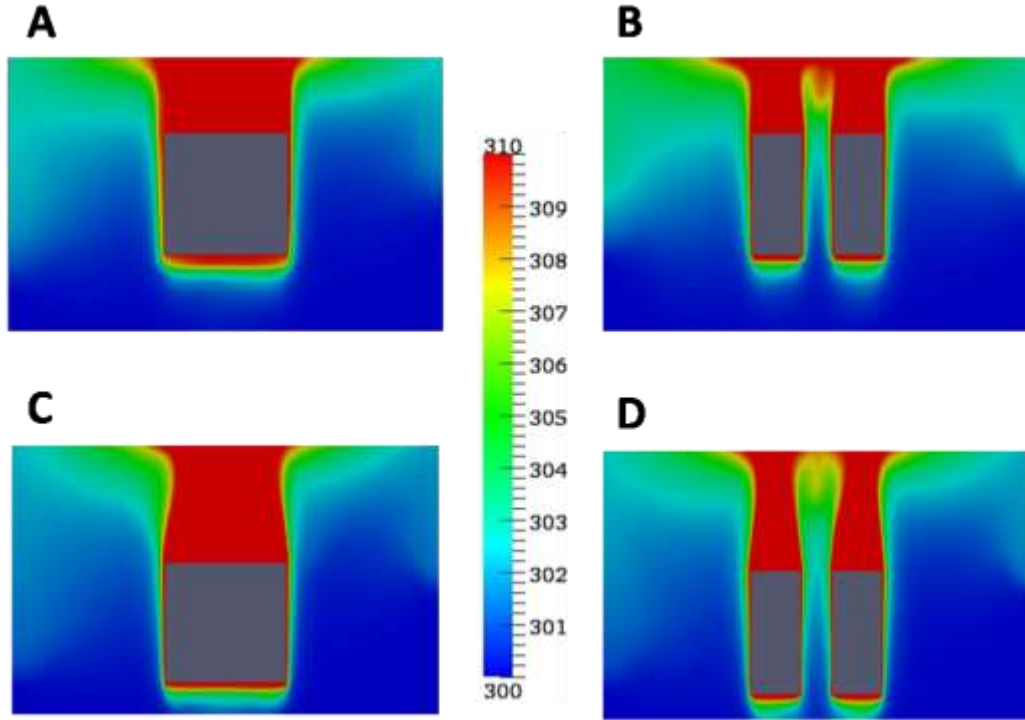


Fig 3.15. Temperature Contours at $t=100s$ at symmetry plane and $\theta = 0^\circ$. (A) 'IC1c1.4', (B) 'IC2c1.4', (C) 'IC1c0.6', (D) 'IC2c0.6',

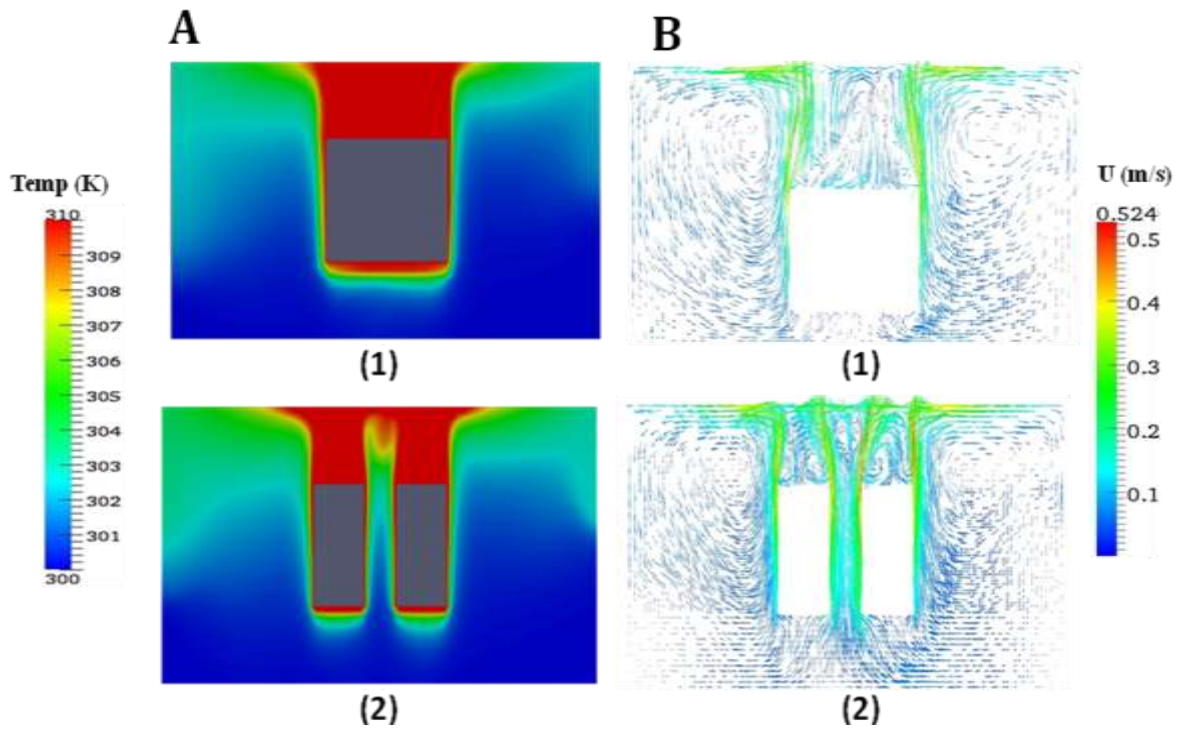
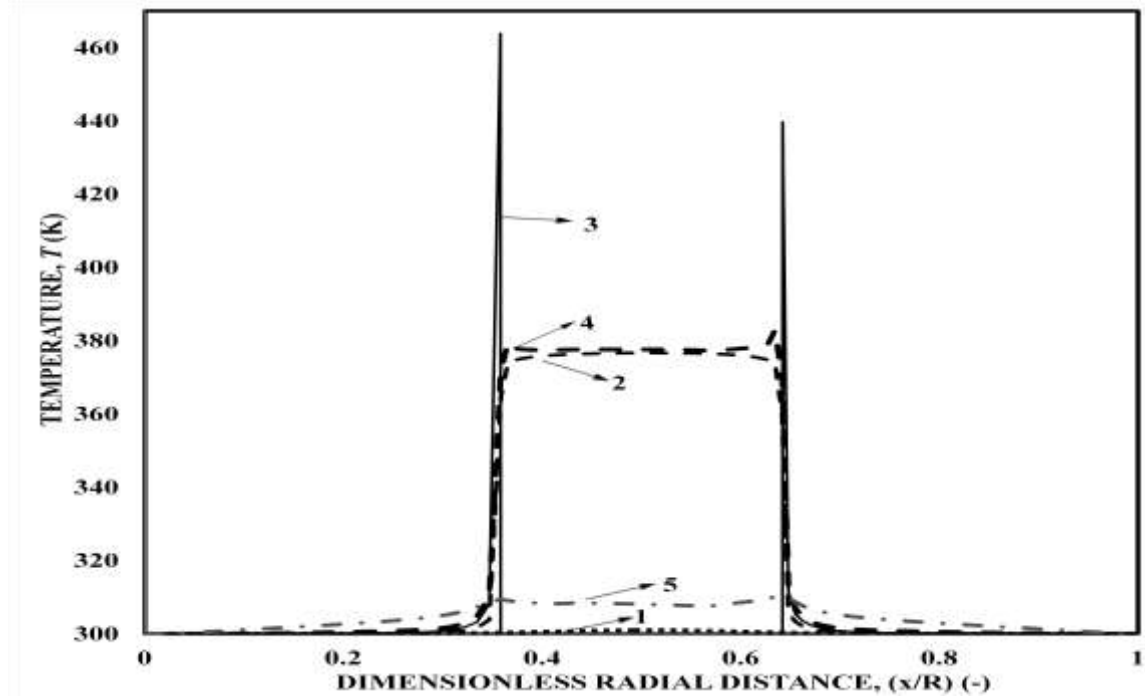
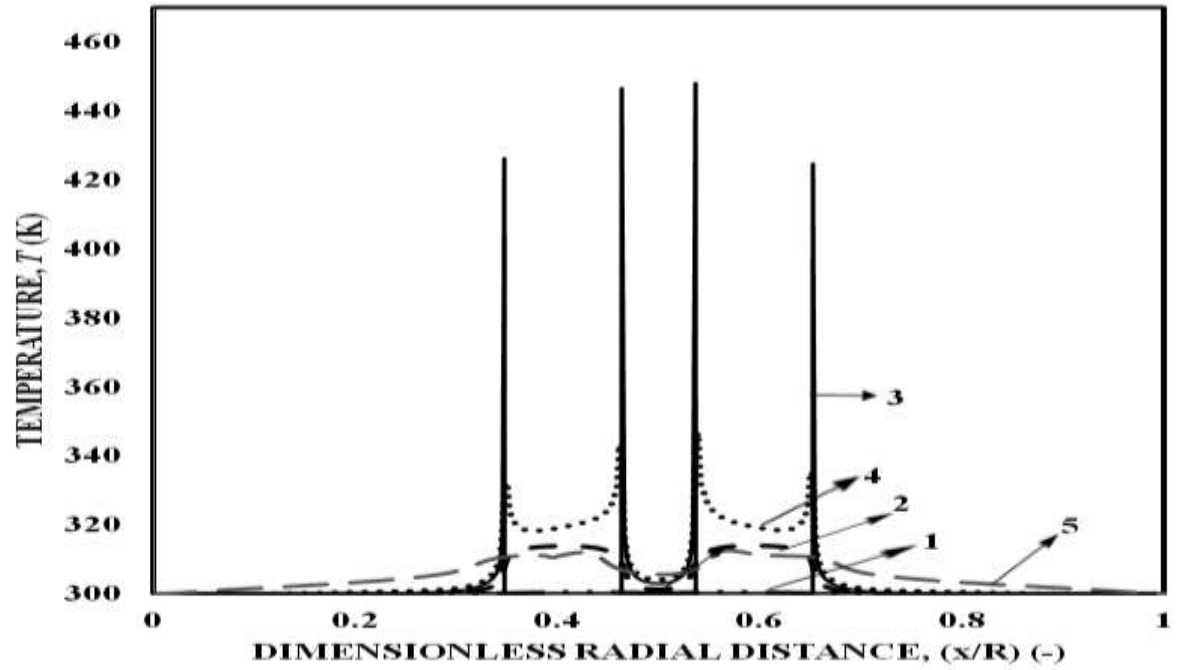


Fig 3.16: (A) Temperature Contours and (B) Flow distribution at symmetry plane ($\theta = 0^\circ$) at $t=100s$ (1) 'IC1c1.4', (2) 'IC2c1.4'.



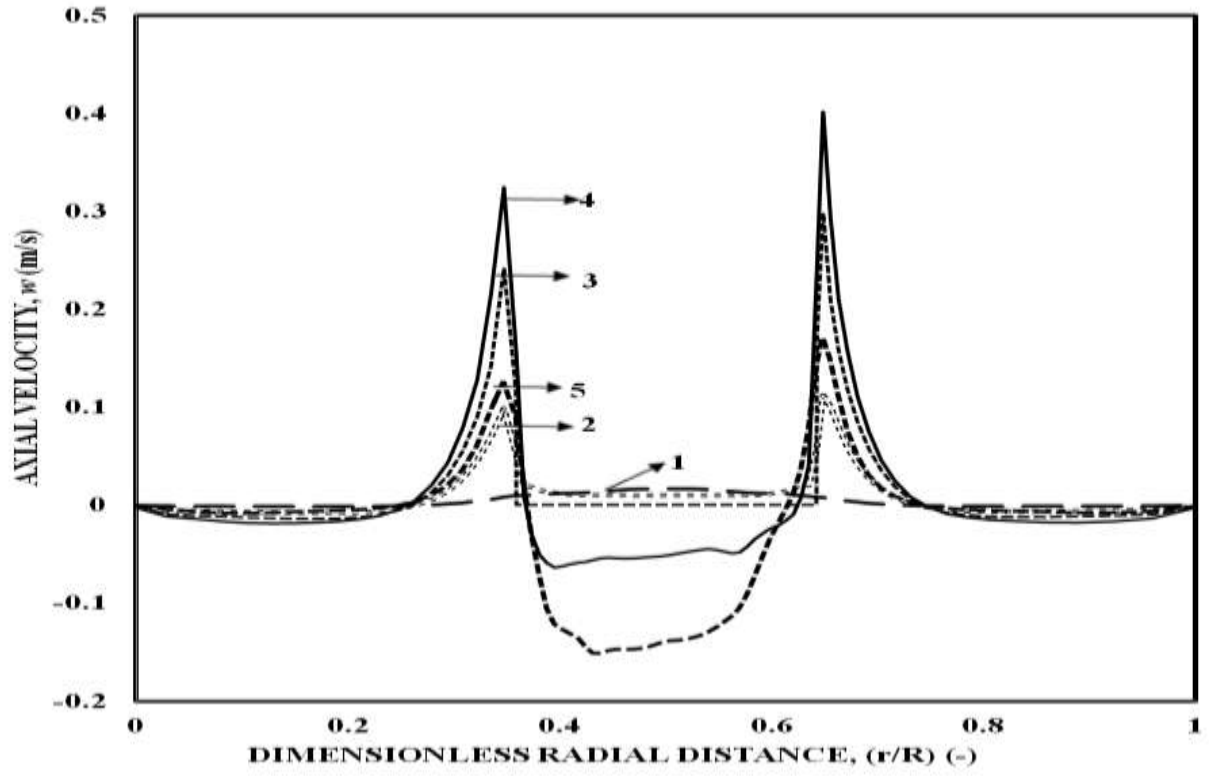
(A)



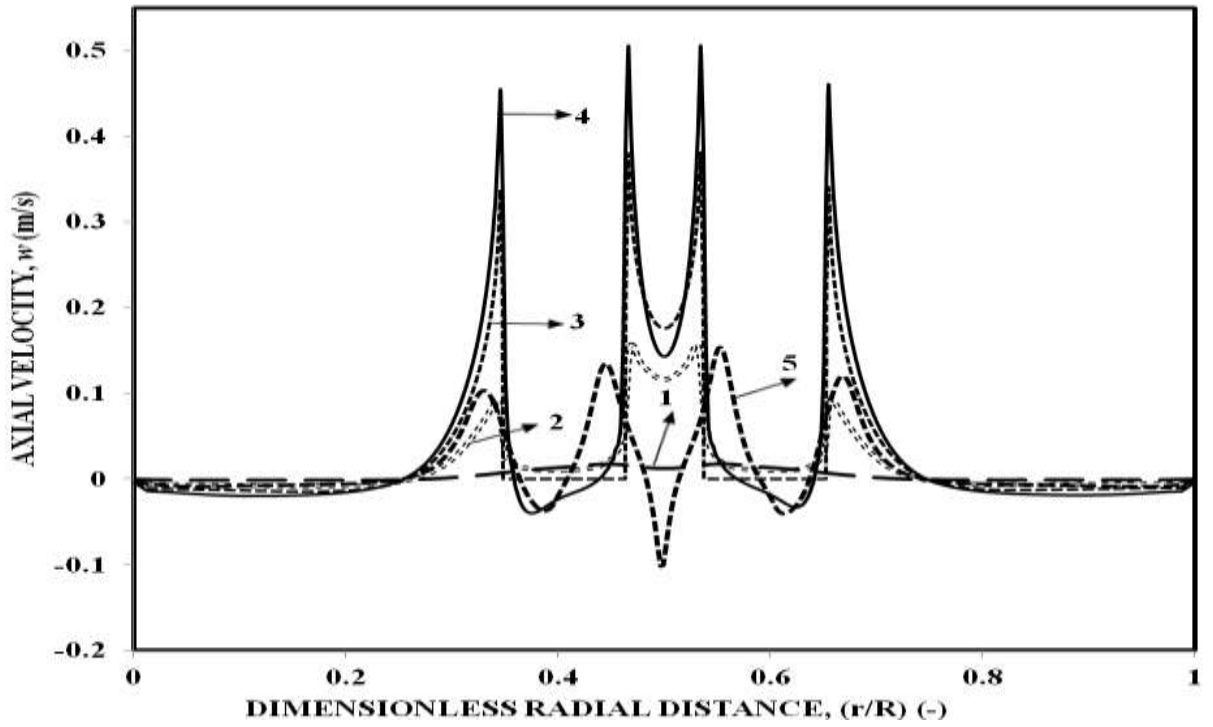
(B)

Fig 3.17: Variation in temperature with dimensionless radial distance at $t=100s$ for symmetry plane ($\theta = 0^\circ$) (A) 'IC1c1.4', (B) 'IC2c1.4'.

(1) $z/H = 0.04$; (2) $z/H = 0.26$; (3) $z/H = 0.5$; (4) $z/H = 0.74$; (5) $z/H = 0.92$;



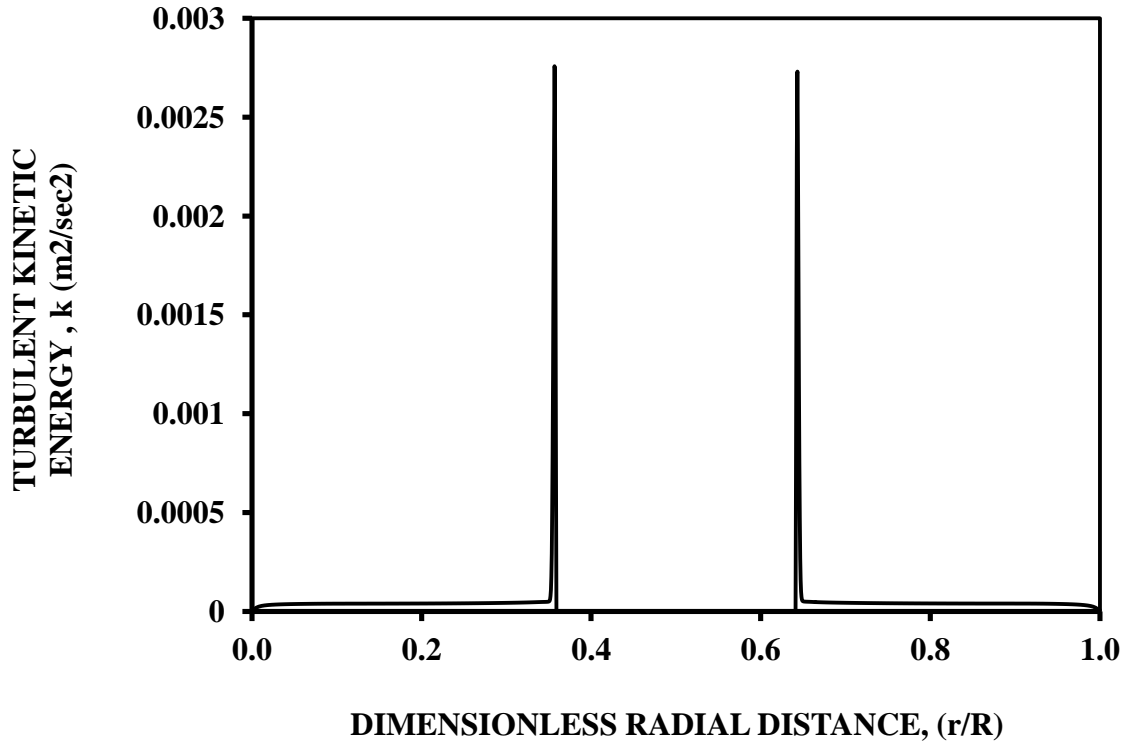
(A)



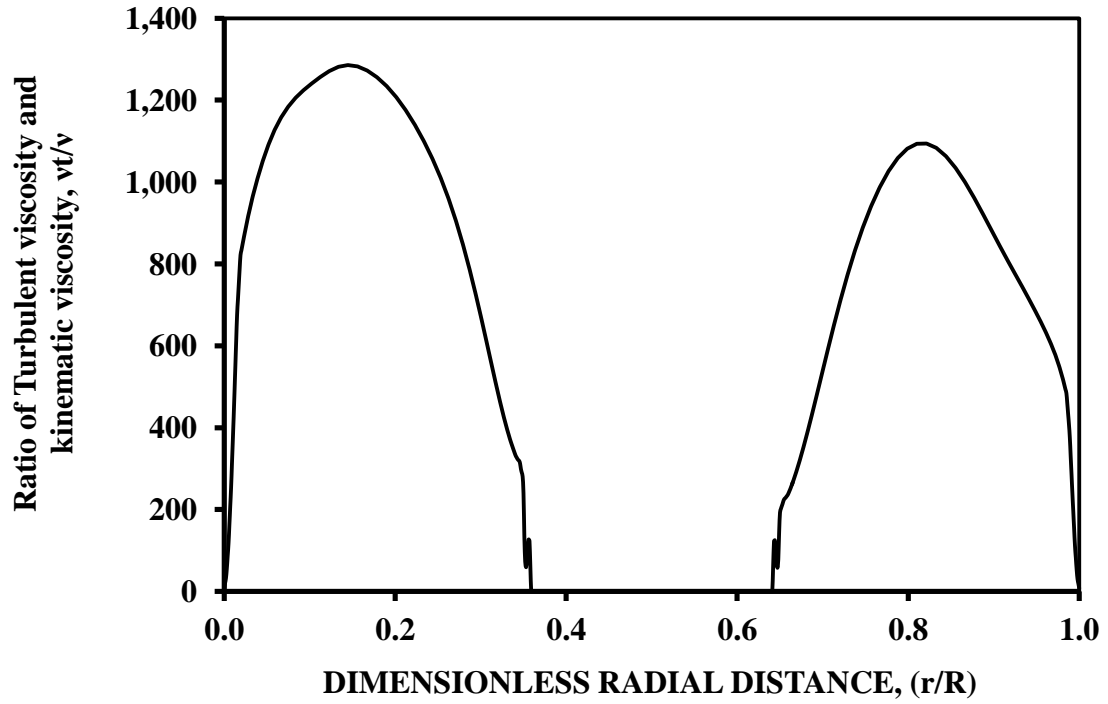
(B)

Fig 3.18: Variation in axial velocity with dimensionless radial distance at $t=100s$ for symmetry plane ($\theta = 0^\circ$) (A) 'IC1cl.4', (B) 'IC2cl.4'.

(1) $z/H = 0.04$; (2) $z/H = 0.26$; (3) $z/H = 0.5$; (4) $z/H = 0.74$; (5) $z/H = 0.92$;



(A)



(B)

Fig 3.19: Variation in (A) Turbulent kinetic energy (k) (B) Ratio of turbulent and kinematic viscosity (ν_t/ν) with dimensionless radial distance for 'IC1c1.4' at $z/H = 0.5$ and $\theta = 0^\circ$ at $t = 100\text{s}$,

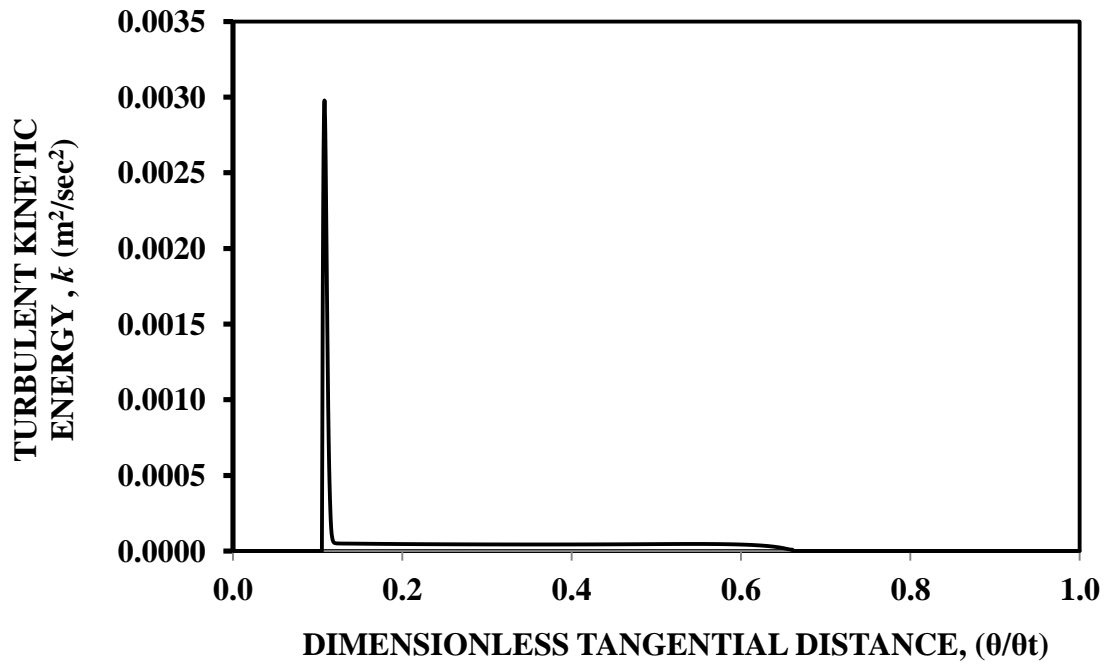
3.5.1.2 Turbulent kinetic energy (k) and turbulent viscosity (ν_t) profiles

The considered pool (GDWP) is very large (9247m^3), huge variations of flow like laminar to turbulent and vice versa occurs inside the pool. The detailed investigation of turbulent flow parameters have been undertaken to check the need of turbulence model. The turbulent kinetic energy (k) and viscosity ratio (ν_t/ν) was investigated at all the locations in the GDWP. For instance, Fig 3.19 and Fig 3.20 shows k and ν_t profiles along the lines P_1 and P_2 in Fig 3.4A. Radially, we observe that the value of turbulent kinetic energy (k) was very high near the IC and approaches to zero away from the IC (Fig 3.19). The value of (ν_t/ν) also shows a huge variation. The value of (ν_t/ν) was 1200 near the IC and approaches to zero away from the IC. Therefore, the turbulence model opted was the one which can also handle the cases of (ν_t/ν) close to zero.

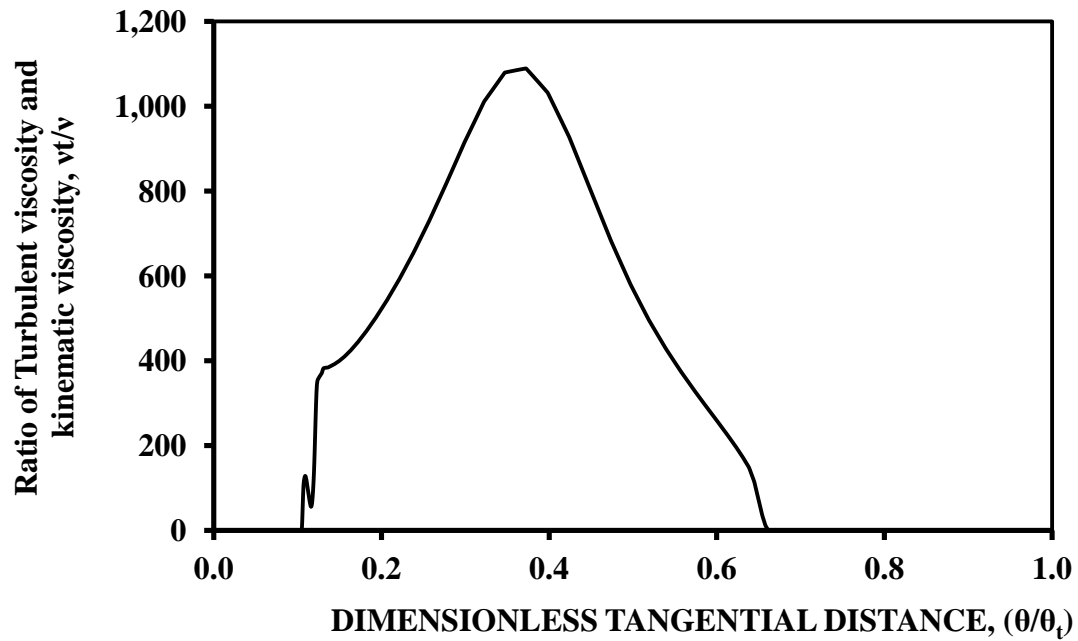
3.5.1.3 Quantification of Stratification and Extent of mixing

At this stage, it is important to appreciate the role of liquid circulation velocity on the extent of mixing. From Table 3.6 it can be seen that, for 'IC1c1.4' at Ra of 7×10^{13} ($\Delta T = 258^\circ\text{C}$), the average circulation velocity at $t=100\text{s}$ works out to be 0.15 mm/s . Further, the maximum circulation loop length is $(9.8+9.8+5+5) 29.6\text{m}$. Therefore, the circulation time ($29.6 / 0.00015$) is 198626 s . The mixing time (θ_{mix}) is considered to be five times the circulation time (Vusse, 1962; Kumaresan and Joshi, 2006) which works out to be 993131 s . Such a high value of mixing time indeed means poor mixing and hence stratification. The thermal stratification means the existence of an axial temperature gradient in the tank. Han et al. (2009) have quantified the extent of stratification in the form of stratification number, S . It is defined as the mean temperature gradient at any time to the maximum mean temperature gradient achieved at the end of the run. The values of S varies from zero to one with zero representing no stratification (complete mixing) and one representing complete

stratification. Mathematically stratification number (S) at any time can be expressed by the following equation (Han et al., 2009).



(A)



(B)

Fig 3.20: Variation in (A) Turbulent kinetic energy (k) (B) Ratio of turbulent and kinematic viscosity (ν_t / ν) with dimensionless tangential distance (θ / θ_t) for 'IC1c1.4' at $z/H=0.5$ and $r/R=0.5$

at $t = 100s$

Table 3.6: Circulation flow rate and mixing time

System	Time (sec)	Average liquid circulation $V_c \times 10^3$ (m/s)	Circulation time (s)	Mixing time θ_{mix} (s)	Mixing number M $M = \frac{(g\beta\Delta T l^3)}{(V_c l)^2}$ (-)	Stratification number (-)
IC1S0.5	50	0.11	280543	1402713	4.0×10^8	0.88
	100	0.15	198626	993131	2.0×10^8	0.87
	200	0.14	219216	1096082	2.4×10^7	0.86
IC1S0.3	50	0.11	265501	1327506	3.6×10^8	0.82
	100	0.16	184366	921829	1.7×10^8	0.83
	200	0.15	195173	975867	1.9×10^8	0.82
IC2S0.5	50	0.16	183944	919721	1.7×10^8	0.77
	100	0.23	127169	635845	0.8×10^8	0.76
	200	0.22	136272	681359	0.9×10^8	0.76
IC2S0.3	50	0.19	159584	797918	1.3×10^8	0.71
	100	0.33	90207	451036	0.4×10^8	0.72
	200	0.31	96422	482112	0.5×10^8	0.71
IC2S0.2	50	0.18	163520	817599	1.4×10^8	0.876
	100	0.12	150768	753839	1.2×10^8	0.877
	200	0.15	192966	964832	1.9×10^8	0.879
ICMS0.2	100	0.20	148525	742626	1.1×10^8	0.59
	200	0.36	81860	409298	0.4×10^8	0.58
	200	0.40	73555	367774	0.3×10^8	0.58
DF0	50	0.33	89697	448485	0.4×10^8	0.86
DF1	50	0.48	61411	307054	0.19×10^8	0.46
DF3	50	0.44	67580	337900	0.23×10^8	0.50

$$S = \frac{\langle (\partial T / \partial z) \rangle}{(\partial T / \partial z)_{\max}} \quad (3.8)$$

$$\left\langle \left(\frac{\Delta T}{\Delta z} \right) \right\rangle = \frac{1}{J-1} \left[\sum_{j=1}^{J-1} \left(\frac{T_{j+1} - T_j}{\Delta z} \right) \right] \quad (3.9)$$

$$\left\langle \frac{\Delta T}{\Delta z} \right\rangle_{\max} = \frac{T_{\max} - T_{\min}}{(J-1) \Delta z} \quad (3.10)$$

The calculation procedure for Eq. (3.8) was as follows: consider the temperature pattern for $Ra = 7 \times 10^{13}$ at $t = 100$ s. Fig 3.21 shows the locations (shown by white spot) of temperature which were used for the estimation of 'S' using Eqs. (3.8) to (3.10). In Fig 3.21, the numbers 1, 2, 3 denote the radial locations (total 10 locations with Δx of 0.0025 m) and the uniformly placed white spots denote the axial locations (total 2000 locations with Δz of 0.0025 m, indicated by the index j). The total number of nodes per radial location is J . The distance between each axial location is given by Δz and was equal to 0.0025m. For each adjacent pair of nodes (j and $j+1$) on a radial location, the quantity [

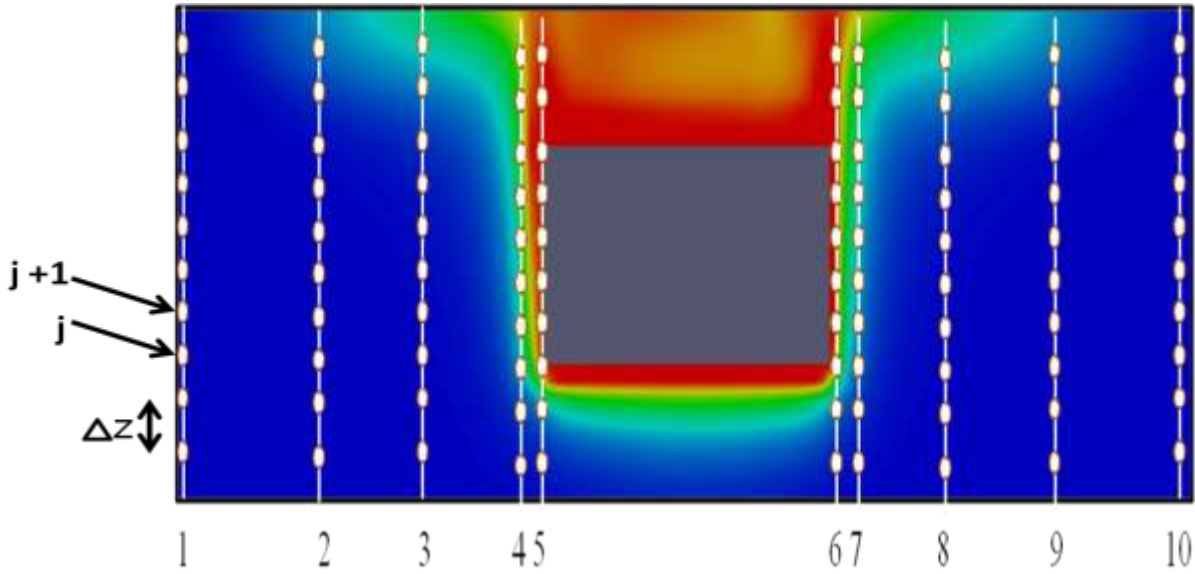


Fig 3.21: Temperature Contours for 'ICICI.4' at $t=100$ s for symmetry plane ($\theta = 0^0$). Calculation of stratification number (S).

$(T_{j+1} - T_j)/\Delta z$] was calculated. As per definition the average $(\Delta T/\Delta z)$ was calculated for all the radial locations (1 to 10). Thus

$$\langle (\Delta T/\Delta z) \rangle = \left[(\Delta T/\Delta z)_1 + (\Delta T/\Delta z)_2 + (\Delta T/\Delta z)_3 + (\Delta T/\Delta z)_4 + (\Delta T/\Delta z)_5 + (\Delta T/\Delta z)_6 + (\Delta T/\Delta z)_7 + (\Delta T/\Delta z)_8 + (\Delta T/\Delta z)_9 + (\Delta T/\Delta z)_{10} \right]$$

Similarly, the present run was carried upto 100 s then according to Eq. (3.10) $\langle \Delta T/\Delta z \rangle_{\max}$ would be calculated using T_{\max} and T_{\min} at all the points at $t = 100$ s. The stratification number was calculated for each radial position according to Eq. (3.8) and the mean of this number for all the radial positions was reported as the average stratification number. The stratification was calculated at $t = 100$ s according to Eqs. 3.8 to 3.10 and was found to have a value of 0.87 for the first case (Table 3.6).

3.5.2 Effect of distribution of heat sources inside GDWP

In the above section, the natural convection phenomenon was discussed for a single heat source (IC) placed at a fixed radial location. It has been observed that, due to concentrated heat source, heat transfer is also concentrated in a very small volume, which results into poor mixing and hence stratification. In order to reduce the extent of thermal stratification, it was thought desirable to have a distribution of heat sources inside a large water pool such as (GDWP). In this section, we will discuss the effect of distribution of heat sources at different locations inside GDWP ('IC2c1.4' design, Fig 3.4B) on the natural convection. The total HT area has been kept constant for both the cases ('IC1c1.4' and 'IC2c1.4'). Similar to the single heat source case 'IC1c1.4' for 'IC2c1.4' also we can see [Fig 3.14B] that the total energy supplied to the system gets accumulated in a small region near the heat source. As a consequence, higher temperature gradient regions or dead zones can be seen near the heat source [Fig 3.14B]. Further, the temperatures in the bulk region and at the bottom region are much less as compared to that at the top of the surface, particularly in the vicinity of heat source (Fig 3.14B). The distance between the two heat sources was selected in such a way that the convective flow [case (2) Fig 3.16B] become more intense in this region which resulted into enhanced mixing and hence reduction in stratification. In the region $(0.45 \leq x/R_o \leq 0.55)$ between the

two heat sources, the fluid very close to the heat source gets heated and becomes lighter. The lighter fluid rises due to buoyancy effect and its velocity increases due to continuous addition of enthalpy along the length of heat source. After reaching top of heat source ($z/H_T = 0.72$), the hot fluid diverts towards the radial direction. In the region ($0.45 \leq x/R_o \leq 0.55$) between the two heat sources, multiple recirculation cells are formed near the free surface at top. These convective cells consist of upward and downward flow. The axial velocity shown in Fig 3.18A and 3.18B at $z/H_T = 0.74$ and $z/H_T = 0.92$ are the velocities above the top of IC. The downward flow above the ICs and in between the two ICs results in negative axial velocity at $z/H_T = 0.74$ and $z/H_T = 0.92$. In the region ($0.45 \leq x/R_o \leq 0.55$) between the two heat sources, 30% increase in the maximum velocity was observed at $z/H_T = 0.74$ as shown in Fig 3.18B. This enhanced mixing results in almost uniform temperature distribution [Fig 3.14A] in the region ($0.45 \leq x/R_o \leq 0.55$) between the two heat sources. For 'IC2C1.4', it has been observed that, by distributing the HT area amongst two heat sources, the average circulation velocity increases by 35% as compared to 'IC1C1.4' (Table 3.6). As a consequence, stratification number was found to reduce by 6%. The variation of stratification number with time in Fig 3.22 shows that stratification number increases very rapidly from 0 to 0.77 within 10s and then remains constant. It indicates that convective flow was not very intense at the beginning ($t = 0$ to 10s) and hence system gets stratified easily. After $t = 10$ s, the convective flow increases which prevent further increase in stratification number.

3.5.3 Effect of Submergence of Isolation Condenser

The placement of condensers or HXs in the pool is one of the important parameters which may play a role in deciding the extent of thermal stratification in the pool. The clearance (c) of the ICs inside the pool was varied with three positions (a) 1.4m (b) 0.6m (c) 0.1m for both single as well as two ICs. Five cases have been considered 'IC1c1.4', 'IC1c0.6', 'IC2c1.4', 'IC2c0.6' and 'IC2c0.1'. It was observed that the higher submergence [Fig 3.15C and Fig 3.15D] results in more uniform

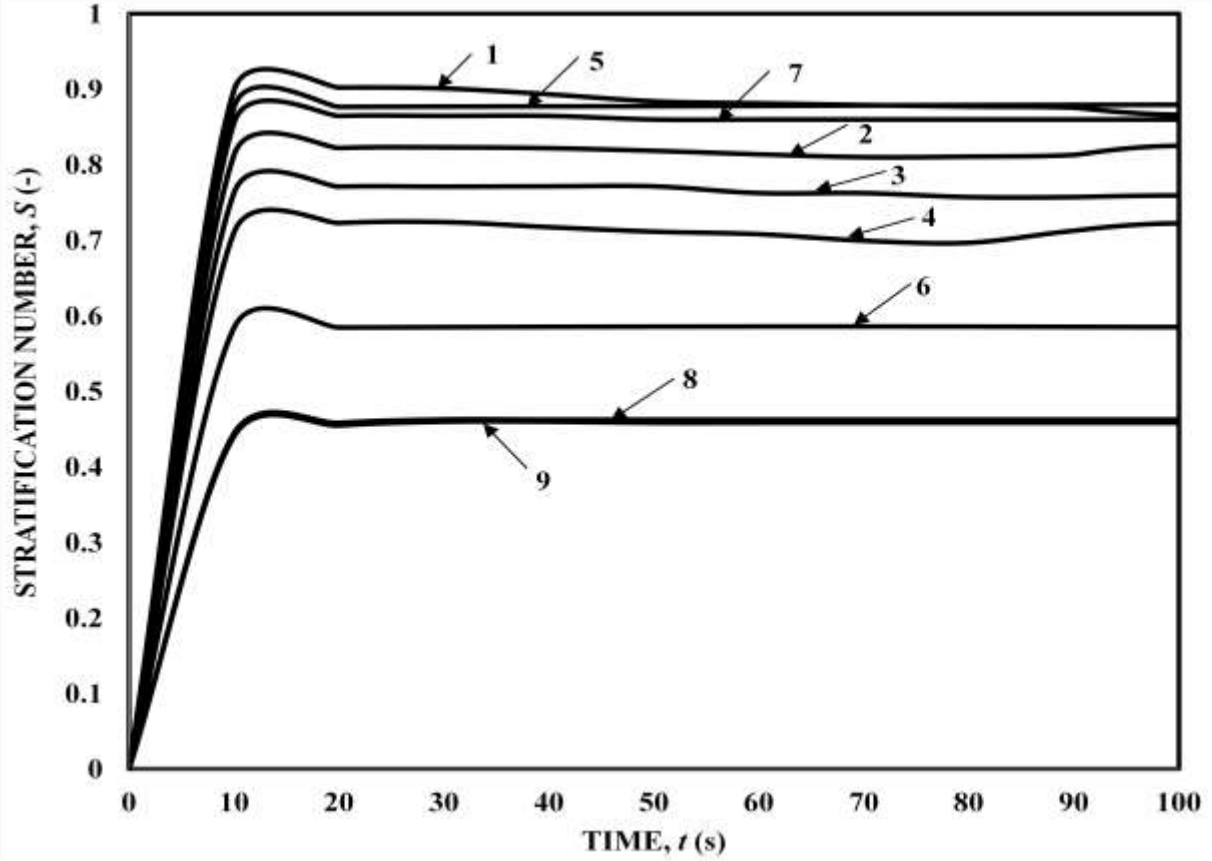


Fig 3.22: Effect of various designs on stratification number (S) with time (1) $IC1c1.4$; (2) $IC1c0.6$; (3) $IC2c1.4$; (4) $IC2c0.6$; (5) $IC2c0.1$; (6) $ICMc0.1$; (7) $DF0$; (8) $DF1$; (9) $BDF3$;

temperature distribution and reduction in stratification. By submerging the condenser for single heat source ($IC1c0.6$), 13% rise in average circulation velocity was observed and stratification number reduced by 6%. Similarly for $IC2c0.6$, 30% rise in average circulation velocity was observed and the stratification number reduced by 13%. Time varying stratification number in Fig 3.22 also shows that by submerging the condenser, stratification number remains lower in a simulated time ($t = 0$ to 100s).

3.5.4 Effect of Submergence and distribution of heat sources inside GDWP

In order to combine the benefits of (1) heat source distribution and (2) submergence of heat source, case $ICMc0.1$ (Fig 3.5) was simulated. It consists of 36 box type heat sources having

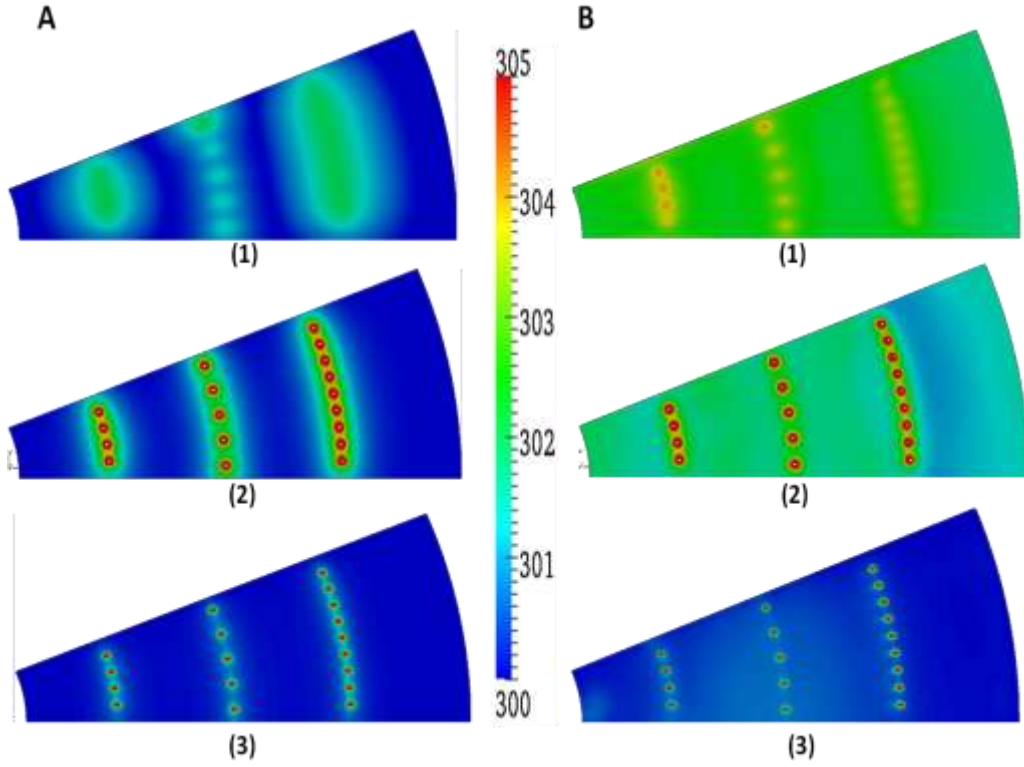


Fig 3.23: Temperature Contours for '*ICMc0.1*' design. (A) $t=100s$, (B) $t=300s$,
(1) $z/H = 0.90$; (2) $z/H = 0.44$; (3) $z/H = 0.02$.

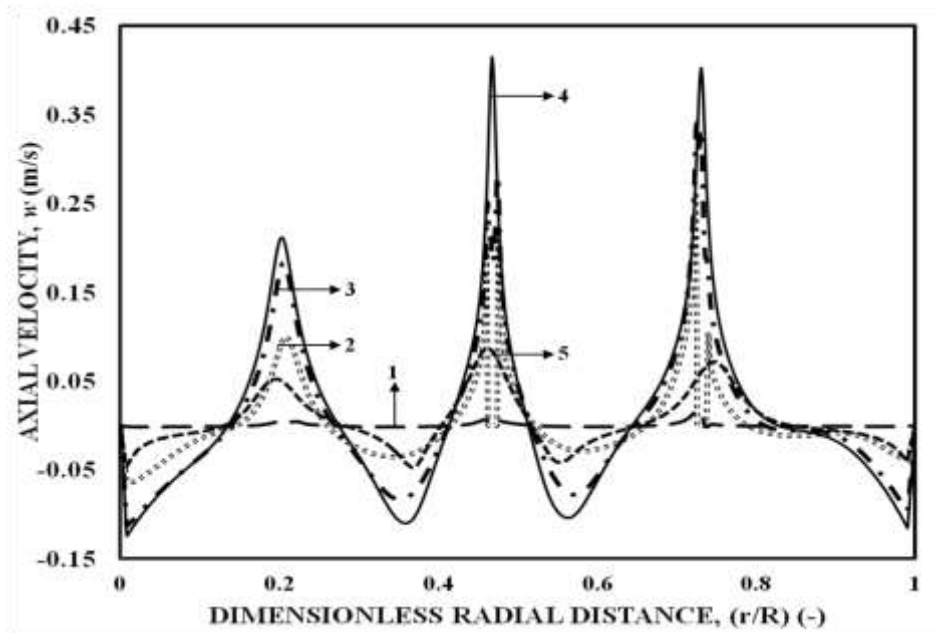


Fig 3.24. Variation in axial velocity with dimensionless radial distance for '*ICMc0.1*' at
 $t=100s$ for symmetry plane ($\theta = 0^0$).

(1) $z/H = 0.01$; (2) $z/H = 0.24$; (3) $z/H = 0.48$; (4) $z/H = 0.62$; (5) $z/H = 0.96$;

clearance (c) of 0.1m from bottom of the tank. In order to have uniform heat distribution in the tank, number of heat sources have been increased in the direction of ($r/R=0$) to ($r/R=1$). Temperature contours in Fig 3.23 shows that the presence of multiple heat sources results in almost uniform temperature distribution near the top ($z/H_T = 0.9$) of the tank. Multiple convective cells are formed in the entire tank. The length of natural circulation loop has been decreased in the presence of multiple heat sources, which results in enhancement in average circulation velocity (Fig 3.24) and hence reduction in circulation time. Axial velocities are very high and positive in the vicinity of heat source because flow rises near the heat source. In between the heat sources and near the tank wall, the negative axial velocities indicate down flow. In the presence of uniformly distributed multiple (36) heat sources ($'ICMc0.1'$), 58% enhancement in average circulation velocity was observed in comparison to single heat source at centre ($'IC1c1.4'$). Consequently, thermal stratification was reduced by 33%.

3.5.5 Effect of Draft tubes

From the above discussion, it is clear that the optimization of the number of heat sources and their position within the pool is possible. In addition to these two parameters, it was thought desirable to incorporate draft tubes. For this purpose, two designs [$'DF1'$ and $'BDF3'$ (Fig 3.6)] were considered. The design details of draft tubes are given in Table 3.4. The draft tube height was 4.4 m so that it can directly activate the hot dead zone located at about 4.8m from the bottom and near the top free surface (Fig 3.25). The draft tube design $'DF1'$ is symmetric with respect to heat source and have inside volumes of 15% of the total liquid volume. The fluid inside the draft tube ($DF1$) is in direct contact with the heat source and hence it is at higher temperature (Fig 3.25) and become lighter as compared to the fluid outside the draft tube. The temperature difference results into density difference. As a result, the lighter hot fluid rises inside the draft tube and descends in the heat source is the most crucial parameter in the design of draft tube. In order to avoid the formation of recirculating cells within the draft tube, it is deliberately kept closer to the heat source. Enhanced

natural circulation has been observed in the region between the heat source and the draft tube which can be seen in Fig 3.26. This causes the temperature gradient to decrease in the vicinity of the tube

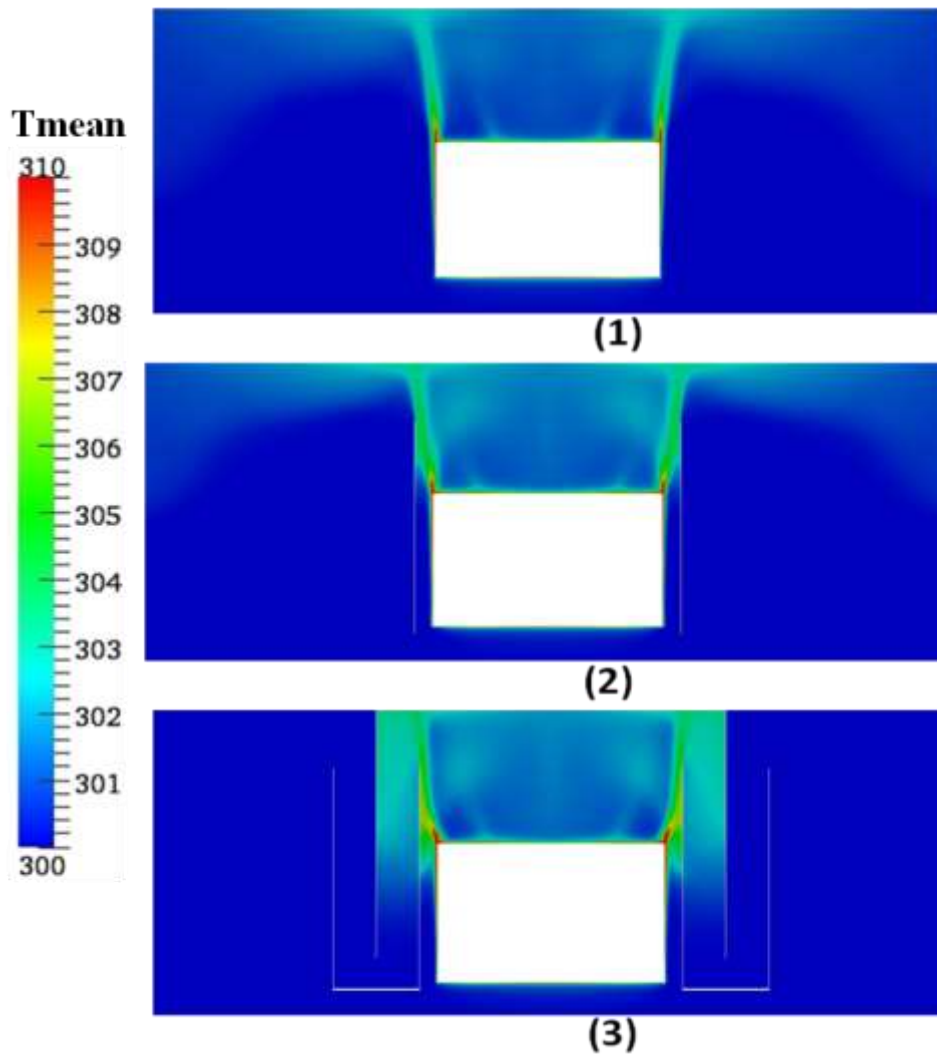


Fig 3.25. Temperature contours for different draft tube designs at $t = 50s$ at symmetry plane ($\theta = 0^\circ$) (1) *DF0*; (2) *DF1*; (3) *BDF3*

wall. As a consequence, the axial velocity increases and this results into a reduction in the mixing time (Table 3.6) by 43%. Temperature is diffused away from the heat source in the presence of single draft tube as compared to the no draft tube (*DF0*) case. It results in reduction in the stratification number (Table 3.6) by 46% as compared to the '*DF0*'. In addition, the combination of three draft tubes and baffle (*BDF3*) prevents the accumulation of hot fluid at the top by providing a flow path to it and results in 40% reduction in stratification [Fig 3.22].

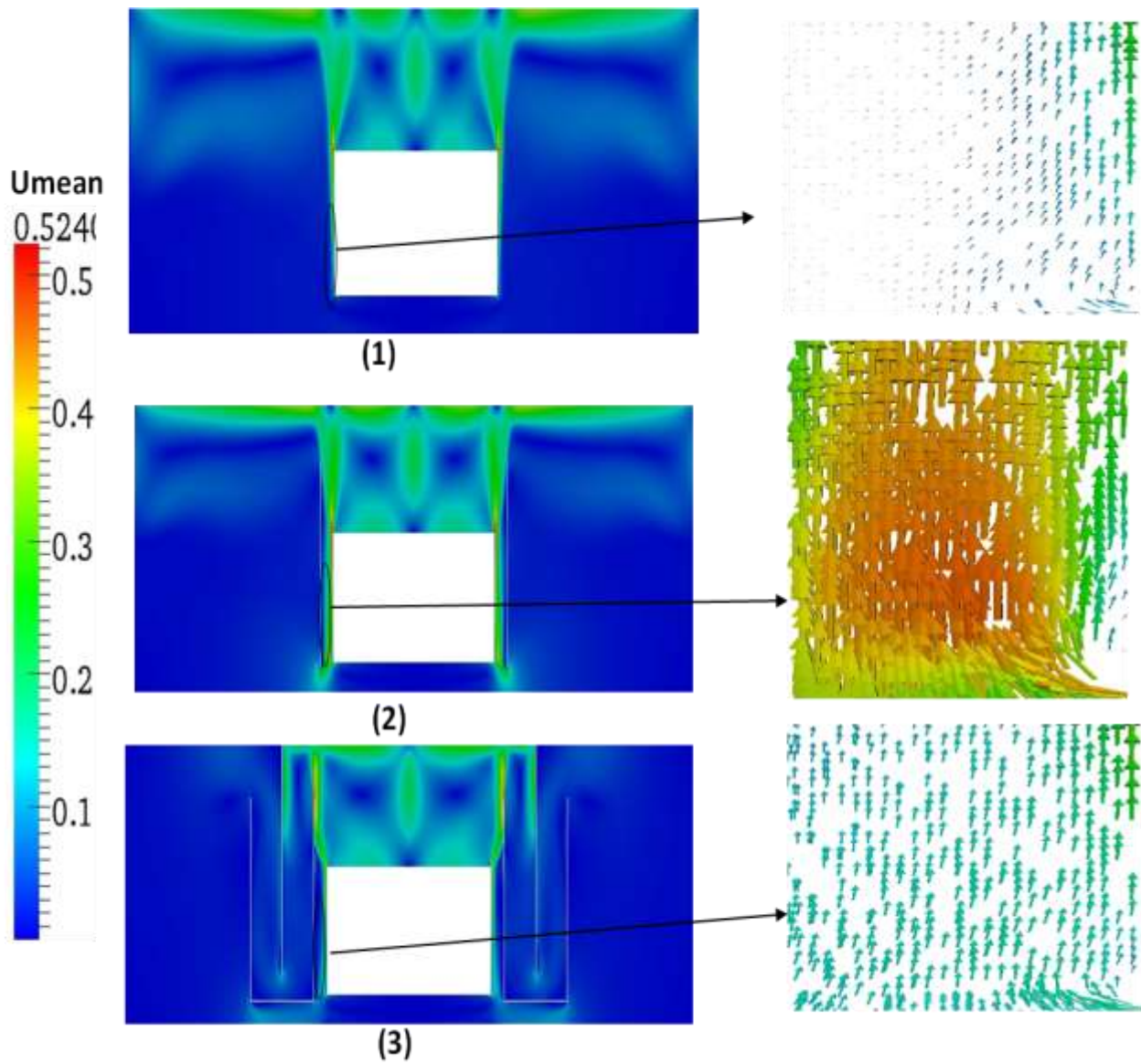


Fig 3.26: Flow distribution for different draft tube designs at $t = 50\text{s}$ at symmetry plane ($\theta = 0^\circ$) (1) *DF0*; (2) *DF1*; (3) *BDF3*

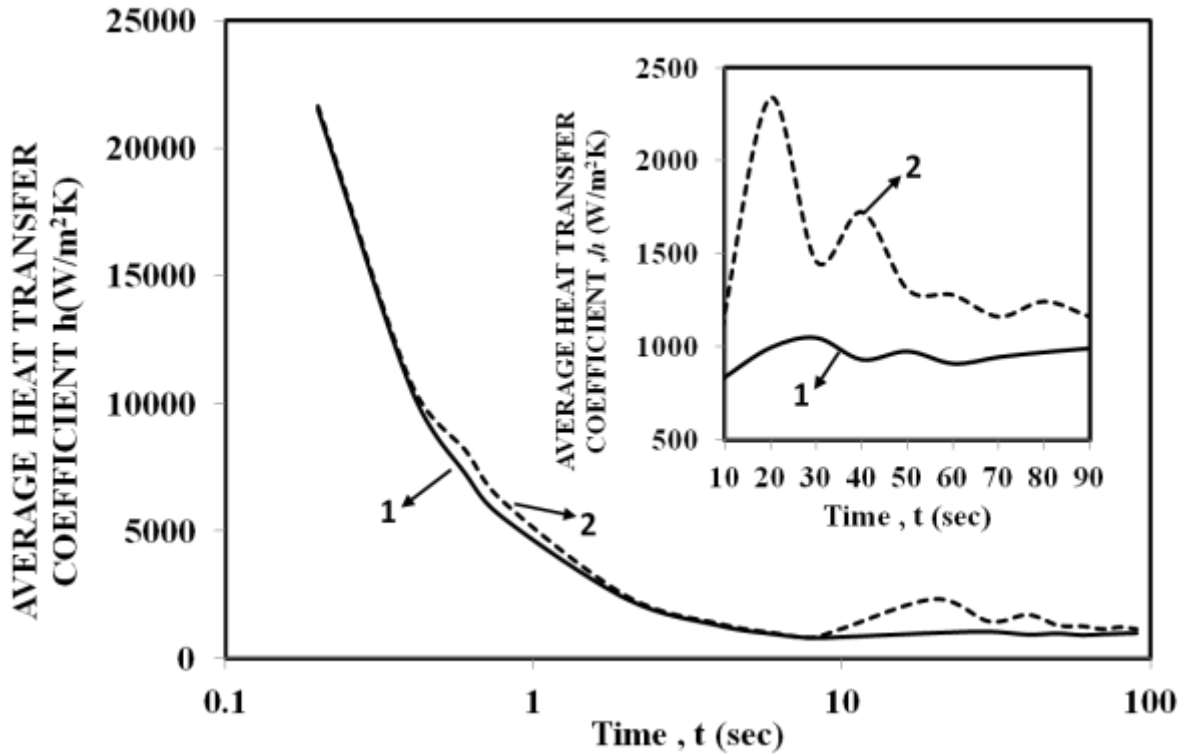


Fig 3.27: Variation of average heat transfer coefficient (h) with time (1) *DF0* (2) *DF1*

3.5.5.1 Transient Heat Transfer

The transient heat transfer behavior in Fig 3.27 of the IC indicates that heat transfer performance was maximum at the beginning ($t = 0$ s) because of large $\Delta T = 258$ K and then it decreases very sharply for few seconds till it reaches a constant value. Boetcher et al. (2012) have observed similar behavior and four heat transfer domains have been identified: conduction, quasi-steady, fluctuating, and decay. In the present study, the decay period has not been captured because the transient CFD studies are limited to 90s only and decay period starts at later stages. The entire transient ($0 < t < 90$ s) heat transfer behavior has been divided into three domains: conduction ($0 < t < 0.4$ s), quasi-steady ($0.4\text{s} < t < 10$ s) and fluctuating period ($10\text{s} < t < 90$ s). Initially, the fluid is at rest. Hence, heat transfer occurs by conduction only. The decay in HTC is very steep in the conduction period ($0 < t < 0.4$ s). As time proceeds, the convective flow starts to develop near the heat source (IC) and heat transfer becomes increasingly dominated by convection. This period ($0.4\text{s} < t < 10$ s) is referred to as quasi-steady and lasts until the circulating flow in the GDWP tank begins to disrupt the

boundary layer near the IC during the fluctuating period. After ($t > 10s$) the convective flow near the IC becomes very intense and results in perturbation in the boundary layer. Further, results in increase in HTC. This period is known as fluctuating period and characterized by intermittent disruption and growth of the boundary layer surrounding the IC. In the conduction period, no difference in the heat transfer behavior has been observed in the presence of draft tube. The effect of draft tube (DFI) can be seen during the quasi-steady period and it becomes more intense during the fluctuating period as convection becomes the more dominant mode of heat transfer. In the presence of draft tube (DFI), 57% enhancement in HTC can be seen in Fig 3.27 at $t = 20s$. As time proceeds ($t > 20s$) the difference in HTC between (DFI and $DF0$) becomes smaller and smaller. The amplitude of fluctuations in HTC is also very large for DFI as compared to $DF0$ because of intense convective flow in the presence of draft tube. As time progresses ($t > 20s$), the fluctuations in HTC dies out.

3.5.5.2 Onset of Secondary Flow (Longitudinal Vortices)

The transient temperature contours at 10cm above ($z/H = 0.562$) the top of IC are shown in Fig 3.28A. For ($t < 20s$), the temperature distribution is more or less uniform along the surface, except near the edges, where the temperature is high. The uniform temperature distribution indicates that natural convection flow is two dimensional and laminar at the beginning. At ($t = 30s$), the temperature distribution shows an array of high temperature streaks arranged across the width of the plate. Since, the fluid is present all along the top surface of IC, the presence of discrete high temperature streaks is indicative of span wise motion of a cellular nature known as longitudinal vortices (secondary flow). The secondary flow results from the destabilizing effect of the buoyancy force component (Sparrow and Husar, 1969), normal to the plate surface. These vortices are pair wise counter-rotating and their rotation axis is parallel to the radial (x axis) direction. The presence of these vortices disrupts the boundary layer at the top surface of IC. Further, it creates regions of

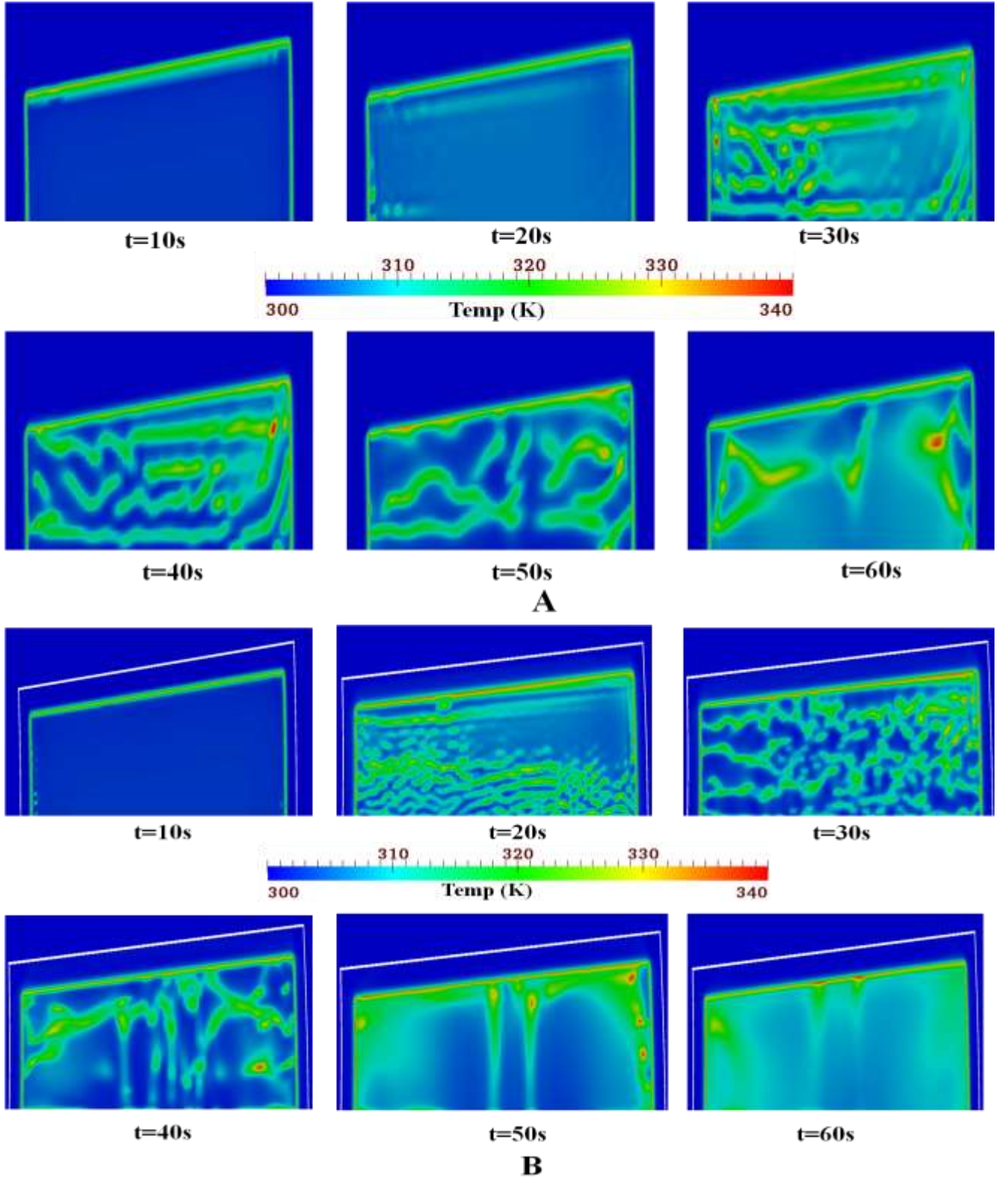


Fig 3.28: Temperature Contours at $z/H=0.562$ for $t=10s, 20s, 30s, 40s, 50s, 60s$.
(A) $DF0$; (B) $DF1$

strong up- and down-wash, which affect the heat transfer significantly. The enhanced heat transfer in the down-wash region of each vortex pair leads to a lower surface temperature. However, in the up-wash region of the vortex pair the temperature is high, because the heat transfer is decreased. As time progresses ($t > 30s$), these laminar vortices grow stronger and subsequent merging of these vortices occurs. In their later stage, the vortices become unsteady and start a wavy, sinuous like motion, which is called secondary instability. The wavy motion of the longitudinal vortices grows very fast and finally the vortices break up into turbulence (Biertumpfel and Beer, 2003). The presence of draft tube (*DF1*), results in early onset of secondary flow (longitudinal vortices) shown in Fig 3.28B as compared to absence of draft tube (*DF0*). In addition to this, the number of longitudinal vortices is more in presence of draft tube. As a result, the heat transfer is enhanced in the presence of draft tube.

3.6 Closure

The detailed CFD analysis of three dimensional temperature and flow fields has been investigated in real size GDWP. Further, the effect of these fields on mixing and thermal stratification phenomena has also been studied. The simulation also enables the quantification of stratification number calculation. In order to reduce the thermal stratification, various geometrical modifications have been incorporated on the heat exchanger design, such as (1) distributing the heat transfer area of heat exchanger among single, double and multiple heat source (2) submergence of condenser to optimize the location of heat exchanger inside the GDWP (3) provision of draft tubes, around a single heat source at centre.

The main conclusions that may be drawn from the present study are summarized as follows:

1. The optimization in the design of isolation condenser by heat source distribution results in enhancement in the average circulation velocity by 35% and reduction in stratification number by 12%.
2. The submergence of condenser also results in reduction in stratification number by 5% and 17% for one '*IC1c0.6*' and two '*IC2c0.6*' heat sources.

3. The combined effects of distribution and submergence of heat source for case '*TCMc0.1*' results in 33% reduction in thermal stratification.
4. Presence of appropriate size of draft tube at an optimum distance from the heat source results in additional driving force apart from buoyancy in the fluid region inside and outside the draft tube which results in reduction in the stratification number by 46% and 40% for '*DF1*' and '*BDF3*' designs, respectively, as compared to the '*DF0*'. In addition to this, it also reduces the size of hot dead zones near the top free surface.

CHAPTER 4:

Design of an optimized IC and study on the effect of inclination of condenser tube on natural convection and stratification in PDHRS

4.1 Introduction

In order to reduce thermal stratification, various modifications in the design of IC were investigated in Chapter 3, such as (1) uniform distribution of heat transfer area (HTA) (2) submergence of HTA (2) combination of multiple draft tubes and baffles. The above recommendations for the design of IC showed a huge potential. However, the desired level of mitigation of thermal stratification was not possible. In all the cases considered in Chapter 3, the IC tubes were vertical. The phenomenon of thermal stratification was more pronounced in the presence of vertical heat source. As the hot fluid rises upwards along the length of IC, temperature difference (ΔT) between the IC and the nearby fluid decreases which further results in a decrease in heat transfer rate. Therefore, the objective of the present study is to investigate the effect of inclination of IC tube on the 3D temperature and flow fields inside the GDWP. Further, the effect of these fields on the mixing, temperature stratification and the rate of heat transfer have been investigated. Single phase CFD simulation using open source CFD code [OpenFOAM-2.2] has been performed for seven tube inclination angles (α w.r.t to vertical direction) (in the range $0^\circ \leq \alpha \leq 90^\circ$).

4.2 Literature survey

Sparrow and Husar (1969) visualized the flow on an isothermal inclined plate to demonstrate the occurrence of secondary flow. The secondary flow resulted from the destabilizing effect of the buoyancy force component normal to the plate surface and consists of longitudinal vortices distributed more or less periodically across the width of the plate. The number of such vortices increases with an increase in Rayleigh number (Ra), but appeared to be relatively insensitive to the

inclination angle of the plate. However, any relation between the formations of these longitudinal vortices on heat transfer performance of the inclined plate was not reported.

Lloyd and Sparrow (2006) carried out experiments on an isothermal inclined plate (top heated) for inclination angles (α) (in the range $-10^\circ \leq \alpha \leq 70^\circ$). The authors have established a relationship between the inclination angle (α) and the nature of the flow instability. Two modes of instabilities have been identified: wave mode ($\alpha < 14^\circ$), longitudinal vortices ($\alpha > 17^\circ$) and transition ($14^\circ < \alpha < 17^\circ$) in which both types of instabilities can coexist. With a decrease in the inclination angle, the waves become stronger and vortices become weaker. However, the authors have not studied the effect of inclination angle (α) on mixing and thermal stratification inside the tank.

Black and Norris (1975) performed flow visualization over an isothermal inclined flat plate (top heated) to study the near wall heat transfer for inclination angle (α) (in the range $0^\circ \leq \alpha \leq 80^\circ$). The study of flow structures near the wall helps to resolve the turbulent boundary layer into two regions: thermal sub layer (a region of constant thickness) and a core region (consisting of randomly fluctuating fluid typical of turbulent flow). The thermal waves were generated periodically from the thermal sub layer and moved into the core region by the buoyancy forces and resulted into significant variation in the local heat transfer. The frequency of the generation of thermal waves decreased with an increase in inclination angle, which lead to decrease in heat transfer. However, their studies were limited to non-uniformly heated flat plate only.

Arabi and Sarhan (1984) performed experiments to study the effect of inclination angle (α) (in the range $0^\circ \leq \alpha \leq 60^\circ$) on natural convective heat transfer over uniformly heated square and cylindrical tubes. The average heat transfer coefficient was found to increase with an increase in the angle of inclination. The heat transfer coefficient for square tubes was found to be higher than the equivalent cylindrical tubes (under otherwise identical conditions) due to the presence of edge effects.

Komori et al., (2001) visualized the flow fields over an inclined flat plate (top heated) inside a water vessel of 0.36 m^3 volume. Measurements were conducted for inclination angles ($20^\circ \leq \alpha \leq 90^\circ$) at three different heat fluxes (3, 5, 7 KW/m^2). The flow visualization confirmed the boundary layer separation when the value of Ra exceeds a critical value. Flow started to separate early with decreasing inclination angle (α) and with increasing heat flux. The value of HTC was found to be increase with a decrease in the inclination angle, producing a maximum at $\alpha = 30^\circ$. However, their studies were limited to non-uniformly heated flat plate only.

Wei et al., (2002) performed 2D CFD simulations to study natural convection and heat transfer around uniformly heated (constant flux) inclined plates with inclination angles (α) (in the range $0^\circ \leq \alpha \leq 90^\circ$), Rayleigh number (10^6 to 10^8) and heat flux (50, 100, 200 and 500 KW/m^2). It was found that the natural convection heat transfer increased with an increase in the inclination angle of plate. However, the work was limited to laminar flows only. The effect of secondary flow (longitudinal vortices) on the heat transfer performance of plate was also not studied.

Biertümpfel and Beer (2003) performed experiments and 3D CFD simulations to study the onset of secondary flow and to measure the heat transfer during laminar-turbulent transition for an inclined ($\alpha = 26^\circ$) flat plate (constant flux) inside a 0.1 m^3 water tank. The authors have observed the formation of counter rotating longitudinal vortices which were similar to the findings of Sparrow and Hussar (1969). These vortices creates region of strong up-ward and down-ward flow and hence strongly affect the heat transfer. In the down-ward region of each vortex pair, the cold fluid entered, leading to a lower surface temperature and enhanced heat transfer. However, in the up-ward region of the vortex pair, the hot fluid travelled upwards leading to high surface temperature and less heat transfer. As the fluid travels downstream, these laminar vortices grew stronger and in their later stage became unsteady and resulted into a wavy, sinuous like motion, which was called as secondary instability. Further downstream, the wavy motion grew very fast and increased in amplitude which further resulted in enhanced heat transfer. Finally, the vortices were found to mix with each other and

the flow broke down into a turbulent motion which resulted in a decrease in heat transfer. Zuercher et al., (1998) has also reported a significant increase in vorticity just before the longitudinal vortices get transformed into turbulence. However, the authors have not studied the effect of inclination angles on the onset of secondary instability and heat transfer.

Corcione et al., (2011) have performed 2D CFD simulations to study laminar natural convection over inclined thin plates (uniformly heated) for a wide range of inclination angles ($0^\circ \leq \alpha \leq 75^\circ$), Rayleigh number ($10 \leq Ra < Ra_{cr}$) and Prandtl number ($0.7 \leq Pr \leq 140$). It was found that the heat transfer rate increased with increase in the values of Ra and Pr , while decreased with an increase in the inclination angle of plate. The heat transfer performance of the upper and lower side of the plate was also studied independently by keeping one side insulated. However, the work was limited to laminar region only. The effect of secondary flow (longitudinal vortices) on the heat transfer performance of plate was also not studied.

Alzwayi and Paul (2014) have performed 2D steady CFD simulations to study the transition of free convection flow in a parallel walled channel (upper plate heated) for inclination angle ($0^\circ \leq \alpha \leq 85^\circ$), and width of the channel (0.06 m to 0.45m). The $k-\epsilon$ turbulence model was used to model turbulent natural convection. The average heat transfer coefficient was found to decrease with an increase in the inclination angle. On the other hand, as the width of the channel increases, the heat transfer coefficient initially drops to minimum value followed by some increase at a larger width.

From the literature review, it is clear that many successful attempts have been made by various authors to address the interesting as well as challenging problem of natural convection and heat transfer over inclined heated plates submerged in a water pool. However, the published work has been restricted to inclined thin plates and that too the only upper surface was heated. Therefore, prior experimental and numerical investigations of natural convection instabilities on inclined plates have been limited by an inability to completely observe the 3D temperature and flow fields when the plate or tube is uniformly heated from all the sides. The only work related to inclined plates

uniformly heated at both sides was performed by Corcione et al., (2011) but the work was limited to steady, 2D, laminar natural convection. In many applications such as Passive Decay Heat Removal System (PDHRS) of advanced nuclear reactors, IC tubes were cylindrical and heated uniformly from all sides. Very limited literature is available on the turbulent natural convection and heat transfer through inclined cylindrical tubes heated uniformly from all sides.

Framed in this background, the objective of this study is (1) to undertake a comprehensive investigation on natural convection from inclined cylindrical tube heated uniformly from all sides (2) to study the relationship between inclination angle (α) and heat transfer rate and optimize the angle at which the heat transfer is maximum and thermal stratification is minimum (3) design an IC for real size GDWP ($\sim 10000\text{m}^3$) of advanced nuclear reactor and ensure the desired extent of decay heat removal in a stipulated time.

4.3 Numerical Procedure

In the present work, 3D CFD simulations have been performed under unsteady conditions. The governing equations for the single phase transient natural convection are described in Section 3.3.1 of Chapter 3. For the present case of $\beta = 5 \times 10^{-4} (\text{K}^{-1})$, $\Delta T = 258 \text{ K}$, the value of Ra works out to be 3×10^{11} . The Shear Stress Transport (SST) $k - \omega$ turbulence model was used to study turbulent natural convection. The first order implicit scheme was used for the time discretization of all unsteady terms. QUICK spatial discretization scheme was used for modeling the convective terms and central differencing scheme for diffusive terms. All the discretized equations were solved in a segregated manner with the PISO (Pressure Implicit with Splitting of Operators) algorithm. Further, the solutions were considered to be fully converged when sum of scaled residuals was below 10^{-5} .

4.4 Results and discussions

The overall objective of the present work is to design an efficient IC for the PDHRS which ensure efficient removal of decay heat and mitigation of temperature stratification. The effect of inclination of condenser tubes on mixing and thermal stratification phenomenon inside GDWP has

been studied for seven tube inclination angles ($\alpha = 0^\circ, 15^\circ, 30^\circ, 45^\circ, 60^\circ, 75^\circ, 90^\circ$). Initially, such an analysis was performed for a pilot scale GDWP (10 lit) and the optimum results were tested for the large scale GDWP ($\sim 10000\text{m}^3$).

4.4.1 Effect of inclination of IC tube for pilot scale GDWP

4.4.1.1 Geometry and Boundary conditions

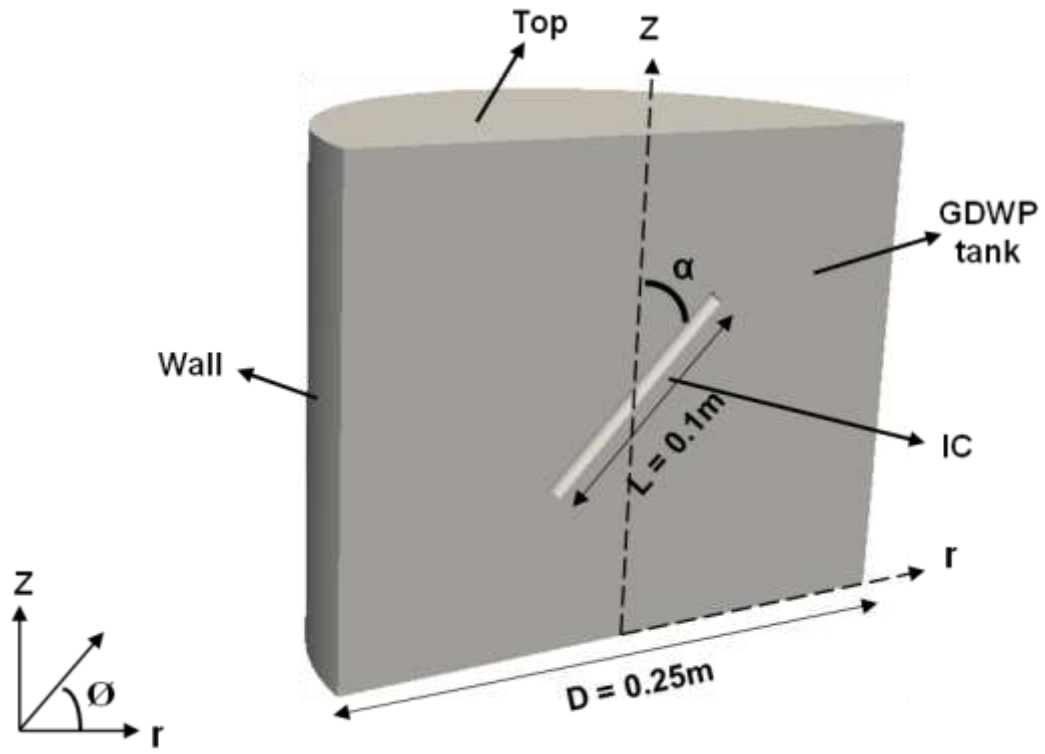
In this section, single phase mixing and thermal stratification phenomenon has been studied inside a pilot scale GDWP (10 liters, Fig 4.1A) provided with a heating tube (IC) at centre. The detailed dimensions of pilot scale GDWP and heating tube are given in Table 4.1. The inclination angle (α) of the tube with respect to vertical axis (z) was varied in the range 0° to 90° ($\alpha = 0^\circ, 15^\circ, 30^\circ, 45^\circ, 60^\circ, 75^\circ, 90^\circ$) by considering tube centre as a point, located 0.1m from the bottom. The details of the boundary conditions for pilot scale GDWP are given in Table 4.2.

Table 4.1: Design details of pilot scale and large scale GDWP and Isolation condenser (ICs)

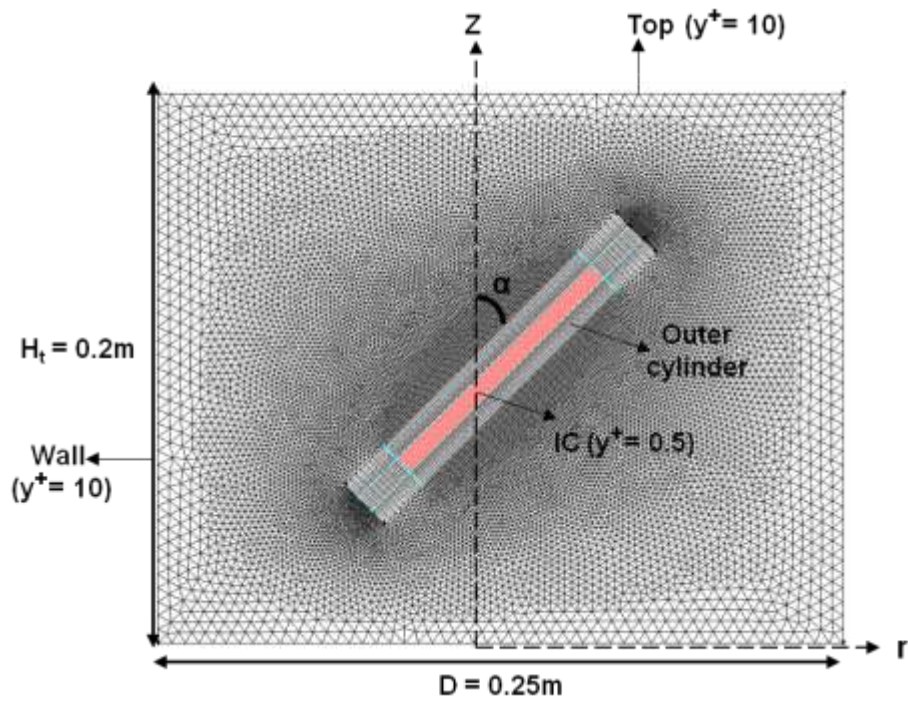
System	Tank dimensions (m)	IC Tube dimensions (m)	Header dimensions (m)
Pilot scale GDWP	$D=0.25, H=0.2\text{m}$	$d=0.0071, h=0.1\text{m}$	
Large scale GDWP	$OD=50, ID=12, H_T=5,$ $\phi = -22.5^\circ \text{ to } 22.5^\circ$	$\text{No. of tubes} = 40$ $D_t = 0.4\text{m}, \text{pitch} = 0.726\text{m},$ $\alpha = 75^\circ,$ $\phi = -11.25^\circ \text{ to } 11.25^\circ$	$D_h = 0.6\text{m}, L_h = 14.5\text{m}$

Table 4.2: Details of the boundary conditions for pilot scale GDWP:

Zone	Boundary Conditions	
	Temperature	Velocity
IC	$T=558\text{k}$	No slip ($u_r = u_\phi = u_z = 0$)
Top	Adiabatic ($\partial T / \partial z = 0$)	Free slip ($\frac{\partial u_r}{\partial z} = \frac{\partial u_\phi}{\partial z} = 0, u_z = 0$)
Walls	Adiabatic ($\partial T / \partial r = 0$)	No slip ($u_r = u_\phi = u_z = 0$)



(A)



(B)

Fig 4.1: (A) Schematic of pilot scale GDWP with single inclined IC tube and (B) Grid generation

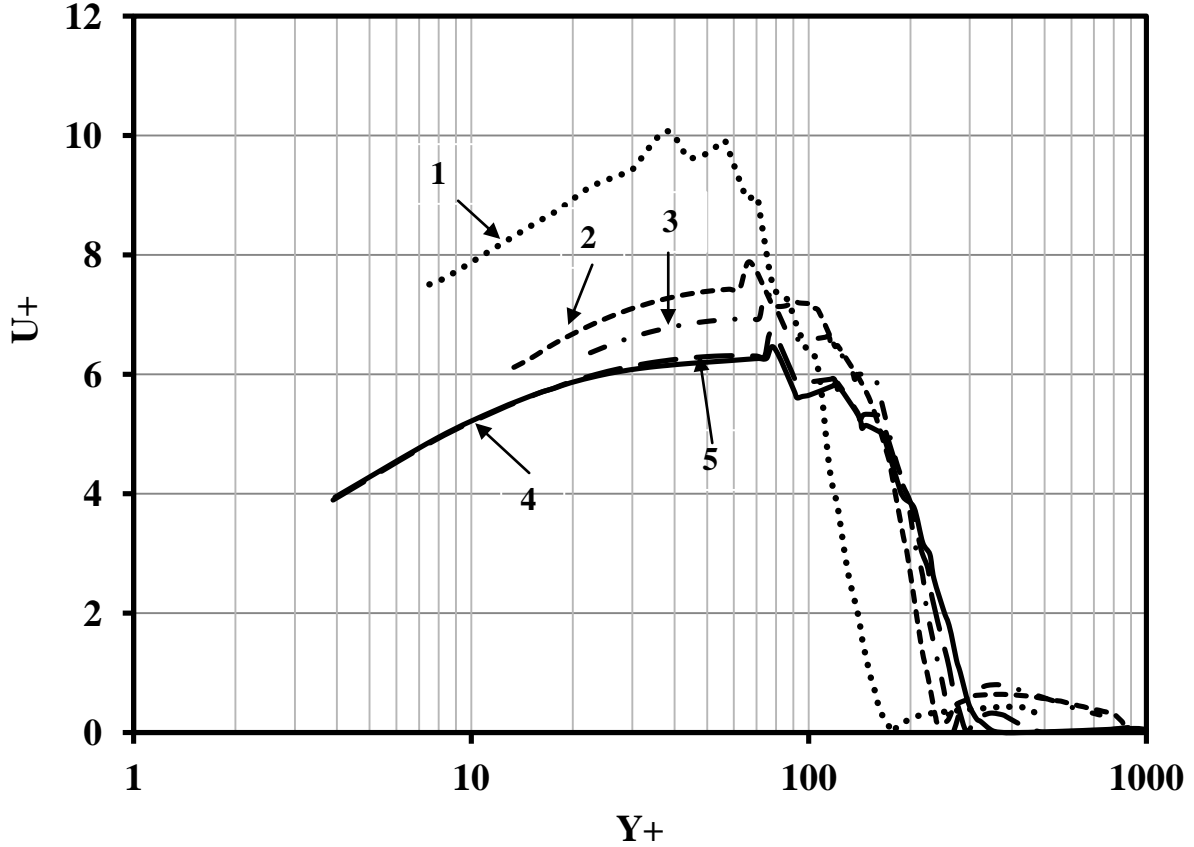


Fig 4.2: Effect of first node distance from wall on non dimensional velocity for inclined heat source ($\alpha = 45^\circ$) at $t = 50s$ for different grid sizes and turbulence models (1) 0.6mm, $k-\epsilon$; (2) 0.3mm, $k-\epsilon$; (3) 0.15mm, $k-\epsilon$; (4) 0.15mm, LRR; (5) 0.15mm, SST $k-\omega$

4.4.1.2 Grid independence and assessment of turbulence models

The grid sensitivity analysis for three tube inclination angles ($\alpha = 0^\circ, 45^\circ, 90^\circ$) was performed for pilot scale GDWP. The open source geometry and mesh generation software Gmsh 2.9 (Remacle et al., 2010) was used for geometry and mesh generation. In natural convective flows, turbulence is mainly concentrated in the thin region close to wall (heat source) and it is almost absent in the core (Henkes et al., 1991). Further, the velocity and temperature gradients are also very high in this region. In order to accurately predict the near wall heat transfer, efficient modeling of this region is required. Accordingly, in the present work, the mesh was adjusted in such a way to ensure that the near wall flow features were properly resolved. An artificial cylindrical volume ($l = 0.14$ m, $d = 20$ mm) shown in Fig 4.1B was created enclosing the IC tube. A non-uniform hexahedral mesh was generated in this cylindrical volume, with finer mesh close to the boundary layer of the IC tube. 30

nodes were assigned along the circumference of 7 mm IC tube and 100 nodes were assigned along the 0.1 m length of IC tube. Away from this volume surrounding the IC tube (Fig 4.1B), a tetrahedral mesh of uniform grid size was employed. The grid independence study was performed for pilot scale GDWP in two steps. In a first step, the y^+ independence was carried out by varying the distance of first node from IC tube. Three cases were considered (1) 0.6mm ($y^+ = 20$) (2) 0.3mm ($y^+ = 10$) (3) 0.15mm ($y^+ = 4$). The dimensions of the artificial cylinder were kept constant in all the cases. The u^+ vs y^+ plot in Fig 4.2 shows that the standard $k-\varepsilon$ model (Launder and Sharma, 1974) over predicts (35%) the velocity profiles when the first node distance was less than 0.6mm ($y^+ = 20$). Further, the turbulent kinetic energy (k) and energy dissipation rate (ε) were over predicted by standard $k-\varepsilon$ model as shown in Fig 4.3. This behaviour is attributed to the wall functions used by standard $k-\varepsilon$ model to obtain boundary conditions for the k and ε equations up to the wall. These wall functions use $\varepsilon = \frac{C_\mu^{3/4} k^{3/2}}{\kappa x}$ at the first node which results into higher values of ε when the first node is taken very close to wall. These wall functions were originally derived for forced convection and do not hold for the natural convection. Hence, it is essential to find other options in place of logarithmic wall functions to solve k and ε equations up to the wall. The SST $k-\omega$ by Menter (1994) is a modified version of the standard $k-\varepsilon$ model with a capability of better prediction of near wall heat transfer. The SST $k-\omega$ model uses the turbulence frequency $\omega = \varepsilon/k$ as the second variable to solve turbulent length scale near the wall. This model behaves as $k-\omega$ model in the near wall region and as the $k-\varepsilon$ model in the fully turbulent region away from the wall. The SST $k-\omega$ model consists of limiters which limits the eddy viscosity to give improved performance in flows with adverse pressure gradients and wake regions. Also, the turbulent kinetic energy (case (5) in Fig 4.3A) is limited to prevent the buildup of turbulence in the stagnation region. The most complex classical turbulence model is the Reynolds stress equation model (RSM). The RSM model does not rely on the turbulent viscosity concept, but instead incorporates transport equations for second order velocity

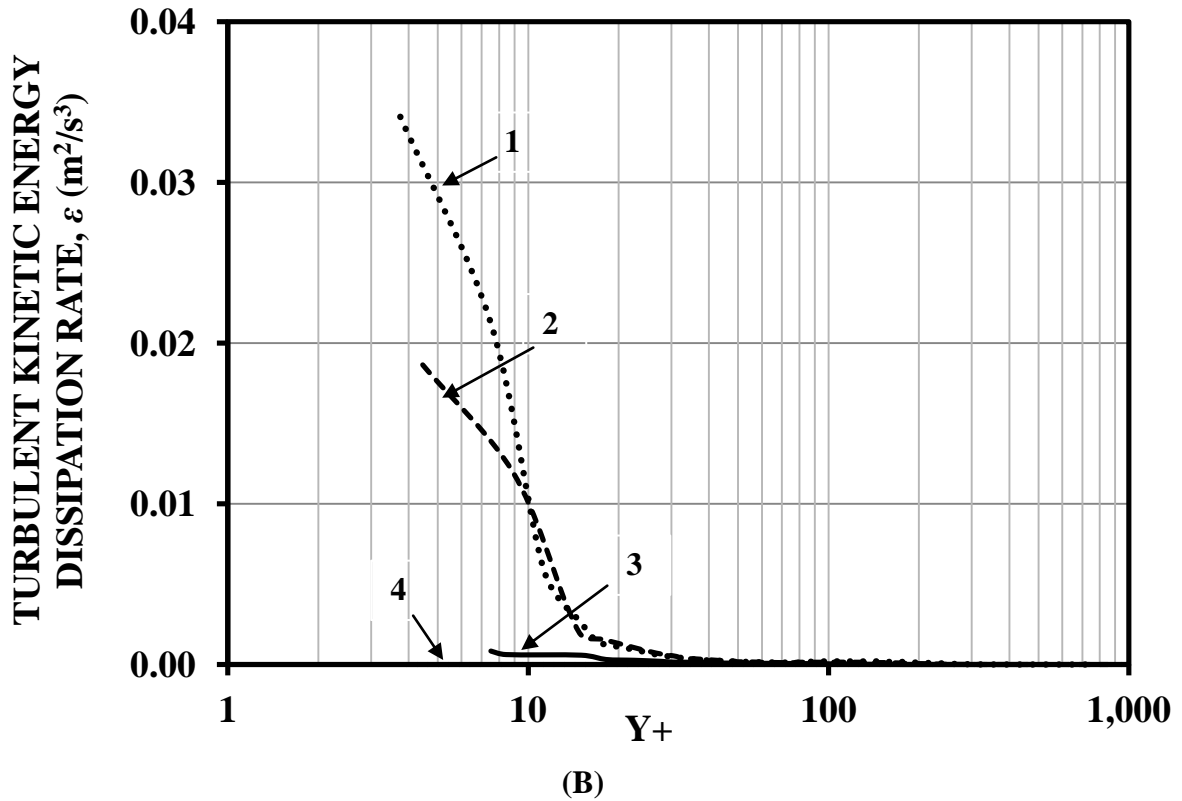
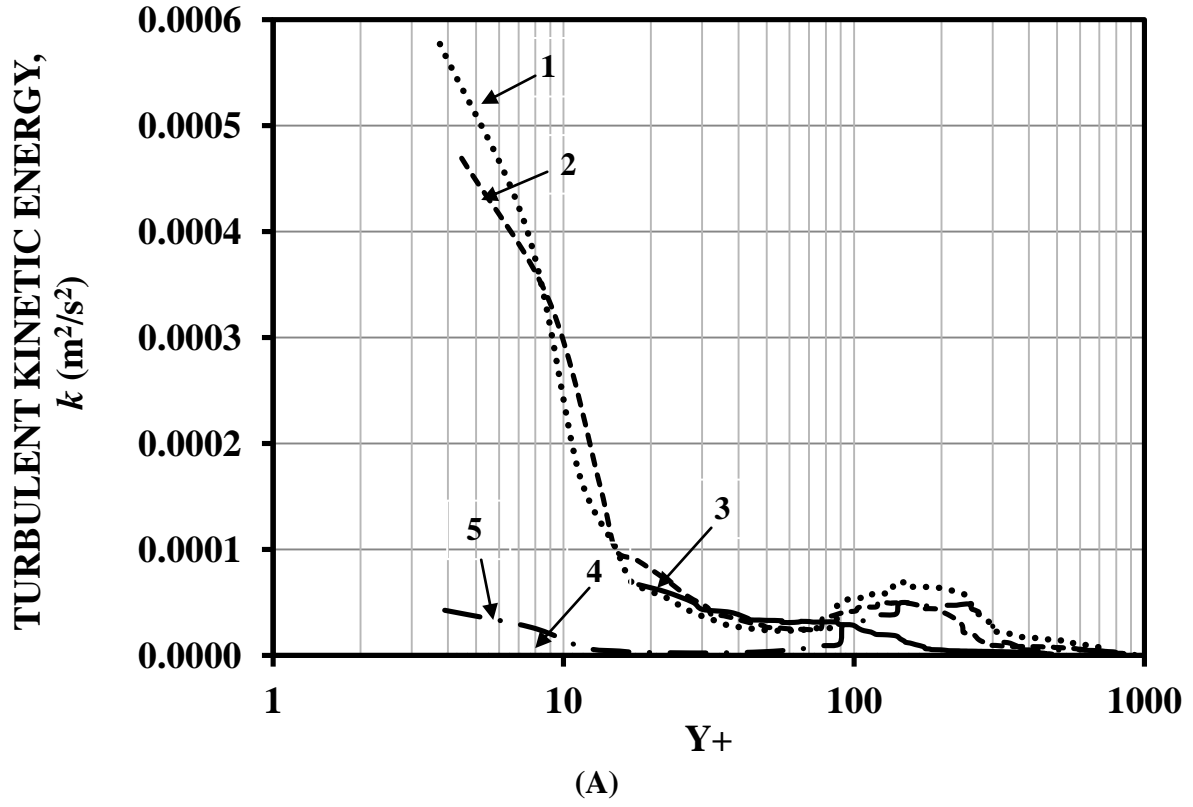


Fig 4.3: Effect of first node distance from wall on (A) turbulent kinetic energy (k) and (B) dissipation rate (ϵ) for inclined heat source ($\alpha = 45^\circ$) at $t = 50s$ for different grid sizes and turbulence models (1) 0.6mm, $k-\epsilon$; (2) 0.3mm, $k-\epsilon$; (3) 0.15mm, $k-\epsilon$; (4) 0.15mm, LRR; (5) 0.15mm, SST $k-\omega$

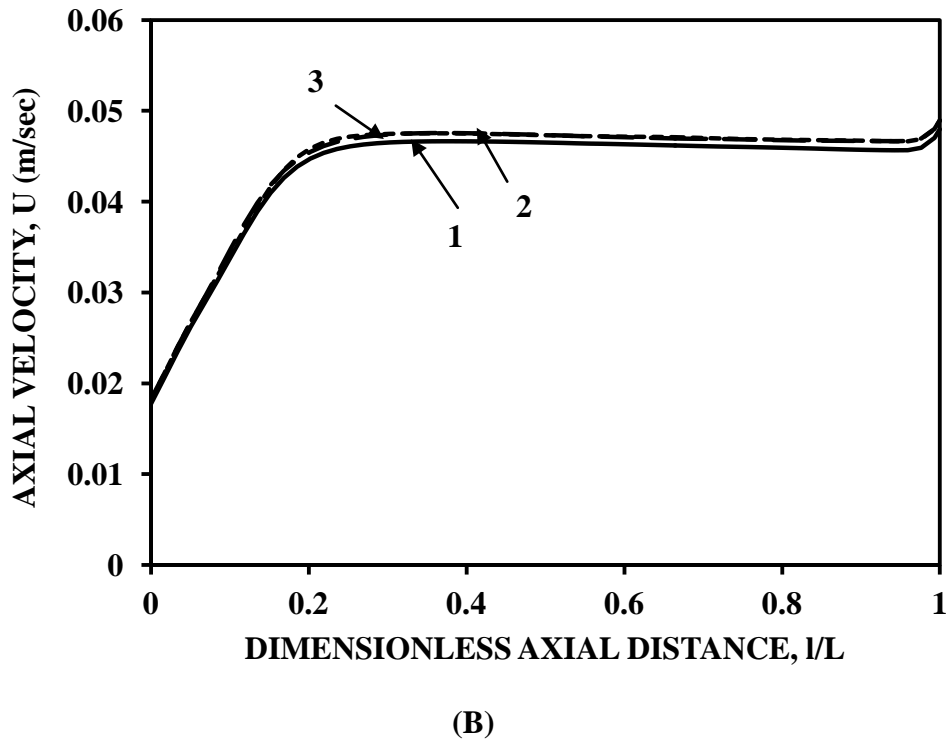
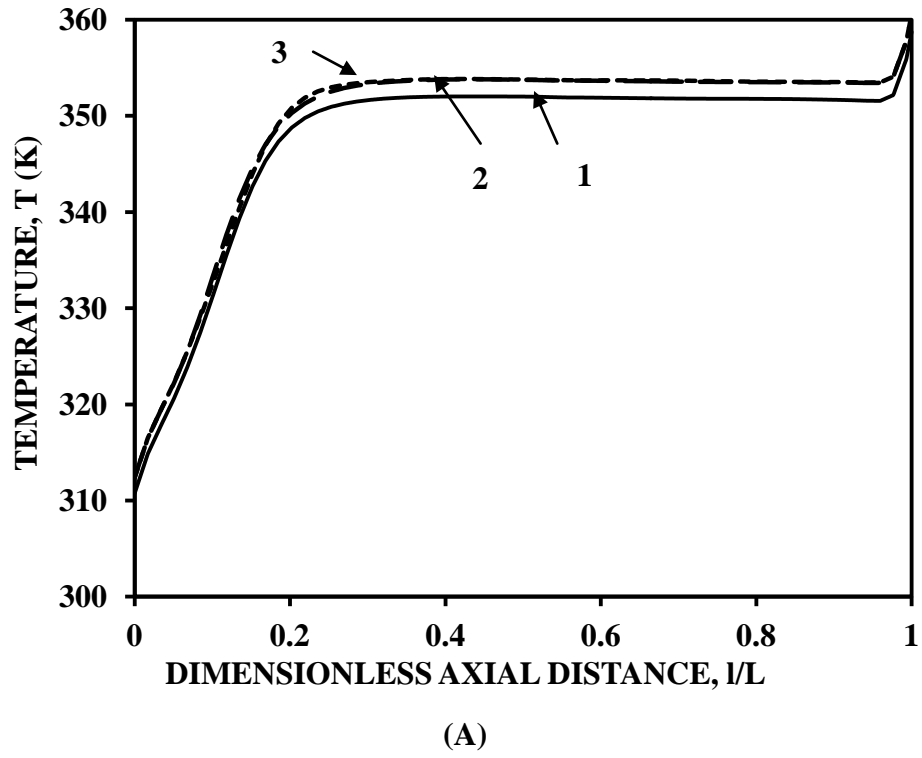


Fig 4.4: Effect of grid size for inclined heat source ($\alpha = 45^\circ$): Variation in (A) Axial temperature and (B) Axial velocity at 2mm away from the IC tube ($\theta = 180^\circ$): at $t = 50$ s for different grid sizes (1) 0.3M; (2) 0.6M; (3) 0.8M.

and temperature correlations. The RSM model solves six equations for the Reynolds stress tensor and another equation for the dissipation rate. The equation of turbulent stresses contains the terms, namely pressure strain rate (which contains fluctuating pressure velocity gradients) and the flux of Reynolds stresses. In addition to the modeling of the terms in the turbulent energy dissipation rate equation, these terms need to be modeled accurately. The SST $k-\omega$ and RSM models were able to capture the large velocity gradients in the near wall region ($y^+ < 10$). For $y^+ < 5$, the SST $k-\omega$ and RSM model predicts $u^+ = y^+$ and hence able to capture the viscous sub layer. The SST $k-\omega$ (case (5) in Fig 4.3) and RSM (case (4) in Fig 4.3) models under predict the turbulent kinetic energy (k) and energy dissipation rate (ϵ) in comparison to standard $k-\epsilon$ model. The near wall turbulence and velocity predictions by SST $k-\omega$ and RSM model were in good (5%) agreement. The RSM model requires large computation time as to solve additional six Reynolds stress equations. In order to save the computation time, the SST $k-\omega$ model has been used for further studies. After finalizing the y^+ in step 1, the effect of mesh size in the bulk (region outside the artificial cylinder) was studied in step 2. Three mesh sizes were selected 3mm, 5mm and 8mm. The total number of grids corresponding to these grid sizes was 0.3M, 0.5M and 0.8M. Fig 4.4A and Fig 4.4B shows the axial temperature and velocity profiles predicted by SST $k-\omega$ at $t = 50s$ at 2mm away from the top ($\theta = 180^\circ$) of the IC tube for three grid densities (0.3M, 0.5M, 0.8M). This particular location was selected because it was close to the flow separation region, where the temperature was found to be maximum. The axial temperature (Fig 4.4A) and velocity (Fig 4.4B) profile shows transition from primary to secondary flow. The temperature and velocity first increases up to transition point and then become constant along the tube length. All the chosen grids predict the temperature and mean flow patterns effectively. Minor differences (less than 1%) was observed between 0.5M and 0.8M cells as shown in Fig 4.4A, B (lines 2 and 3) in terms of temperature and velocities. Therefore, the SST $k-\omega$ model has been used for all the simulations of pilot scale GDWP having the first node at 0.15mm ($y^+ = 4$) and total 0.5M cells.

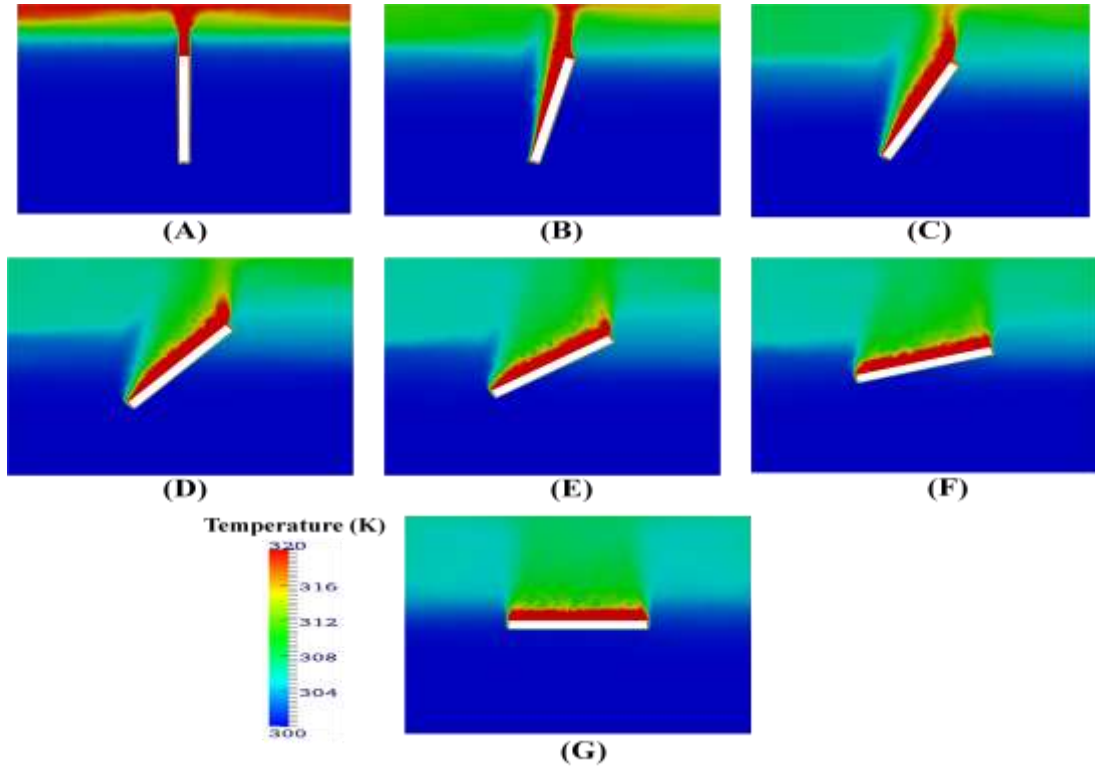


Fig 4.5: Temperature Contours at different inclination angles at $t=100s$ along plane (P): (A) $\alpha=0^\circ$; (B) $\alpha=15^\circ$; (C) $\alpha=30^\circ$; (D) $\alpha=45^\circ$; (E) $\alpha=60^\circ$; (F) $\alpha=75^\circ$; (F) $\alpha=90^\circ$

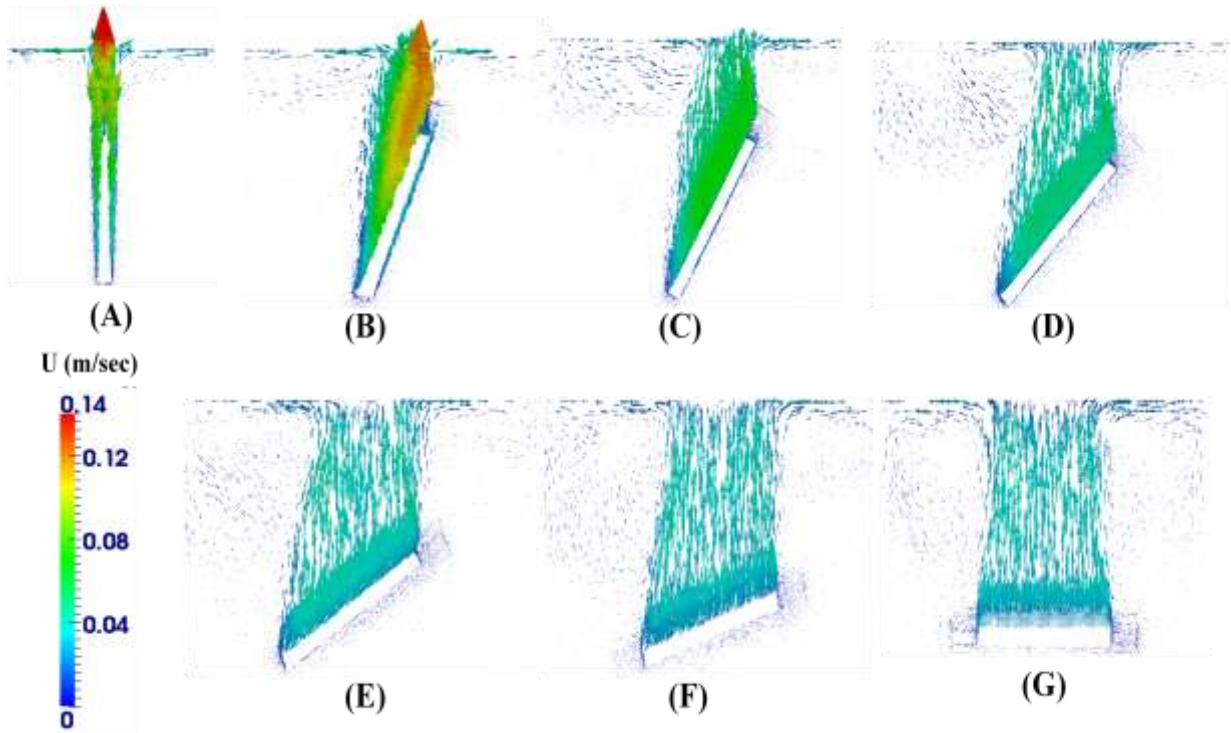


Fig 4.6: Flow distribution at different inclination angles at $t=100s$ along plane (P): (A) $\alpha=0^\circ$; (B) $\alpha=15^\circ$; (C) $\alpha=30^\circ$; (D) $\alpha=45^\circ$; (E) $\alpha=60^\circ$; (F) $\alpha=75^\circ$; (F) $\alpha=90^\circ$

4.4.1.3 Temperature contours and Flow distribution

The temperature contours and flow distribution obtained from the CFD simulations at different inclination angle (α) (in the range $0^\circ \leq \alpha \leq 90^\circ$) at $t = 100\text{s}$ are shown in Fig 4.5 and Fig 4.6. It is apparent that the effect of the inclination angle (α) is to thicken the buoyant fluid plume (Corcione et al., 2011) and to reduce the axial velocity (Fig 4.6). For vertical heated tube ($\alpha = 0^\circ$) (Fig 4.5A), the maximum temperature gradient was observed in the vicinity of the heat source and it became weaker radially away from the heat source. As a result, the fluid adjacent to the heat source got heated, became light and moved upwards. Consequently, the heavier fluid (cold water) from the neighboring areas rushed in to replace the rising fluid. This behavior was also observed in the flow distribution (Fig 4.6A) where a velocity peak was present near the IC tube and then the velocity reduced away from the heat source in transverse directions. In fact, in the bulk of water pool, the liquid velocities were feeble of the order of mm/s. As the hot fluid moved upwards along the tube, the temperature kept increasing because of the continuous addition of enthalpy from the heat source. When, it reached near the top of the heat source (IC), the fluid from all around the tube got mixed and formed a turbulent plume which resulted in enhancement of the velocity (Fig 4.6) and the turbulent kinetic energy. As the rising fluid reached the free water surface at the top, it moved radially outwards direction and reached the tank wall, where it again gets diverted in the downward direction. As a result, circulation patterns get established in the water pool. With time, the accumulated layer of hot water near free surface region extended downwards. However, the temperature near the tank wall was always low (Fig 4.5) which may be due to feeble circulation velocity in the bulk of the fluid. The overall result was that the total energy supplied to the system gets accumulated near the IC tube and near the free surface region.

4.4.1.4 Azimuthal Heat Transfer

The azimuthal ($0^\circ \leq \theta \leq 360^\circ$) variation of heat transfer coefficient for different inclination angles ($\alpha = 0^\circ, 15^\circ, 30^\circ, 45^\circ, 60^\circ, 75^\circ, 90^\circ$) are shown in Fig 4.7. When the tube was vertical ($\alpha = 0^\circ$), the heat

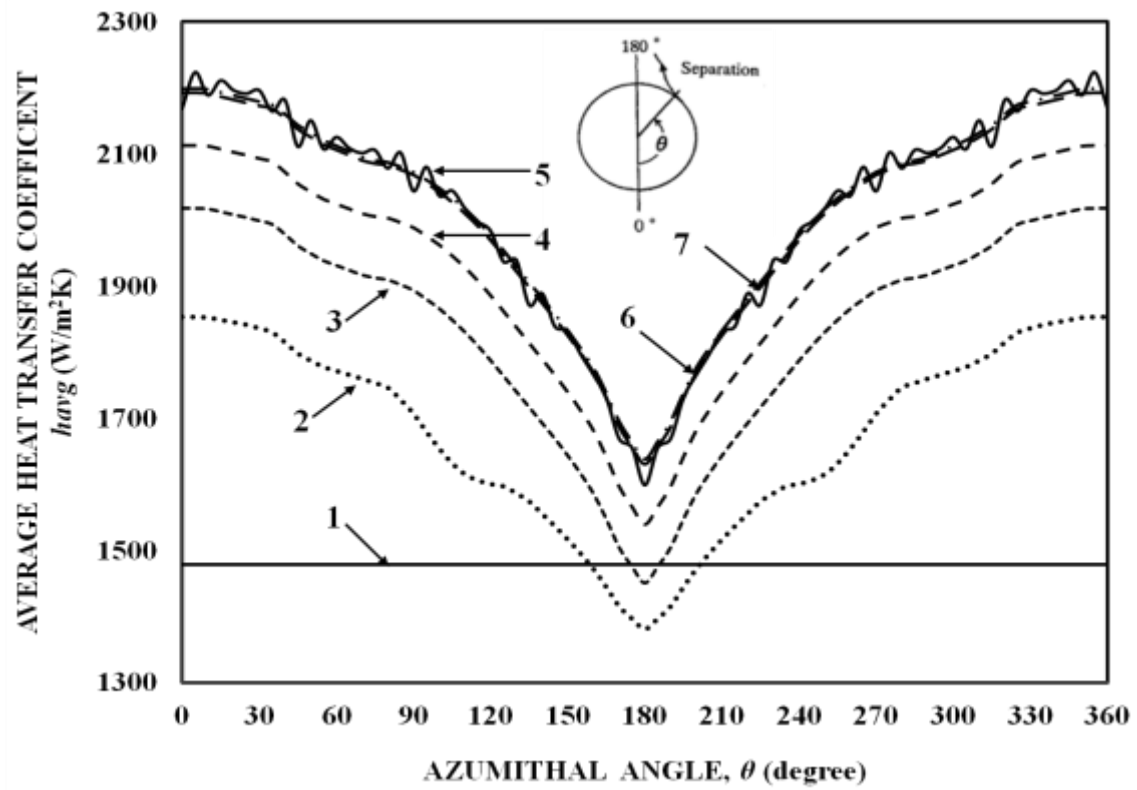


Fig 4.7: Effect of inclination of IC tube on azimuthal heat transfer coefficient at $t = 100\text{s}$; (1) $\alpha = 0^\circ$; (2) $\alpha = 15^\circ$; (3) $\alpha = 30^\circ$; (4) $\alpha = 45^\circ$; (5) $\alpha = 60^\circ$; (6) $\alpha = 75^\circ$; (7) $\alpha = 90^\circ$

transfer coefficient was constant along the azimuthal direction. For the vertical heated tube ($\alpha = 0^\circ$), the buoyancy force due to density difference acts in the vertical direction. Hence, the fluid from all around the tube tends to slide along the tube surface and parallel to the axis of the tube. As a result, nominal variation in azimuthal heat transfer (case (1) in Fig 4.7) was observed for vertical heated tube. When the tube was inclined ($\alpha > 0^\circ$), the heat transfer was maximum at the bottom of the tube ($\theta = 0^\circ$) and minimum at the tube top ($\theta = 180^\circ$). For inclined ($\alpha > 0^\circ$) heated tubes, it was observed that the fluid from the bottom of the tube tends to slide along the tube surface (azimuthal direction) due to the action of buoyancy force in the vertical direction. The fluid was separated from the tube surface at $\theta_{sep} = 160^\circ$ which resulted into creating a low pressure as well as high fluid temperature in the region ($160^\circ \leq \theta \leq 180^\circ$). The high pressure gradient in the region ($160^\circ \leq \theta \leq 180^\circ$) generates a primary flow which drives the fluid along the tube length and results in an increase in the axial velocity (Fig 4.8B) as the fluid travels downstream. With increase in inclination angle (α), the

primary flow (along the tube length due to pressure gradient) became weaker and the secondary flow (along vertical direction due to buoyancy forces) became stronger. Further, it enhanced the fluid sliding motion at the tube bottom and prevents the fluid sliding motion at the top of the tube. The increase in fluid sliding length at the bottom of the tube resulted into enhanced heat transfer. The heat transfer coefficient was found to increase with increase in inclination angle (α) (in the range $0^\circ \leq \alpha \leq 60^\circ$). Beyond ($\alpha = 60^\circ$), nominal variation in heat transfer was observed. As the angle of inclination (α) was increased, the stronger secondary flow provide sufficient kinetic energy to overcome the adverse pressure gradient near the tube periphery and resulted in a delay in the flow separation. Further, it resulted into enhanced heat transfer.

4.4.1.5 Transition from primary to secondary flow

The development of thermal boundary layer along the length of heated tube is shown in Fig 4.5. For vertical heated tube ($\alpha = 0^\circ$), nominal variation was observed in the thickness of boundary layer. For inclined ($\alpha > 0^\circ$) heated tube, significant variation in the boundary layer was observed along the length ($0 \leq l/L \leq 1$) of heated tube. A thin thermal boundary layer was observed near the leading edge. As the hot fluid rises downstream along the length ($0 \leq l/L \leq 1$) of heated tube, the thickness of boundary layer increases very sharply after a point known as transition point. This behavior is due to the interaction between the primary (along the tube length due to pressure gradient) and secondary flow (along vertical direction due to buoyancy forces). As the angle of inclination ($\alpha > 0^\circ$) of the heated tube increases, the transition point comes upstream towards the leading edge. This behavior is attributable to the fact that secondary flow becomes stronger with increase in inclination angle (α). The axial temperature (Fig 4.8A) and velocity (Fig 4.8B) profiles also shows transition from primary to secondary flow after a transition point. The temperature first increases upto transition point and then becomes constant along the tube length. For $\alpha = 15^\circ, 30^\circ, 45^\circ, 60^\circ, 75^\circ$ the transition point occurs at $l/L = 0.3, 0.2, 0.18, 0.12, 0.05$.

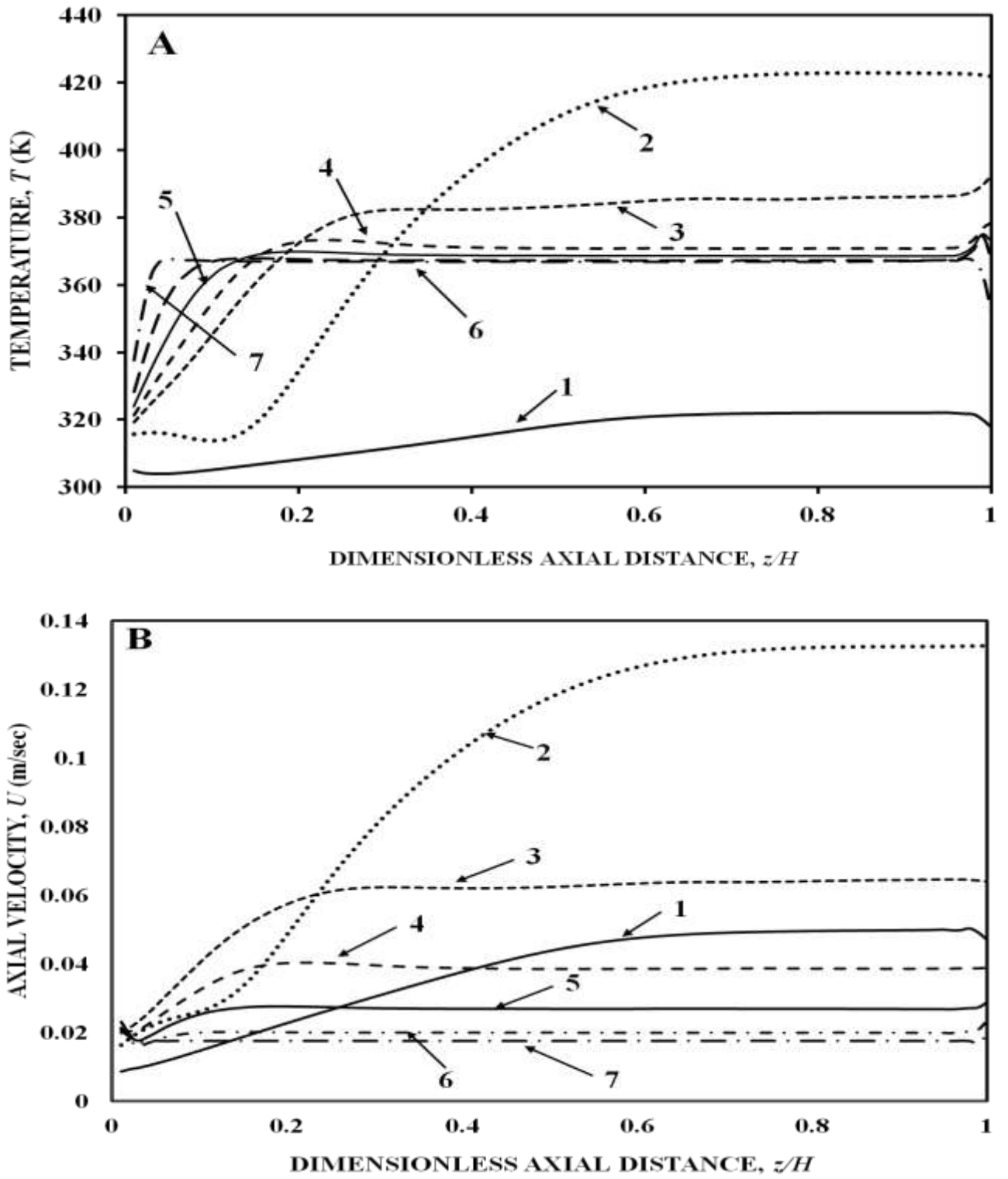


Fig 4.8: Effect of inclination of IC tube on (A) Axial temperature and (B) Axial velocity at $t=100s$ and 1mm away from the tube for different inclination angles; (1) $\alpha=0^\circ$; (2) $\alpha=15^\circ$; (3) $\alpha=30^\circ$; (4) $\alpha=45^\circ$; (5) $\alpha=60^\circ$; (6) $\alpha=75^\circ$; (7) $\alpha=90^\circ$

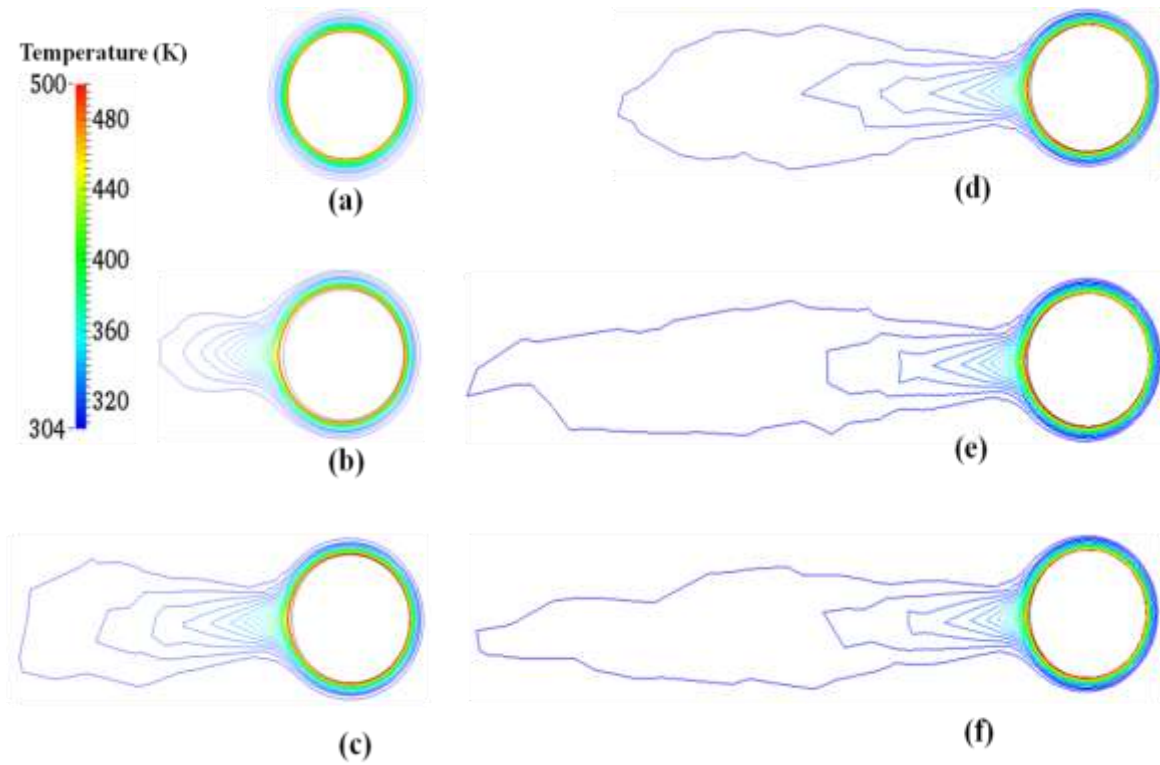


Fig 4.9: Isotherms at different inclination angles at $t=100s$ along plane (P): (a) $\alpha=0^\circ$; (b) $\alpha=15^\circ$; (c) $\alpha=30^\circ$; (d) $\alpha=45^\circ$; (e) $\alpha=60^\circ$; (f) $\alpha=75^\circ$

4.4.1.6 Fluid flow near the upward and downward face of the heated tube

The temperature contour in Fig 4.5 clearly indicates that the temperature at the upward face ($\theta = 180^\circ$) of the heated tube was higher than that at the downward face ($\theta = 0^\circ$). The temperature at the upward face of the heated tube also shows significant variations due to the transitional behavior of the fluid. On the other hand, the temperature at the downward face ($\theta = 0^\circ$) was more or less uniform in comparison to the temperature behavior at the upper face ($\theta = 180^\circ$). This can be attributed to the fact that the fluid flow below the plate was promoted mainly by the heat contribution of the lower side. On the other hand, owing to the heating of the lower side, the whole tube is embedded in an upward-moving convection (secondary flow) pattern whose global effect is to decrease the temperature difference (Ra) between the upper side of the plate and the adjacent fluid, and therefore to lessen the magnitude of the local heat transfer. This leads to an increase in the temperature of the

fluid adjacent to the upper face ($\theta = 180^\circ$). This effect can be seen clearly in the isotherms plotted in Fig 4.9. The flow distribution in Fig 4.6 also shows a similar behavior. The velocity was high at the upward face of the heated tube than the downward face. The temperature and axial velocity at the downward face of the tube was almost independent of the inclination angle. On the other hand, the fluid flow and heat transfer at the upward face of the heated tube increases with increase in inclination angle from $\alpha = 15^\circ$ to $\alpha = 45^\circ, 60^\circ, 75^\circ, 90^\circ$.

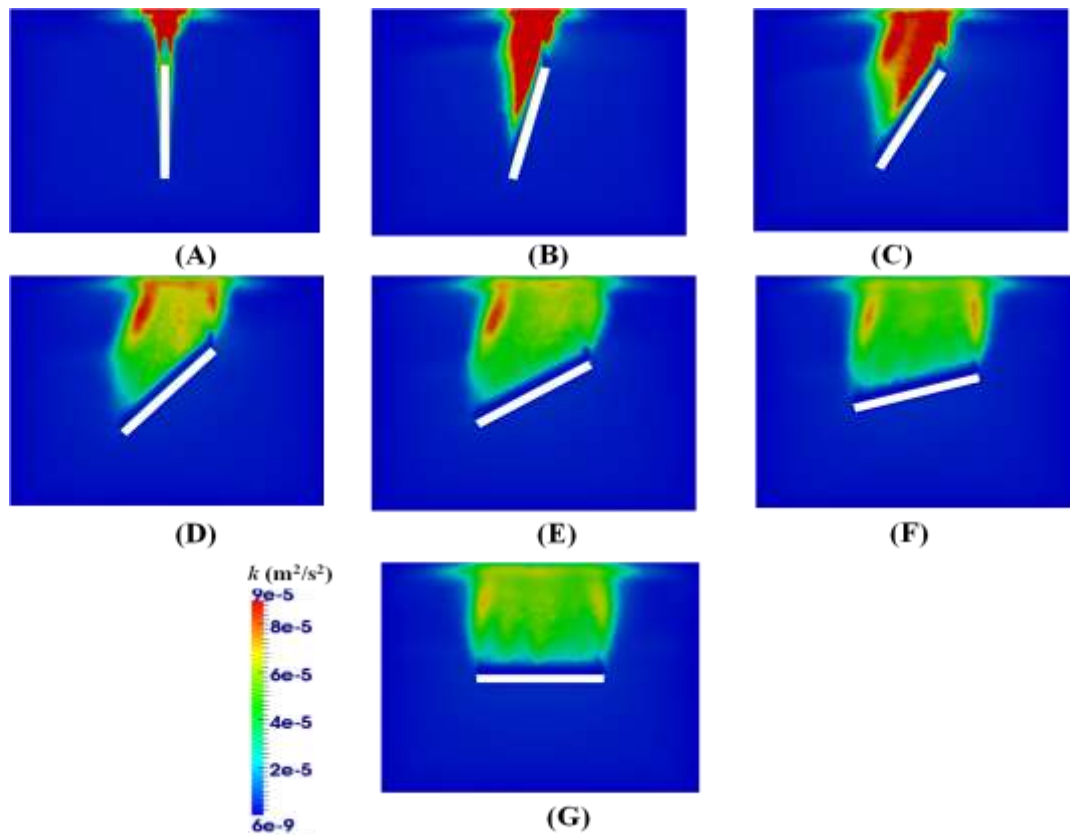


Fig 4.10: Turbulent kinetic energy Contours at different inclination angles at $t=100s$ along plane (P):
 (A) $\alpha = 0^\circ$; (B) $\alpha = 15^\circ$; (C) $\alpha = 30^\circ$; (D) $\alpha = 45^\circ$; (E) $\alpha = 60^\circ$; (F) $\alpha = 75^\circ$

4.4.1.7 Turbulent kinetic energy (k) contour

The turbulent kinetic energy (k) contours shown in Fig 4.10 indicates that the maximum value of k decreases with an increase in the inclination angle (α). This behavior was due to decrease in the axial velocity (Fig 4.8B) with an increase in the inclination angle. The maximum value of k

was very low before the transition point, and it reaches a high value just after the separation point. For $\alpha = 15^\circ, 30^\circ, 45^\circ, 60^\circ, 75^\circ, 90^\circ$, the k profiles show that, in the vicinity of heated tube, the value of k was almost zero implying no turbulence. The turbulence becomes increasingly prominent with an increase in distance from the heated tube. This particular trend in the k profiles was due to the superimposition of secondary flow on the primary flow. Fig 4.11B shows the transient behavior of volume average turbulent kinetic energy (k_{avg}). For vertical heated tube ($\alpha = 0^\circ$), the k_{avg} decreased with time. When the tube was inclined ($15^\circ \leq \alpha \leq 90^\circ$), the value of k_{avg} was relatively large for ($0 < t < 20s$). It can be attributed to the intense convective flow in the period ($0 < t < 20s$). As the time proceeded ($t > 20s$), the value of k_{avg} decreased. As the angle of inclination increased, the average turbulent kinetic energy (k_{avg}) increased due to stronger secondary flow superposed on the primary flow.

4.4.1.8 Transient heat transfer

The transient heat transfer behavior in Fig 4.11A indicates that the heat transfer rate was maximum at the beginning ($t = 0s$) because of large ΔT and then it decreased very sharply for few seconds till it reached a constant value. The average heat transfer coefficient (h_{avg}) was calculated as follows:

$= mC_p \overline{\Delta T}_{w,t}$, where $\overline{\Delta T}_{w,t}$ is the average rise in temperature of the pool after time t

$$\overline{\Delta T}_{w,t} = \bar{T}_{w,t} - T_{w,t=0} \quad (4.1)$$

$$\bar{T}_{w,t} = \frac{\iiint_{r,\theta,z}^{R,\theta,Z} T_{w,t} dr d\theta dz}{\iiint_{r,\theta,z}^{R,\theta,Z} dr d\theta dz} \quad (4.2)$$

$Q = hA\overline{\Delta T}_{s,t}$, where $\overline{\Delta T}_{s,t}$ is the temperature difference between the average tube surface temperature and average pool temperature.

$$\overline{\Delta T}_{s,t} = T_{s,t} - \bar{T}_{w,t} \quad (4.3)$$

$$\bar{T}_{s,t} = \frac{\iint_{l,\theta}^{L,\theta} T_{s,t} dl d\theta}{\iint_{l,\theta}^{L,\theta} dl d\theta} \quad (4.4)$$

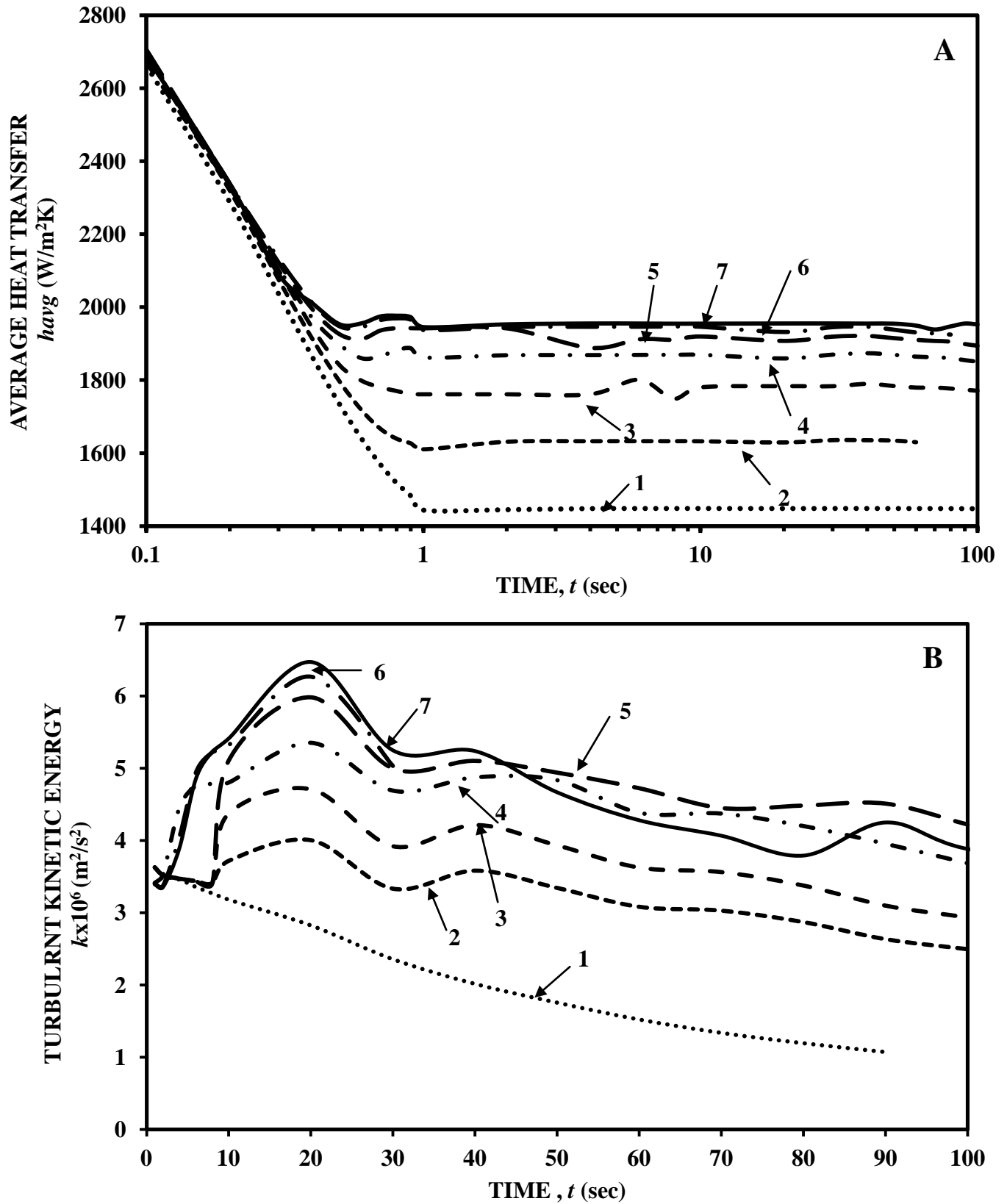


Fig 4.11: Transient Variation of (A) Average heat transfer coefficient (h_{avg}) and (B) Volume average Turbulent kinetic energy (k_{avg}) for different inclination angles;

(1) $\alpha = 0^\circ$; (2) $\alpha = 15^\circ$; (3) $\alpha = 30^\circ$; (4) $\alpha = 45^\circ$; (5) $\alpha = 60^\circ$; (6) $\alpha = 75^\circ$; (7) $\alpha = 90^\circ$

$h_{avg} = \frac{mC_p\overline{\Delta T}_{w,t}}{A\Delta T_{s,t}}$, where h_{avg} is the average heat transfer coefficient and it has been calculated at different time intervals. Boetcher et al., (2012) have also observed similar behavior in the heat transfer and four heat transfer domains have been identified: conduction, quasi-steady, fluctuating, and decay. In the present study, the decay period was not captured because the transient CFD studies are limited to 100s only and the decay period starts at later stages. The entire transient ($0 < t < 100s$) (Fig 4.11A) heat transfer behavior has been divided into three domains: conduction ($0 < t < 0.4s$), quasi-steady ($0.4s < t < 10s$) and fluctuating period ($10s < t < 100s$). Initially, the fluid is at rest. Hence, heat transfer occurs by conduction only. The decay in HTC is very steep in the conduction period ($0 < t < 0.4s$). As time proceeds, the convective flow starts to develop near the heated tube (IC) and heat transfer becomes increasingly dominated by convection. This period ($0.4s < t < 1s$) is referred to as quasi-steady and lasts until the circulating flow in the GDWP tank begins to disrupt the boundary layer near the IC tube during the fluctuating period. After ($t > 1s$) the convective flow near the IC becomes very intense and results in perturbation in the boundary layer and increase in the value of HTC. This period is known as fluctuating period and characterized by intermittent disruption and growth of the boundary layer surrounding the IC. In the conduction period, the heat transfer behavior was found to be independent of inclination angle (α). The effect of inclination angle can be seen during the quasi-steady period and it becomes more intense during the fluctuating period as the convection phenomenon becomes relatively dominant mode of heat transfer. The heat transfer coefficient was found to be dependent on inclination angle (α) in the fluctuating period. The heat transfer was found to be maximum for $\alpha = 90^\circ$ and minimum for $\alpha = 15^\circ$. This behavior was due to the interaction between the primary and secondary flow. The primary component results in enhancement in fluid sliding motion at the top whereas the secondary flow results in larger sliding distance at the bottom of the tube. As the angle of inclination (α) increases, the secondary flow increases and the primary flow decreases. The increase in fluid sliding motion at the bottom more

than offsets the decrease in fluid sliding motion at the top and results in maximum total heat transfer coefficient for inclination angle $\alpha = 90^\circ$.

4.4.1.9 Quantification of Stratification and Extent of mixing

The procedure to calculate thermal stratification number was described in great detail in Section 3.5.1.3 of Chapter 3. The stratification number was calculated at $t = 100\text{s}$ and was found to have a value of 0.9 (Fig 4.12) for the vertical heated tube ($\alpha = 0^\circ$). The stratification number first increases with an increase in the inclination angle and reaches a maximum value at $\alpha = 15^\circ$. For $\alpha > 15^\circ$, the stratification number decreases with increase in inclination angle. This behavior was due to the interaction between primary and secondary flow. The primary flow results in enhancement in fluid sliding motion at the top whereas the secondary flow results in larger sliding distance from the bottom of the tube till the separation point. As angle of inclination (α) increases, the secondary flow increases and primary flow decreases. The increase in fluid sliding motion from the tube bottom more than offsets the decrease in fluid sliding motion at the top and results in minimum stratification number ($S = 0.15$) and maximum total heat transfer coefficient for inclination angle $\alpha = 90^\circ$.

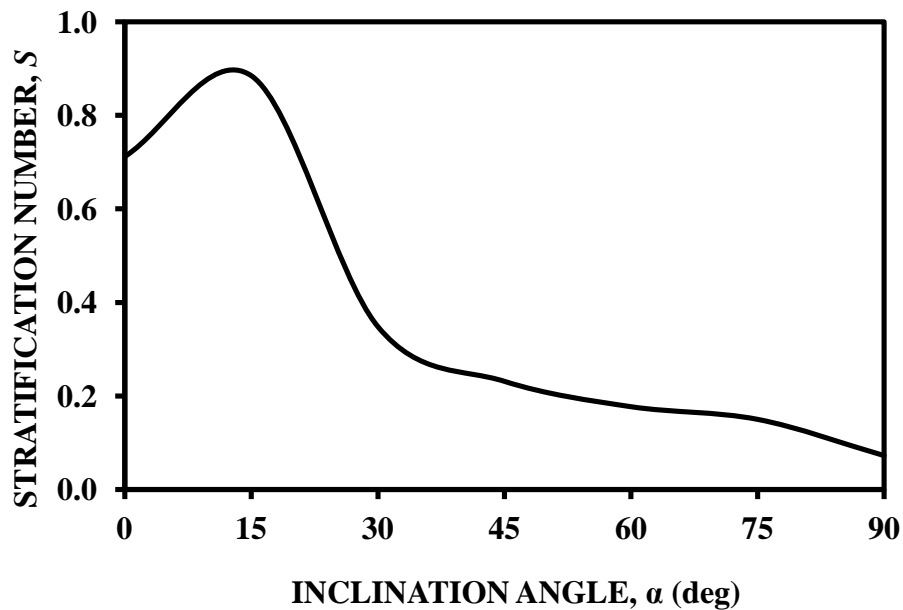


Fig 4.12: Effect of inclination of IC tube on thermal stratification (S) for small scale GDWP

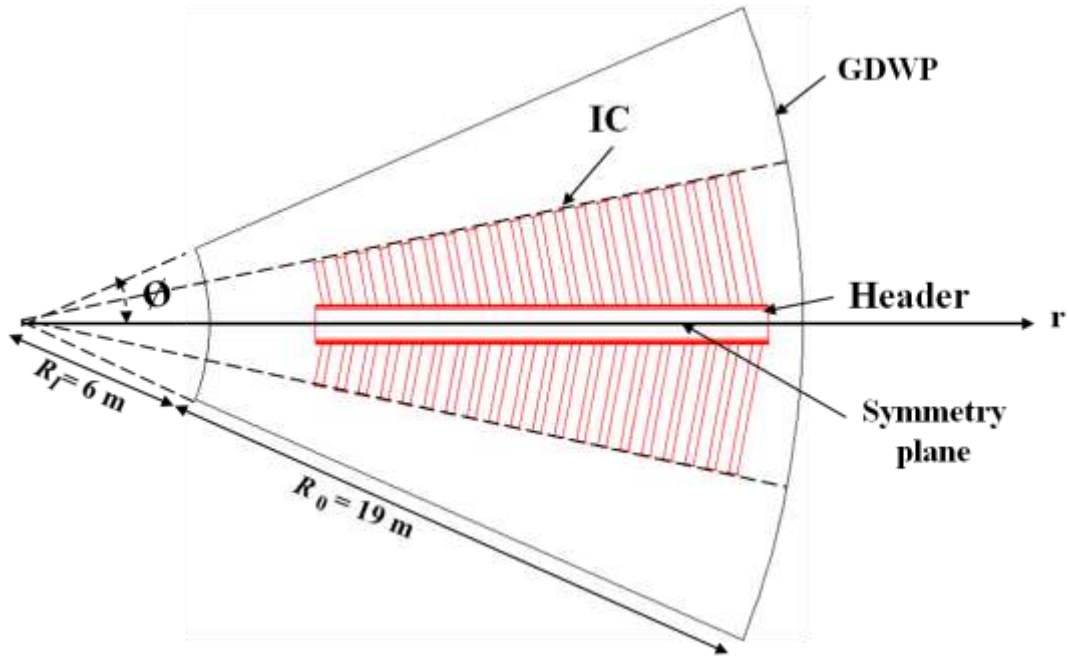
4.4.2 Natural convection and heat transfer for new design of IC for real size GDWP

This section deals with the extension of the knowledge gained from the pilot scale in section 4.4.1 to a real size GDWP ($\sim 10000\text{m}^3$) shown in Fig 4.13. The pilot scale studies in Section 4.4.1 indicated that heat transfer increases with increase in inclination angle (α). The heat transfer was found to be minimum at $\alpha = 0^\circ$ and maximum at $\alpha = 90^\circ$. The stratification number (S) was also found to be minimum at $\alpha = 90^\circ$. The horizontal ($\alpha = 90^\circ$) heat exchanger provides maximum heat transfer but suffers from the problem of condensation induced water hammer (Bae et al., 2012) depending upon the flow regime inside the condensation tubes. In order to prevent the occurrence of condensation induced water hammer and allowing the efficient drainage of the condensate water inside the tube, an optimum inclination angle of $\alpha = 75^\circ$ has been selected for the design of isolation condenser of real size GDWP.

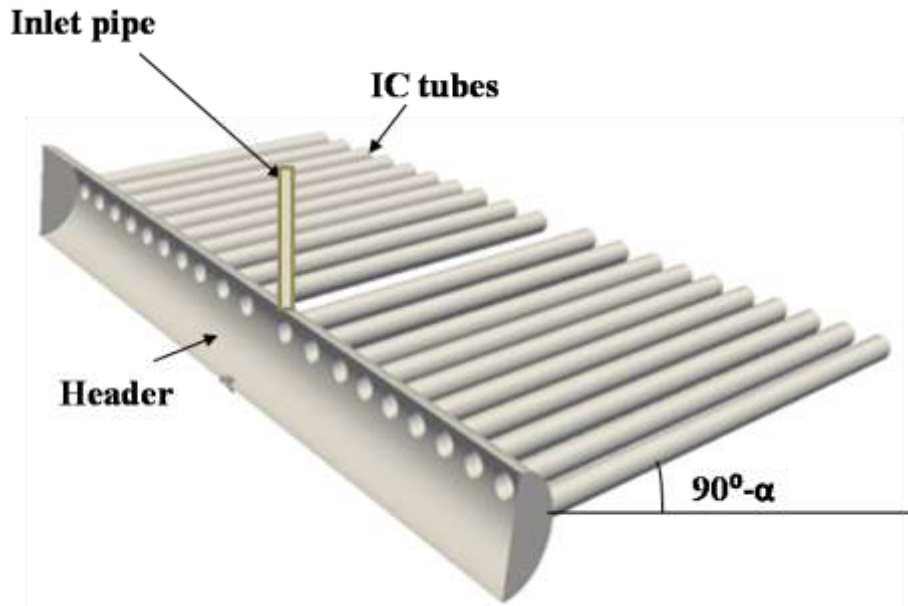
4.4.2.1 Geometry and Boundary conditions

The new design of IC for real size GDWP (Fig 4.13) consists of a cylindrical header ($D_h = 0.6\text{m}$) and a bundle of 40 inclined ($\alpha = 75^\circ$) tubes. The detailed dimensions of real size GDWP along with IC tubes are given in Table 4.1. The length of the IC tubes varies in radial direction (r) according to the availability of free water to provide uniform up and down flow throughout. The length of the shortest and longest tube was 1.33m and 4.03m respectively. The lengths of the two neighboring tubes differ by 0.14m. In the tangential direction (\emptyset), the tubes were located at $-11.25 \leq \emptyset \leq 11.25^\circ$. The IC tubes are submerged so that the centerline of the steam header was at 0.5m ($z = 0.5\text{m}$) from the GDWP tank bottom ($z = 0$). Fig 4.13A shows the $1/8^{\text{th}}$ sector ($-22.5 \leq \emptyset \leq 22.5^\circ$) of GDWP tank. The IC tubes are uniformly distributed inside GDWP to prevent non-uniform temperature distribution and hence thermal stratification. Due to the symmetry in tangential (\emptyset) direction, $1/16^{\text{th}}$ sector ($0 \leq \emptyset \leq 22.5^\circ$) of GDWP has been considered for simulations. The grid generation for real size GDWP is shown in Fig 4.14A. The non-uniform hexahedral grid consisting of dense meshing was employed in the cylindrical volume surrounding the IC tubes which was finer ($y^+ = 4$) close to the boundary

layer of the IC tube. 120 nodes assigned along the circumference of 0.2m IC tube. Away from this volume surrounding the IC tube (Fig 4.14B), a hexahedral mesh of uniform grid size (5mm) was employed. The details of the boundary conditions for the transient CFD simulations of $1/16^{\text{th}}$ sector of a real size GDWP ($\sim 10000\text{m}^3$) are given in Table 4.3.

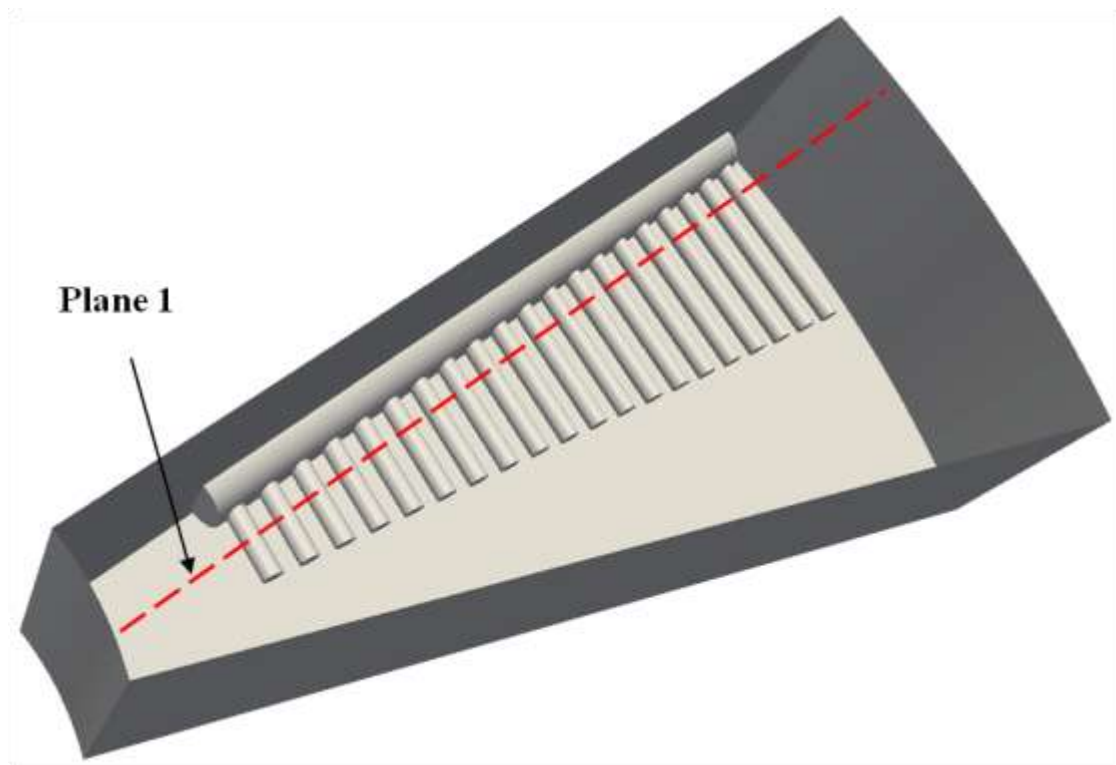


(A)



(B)

Fig 4.13: (A) Schematic of the (A) top view of large scale GDWP and (B) Isolation condenser with inclined ($\alpha = 75^\circ$) IC tubes



(A)



(B)

Fig 4.14: (A) Schematic of the (A) $1/16^{\text{th}}$ of real size GDWP with IC and (B) Grid generation along Plane 1

Table 4.3: Details of the boundary conditions for large scale GDWP:

Zone	Boundary Conditions	
	Temperature	Velocity
IC	$T=558\text{k}$	No slip $(u_r = u_\phi = u_z = 0)$
Header	$T=558\text{k}$	No slip $(u_r = u_\phi = u_z = 0)$
Top	Adiabatic $(\partial T / \partial z = 0)$	Free slip $\left(\frac{\partial u_r}{\partial z} = \frac{\partial u_\phi}{\partial z} = 0, u_z = 0 \right)$
Walls	Adiabatic $(\partial T / \partial r = 0)$	No slip $(u_r = u_\phi = u_z = 0)$
Symmetry	$(\partial T / \partial \phi = 0)$	$\frac{\partial u_r}{\partial \phi} = \frac{\partial u_\phi}{\partial \phi} = \frac{\partial u_z}{\partial \phi} = 0$

4.4.2.2 Laminar-turbulent natural convection and heat transfer

The azimuthal ($0^\circ \leq \theta \leq 180^\circ$) variation of temperature and turbulent kinetic energy at 2mm away from the IC tube are shown in Fig 4.15A and Fig 4.15B. The temperature of the fluid increases with increase in azimuthal angle ($30^\circ \leq \theta \leq 90^\circ$) due to continuous gain of enthalpy from the heated tube. The continuous increase in fluid temperature along azimuthal direction ($30^\circ \leq \theta \leq 90^\circ$) implied that the natural convection was 2D and laminar because the fluid velocities were present only in axial (z) and radial (r) direction. There was no flow in tangential (Φ) direction near the tubes. But a little bit downstream, the flow became unstable to 3D longitudinal vortices. The presence of these vortices results in generating flows along tangential (Φ) direction. Since, the total kinetic energy is conserved, an increase in the tangential velocity (u_ϕ) prevent the further increase in axial velocity (u_z). These vortices created a region of strong up-ward and down-ward flow near the IC tubes and disrupted the boundary layer near the tubes. Further, it resulted in an enhanced heat transfer and prevents the rise in fluid temperature as the flow travelled ($80^\circ \leq \theta \leq 110^\circ$) downstream. This change of a 2D laminar flow to a 3D laminar flow with longitudinal vortices is known as primary instability. This behavior is in accordance with the experimental observation of Biertümpfel and Beer (2003). As the fluid travels further downstream, the main flow separated from the tube due to adverse pressure gradient

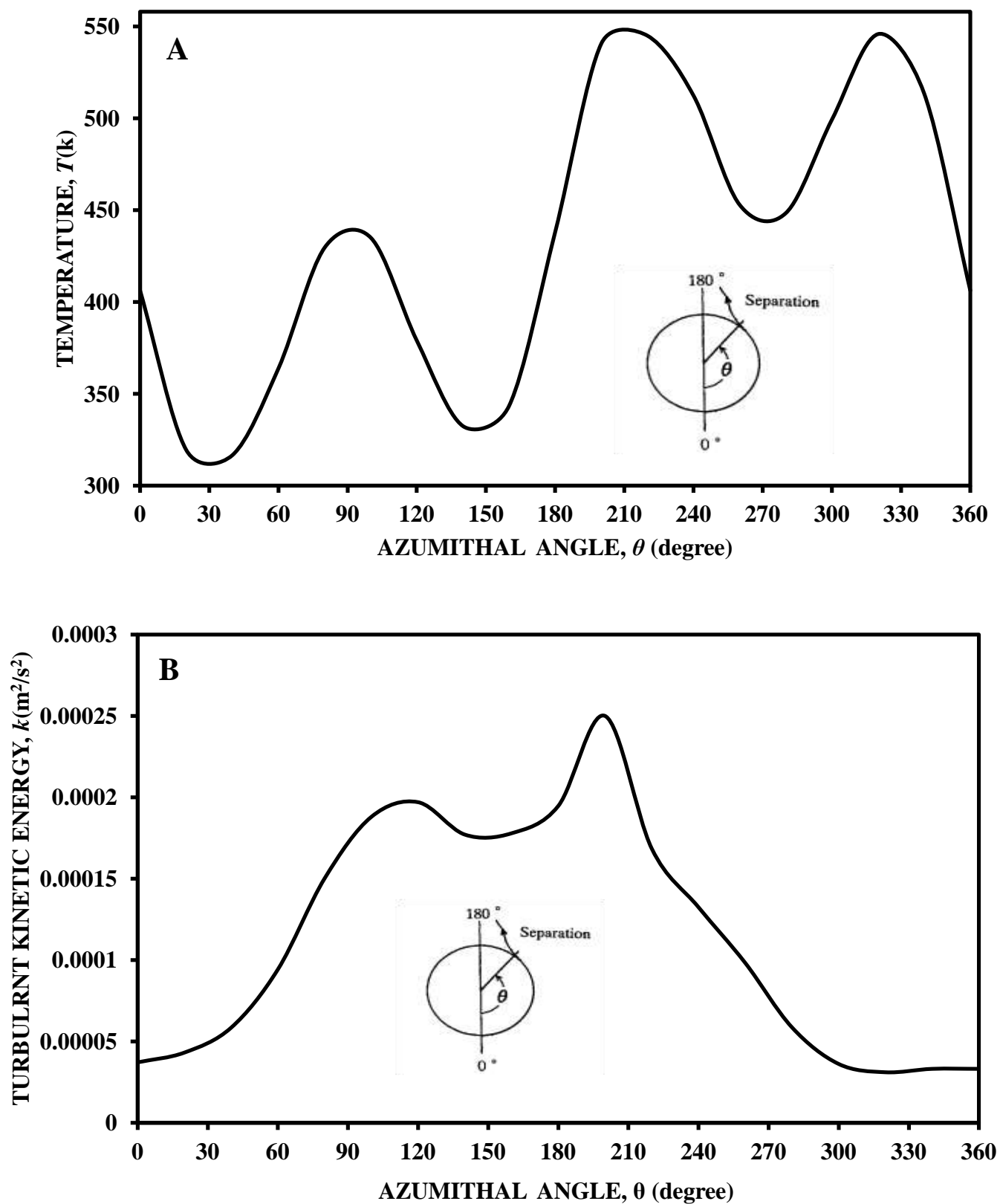
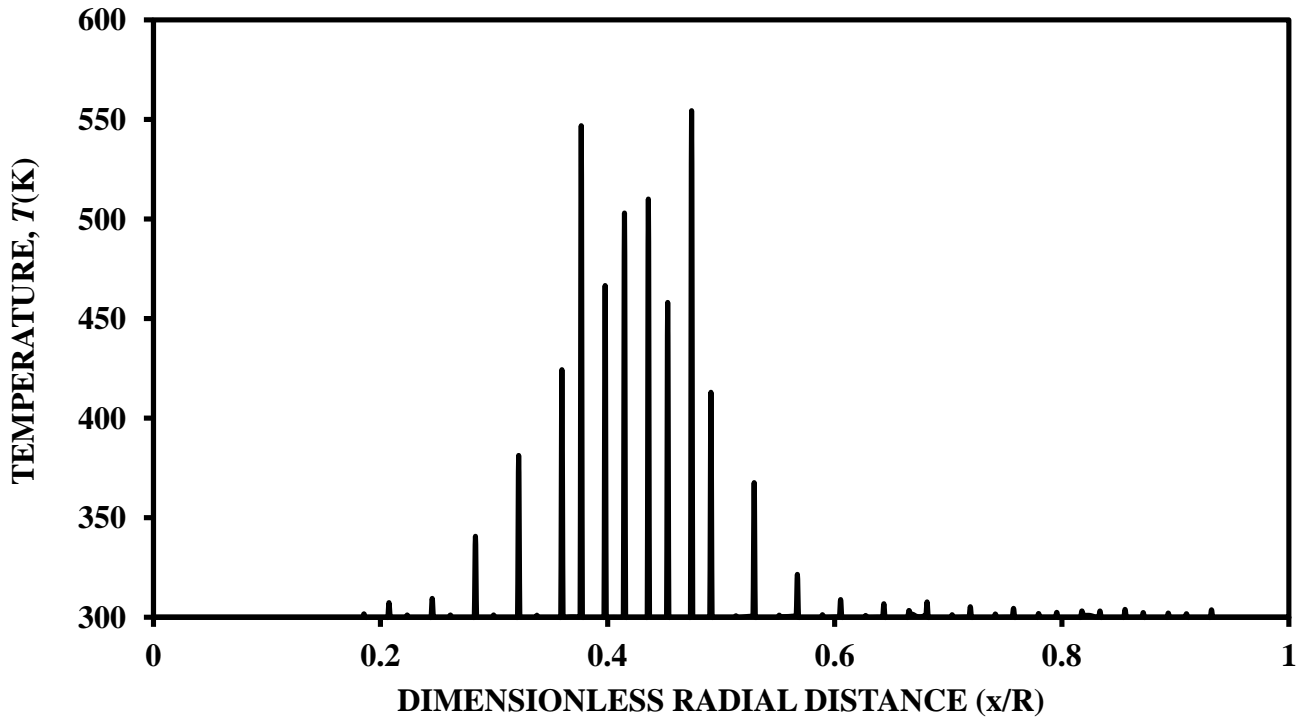
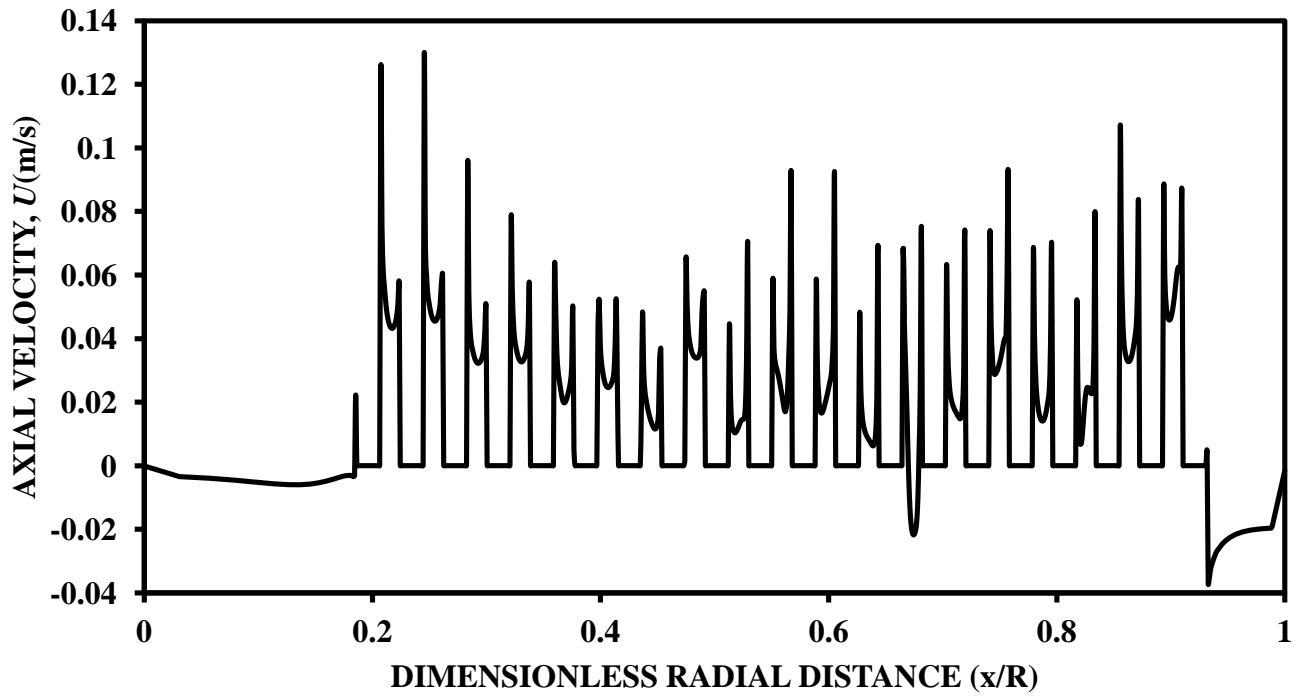


Fig 4.15: Azumithal variation of (A) Temperature and (B) Turbulent kinetic energy (k) for new design of IC at 2mm away from the IC tubes at $t = 90s$

near the tube periphery. Beyond the separation point, the 3D laminar vortices grew stronger and initiated a laminar-turbulent transition. In the transition region ($110^\circ \leq \theta \leq 145^\circ$), turbulent kinetic energy decreased because of an extra production term created by the longitudinal vortices (Shahinfar et al., 2012). The extra production term, namely the Reynolds stress $-\overline{u_\phi' u_z'}$ acted on $\partial U / \partial \Phi$, in addition to the wall-normal production term $-\overline{u_z' u_r'} \partial U / \partial z$. The extra production term turns out to be of negative sign and can together with the viscous dissipation, quench the wall normal production term and result in a decrease in the turbulent kinetic energy (k). In order to conserve the total kinetic energy ($K + k$), the mean flow increased which implied that the mean flow fed on the turbulence and extracted energy from the turbulent kinetic energy. As a result, the heat transfer was relatively high in the transition region ($110^\circ \leq \theta \leq 145^\circ$), which further resulted in lower fluid temperature (Fig 4.15A). As the fluid travels further downstream ($150^\circ \leq \theta \leq 210^\circ$), the inertia forces overcome the viscous forces and resulted in breakdown of vortices into turbulence. The enhanced turbulent kinetic energy shown in Fig 4.15B in the region ($180^\circ \leq \theta \leq 210^\circ$) confirmed the breakdown of the vortices into turbulence production. In the turbulent regime ($150^\circ \leq \theta \leq 210^\circ$), the heat transfer was decreased (Kitamura et al., 1999) which results in higher fluid temperature (Fig 4.15A). Fig 4.15A also shows that temperature distribution was not symmetric around the IC tubes. The fluid temperature was more on the right side ($180^\circ \leq \theta \leq 360^\circ$) of the tube as compared to the temperature on the left side ($0^\circ \leq \theta \leq 180^\circ$) of the tube. This is due to the availability of more water volume on the right side of the IC tube as compared to the left side which further resulted in enhanced heat transfer and lower fluid temperature. The radial distribution of temperature (Fig 4.16A) and axial velocity (Fig 4.16B) profiles further confirmed this behavior.



(A)



(B)

Fig 4.16: Radial distribution of (A) Temperature and (B) Axial velocity at $z/H=0.2$ along plane 1 at $t = 50s$ for New design of IC

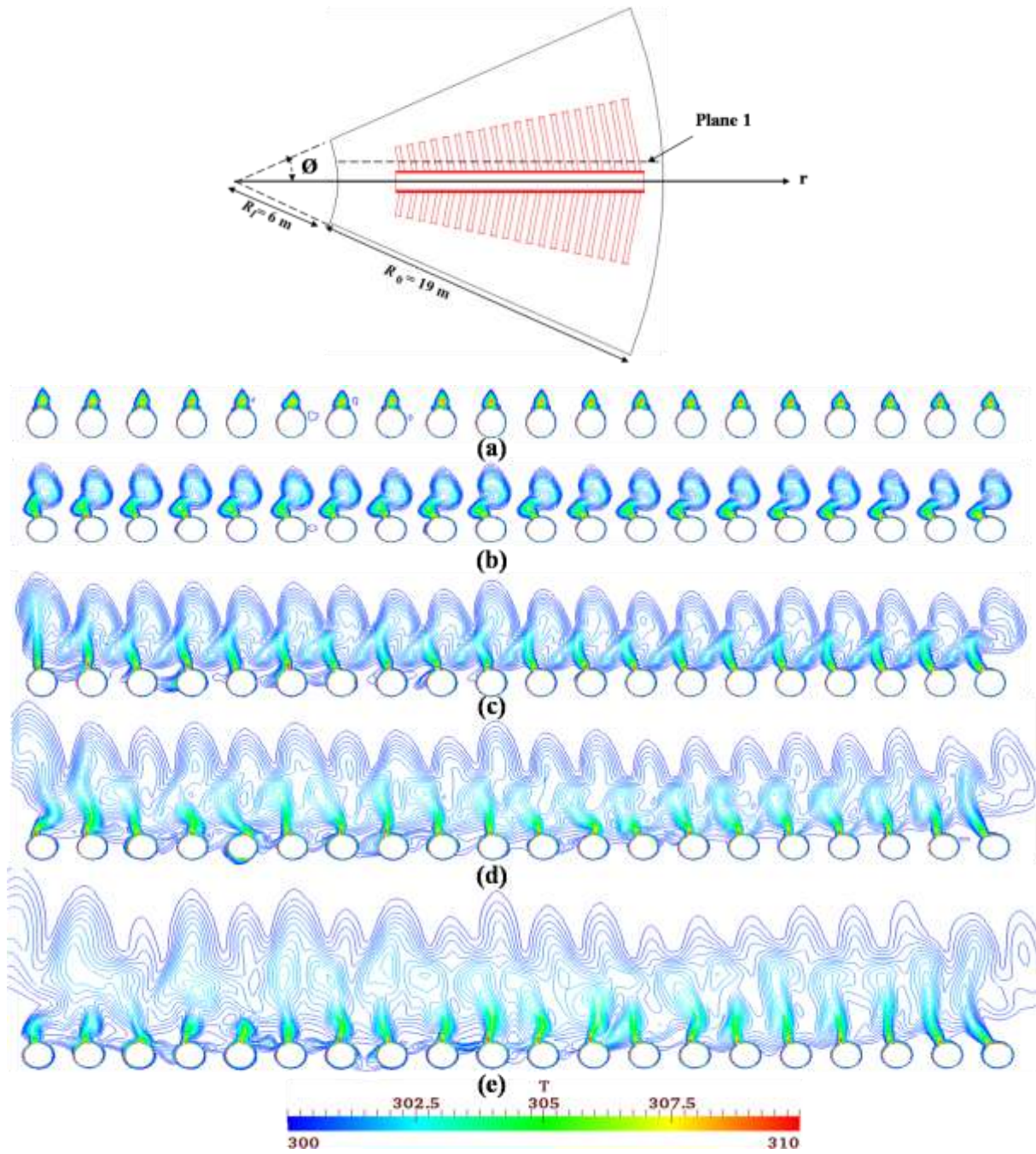


Fig 4.17: Transient variation of isotherms for new design of IC along Plane 1: (a) $t = 10\text{ s}$; (b) $t = 20\text{ s}$; (c) $t = 30\text{ s}$; (d) $t = 40\text{ s}$; (e) $t = 50\text{ s}$

4.4.2.3 Temperature Contours and Flow distribution

The isotherms and flow distribution in Fig 4.17 and Fig 4.18 shows the transient nature of flow along Plane 1 as fluid travels downstream in the vertical direction. The flow was 2D and laminar at beginning. But near the top of the tube, the flow became separated and resulted in relatively high

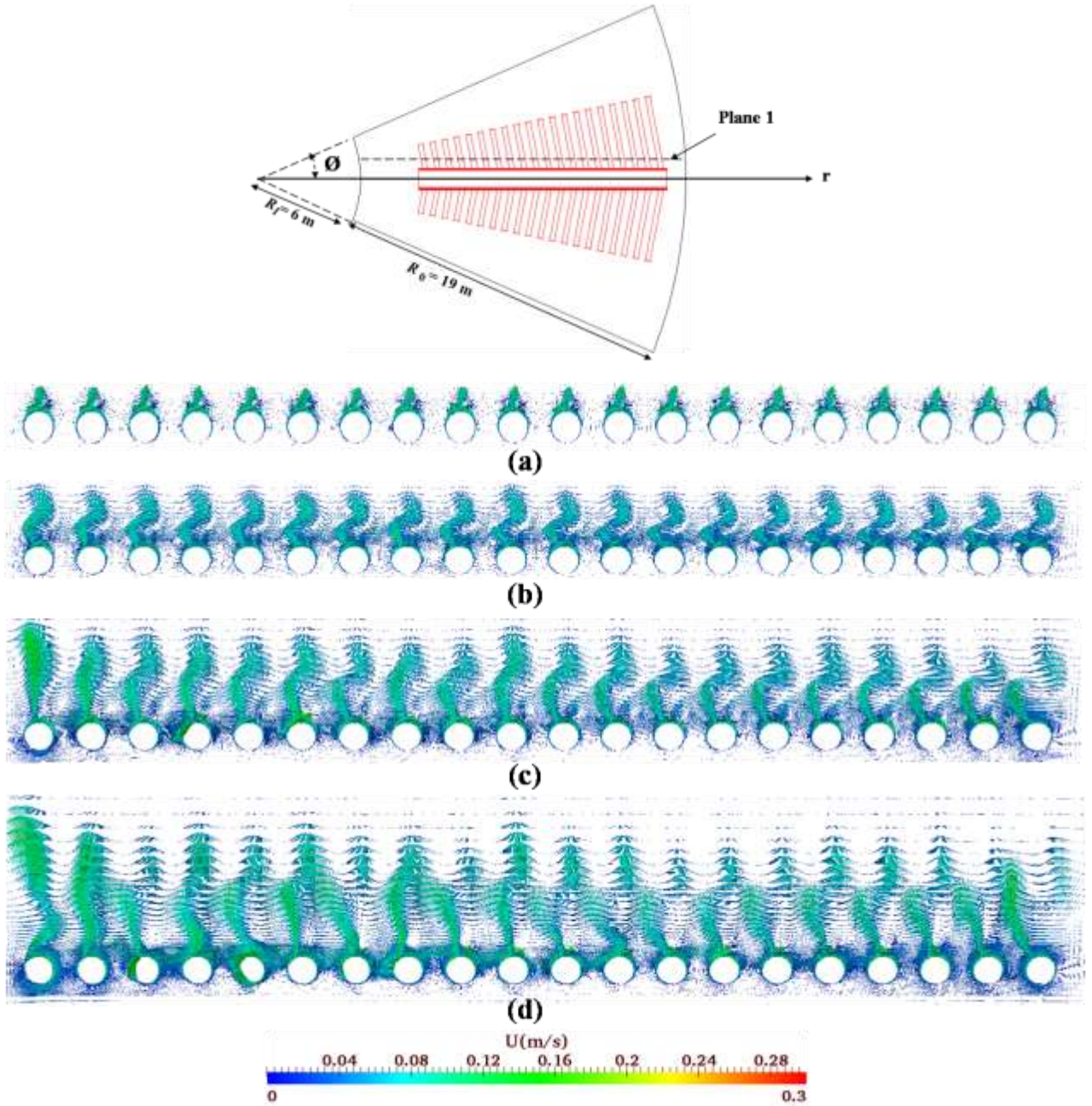
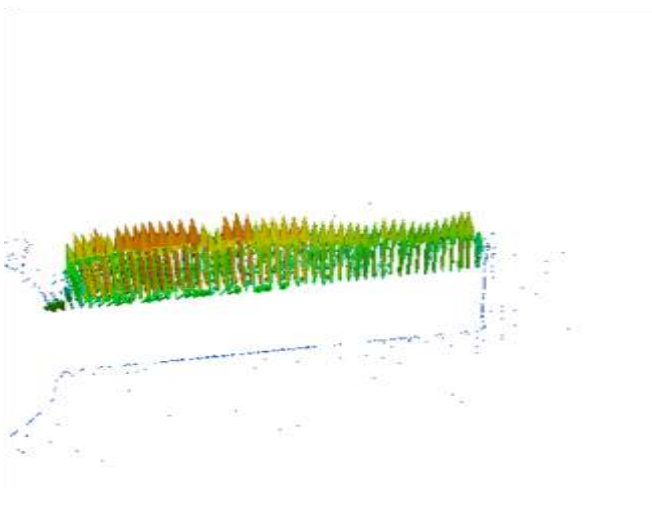
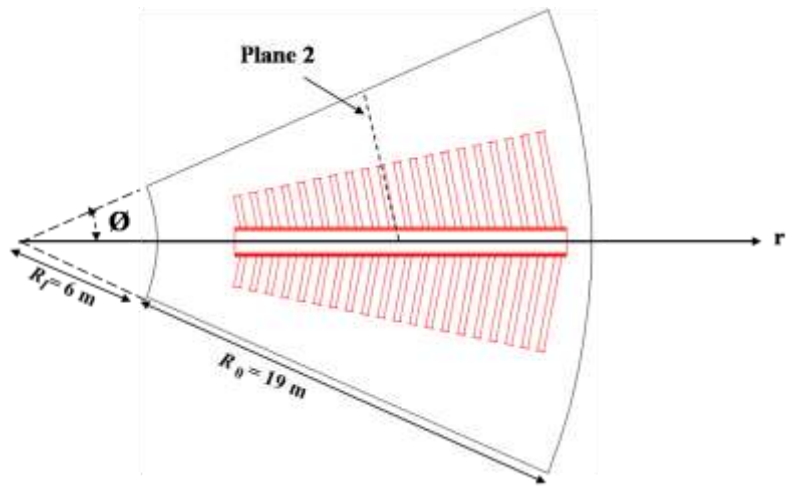
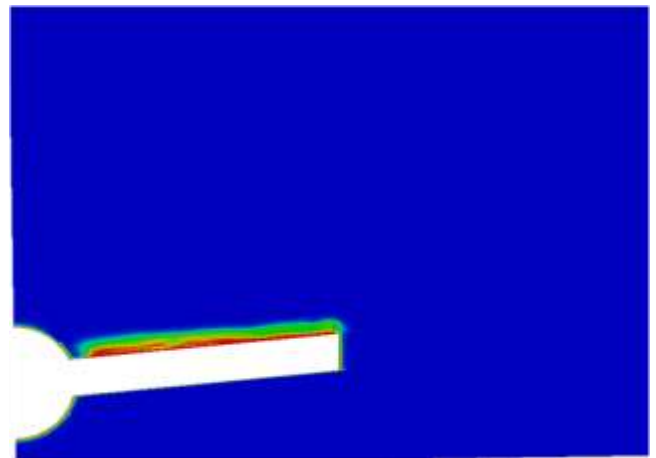


Fig 4.18: Transient variation of flow distribution for new design of IC along Plane 1: (a) $t = 10$ s; (b) $t = 20$ s; (c) $t = 30$ s; (d) $t = 40$ s; (e) $t = 50$ s

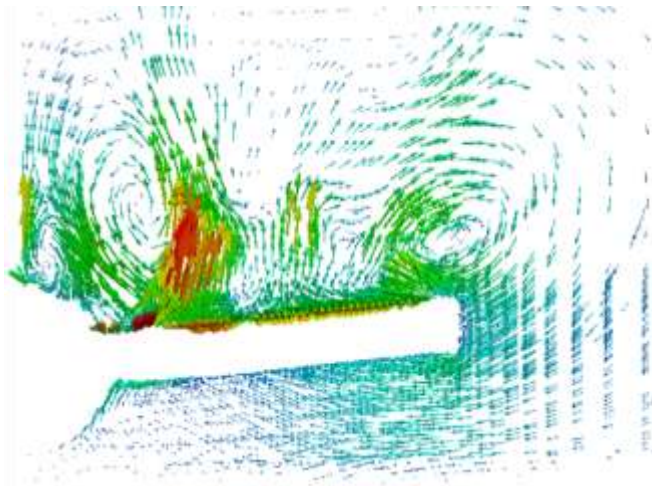
fluid temperature (Fig 4.17a). The buoyant plume from both sides of the tube come together and interacted with each other at some distance away from the top of the tube. The interaction resulted in large velocity fluctuations. Further, it resulted in enhanced turbulence production and formation of mushroom shape eddies (Fig 4.17b). The turbulent eddies resulted in enhanced mixing and lowering fluid temperature. As time evolved, the buoyant plume shifted left and right in a similar



$t = 20\text{ s}$

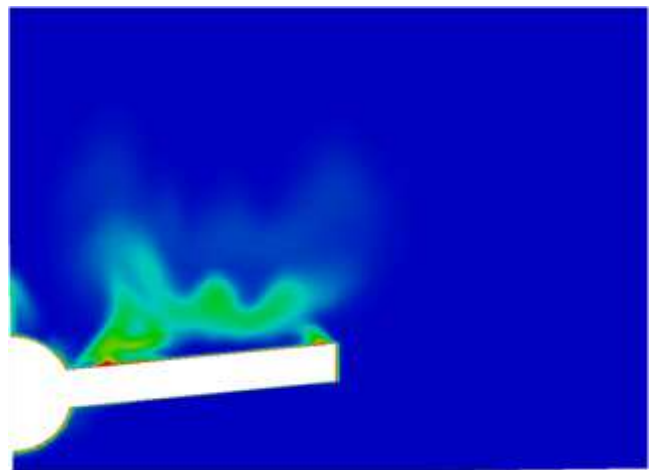


$t = 20\text{ s}$



$t = 100\text{ s}$

(A)



$t = 100\text{ s}$

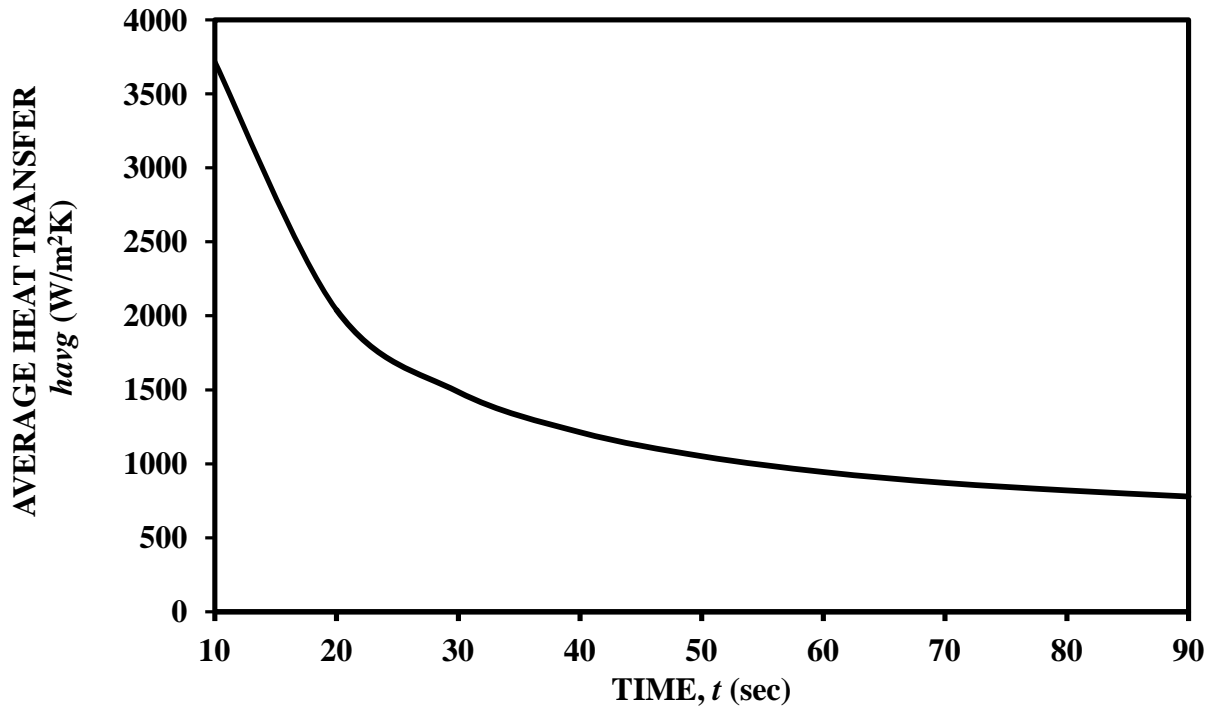
(B)

Fig 4.19: (A) Flow distribution and (B) Temperature Contours for new design of IC along Plane 2

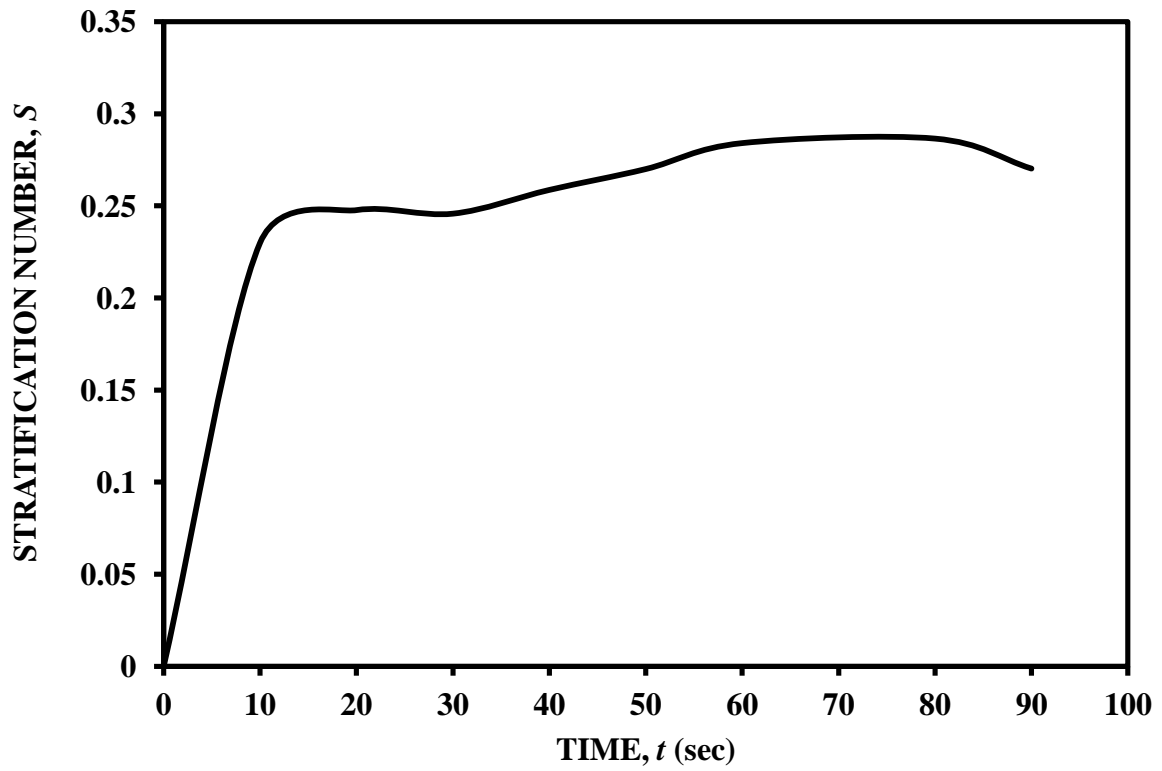
manner as for vortex shedding. For the initial period ($0 \leq t \leq 20\text{s}$), the tubes were not interacting with each other. As a result, distinguishable isotherms can be seen near the tubes. As time proceeded ($t > 20\text{s}$), the thermal boundary layer around the tubes started interaction with each other. Hence, the fluid flow and temperature distribution shows significant variation among all the tubes. Fluid flow was high near some of the tubes and results in enhanced heat transfer near those tubes. Further, it results in lower fluid temperature amongst those tubes. The radial distribution of temperature and axial velocity profiles for $t = 50\text{s}$ are shown in (Fig 4.16A) and (Fig 4.16B). The positive axial velocity near the tubes indicate the upward flow due to rise of hot fluid whereas the negative velocity near the tank wall indicate the downward flow to complete the material balance. As a result a natural circulation loop got formed. Fig 4.16A and Fig 4.16B also shows that the temperature and velocity are not symmetric for all the tubes. The large axial velocity was observed for the tubes closer to the tank wall. Further, it resulted in enhanced heat transfer and lower fluid temperature near those tubes. This can be attributed to the availability of free water near those tubes which prevent the rise of fluid temperature. As we proceed in the radial direction ($0 \leq r/R \leq 1$), the velocities increase initially for ($r/R < 0.25$) and then it decreases ($0.25 < r/R < 0.4$). After $r/R > 0.4$, velocity increases again for some distance and then again decreases. After $r/R > 0.6$, the velocities are almost uniform. The temperature distribution further confirms this behavior. The high temperature was present near the low velocity region and low temperature near high velocity region. The flow distribution and temperature contours in Fig 4.19 show the transient nature of flow along the tube length. As time evolved ($t > 20\text{s}$), the temperature distribution along the tube length became non-uniform due to formation of convective cells along the tube length.

4.4.2.4 Transient heat transfer and Thermal Stratification

The transient heat transfer behavior and thermal stratification are shown in Fig 4.20. The heat transfer rate (Fig 4.20A) was maximum at the beginning ($t = 0\text{s}$) because of large $\Delta T = 258\text{K}$ and then it reduced very sharply for few seconds. The entire transient ($0 < t < 90\text{s}$) heat transfer behavior has



(A)



(B)

Fig 4.20: Transient variation of (A) average heat transfer coefficient (h_{avg}) and (B) Stratification number (S) for real size of GDWP

been divided into two domains: conduction ($0 < t < 20\text{s}$) and convection period ($20\text{s} < t < 90\text{s}$). Initially ($t = 0\text{s}$), the fluid was at rest and hence the heat transfer occur mainly by conduction. The decay in HTC was very steep in the conduction period ($0 < t < 20\text{s}$). The thermal stratification (S) (Fig 4.20B) was also increased from the value $S = 0$ at $t = 0\text{ s}$ to $S = 0.25$ at $t = 20\text{ s}$ in the conduction period. As the time evolved the temperature of the fluid near the IC tubes increases which result into decrease in the temperature difference (driving force) between the IC tubes and nearby fluid. Further, it resulted into decrease in heat transfer. With time ($t > 20\text{s}$), the convective flow start to develop near the heated tube (IC) and heat transfer became increasingly dominated by convection. After ($t > 20\text{s}$) the convective flow near the IC becomes very intense (large velocity gradients) which perturbed the boundary layer and resulted into enhanced heat transfer. The intense convective flow lowers down the rate of increase in thermal stratification (Fig 4.20B). This period was known as convective period and characterized by intermittent disruption and growth of the boundary layer surrounding the IC tubes.

4.5 Closure

The effect of inclination of condenser tube on three dimensional temperature and flow fields was investigated inside a pilot scale (10 l) GDWP. Further, the knowledge of these fields was used for the quantification of heat transfer and thermal stratification phenomenon. Based on the above studies, a new design of IC has been proposed for real size GDWP ($\sim 10,000\text{ m}^3$).

The main conclusions that may be drawn from the present study are summarized as follows:

1. The increase in tube inclination angle (α w.r.t. to vertical) results in enhanced heat transfer.

The heat transfer was found to be maximum for $\alpha = 90^\circ$ and minimum for $\alpha = 15^\circ$. The enhanced transfer at $\alpha = 90^\circ$ ensures better thermal mixing and reduction in thermal stratification by 80% as compared to $\alpha = 0^\circ$. The thermal stratification was found to be 0.15 for $\alpha = 90^\circ$.

2. The effect of inclination of IC tube on the fluid flow and temperature distribution at the top and bottom of the IC tube has been studied. The temperature at the top ($\theta = 180^\circ$) increases and bottom ($\theta = 0^\circ$) decreases with an increase in inclination angle (α) due to reduced fluid sliding motion at the top and enhanced fluid sliding motion at the bottom of the tube.
3. The natural convection and heat transfer in the regime of laminar-turbulent transition has been studied in the presence of longitudinal vortices. The heat transfer enhances in the transition regime due to vortices and reduces in the turbulent regime due to decay of vortices.
4. The present work can be used as a numerical reference solution for understanding (1) the methodology of grid generation for different turbulence models (2) the performance of eddy viscosity and RSM turbulence models in predicting the near wall turbulence (3) the relationship between the flow patterns and heat transfer/thermal stratification.

CHAPTER 5

3D CFD Simulation to study pressure and flow distribution in isolation condenser

5.1 Introduction

The heat transfer through the condenser tubes depends on the steam distribution inside the tubes. The steam distribution in header and tubes assembly of steam condenser (IC) influence the overall performance of IC. The non-uniform steam distribution lowers the decay heat removal efficiency of the IC because some portion of the IC becomes ineffective. In addition to enhanced heat transfer, the uniform steam distribution also reduces the possibility of dead zones and hot spots inside the IC header. Hence, it is necessary to optimize the design of IC to ensure uniform steam distribution and hence uniform temperature distribution. In an IC header, the main fluid stream is decelerated due to the loss of fluid through the condenser tubes. Therefore, pressure will rise in the direction of flow. On the other hand, the friction effects cause a decrease of pressure in the flow direction. In this way, the friction and momentum effects work in opposite directions, the first tending to produce a pressure drop and the second a pressure rise. As a result it is not possible to keep the fluid pressure perfectly constant inside the IC header, and there is a non uniform steam distribution through the IC tubes. In order to attain a uniform flow rate through all channels (IC tubes), proper balance between friction and momentum effects need to be maintained throughout the header length of IC. Therefore, the effect of design parameters on the extent of non-uniformity (ENU) has been investigated over a wide range such as the tube pitch, tube diameter, inlet tube diameter, perforated plate inside header. The 3D CFD simulation has been performed using OpenFoam 2.2. The CFD is a detailed approach in which the 3D pressure and flow distribution can be predicted without the knowledge of flow coefficients, such as the friction and pressure recovery coefficients.

5.2 Numerical procedure

5.2.1 Flow geometry considered for present study

The conventional design of isolation condenser shown in Fig 5.1 consists of a inlet tube ($d_{in} = 0.14\text{m}$, $l_{in} = 0.5\text{m}$) placed at the centre of a cylindrical header or distributor manifold of dimensions ($D_h = 0.6\text{m}$, $L_h = 14.5\text{m}$). A bundle of 40 inclined ($\alpha = 75^\circ$) condenser tubes attached to the cylindrical header. The condenser tube (1st tube) near to the inlet tube is placed at 0.2m ($D_{ptl} = 0.2\text{m}$) away from the inlet tube. The distance (D_{pt}) between the condenser tubes is 0.244m . The length of the IC tubes varies in radial direction (r). Due to the symmetry, half of IC has been considered for simulations. The details of the boundary conditions for the single phase steady state CFD simulations are given in Table 5.1. In order to attain uniform steam distribution through the IC tubes, the effects of various design parameters such as 1st tube pitch ($0.1 < D_{ptl} < 2\text{m}$), inlet tube diameter ($0.15 < d_{in} < 0.25\text{m}$), header diameter ($0.5 < D_h < 0.8\text{m}$), number of tubes ($40 < n_t < 64$), mass flow rate ($0.05\text{-}5\text{kg/sec}$) and perforated baffle.

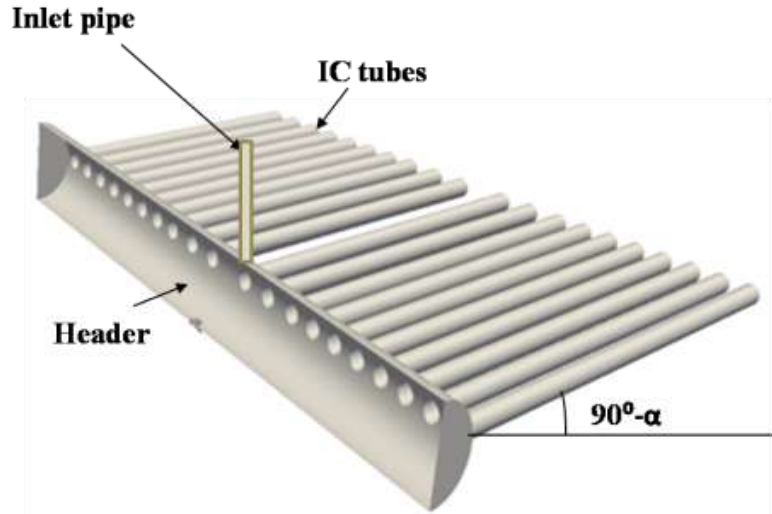


Fig 5.1: Schematic diagram of conventional design of IC

5.2.2 Governing equations

In order to model the steady state steam distribution in IC, the governing equations (continuity and momentum) with the appropriate Reynolds stress closure need to be solved with the boundary

conditions. The realizable $k - \varepsilon$ turbulence model has been used. The flow is considered to be turbulent on the basis of general criteria of Reynolds number ($Re > 2000$).

Table 5.1: Details of the boundary conditions for conventional design of IC:

Zone	Boundary Conditions	
	Pressure	Velocity
Inlet	Zero gradient ($\partial p / \partial z = 0$)	Uniform 5.14m/s
Outlet	Uniform 7MPa	Zero gradient ($\partial u / \partial z = 0$)
Walls	Zero gradient ($\partial p / \partial z = 0$)	No slip ($u_r = u_\phi = u_z = 0$)

5.2.3 Simulation details

In the present study, steam has been used as a working fluid. The mass flow rate has been varied in the range of kg/s, which results in variation in Reynolds number from. CFD simulations were carried out with following assumptions:

5.2.4 Model Assumptions

- (1). No phase change takes place inside the IC header as heat transfer aspects are not studied in the present work.
- (2). The density variation has been considered negligible and the flow is assumed to be incompressible
- (3). The steam is coming at a constant saturation temperature ($T_s = 558$ K) corresponding to the saturated steam pressure ($P_s = 7$ MPa).system under consideration is isothermal.

5.2.5 Method of solution

In the present work, at the inlet, uniform fluid velocity has been set as a boundary condition. The inlet steam velocity has been varied in the range of 0.5–5 m/s. At the outlet, an outflow condition has been set. At wall no slip boundary condition has been specified. The realizable $k - \varepsilon$ model has been used as a turbulence model. The governing equations have been solved for steady state conditions using simple-Foam solver of open source CFD code OpenFOAM-2.2. All the discretized equations were solved in a segregated manner with the SIMPLE (Semi Implicit

Pressure Linked Equation) algorithm. According to SIMPLE, the purpose of obtaining the pressure correction equations is twofold. First, pressures are to be corrected. Second, velocities are corrected through a linearized momentum equation so as to satisfy the continuity. The second-order upwind scheme has been used for discretization. The under relaxation parameters were set to 0.3 for pressure, 1 for density and body forces and 0.7 for the momentum terms. All the solutions were considered to be fully converged when the sum of residuals was below 1×10^{-5} .

The additional boundary conditions are as follows:

$$I_T = \text{turbulent intensity} = 5\%$$

$$k = \frac{3}{2} I_T^2 V_{avg}^2$$

$$V_{avg} = \frac{\dot{m}}{\rho A} = 5.14 \text{ m/sec}$$

$$Re = \frac{\rho D V}{\mu} = \frac{5.14 * 0.144}{5.2 \times 10^{-7}} = 1.42 \times 10^6$$

$$k = \frac{3}{2} (5.14)^2 (0.05^2) = 0.066$$

$$\varepsilon = C_u^{3/4} \frac{k^{3/2}}{l}$$

Where (according to Davis, 1972) l is in the range of 1/20 to 1/10 of pipe diameter (D_t)

$$\varepsilon = C_u^{3/4} \frac{k^{3/2}}{l(1/20D_t)} = \frac{(0.09)^{3/4} (0.066)^{3/2}}{0.3 * 0.144} = 0.39$$

5.3 Results and discussions

The objective of the present work is to optimize the design of isolation condenser to attain uniform steam distribution in condenser tubes. The pressure and flow distribution inside the isolation condenser have been investigated. In order to attain uniform steam distribution through the IC tubes, the effects of various design parameters such as tube pitch ($0.2 < D_{ptl} < 2m$), inlet tube diameter ($0.1 <$

$d_{in} < 0.3\text{m}$), header diameter ($0.5 < D_h < 0.8\text{m}$), number of tubes ($40 < n_t < 64$), mass flow rate (0.05-5kg/sec) and baffle plate. The flow maldistribution inside the individual condenser tube has been quantified using extent of non-uniformity (%ENU) defined as:

$$ENU_i = \frac{(\dot{m}_i - \dot{m}_{avg}) * 100}{\dot{m}_{avg}}$$

where, \dot{m}_i is the mass flow rate through individual tube, i stands for tube number and \dot{m}_{avg} is the average mass flow rate.

5.3.1 Conventional design of isolation condenser(IC)

The velocity vectors in Fig 5.2 shows a very serious flow maldistribution in Cross-section 1 located at the central axis and facing the inlet tube. Since, the superheated steam from the steam drum is at very high velocity, it flows parallel to the inlet tube and collide with the bottom walls of the header. In the region away from the inlet tube, a vortex is generated. A dead zone (Fig 5.2) is formed for the reverse flow, thus fluid is distributed very non-uniformly in axial (y) direction. The mass flow rate through the tube 1(near to inlet tube) is negligible and the ENU was around 400%. This behavior is due to the sudden enlargement of fluid boundary after it enters into the IC header. The main flow separates from the surface to form vortex. The vortex can result in the loss of mechanical energy by converting into thermal energy. The energy loss can be quantified in terms of energy dissipation rate (ϵ). The energy dissipation rate (ϵ) is very high inside the header near the inlet tube. The cross-section 2 (Fig 5.2) is deviated from the inlet tube and it is at the centre of the second tube. As the distance from the inlet tube increases, small vortex enlarges gradually into large-scale vortex. So it can be concluded that fluid of this portion in the header is mainly distributed by the diffusion of vortex. It is because that fluid flows to the two sides of the header by the transverse pressure gradient at the outlet cross-section. Minority of the fluid reaches IC tubes and goes through, while the majority impacts on the boundary walls of header and is blocked. The fluid separates from the surface to form vortex and diffuses all around. And as the distance from the inlet tube further increases, the vortex may vanish for the viscous dissipation with all around fluid. As the distance

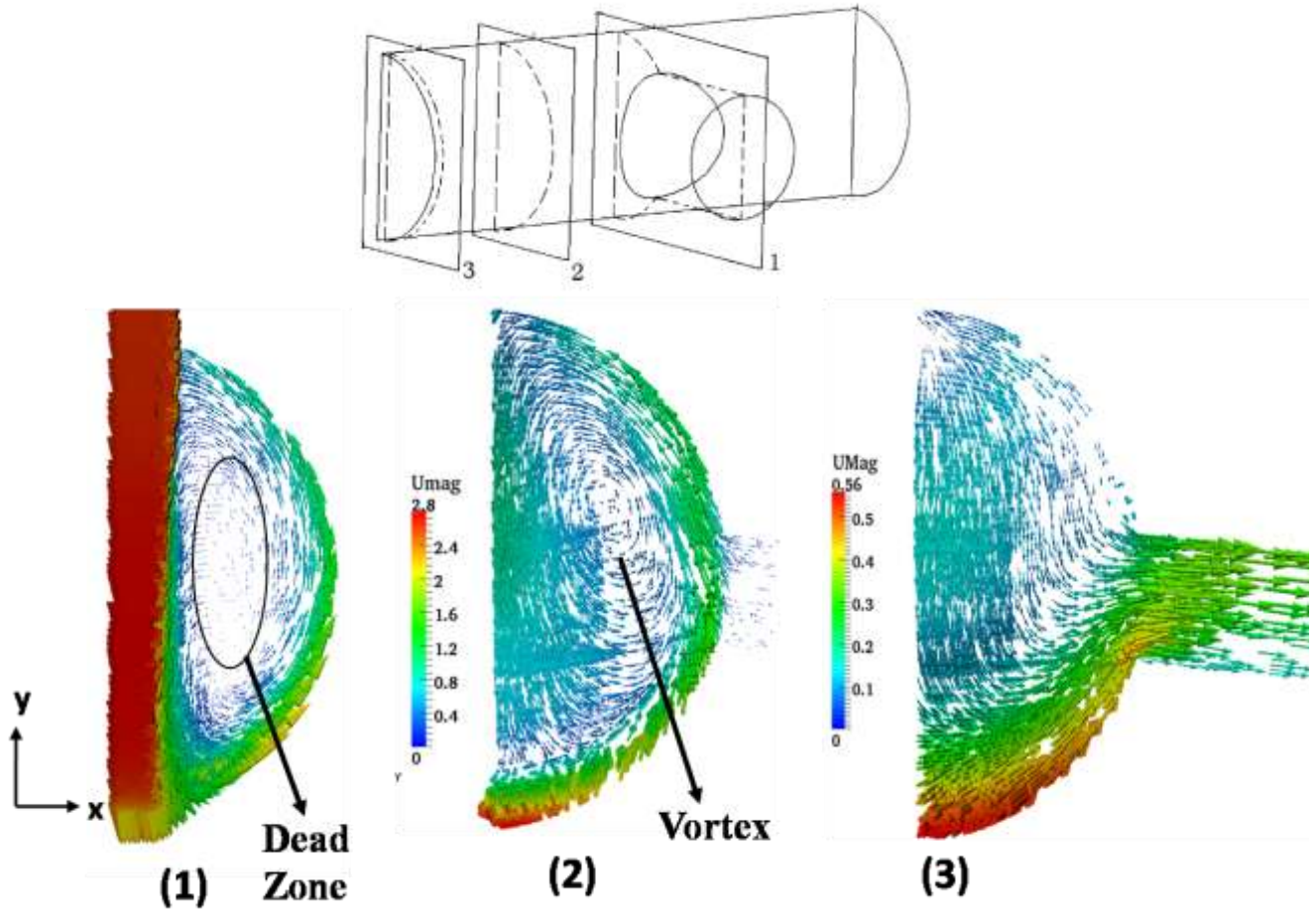


Fig 5.2: Flow distribution inside header for conventional IC at different cross sections

(A) $z = 0$ (at centre); (B) $z = 0.5\text{m}$; (C) $z = 2.5\text{m}$.

from the inlet tube increases, the energy dissipation rate (ϵ) keeps on decreases till it reaches a constant value. The cross-section 3 (Fig 5.2) is near the boundary of the header and is the farthest away from the inlet tube. The majority of fluid has been branched off before it reaches this section and fluid kinetic energy is consumed by vortex, which results in the decrease of fluid velocity. And for the viscous dissipation between the fluid and the boundary, vortex vanishes and the streamlines are parallel to the IC tube. Based on the above investigations, it can be concluded that it is mainly the fluid vortex and transverse pressure gradient that result in the fluid distribution in the IC header and tubes assembly. Besides the fluid distributed non uniformly, the energy loss caused by the vortex is high. So the design of isolation condenser should be improved to achieve uniform steam distribution through the IC tubes.

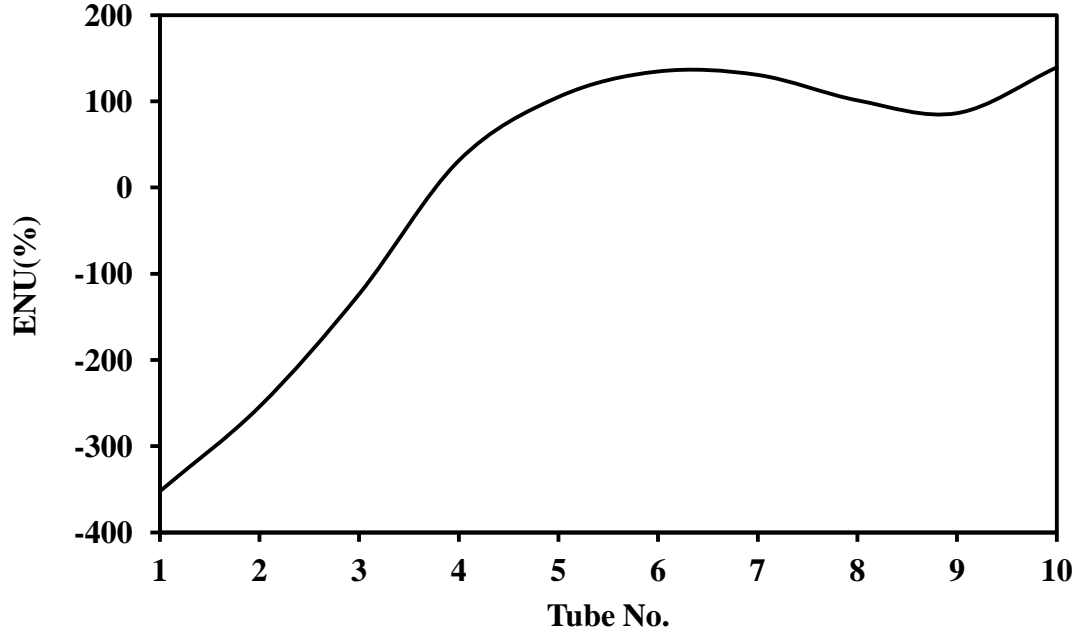


Fig 5.3: Extent of non-uniformity for conventional header

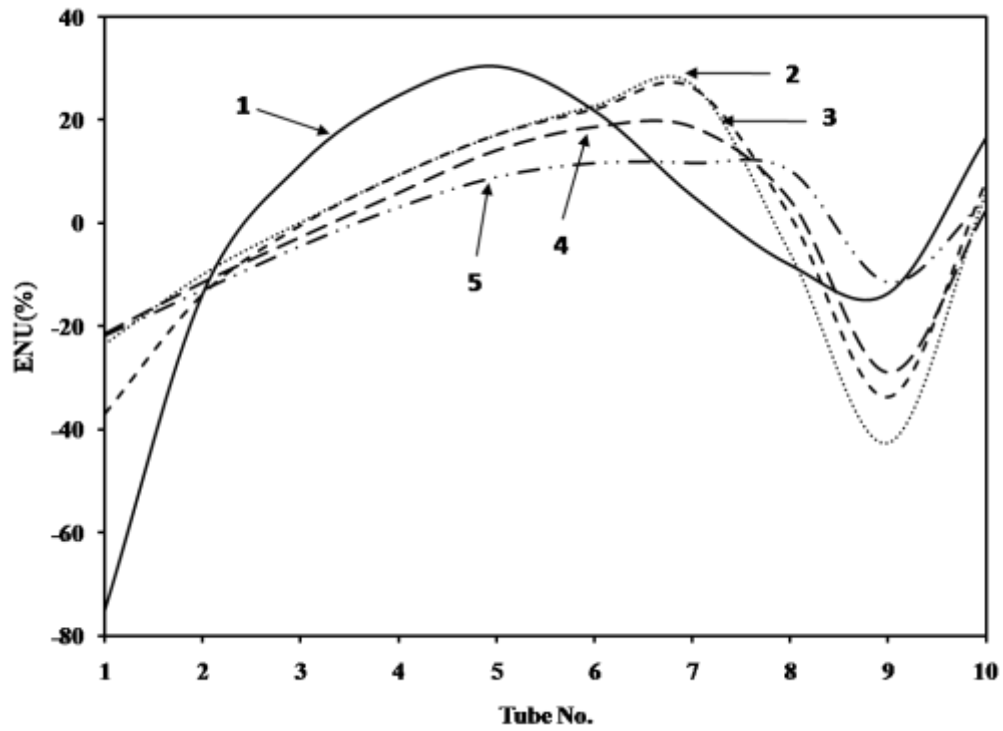


Fig 5.4: Effect of 1st tube pitch (D_{pt1}) on extent of non-uniformity (ENU): (1) $D_{pt1} = 1\text{m}$; (2) $D_{pt1} = 1.3\text{m}$; (3) $D_{pt1} = 1.5\text{m}$; (4) $D_{pt1} = 1.7\text{m}$; (5) $D_{pt1} = 2\text{m}$

5.3.2 Effect of tube pitch

In order to uniformly distribute the fluid flow and minimize the energy loss due to dissipation, the tube 1 is shifted away from the inlet tube. Fig 5.4 shows that ENU decrease with increase in the

distance between the inlet tube and tube1. Five cases were considered by varying the distance ($0.2 < D_{pt1} < 2m$) between the tube1 and inlet tube. The fluid flow through the tube1 was found to be very minimum in all the cases. The ENU was found to be maximum (80%) for tube 1 when it was placed at 1m away from the inlet tube. This behavior is attributed to the vortex formation inside the header. As the tube1 is shifted away ($D_{pt1} > 1m$) from the inlet tube, the vortex may vanish before it reaches the tube 1. Further, it results in increase in fluid flow and decrease in ENU. The overall ENU was found to be minimum for $D_{pt1} = 2m$.

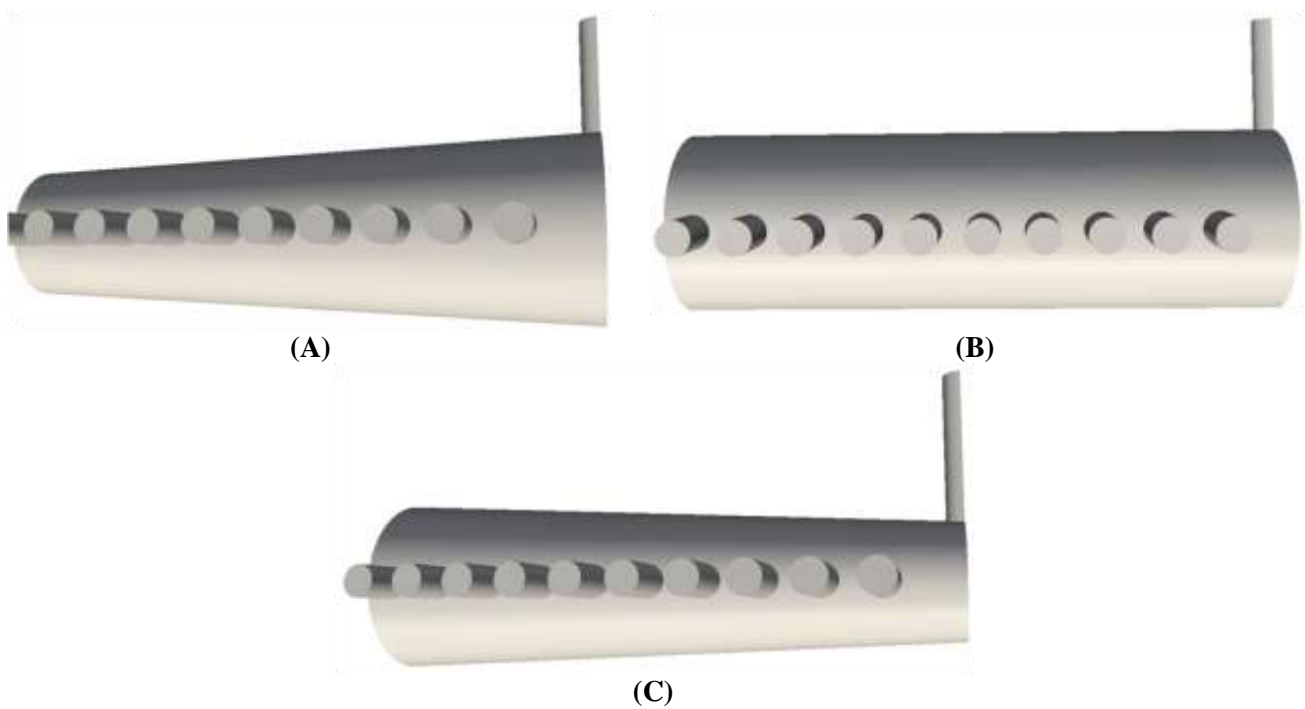


Fig 5.5: Schematic diagram of (A) Converging header (B) Cylindrical header
(C) Diverging header

5.3.3 Effect of header shape

The effect of tube pitch in Section 5.3.2 shows that a large header length is required in order to obtain uniform flow distribution in an IC. It is exactly the opposite of what one needs to do to optimize any heat exchanger. Furthermore, the flow rates concentrate more in the tubes (tube 5 to tube 7) midway between the inlet tube and header wall. Since the flow distribution in the IC is strongly affected by the vortex formation and pressure distribution inside the header, it was speculated that a more desirable flow distribution could be obtained by the modification of the

header shape. Hence, the present section focused on the effect of header shape to obtain a uniform fluid distribution without increase in header length. Three different header designs shown in Fig 5.5 were chosen; (A) Converging header (B) Cylindrical header (C) Diverging header. Fig 5.6A and 5.6B shows the fluid flow and pressure distribution for three different header shapes. The results shown in Fig 5.6A demonstrate that the flow distribution in an IC highly depends on the header shape. Among the three headers, the converging header produces the most uniform flow distribution. The ENU was very high for cylindrical (ENU = -350%) and diverging header (ENU = -250%). It was found that no flow occurs through the tubes (tube 1 to 3) near the inlet tube and majority of the fluid flow occurs through the tube 5 to 10. This behavior is due to the vortex formation inside the header and the dominance of inertia effect. This phenomenon is significantly reduced in converging header which results into more uniform fluid distribution and reduction in ENU. The maximum ENU was found to be -110% for converging header in comparison to cylindrical and converging header (H1) where maximum ENU was -350% and -250% respectively.

The flow distribution in an IC is a direct consequence of the pressure difference between the header and the outlet of condenser tubes. Fig 5.6B shows the axial pressure distribution inside the header (near the inlet of condenser tubes) and the outlet of condenser tube for the three different designs of header shape. The pressure distribution was found to be uniform in converging header as compared to other header designs. The pressure distribution inside the header is controlled by two opposing factors: friction which decrease the pressure and momentum loss which results in pressure raise. In the region ($0 \geq z/L \geq 0.3$) near the inlet tube, the friction effect dominates which results in decrease in pressure. On the other hand, in the region ($0.3 \geq z/L \geq 1$) away from the inlet tube, the pressure recovery due to momentum loss was very high. The pressure recovery in the region ($0.3 \geq z/L \geq 1$) was found to be minimum for converging header and hence prevent the excessive fluid flow through the condenser tubes (tube 5 to 10) in this region.

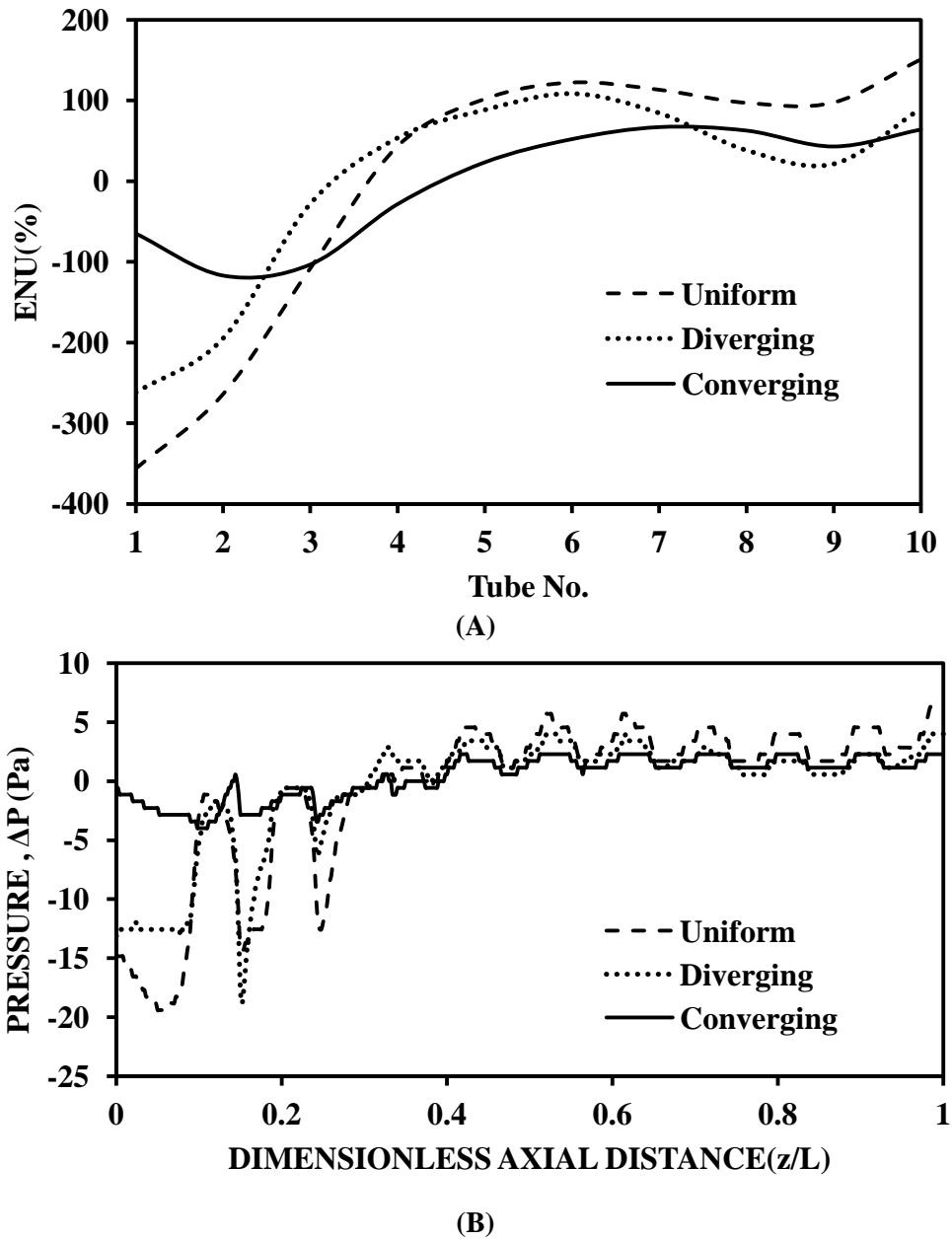


Fig 5.6: Effect of header shape on (A) Extent of non-uniformity (ENU) and (B) Pressure distribution

(1) Converging header (2) Cylindrical header (3) Diverging header

5.3.4 Effect of inlet tube diameter

The effect of inlet tube diameter on fluid flow and pressure distribution has been shown in Fig 5.7A,B. The increase in inlet tube diameter from 0.072m to 0.1m results in increase in the pressure recovery as compared to friction losses as shown in Fig 5.7B. The increase in pressure recovery results in more uniform fluid distribution and reduction in extent of non-uniformity. The increase in

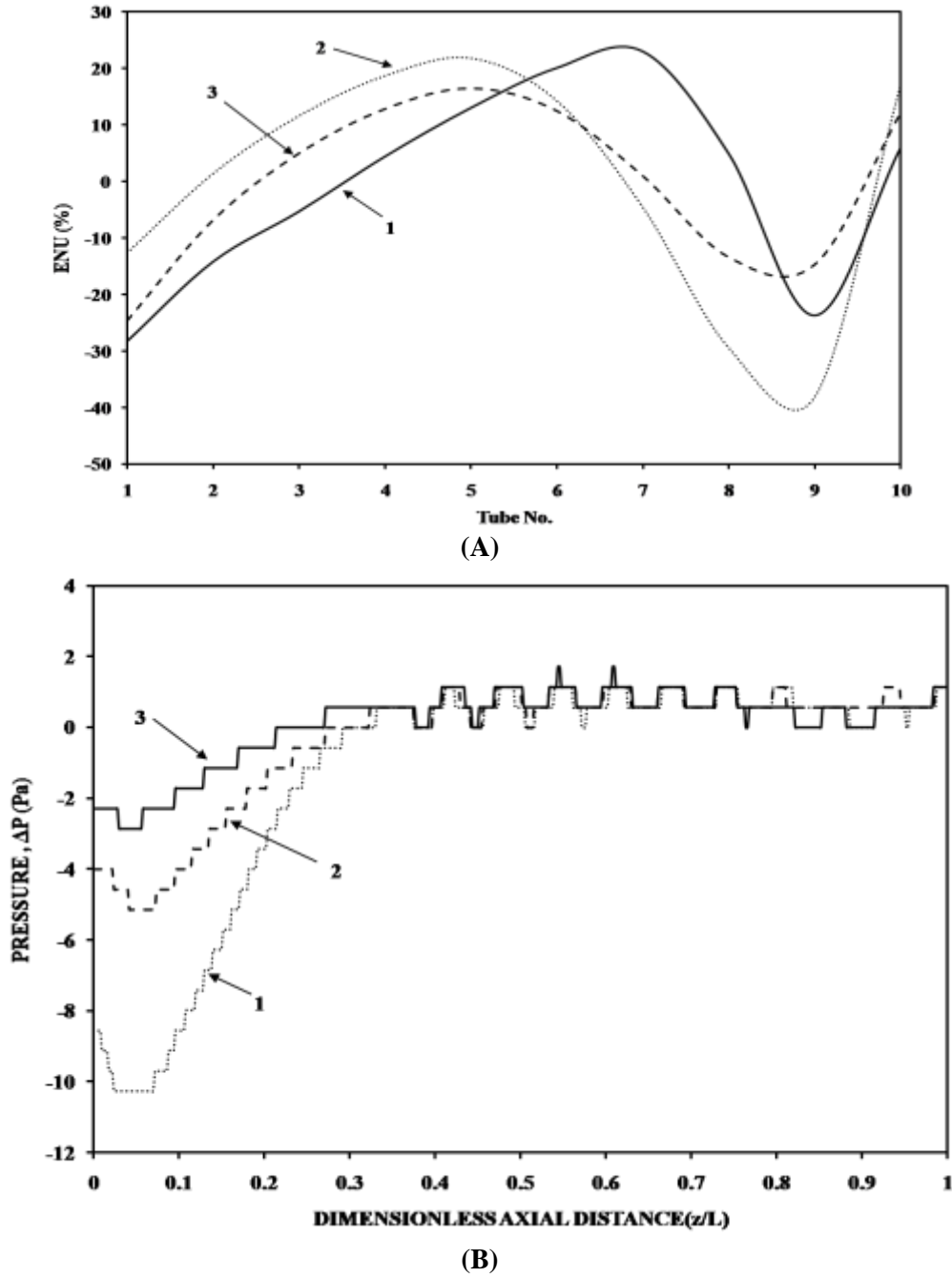


Fig 5.7: Effect of inlet tube diameter (d_{in}) on (A) Extent of non-uniformity (ENU) and (B) Pressure distribution; (1) $d_{in}=0.15\text{m}$; (2) $d_{in}=0.2\text{m}$; (3) $d_{in}=0.25\text{m}$;

inlet tube diameter from 0.072m to 0.1m results in increase in mass flow through the tube 1 -5 by 10% whereas the mass flow through the tubes 6-9 decreases by 25%. In order to increase the mass flow through the tube 7-9, tube diameter was increased from 0.1m to 0.125m. The increase in tube diameter from 0.1m to 0.125m results in increase in mass flow by 25% through the tubes 7-9. Further, it results in reduction in extent of non-uniformity.

5.3.5 Effect of number of tubes

The effect of increase in number of tubes from 40 to 64 for two different tube pitches are shown in Fig 5.8. The header length increases to accommodate more number of tubes which results in increase in friction pressure drop. The mass flow rate through the condenser tubes decreases with increase in number of tubes. The increase in number of tubes from 40 to 52 results in reduction in mass flow rate reduced by 24%. The mass flow rate reduced by 38% when the number of tubes was increased from 40 to 60. The extent of non uniformity increases with increase in number of tubes. The maximum ENU was increased from -94% to -140% for increase in number of tubes from 40 to 52. The ENU increased further to -170% for 60 tubes. The extent of non uniformity decreases with increase in the 1st tube pitch ($D_{pt1}=2m$) from 1m to 2m.

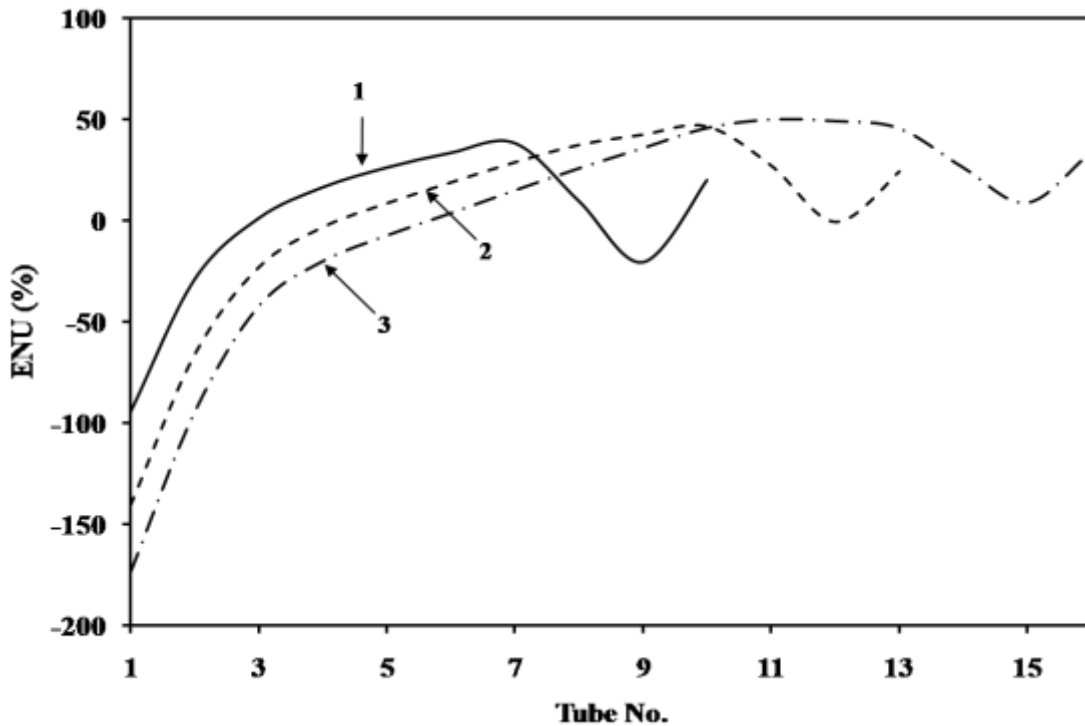


Fig 5.8: Effect of number of tubes on Extent of non-uniformity (ENU); (1) 40 tubes; (2) 54 tubes; (3) 60 tubes;

5.3.6 Effect of header diameter

The effect of header diameter on fluid flow and pressure distribution was investigated for three different header diameters in the range ($0.5 < D_h < 0.8m$). The increase in header diameter results in decrease in pressure drop and increase in momentum recovery as shown in Fig 5.9B. As a result, the mass flow rate

through the tubes 1-2 increases with increase in header diameter. For header diameter (D_h) 0.6m, the mass flow rate through the tube 1 and 2 increased by 180% and 58% respectively in comparison to a header of diameter 0.5m. The increase in header diameter from 0.5m to 0.6m results in decrease in ENU from -190% to -28% for tube 1 as shown in Fig 5.9A. When the header diameter (D_h) increased to 0.8m, the mass flow rate through the tube 1 and 2 increased by 230% and 90% respectively. The ENU decreases from -190% to 15%. The overall result of the increase in header diameter is increase in mass flow rate through the tubes and decrease in ENU.

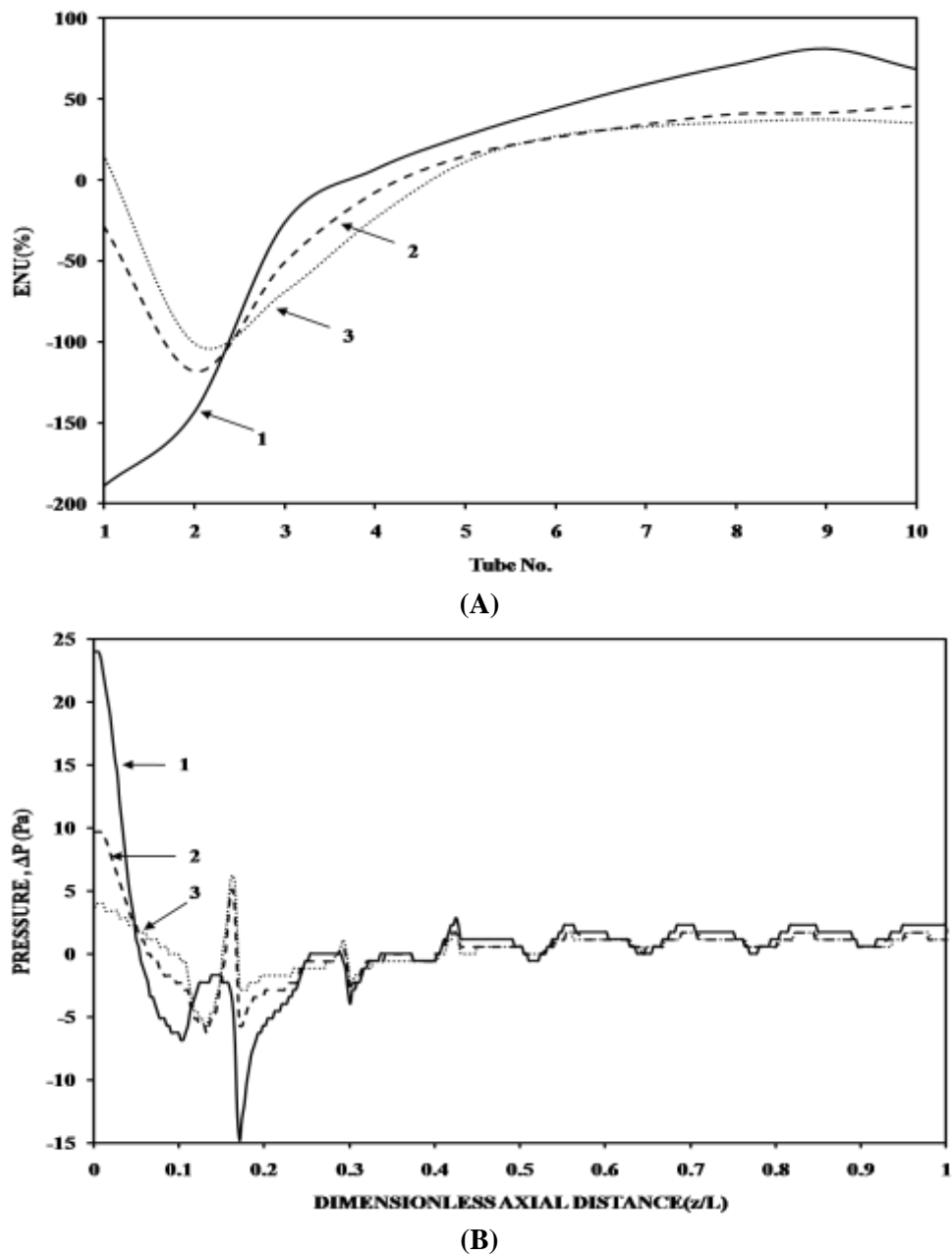


Fig 5.9: Effect of header diameter (d_h) on (A) Extent of non-uniformity (ENU) and (B) Pressure distribution;
(1) $d_h = 0.4\text{m}$; (2) $d_h = 0.6\text{m}$; (3) $d_h = 0.8\text{m}$;

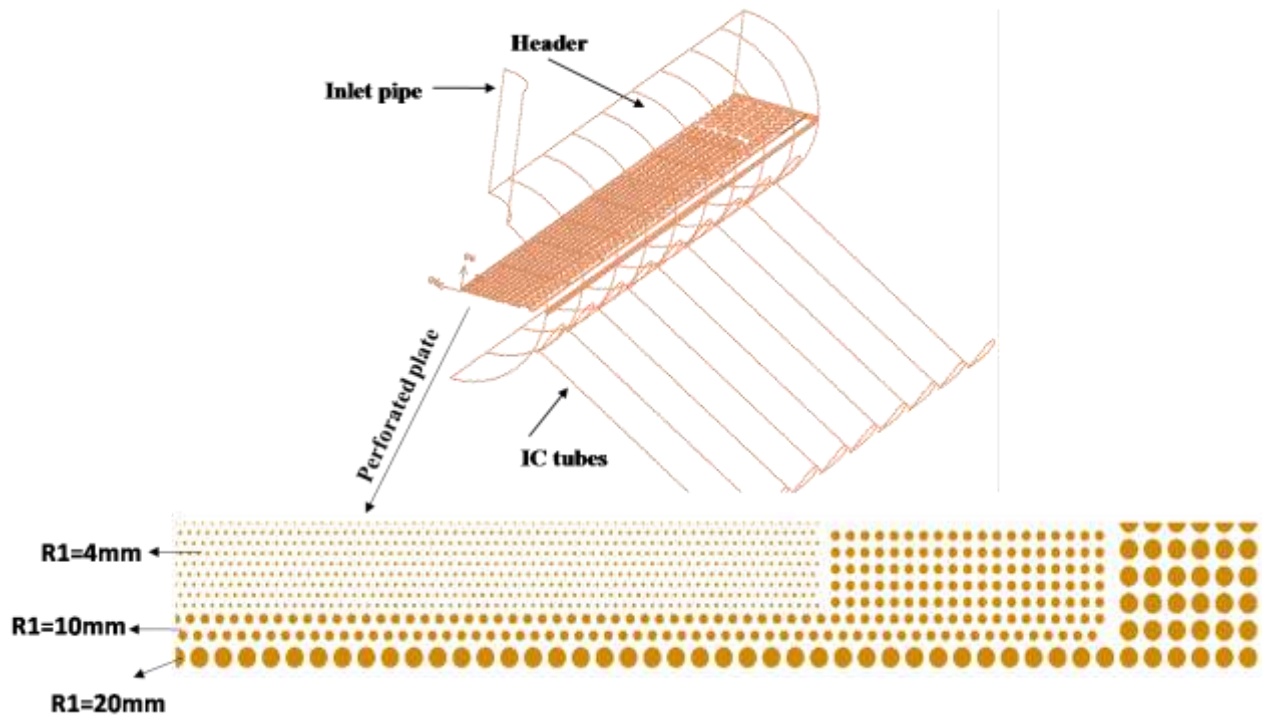


Fig 5.10: Schematic diagram of IC along with perforated baffle inside the header

5.3.7 Effect of perforated baffle

The Section 5.3.1 clearly indicates that it is mainly the vortex formation and the pressure distribution that results in non uniform flow distribution in the conventional design of header. The maximum ENU was found to be -350% for conventional header design. So, the header configuration should be improved to make the fluid distributed more uniformly. It was thought desirable to incorporate perforated baffle inside the header to reduce the (1) vortex formation and (2) to prevent non uniform flow distribution (3) to reduce energy dissipation and formation of hot spots. The perforated baffle shown in Fig 5.10 have the dimension of 12 x 2 x 0.5 m (length x width x height), on which three different kinds of holes of small ($r = 4\text{mm}$), medium ($r = 10\text{mm}$) and large ($r = 20\text{mm}$) were spotted symmetrically. The holes are distributed inside the header according to the velocity distribution inside the conventional header. The small holes are spotted at the centre and the punched ratio is gradually increasing in symmetry from the central axis to the header walls.

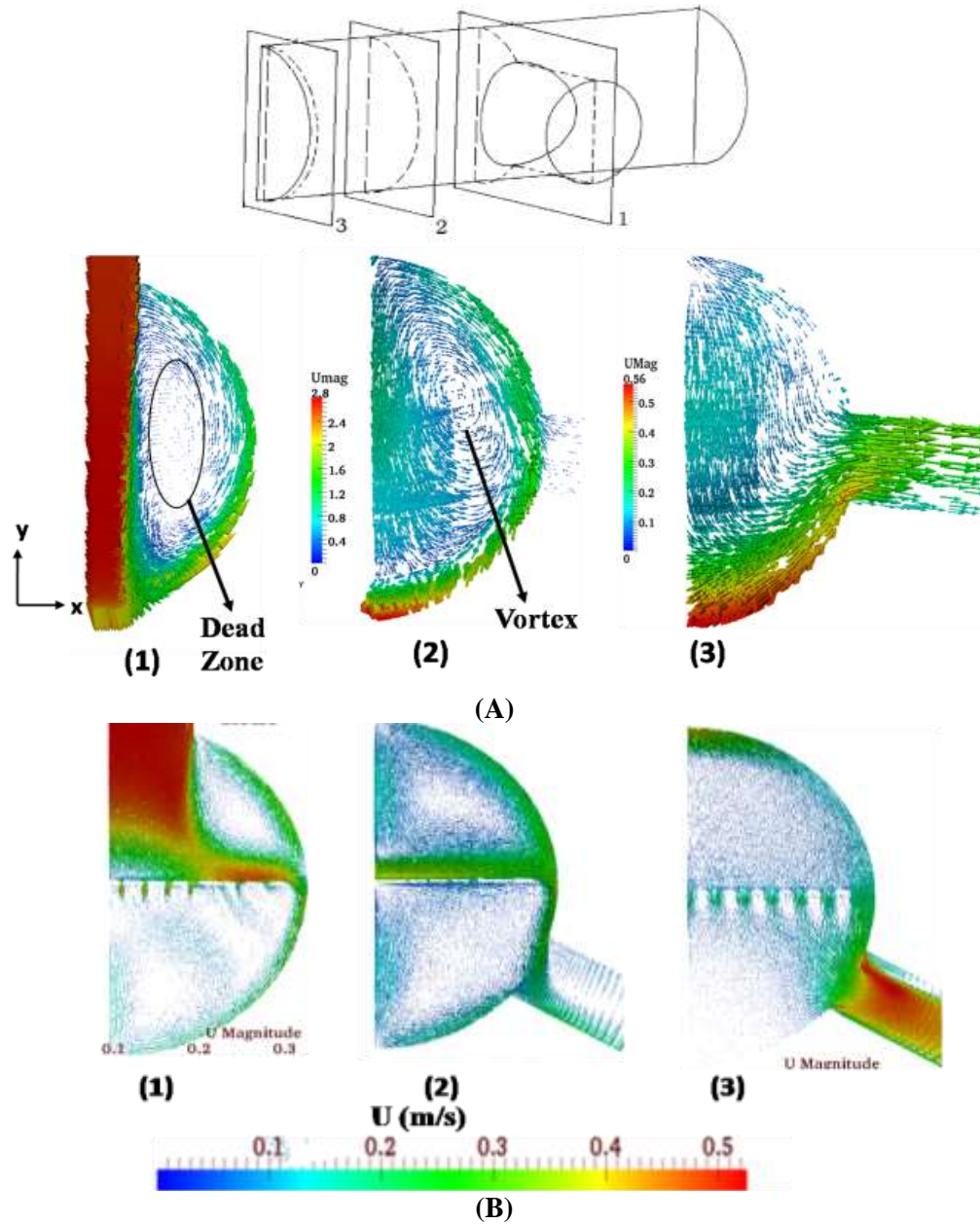
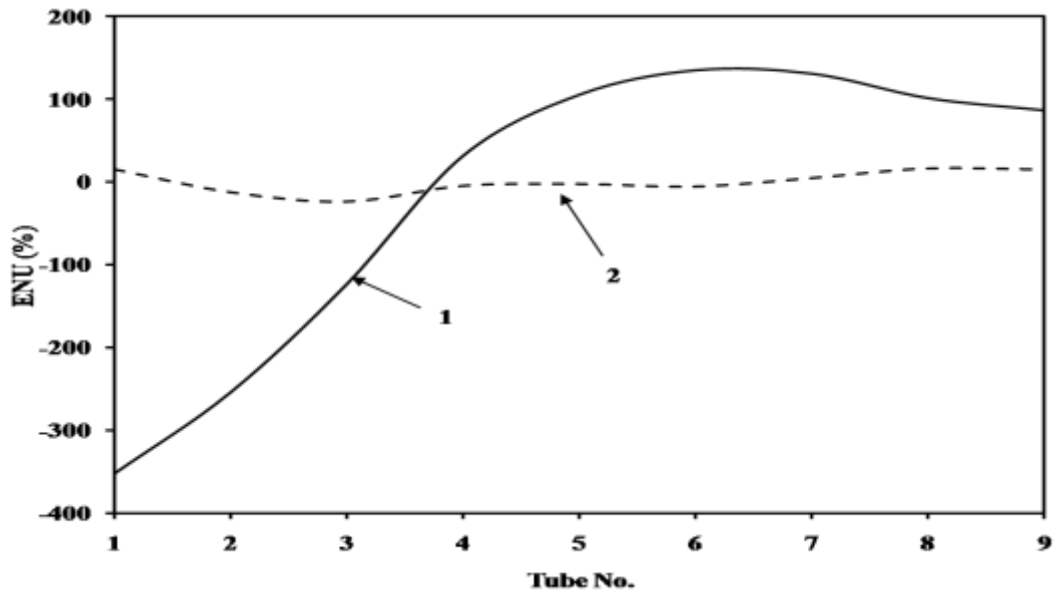


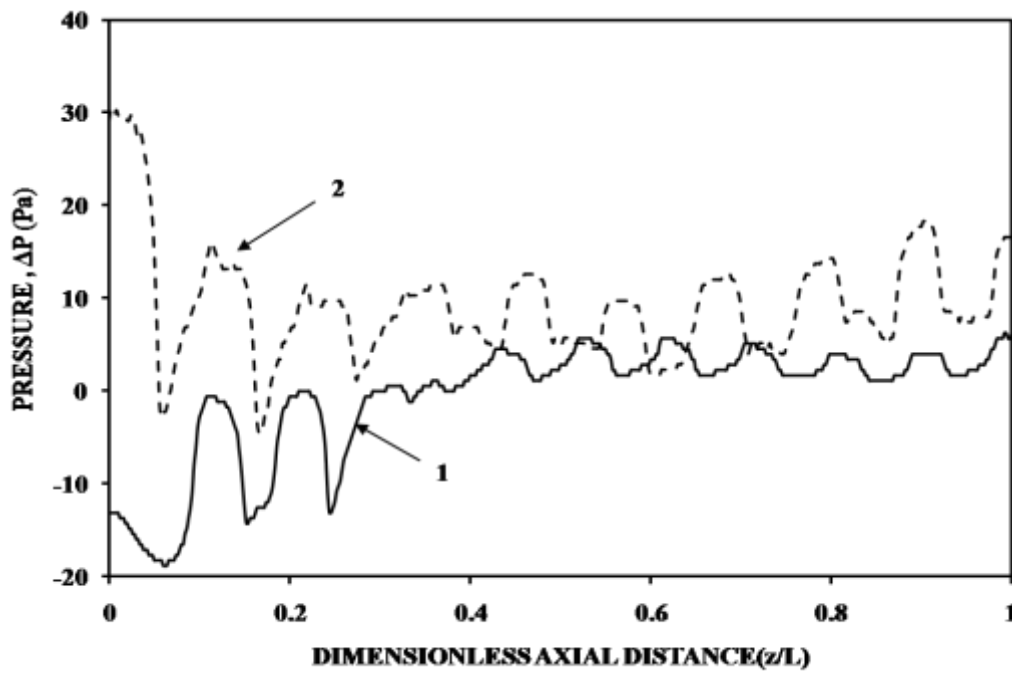
Fig 5.11: Comparison of flow distribution inside header (A) Conventional header (B) Header with perforated baffle at different cross sections; (1) $z = 0$ (at centre); (2) $z = 0.5\text{m}$; (3) $z = 2.5\text{m}$.

Lalot et al. (1999) have found that the best position for the punched baffle is in the midway between the inlet tube and the core of the header. The velocity vectors in Fig 5.12 shows the comparison between the fluid flow distribution in conventional header and header with perforated baffle. The addition of perforated baffle inside the header decreased the size of vortex formation inside the header. The dead zone vanishes in the y direction of cross section-1. In conventional header, the majority of fluid flow occurs through the tubes 5-10 whereas no fluid goes through the tubes 1-3. In

case of conventional header, the ENU was -352% for tube 1 and 86 % for tube 10. The perforated baffle results in enhancement in fluid flow through the tube 1-3 and prevents the excessive fluid flow through the tubes 5-10. The ENU was found to be 15% for tube 1 and 14% for tube 10. The small holes in the center of the baffle create resistance to the fluid flow and a large diameter holes at the periphery allows the fluid to pass through the condenser tubes.



(A)



(B)

Fig 5.12: Effect of header configuration on (A) Extent of non-uniformity (ENU) and (B) Pressure distribution
(1) Conventional header; (2) Cylindrical header along with perforated baffle

5.4 Closure

The detailed CFD analysis of fluid flow and pressure distribution inside the header and tube assembly of IC with inclined tubes has been performed. The effect of various design parameters such as tube pitch, inlet tube diameter, number of tubes, header shape, header diameter, header configuration has been investigated over a wide range. The present study shows that flow and pressure distribution inside the condenser tubes depends upon two parameters: pressure drop due to friction and pressure rise due to momentum loss inside the condenser tubes. The uniform fluid distribution inside the condenser tubes can be achieved by (a) increase in the tube pitch (b) increase in the header diameter (c) decrease the number of tubes (d) increase the inlet tube diameter. An improved header design has been proposed which can provide uniform fluid flow and pressure distribution.

CHAPTER 6

3D CFD Simulation of passive decay heat removal system under boiling conditions: role of bubble sliding motion on inclined heated tubes

6.1 Introduction

In PDHRS, the decay steam at very high temperature (285°C, 7MPa) flows through the condenser tubes which results in sub-cooled nucleate boiling over the tube surfaces. The mechanism of nucleate boiling heat transfer has been investigated due to its ability to enhance heat transfer in a limited space. However, the heat transfer can be enhanced further when the bubble slides over the tube surface. The effect of inclination of condenser tube on sliding bubble dynamics and associated heat transfer has been studied for seven angles of tube inclination α (with respect to vertical direction), in the range $0^\circ \leq \alpha \leq 90^\circ$. For this purpose, two phase transient 3D CFD simulations using mixture model (based on Euler-Euler approach) have been performed. The model considers different mechanisms such as single phase natural convection, latent heat transfer due to evaporation, transient conduction due to disruption of thermal boundary layer and enhanced liquid convection due to bubble sliding motion (quenching). A brief summary of previous work has been given in Literature survey (Section 6.2).

6.2 Literature survey

Cornwell and Einarsson (1990), Cornwell and Houston (1994) performed experiments to study nucleate boiling on a horizontal tube ($d = 27\text{mm}$) at different heat fluxes (15, 25, 40 kW/m²) and upstream liquid velocities ($0 \leq u \leq 0.37\text{m/s}$) for saturated or subcooled ($\Delta T_{sub} \leq 1^\circ\text{C}$) liquid. In the absence of upward flow ($u = 0\text{ m/s}$), the heat transfer was found to be maximum at the base ($\theta = 0^\circ$) of the tube. The angle (θ) at which maximum heat transfer occurred was found to increase with an increase in the upward flow. The nucleate boiling was dominant at the base ($\theta = 0^\circ$) and gave rise

to bubble sliding motion on the sides of the tube. The sliding bubbles result in enhanced heat transfer due to micro layer evaporation and enhanced liquid convection.

Addlesee and Cornwell (1997) studied the effect of sliding bubbles on an inclined ($8^\circ \leq \alpha \leq 23^\circ$) tube ($d=100\text{mm}$, $l=1\text{m}$) using a non-intrusive fiber optic technique. The authors have proposed an analytical model to measure liquid film thickness between wall and bubble and the results were typically in the range 200 to 400 μm for fluids under normal conditions. The film thickness was found to depend upon the principal mechanism (enhanced turbulent convection or evaporation) of heat transfer

Aszodi et al. (2000) investigated the mixing and thermal stratification in a small cylindrical water tank ($D=0.25\text{m}$, $H=0.25\text{m}$) for subcooled ($\Delta T_{sub} = 80^\circ\text{C}$) liquid by performing experiments and 2D CFD simulations. The side wall heating gave rise to non-uniform temperature distribution in the tank which resulted into thermal stratification. Further, an accumulation of hot fluid occurred in the top region which gave rise to early evaporation at the top surface. The evaporation resulted into mixing in the upper region while the fluid in the lower region was found to remain stratified. As the time progressed (1300s), the steam generation became more intense and a part of the produced steam got entrained into the bulk, which in turn, enhanced the thermal mixing or reduced the thermal stratification.

Kang (2002) performed experiments to study mixing and thermal stratification inside a water tank ($L=790\text{mm}$, $B=860\text{mm}$, $H=1000\text{mm}$) consisting of a heated tube ($d=19\text{mm}$, $l=530\text{mm}$) at two different inclinations ($\alpha = 0^\circ, 90^\circ$). For both inclinations ($\alpha = 0^\circ, 90^\circ$), the thermal stratification was observed in the vertical direction whereas there was excellent radial mixing. The time elapsed ($t=18,000\text{s}$) to saturate the water was almost the same, regardless of the tube orientation (α). The heat transfer coefficient increased with a decrease in the liquid sub cooling which occurred due to enhanced liquid agitation and bubble generation and consequently resulted in reduction in thermal stratification.

Qiu and Dhir (2002) performed experiments in a sub-cooled ($\Delta T_{sub} \leq 5^\circ\text{C}$) and saturated liquid to study the flow distribution and heat transfer associated with a bubble sliding motion on downward facing inclined heater surface ($B=49.5\text{mm}$, $L=185\text{mm}$). They found that the bubbles changed shape (a sphere at initial position to an ellipsoid at the upper end of the inclined plate) during sliding motion over the inclined tube. For large inclination angle ($\alpha \geq 30^\circ$) at saturated boiling, the major flow pattern consisted of a wavy motion of the liquid near the heater surface and the wavy structures spread out into the bulk. In the subcooled condition, the major heat transfer occurred by the formation and shedding of vortices from the thermal boundary layer and migration into the bulk liquid. The enhanced liquid convection due to bubble sliding motion led to 10% enhancement in heat transfer as compared to single phase convection.

Kang (2003) carried out experiments to study the effect of inclination (α) of condenser tube on nucleate pool boiling heat transfer. Experiments were performed for saturated ($\Delta T_{sub} = 0^\circ\text{C}$) liquid at inclination angles (in the range $0^\circ \leq \alpha \leq 90^\circ$), tube diameters ($d=12.7\text{mm}$ and 19.1mm) and heat flux ($40 \leq Q \leq 120\text{kW/m}^2$). Horizontal tubes ($\alpha = 90^\circ$) gave rise to maximum heat transfer coefficient and vertical tubes ($\alpha = 0^\circ$) gave rise to minimum heat transfer coefficient. The major heat transfer mechanisms in the presence of bubbles were proposed to be (1) liquid agitation and (2) bubble slug formation. The liquid agitation results in enhanced heat transfer whereas the bubble slug formation reduces the heat transfer. The heat transfer coefficient was found to decrease with an increase in the tube diameter except some inclination angles ($\alpha = 60^\circ$ and 75°), which were affected by strong liquid agitation.

Kang (2005, 2013) performed experiments to study the azimuthal (θ) variation of heat transfer coefficient around an inclined ($\alpha = 87^\circ$ and 90°) tube ($d = 51\text{mm}$, $l=300\text{mm}$) at heat flux ($Q = 25, 50, 75, 100 \text{ kW/m}^2$) for sub cooled ($\Delta T_{sub} \leq 20^\circ\text{C}$) and saturated liquid. The locations of the maximum and minimum heat transfer coefficients were found to depend on the inclination angle (α) and the degree of sub cooling (ΔT_{sub}). The heat transfer was maximum at $\theta = 45^\circ$ for horizontal tube

($\alpha = 90^\circ$) and at $\theta = 0^\circ$ for inclined ($\alpha = 87^\circ$) tube. The minimum heat transfer was found to occur at $\theta = 180^\circ$, regardless of the inclination angle. This was attributed to the fact that at $\theta = 45^\circ$, the intensity of liquid agitation due to sliding bubble was very high and the region was relatively free from bubble coalescence. The azimuthal angle (θ) at which maximum heat transfer occurs was found to decrease with an increase in the heat flux because bubble clusters were found to surround the lower side of the tube.

Sateesh et al. (2005) developed an analytical model to study the effect of bubble sliding motion on pool boiling heat transfer. The model considers different mechanisms such as latent heat transfer due to micro layer evaporation, transient conduction due to thermal boundary layer reformation and natural convection. At low wall superheats, the bubble interaction was found to be absent and the major heat transfer occurred by the bubble sliding motion. At high wall superheats, the bubble sliding distance decreased and the contribution of bubble interaction to heat transfer was found to increase.

Genske and Stephan (2006) carried out 2D CFD simulations to study the effect of flow pattern inside the bubble on the flow distribution and heat transfer in the surrounding liquid (macro region). The fluid in the macro-region transported cooler liquid towards the heater surface, thus increasing the heat transfer significantly. Most of the previous studies have neglected the influence of flow pattern inside the bubble on the macro region and hence under predicted the rate of heat transfer. This numerical model consisted of a moving mesh to track the bubble surface and was found to result in accurate prediction of fluid flow and heat transfer in both vapor and liquid phases.

Sateesh et al. (2009) have carried out experiments to study the effect of tube inclination (α) on nucleate pool boiling heat transfer for saturated liquid. The results show that, as the tube inclination angle (α) increases, the bubble sliding length increases at the bottom and decreases at the top. The enhanced liquid convection associated with the bubble sliding motion results in enhanced heat transfer at the tube bottom. The increase and decrease in heat transfer at the tube bottom and top

balance each other and results in nominal variations of the average heat transfer coefficient with the inclination.

Krepper and Beyer (2010) have performed experiments as well as 2D CFD simulations to study the natural circulation inside a water tank ($D = 2\text{m}$, $H = 6\text{m}$) consisting of a bundle of horizontal tubes ($d = 0.045\text{m}$, $L=10\text{m}$, $N=8$). The maximum stratification was found to occur after about 1800s, which was then followed by a destruction of the stratification by increased steam production. Similar phenomena of establishment and destruction of temperature stratification has also been reported by Aszodi et al. (2000) and Kang (2002). Such a phenomenon is very useful for the overall performance, however, it appears to be very much system dependent (geometry, heat flux) and is difficult to scale up. Further, in actual nuclear reactors, the system geometry is very large which can cause significant delay in the destruction of thermal stratification by uniform steam distribution. On contrast, such a time frame is not available in PDHRS as the decay is expected to decrease sharply from 6% to 3% (of the total power) in about 100s.

Manickam and Dhir (2012) have carried out experiments to study the heat transfer mechanism associated with a vapor bubble which is sliding along a downward facing inclined ($\alpha = 75^\circ$) heater surface ($L=185\text{mm}$, $B=49.5\text{mm}$). The experiments were performed for a sub cooled ($\Delta T_{sub} \leq 1.2^\circ\text{C}$) liquid inside the tank. The bubble sliding motion along the heater surface showed changes in the bubble shape from spheroids to elongated cylinders and then to segment of spheres. This behavior is consistent with the experimental observation of Qiu and Dhir (2002). The evaporation at the bubble base exceeds condensation at the bubble-liquid interface and resulted in continuous bubble growth. The bubble sliding motion was found to result into about two times enhanced heat transfer as compared to the single phase natural convection.

From the literature review, it is clear that many attempts have been made by various authors to understand the mechanism of bubble sliding motion and heat transfer associated with it. The literature review also shows that the bubble sliding motion over the tube surface is very much

dependent on the tube inclination (α) and the degree of sub cooling (ΔT_{sub}). However, the assumption of saturated water or low sub-cooling ($\Delta T_{sub} \leq 20^\circ\text{C}$) for the initial tank condition used by various authors could result in incorrect predictions of heat transfer, since the water in the tank may be initially sub cooled ($\Delta T_{sub} = 70^\circ\text{C}, 1\text{atm}$) and the time taken by the fluid to reach saturation temperature varies from few hours to few days depending upon the volume of the tank. For instance, Kang (2002) has reported that the time required to reach the saturation temperature was more than 4h for the (a) rectangular water tank of 680 lit volume (b) heat transfer area = 0.032 m^2 (c) initial sub cooling (ΔT_{sub}) = 70°C .

It may be pointed out that, in the past studies, scant attention has been given to the 3D CFD simulations of bubble sliding motion over an inclined tube. Therefore, it was thought desirable to develop a simulation tool (validated within a certain region of approximation) for performing 3D CFD simulations of fluid flow and temperature fields associated with the bubble sliding motion (1) to improve upon current understanding of bubble induced motion (2) to study the effect of inclination (α) of condenser tubes on bubble sliding motion and the associated heat transfer rate (3) to find the optimum inclination angle (α) at which the heat transfer is maximum and thermal stratification is minimum (4) to design an IC for a real size GDWP ($\sim 10000\text{m}^3$). In this case, a large number of numerical experiments need to be performed before arriving at an optimum hardware (5) to understand the transient heat transfer phenomena from sub cooled condition ($\Delta T_{sub} = 70^\circ\text{C}$) to boiling condition ($\Delta T_{sub} = 0^\circ\text{C}$) and to estimate the time required for the 50% decay (1300MJ to 650MJ) in 100s.

6.3 Numerical procedure

6.3.1 State of art in the code for multiphase flow

The two common approaches for the numerical calculation of multiphase flows are: the Euler-Euler approach and the Euler-Lagrange approach.

6.3.1.1 Euler-Euler approach

In the Euler-Euler approach, the different phases (liquid and vapor) are treated mathematically as interpenetrating continua. Since the volume of one phase cannot be occupied by the other phases, the concept of phasic volume fraction is introduced. These volume fractions are assumed to be continuous functions of space and time and their sum is equal to one. Conservation equations for each phase are derived to obtain a set of equations, which have similar structure for all phases. These equations are closed by providing constitutive relations that are obtained from empirical information. In ANSYS CFD 15, three different Euler-Euler multiphase models are available: the volume of fluid (VOF) model, the mixture model, and the Eulerian model.

6.3.1.1.1 Volume of Fluid (VOF) Model

The VOF model is a surface-tracking technique applied to a fixed Eulerian mesh. It is designed for two or more immiscible fluids (liquid and vapor) where the position of the interface between the fluids is of interest. Typical applications include the motion of large bubbles in a liquid and the steady or transient tracking of any liquid-gas interface. The volume fraction of each of the fluids in each computational cell is tracked throughout the domain. The tracking of the interface between the phases is accomplished by the solution of a continuity equation for the volume fraction of one of the phases.

$$\frac{\partial(\rho_G \epsilon_G)}{\partial t} + \nabla \cdot (\epsilon_G \rho_G \langle u_m \rangle) = S_{\epsilon_G} + \sum \dot{m}_{LG} - \dot{m}_{GL} \quad (6.1)$$

The volume fraction equation is not solved for the primary phase and computed from

$$\epsilon_L = 1 - \epsilon_G \quad (6.2)$$

In Fluent 6.3 (available at ICT), the source term (S_{ϵ_G}) for mass transfer through phase change (boiling and condensation) can be obtained by (1) constant value (2) User defined Function (UDF) (3) Cavitation Model (Singhal et al., 2001). In addition to above three methods, ANSYS CFD 15 consist of Evaporation-Condensation Model (Lee, 1979) to obtain source term for mass transfer. The

volume fraction equation can be solved either through implicit or explicit time discretization. When the implicit scheme is used for time discretization, Fluent 6.3 (available at ICT) and ANSYS CFD 15 uses standard finite-difference interpolation schemes such as QUICK, second order Upwind, first order Upwind, and the Modified HRIC schemes to obtain the face fluxes for all cells, including those near the interface. When the explicit scheme is used for time discretization, the face fluxes can be interpolated either using interface reconstruction or using a finite volume discretization scheme (interpolation near the interface). The cells near the interface are treated by special interpolation schemes such as geometric reconstruction and donor-acceptor schemes. In Fluent 6.3, the discretization schemes available with explicit schemes are QUICK, second order upwind, first order upwind, modified HRIC and compressive interface capturing scheme for arbitrary meshes (CICSAM). In addition to above schemes, ANSYS CFD 15 also consist of (a) compressive and zonal discretization scheme (b) Bounded gradient maximization (BGM) scheme. A single set of momentum equation is solved throughout the domain and the resulting velocity field is shared among the phases.

$$\frac{\partial(\rho_m \langle u \rangle)}{\partial t} + \nabla \cdot (\rho_m \langle u \rangle \langle u \rangle) = -\nabla \langle p \rangle + \nabla \cdot \left(\mu_m \left(\nabla \langle u \rangle + (\nabla \langle u \rangle)^T \right) \right) + \rho_m g + F \quad (6.3)$$

The energy equation also shared among the phases as shown below

$$\frac{\partial(\rho_m E)}{\partial t} + \nabla \cdot (\langle u_i \rangle (\rho_m E + p)) = \nabla \cdot (k_{eff} \nabla T) + S_E \quad (6.4)$$

The VOF model treats energy (E) and temperature (T) as mass-averaged variables:

$$E = \frac{\epsilon_L \rho_L E_L + \epsilon_G \rho_G E_G}{\epsilon_L \rho_L + \epsilon_G \rho_G} \quad (6.5)$$

The VOF model also includes the effect of surface tension along the interface between each pair of phases. In ANSYS CFD 15, two surface tension models exists (a) continuum surface force (CSF) by Brackbill et al. (1992) and (b) continuum surface stress (CSS) whereas Fluent 6.3 (available at ICT) consist of only continuum surface force (CSF) model. The limitations of this model are (i) the accuracy of the velocities and temperature computed near the interface can be adversely affected

when large velocity differences or temperature difference exist between the phases (ii) convergence difficulties if the viscosity ratio is more than 1000.

6.3.1.1.2 Mixture Model

The mixture model is a simplified multiphase model and can be used to model multiphase flows where the phases move at different velocities, but assume local equilibrium over short spatial length scales. In the mixture model, the phases are treated as interpenetrating continua. The volume fractions ϵ_G and ϵ_L for a control volume can individually take any value between 0 and 1 while keeping the sum ($\epsilon_G + \epsilon_L$) equal to one. The mixture model solves momentum, continuity and energy equations for the mixture, the volume fraction equations for the secondary phases and algebraic expressions for the relative velocities. The continuity equation for the mixture model (Table 6.1) is defined as:

$$\frac{\partial(\rho_m)}{\partial t} + \nabla \cdot (\rho_m \langle u_m \rangle) = 0 \quad (6.6)$$

The volume fraction equation for the secondary phase in mixture model (Table 6.1) is defined as

$$\frac{\partial(\rho_G \epsilon_G)}{\partial t} + \nabla \cdot (\epsilon_G \rho_G \langle u_m \rangle) = S_{\epsilon_G} + \sum \dot{m}_{LG} - \dot{m}_{GL} \quad (6.7)$$

The source term for mass transfer through phase change (boiling and condensation) is obtained by evaporation-condensation model. The evaporation-condensation model is a mechanistic model given by Lee (1979). The liquid-vapor mass transfer (evaporation and condensation) is governed by the vapor transport equation given in Table 6.1. When liquid temperature becomes greater than the saturation temperature ($T > T_s$), vapors are generated in the system. The extent of vaporization (\dot{m}_{LG}) is given by:

$$\dot{m}_{LG} = \text{coeff}(\epsilon_L \rho_L) \left(\frac{T - T_s}{T_s} \right) \quad (6.8)$$

However, when ($T < T_s$), condensation occurs and the extent is given by:

Table 6.1: Governing Equations for two phase CFD simulations using Mixture model

Property	Equations
Continuity	$\frac{\partial(\rho_m)}{\partial t} + \nabla \cdot (\rho_m \langle u_m \rangle) = 0$ <p>where $\langle u_m \rangle$ is mass-average velocity $\langle u_m \rangle = \frac{(\epsilon_G \rho_G \langle u_G \rangle + \epsilon_L \rho_L \langle u_L \rangle)}{\rho_m}$ and</p> $\rho_m = \epsilon_G \rho_G + \epsilon_L \rho_L$
Momentum	$\frac{\partial(\rho_m \langle u_m \rangle)}{\partial t} + \nabla \cdot (\rho_m \langle u_m \rangle \langle u_m \rangle) = -\nabla \langle p \rangle + \nabla \cdot \left(\mu_m \left(\nabla \langle u_m \rangle + (\nabla \langle u_m \rangle)^T \right) \right) + \nabla \cdot (\rho_G \epsilon_G \langle v_{dr,k} \rangle \langle v_{dr,k} \rangle + \rho_L \epsilon_L \langle v_{dr,k} \rangle \langle v_{dr,k} \rangle) + S_\phi$ <p>where μ_m is viscosity of mixture $\mu_m = \epsilon_G \mu_G + \epsilon_L \mu_L$</p> <p>$S_\phi$ is the source terms which include gravitational term, interfacial forces.</p>
Energy	$\frac{\partial(\rho_G \epsilon_G E_G + \rho_L \epsilon_L E_L)}{\partial t} + \nabla \cdot ((\epsilon_G \langle u_i \rangle (\rho_G E_G + p)) + (\epsilon_L \langle u_i \rangle (\rho_L E_L + p))) = \nabla \cdot (k_{eff} \nabla T) + S_E$ <p>where k_{eff} is effective conductivity $k_{eff} = (\epsilon_G (k_k + k_t) + \epsilon_L (k_k + k_t))$</p>

Volume
fraction
equation
for gas
phase

$$\frac{\partial(\epsilon_G \epsilon_G)}{\partial t} + \nabla \cdot (\epsilon_G \rho_G \langle u_m \rangle) = S_{\epsilon_G} + \sum \dot{m}_{LG} - \dot{m}_{GL} - \dot{m}_{de}$$

$$\frac{\partial(\epsilon_L \rho_L k_L)}{\partial t} + \nabla \cdot ((\epsilon_L \langle u_i \rangle \rho_L k_L)) = \nabla \cdot \left[\left(\mu + \frac{\mu_{t,L}}{\sigma_{k,L}} \right) \nabla \cdot k_L \right] + G_{k,L} + G_{b,L} - Y_{k,L}$$

Turbulent kinetic energy $G_{k,L} = \nu_t |\bar{S}|^2$ where $|\bar{S}| = \sqrt{2 \overline{S_{ijk} S_{ijk}}}$ and $|\overline{S_{ijk}}| = \frac{1}{2} \left(\frac{\partial u_x}{\partial z} + \frac{\partial u_z}{\partial x} + \frac{\partial u_y}{\partial z} + \frac{\partial u_z}{\partial y} + \frac{\partial u_x}{\partial y} + \frac{\partial u_y}{\partial x} \right)$

Turbulent
kinetic
energy

Generation of turbulence due to buoyancy $G_{b,L} = -\beta g \frac{\nu_t}{\sigma_{t,L}} \frac{\partial \langle T \rangle}{\partial z}$

Dissipation of this turbulence kinetic energy, $Y_{k,L} = \epsilon_L \rho_L \beta_\infty^* f_{\beta^*} k_L \omega_L$

where $\beta_\infty^* = 0.09$, $f_{\beta^*} = \begin{cases} 1, & \chi_k \leq 0 \\ \left[\frac{1+680\chi_k^2}{1+400\chi_k^2} \right], & \chi_k > 0 \end{cases}$ and $\chi_k = \frac{1}{\omega^3} \frac{\partial k}{\partial z} \frac{\partial \omega}{\partial z}$

Specific
dissipation
rate

$$\frac{\partial(\epsilon_L \rho_L \omega_L)}{\partial t} + \nabla \cdot (\epsilon_L \langle u_i \rangle \rho_L \omega_L) = \nabla \cdot \left[\left(\mu + \frac{\mu_{t,L}}{\sigma_{\omega,L}} \right) \nabla \omega_L \right] + G_{\omega,L} - Y_{k,L}$$

Production of specific dissipation rate, $G_{\omega,L} = \frac{\alpha_\infty}{\nu_t} G_{k,L}$ where α_∞ , $\alpha_{\infty,1}$ and $\alpha_{\infty,2}$ are constants.

$\alpha_{\infty,1} = 1$, $\alpha_{\infty,2} = 0.52$ and $Y_{\omega,L} = \rho_L \beta_r \omega_L^2$

$$\dot{m}_{GL} = coeff (\epsilon_G \rho_G) \left(\frac{T - T_s}{T_s} \right) \quad (6.9)$$

The source term for the energy equation in Table 6.1 is obtained by multiplying the rate of mass transfer with the latent heat.

$$S_E = -\dot{m}_{LG}\lambda = \dot{m}_{GL}\lambda \quad (6.10)$$

The term "*coeff*" in Eqs. (6.8) and (6.9) can be interpreted as a relaxation time. The value of "*coeff*" for the evaporation model was calculated by two methods as follows:

(1) A simple estimation of the bubble departure frequency as the terminal rise velocity over the bubble departure diameter is adopted here (Cole, 1960).

$$f = \sqrt{\frac{4g(\rho_L - \rho_G)}{3d_w\rho_L}} \quad (6.11)$$

The value of "*coeff*" is then given by:

$$coeff1 = f \epsilon_G \quad (6.12)$$

(2) The evaporation flux given by Hertz-Knudsen (Kolasinski, 2012) equation (based on the kinetic theory for a flat interface) was assumed to be valid and can be used for calculating "*coeff*" in Eq. (6.9) as per the following procedure:

$$F = \beta_b \left(\sqrt{\frac{M_w}{2\pi T_s R_G}} \right) (p^* - p_{sat}) \quad (6.13)$$

The Clapeyron-Clausius (Kenneth, 1988) equation relates the pressure and temperature for the saturation condition by equating the vapor and liquid chemical potentials as:

$$\frac{dp}{dT} = \frac{\lambda}{T(v_G - v_L)} \quad (6.14)$$

After integrating Eq. (6.14) near the saturation condition, we get:

$$(p^* - p_{sat}) = -\frac{\lambda}{T(v_G - v_L)} (T^* - T_s) \quad (6.15)$$

Substituting Eq. (6.15) in Eq. (6.13), we get the following equation:

$$F = \beta_b \left(\sqrt{\frac{M_w}{2\pi T_s R_G}} \right) \left(\frac{\rho_G \rho_L}{\rho_L - \rho_G} \right) (T^* - T_s) \quad (6.16)$$

In addition, in the mixture model it has been considered that the vapor phase is dispersed and we have further assumed that the vapor bubbles have the same diameter. Therefore, the interfacial area density is given by the following equation:

$$\frac{A_i}{V_{cell}} = \frac{6 \epsilon_G}{d_w} \quad (6.17)$$

Multiplying Eq. (6.17) with Eq. (6.16), we get:

$$F \frac{A_i}{V_{cell}} = \frac{6 \epsilon_G}{d_w} \beta_b \left(\sqrt{\frac{M_w}{2\pi T_s R_G}} \right) \left(\frac{\rho_G \rho_L}{\rho_L - \rho_G} \right) (T^* - T_s) \quad (6.18)$$

From Eq. (6.18) we get the "*const*" as:

$$const = \frac{6}{d_w} \beta_b \left(\sqrt{\frac{M_w}{2\pi T_s R_G}} \right) \left(\frac{\rho_L}{\rho_L - \rho_G} \right) \quad (6.19)$$

The value of "*const*" was then multiplied by the gas volume fraction and we get "*coeff2*" as:

$$coeff2 = const \times (\epsilon_G) \quad (6.20)$$

Eqs. (6.10) and (6.20) give the two values for coefficient for Eq (6.1) and the lower of the two values.

The momentum equation for the mixture model (Table 6.1) is defined as:

$$\frac{\partial(\rho_m \langle u_m \rangle)}{\partial t} + \nabla \cdot (\rho_m \langle u_m \rangle \langle u_m \rangle) = -\nabla \langle p \rangle + \nabla \cdot \left(\mu_m \left(\nabla \langle u_m \rangle + (\nabla \langle u_m \rangle)^T \right) \right) + \quad (6.21)$$

$$\nabla \cdot (\rho_G \epsilon_G \langle v_{dr,k} \rangle \langle v_{dr,k} \rangle + \rho_L \epsilon_L \langle v_{dr,k} \rangle \langle v_{dr,k} \rangle) + S_\phi \quad (6.22)$$

$$\langle v_{dr,k} \rangle = \langle v_k \rangle - \langle v_m \rangle$$

The relative velocity $\left(\langle v_{pq} \rangle = \langle v_p \rangle - \langle v_q \rangle\right)$ between the phases is defined as velocity of secondary (vapor) phase relative to the primary phase (liquid). The mass fraction for any phase (k) is defined as

$$c_k = \frac{\epsilon_k \rho_k}{\rho_m} \quad (6.23)$$

The drift velocity and the relative velocity are connected by the following expression

$$\langle v_{dr,p} \rangle = \langle v_{pq} \rangle - \sum_{k=1}^2 c_k \langle v_{qk} \rangle \quad (6.24)$$

The relative velocity $\langle v_{pq} \rangle$ is calculated as per the procedure recommended by Mannien et al., (1996). In Fluent 6.3, the drag function required for solving the slip velocity can be calculated by:

(i) Schiller-Naumann (Schiller and Naumann, 1935) (ii) universal drag laws (Kolev, 2005) (iii) constant value (iv) user defined function. In ANSYS CFD 15, three additional models are available (a) Morsi and Alexander (1972) (b) Grace (Clift et al., 1978) (c) Tomiyama (Takamasa and Tomiyama, 1999). For turbulent flow, diffusion term due to dispersion is being added in the relative velocity term of momentum equation. The energy equation for the mixture model (Table 6.1) is as follows:

$$\begin{aligned} & \frac{\partial (\rho_G \epsilon_G E_G + \rho_L \epsilon_L E_L)}{\partial t} + \nabla \cdot \left((\epsilon_G \langle u_i \rangle (\rho_G E_G + p)) + (\epsilon_L \langle u_i \rangle (\rho_L E_L + p)) \right) \\ & = \nabla \cdot (k_{eff} \nabla T) + S_E \end{aligned} \quad (6.25)$$

In two-fluid flow systems, such as vapor-liquid in the case, the size and its distribution of the vapor or bubbles can change rapidly due to growth (mass transfer between phases), expansion due to pressure changes, coalescence, breakage and/or nucleation mechanisms. Interfacial area concentration is defined as the interfacial area between two phases per unit mixture volume. This is an important parameter for predicting mass, momentum and energy transfers through the interface between the phases. The interfacial area concentration model uses a single transport equation per secondary phase and is specific to bubbly flows in liquid at this stage. In ANSYS 15, two sets of models (1) the Hibiki-Ishii model (Hibiki and Ishii, 2000) and (2) the Ishii-Kim model (Kim et al.

(1997); Ishii and Kim (2001) exists for the source and sink term of interfacial area concentration. In ANSYS 15, three mechanism of interactions between the vapor-liquid phase are considered: (1) Coalescence due to random collision driven by turbulence (2) breakage due to the impact of turbulent eddies (3) Shearing off small bubbles from large cap bubbles

The mixture model is a good substitute for the full Eulerian multiphase model when (i) there is a wide distribution of the particulate (vapor) phase (ii) interphase laws are unknown (iii) big geometries having very high (few millions) number of grids.

6.3.1.1.3 Eulerian Model

The Eulerian model solves mass, momentum and energy balance equations for each phase separately. The volume fraction for each phase is calculated from a continuity equation

$$\frac{1}{\rho_{rq}} \left(\frac{\partial (\rho_q \epsilon_q)}{\partial t} + \nabla \cdot (\epsilon_q \rho_q \langle u_q \rangle) \right) = \sum \dot{m}_{pq} - \dot{m}_{qp} \quad (6.26)$$

The conservation of momentum for a fluid phase q in ANSYS 15 is defined as:

$$\begin{aligned} \frac{\partial (\epsilon_q \rho_q \langle u_q \rangle)}{\partial t} + \nabla \cdot (\epsilon_q \rho_q \langle u_q \rangle \langle u_q \rangle) = & - \epsilon_q \nabla \langle p \rangle + \nabla \cdot \langle \tau_q \rangle + \epsilon_q \rho_q g + \sum_{p=1}^n \left(K_{pq} (\langle u_p \rangle - \langle u_q \rangle) \right) + \\ & \sum_{p=1}^n \left(\dot{m}_{pq} \langle u_{pq} \rangle - \dot{m}_{qp} \langle u_{qp} \rangle \right) + F_q + F_{lift,q} + F_{wl,q} + F_{vm,q} + F_{td,q} \end{aligned}$$

In Fluent 6.3, $F_{wl,q}$ and $F_{td,q}$ are not included in momentum equation. $\langle u_{qp} \rangle$ is the interphase velocity, defined as follows. If $\dot{m}_{pq} > 0$ (phase p mass is transferred to phase q), $\langle u_{qp} \rangle = \langle u_p \rangle$; If $\dot{m}_{pq} < 0$ (phase p mass is transferred to phase q), $\langle u_{qp} \rangle = \langle u_q \rangle$. The Euler model in ANSYS 15 computes the interfacial areas by two ways: (1) use a transport equation for interfacial area concentration as described for mixture model in Section 6.3.1.1.2. (2) use an algebraic relationship between a specified bubble diameter and interfacial area concentration. The interphase momentum exchange coefficient is defined as:

$$K_{pq} = \frac{\rho_q f}{6\tau_p} d_p A_i \quad (6.27)$$

The drag model available in Fluent 6.3 and ANSYS 15 were mentioned in Section 6.3.1.1.2. In contrast to mixture model, the turbulent dispersion in Euler model is treated as a turbulent diffusion term in phasic volume fraction equation. The energy equation is defined as follows:

Table 6.2: Modeling heat flux at the tube wall for two phase CFD simulations

Total heat supplied at the tube wall $\left(q_{tot} \right)$	$q_{tot} = q_N + q_E + q_q$
Natural convection heat flux $\left(q_N \right)$	$q_N = h_c * (T_w - T_L) * (1 - A_i)$ where, A_i = interfacial area density, $A_i = \min\left(1, 0.57 * N_A * \pi * d_w^2\right)$ d_w = bubble departure diameter (mm), $d_w = \min\left(0.0014, 0.0006 * \exp\left(-\frac{\Delta T_{sup}}{45}\right)\right)$ ΔT_{sup} = wall super heat, $\Delta T_{sup} = T_w - T_s$
Evaporating heat flux $\left(q_E \right)$	$q_E = V_d * N_A * \rho_G * \lambda * f$ where, N_A = Number of active site density, $N_A = \left(210 * \Delta T_{sup}\right)^{1.805}$ f = frequency of bubble departure (s^{-1}), $f = \frac{1}{t_p} = \sqrt{\frac{4 * g * (\rho_L - \rho_G)}{3 * d_w * \rho_L}}$
Quenching heat flux $\left(q_q \right)$	$q_q = \frac{2k_{eff}}{\sqrt{\pi\alpha_L t_p}} * (T_w - T_L)$

$$\frac{\partial(\epsilon_q \rho_q h_q)}{\partial t} + \nabla \cdot (\epsilon_q \rho_q \langle u_q \rangle h_q) = -\epsilon_q \frac{\partial(p_q)}{\partial t} + \langle \tau_q \rangle : \nabla \langle u_q \rangle - \nabla \langle Q_q \rangle + S_q + \sum_{p=1}^n (Q_{pq} + \dot{m}_{pq} h_{pq} - \dot{m}_{qp} h_{qp}) \quad (6.28)$$

The heat exchange between phases must comply with the local balance conditions

$$Q_{pq} = -Q_{qp} \text{ and } Q_{qq} = 0$$

The volumetric rate of energy transfer between phases (Q_{pq}), is assumed to be a function of the temperature difference and the interfacial area, A_i :

$$Q_{pq} = h_{pq} A_i (T_p - T_q) \quad (6.29)$$

The heat transfer coefficient is related to the p^{th} phase Nusselt number, by

$$h_{pq} = \frac{k_q N U_p}{d_p} \quad (6.30)$$

In Fluent 6.3, Ranz-Marshall (Ranz and Marshall, 1952) model is used for calculating the NU_p whereas in ANSYS 15 many more options are available (1) Tomiyama Model (Tomiyama, 1998) (2) Hughmark model (Hughmark, 1967) (3) Gunn Model (Gunn, 1978) (4) Two resistance model (Lavieville et al., 2005). The ANSYS 15 consists of wall boiling models such as RPI nucleate boiling model of Kurual and Podowski (1991). According to the basic RPI model (Table 6.2), the total heat flux from the wall to the liquid is partitioned into three components, namely the convective heat flux, the quenching heat flux, and the evaporative heat flux.

6.3.1.2 Limitations of RPI model at low pressures or large void-fractions

Although the RPI model for sub cooled nucleate boiling has been satisfactorily validated for high pressures ($P > 10$ bar), the model is not valid for low pressure boiling applications. The experimental and computational studies reported in literature have indicated that the bubble behavior determining the void change at low pressure differ significantly from that at high pressure. Bibeau and Salcudean (1994) pointed out that the rate of change in void fraction with the quality at low pressure was far more significant than at high pressures. Zeitoun and Shoukri (1996) found that the void growth under the low-pressure conditions was caused by bubble size increase because larger bubbles were formed in low-pressure sub cooled boiling flows, whereas bubbles tended to be very small at high pressures. The numerical study by Tu et al., 1999 also showed that the RPI model, validated for high pressures,

gave un-satisfactory predictions of mean bubble size distribution in a sub cooled boiling flow at low pressures. Zeitoun and Shoukri (1996, 1997) have pointed out various modeling issues that need to be considered in developing accurate mechanistic models for predicting void fraction distributions in sub cooled boiling flows. The most important modeling issues at low pressures are: (i) bubble size distribution and interfacial area concentration (which determines inter phase momentum transfer and more importantly inter phase heat transfer); (ii) partition of the wall heat flux (which determines the inter-phase mass transfer near a heated surface); and (iii) bubble departure diameter and the related bubble departure frequency (which are used to model the partition of the wall heat flux). Tu and Yeoh (2002) focuses on the effect of these issues or parameters on the mechanistic closure relationships and on void fraction distributions at low pressures. The authors have found that a low-pressure bubble size correlation is essential for accurate determination of the total rate of interfacial momentum, energy and mass transport between two phases in a low-pressure sub cooled boiling flow. This is because bubble size correlations commonly used for high-pressure conditions, only apply to the very small bubbles that occur at these pressures, whereas large bubbles occur in low pressure flows. The authors have also found that the wall heat transfer due to surface quenching, commonly not accounted for in high pressure sub cooled boiling models, was significant at low pressures because of the formation of larger bubbles before departure from the heated surface. Recently, the authors have various correlations and closure relationship for low pressure applications.

6.3.1.2.1 Mean bubble diameter

Zeitoun and Shoukri [1996,1997] proposed a low pressure correlation for mean bubble diameter

$$\frac{D_s}{\sqrt{\sigma/g\Delta\rho}} = \frac{0.0683(\rho_l/\rho_g)^{1.326}}{Re^{0.324} \left(Ja + \frac{149.2(\rho_l/\rho_g)^{1.326}}{Bo^{0.487} Re^{1.6}} \right)}$$

6.3.1.2.2 Wall heat flux partitioning

The numerous experimental and theoretical investigations for low pressure sub cooled boiling flow suggest that there are in fact three components of the wall heat flux: (i) heat transferred by microlayer evaporation or vapor generation, Q_e ; (ii) heat transferred by transient conduction to the superheated layer (nucleate boiling or surface quenching), Q_q ; and (iii) heat transferred by turbulent convection, Q_c .

Cooper (1969) and Cooper and Lloyd (1969) suggested that a low system pressure will significantly influence the growth of bubbles, promoting the formation of a liquid microlayer and forming large vapor bubbles on the heating surface. On the basis of their experimental results, Fath and Judd (1978) stressed that the microlayer evaporation phenomenon was definitely a significant heat transfer mechanism at atmospheric pressure, and, depending on the heat flux, may be significant at above atmospheric pressures. This significance, however, decreases with increasing system pressure and decreasing heat flux. Recently, an experimental investigation at atmospheric pressure (Victor et al. (1985) showed that the transient conduction during the surface quenching process was the most important heat transfer mechanism, contributing up to 90 percent of the total wall heat flux. This might have been attributed to the increased quenching area resulting from the formation of large vapor bubbles and also to the subsequent enhanced degree of overlapping bubble influence area at low pressures. Explanations of the mechanism for each of the heat transfer processes and formulation of empirical correlations and models were summarized by Hsu and Graham (1976). Cooper (1969) presented a theory for predicting the rate of growth of a bubble in a saturated boiling condition, allowing microlayer evaporation. Graham and Hendricks (1967) formulated a model which combines time-averaged and surface averaged values of (i) a transient thermal conduction mechanism involving the thermal layer formed at the nucleation sites between periods of bubble nucleation; (ii) turbulent convection in regions with no bubble nucleation; and (iii) microlayer evaporation at nucleation sites while bubbles are present. Experimental verification of their model showed how these three mechanisms could adequately predict surface-averaged boiling heat fluxes. Later, Judd

and Hwang (1976) presented a comprehensive model for predicting the heat flux comprised of the above three components. Fath and Judd's (1978) experimental data validated the model proposed by Judd and Hwang. More recently, Judd (1999) studied the effect of some important parameters, such as bubble departure diameter and departure frequency, on the model prediction of boiling heat transfer. The most important parameters in the wall heat flux partition model are the bubble departure diameter and the bubble departure frequency which are discussed below:

6.3.1.2.3 Bubble departure diameter and frequency

The correlations for bubble departure diameter and frequency at low pressures are as follows:

$$d_{Bw} = \frac{2.42 \times 10^{-5} p^{0.709} a}{\sqrt{b\phi}} \quad [Unal et al., 1976]$$

$$d_{Bw} = 0.208 \phi \sqrt{\frac{\sigma}{g(\rho_l - \rho_g)}} \quad [Fritz et al., 1935]$$

$$f = \sqrt{\frac{4g(\rho_l - \rho_g)}{3d_{Bw}\rho_l}} \quad [Cole 1960]$$

$$f = 0.9 \sqrt{\frac{g}{d_{Bw}}} \quad [Ivey 1967]$$

$$f = \frac{1}{\pi} \sqrt{\frac{g}{2d_{Bw}}} \left[1 + \frac{4\sigma}{d_{Bw}^2 \rho g} \right] \quad [Stephan 1992]$$

6.3.1.3 Euler-Lagrange approach

The fluid (water) phase is treated as a continuum by solving the Navier-Stokes equations, while the dispersed phase (bubbles) is solved by tracking a large number of bubbles through the calculated flow field. The bubbles can exchange momentum, mass and energy with the liquid phase. This approach is made considerably simpler when bubble-bubble interactions can be neglected, and this requires that the bubble occupies a low volume fraction. Hence, it is not applicable in this case because vapor fraction is very high at some locations.

6.3.2 Governing equations

In order to model the unsteady two-phase thermal stratification, the governing equations (continuity, momentum, and energy) with the appropriate Reynolds stress closure need to be solved with the boundary conditions. All the governing equations for the natural convection with boiling (i.e. two-phase simulations using mixture model) are given in Table 6.1. The physical properties of fluid are given in Table 6.3. For the present case of $\beta = 5 \times 10^{-4} \text{ (K}^{-1}\text{)}$, $\Delta T = 258 \text{ K}$, the value of Ra works out to be 3×10^{11} . For CFD simulations, Shear Stress Transport (SST) $k - \omega$ turbulence model was used. The flow is considered to be turbulent on the basis of general criteria of Rayleigh number ($Ra > 10^9$). Two phase CFD simulations using the mixture model (based on Euler-Euler approach) explained in Section 6.3.1.1.2 have been performed using the commercial CFD code FLUENT-6.3 (Didio, 1992)

Table 6.3: Physical properties of fluid used for CFD simulations

Characteristic length (l) (m)	0.4m
Thermal expansion coefficient (β) (K^{-1})	0.0005
Gravitational force (g) (m/s^2)	9.81
Fluid density (ρ) (kg/m^3)	980
Kinematic viscosity (ν) (m^2/s)	1.38×10^{-6}
Thermal diffusivity (α_l) (m^2/s)	2.3×10^{-7}
Operating temperature (T_o) (K)	300
Heat source wall temperature (T_w) (K)	558
Temperature driving force (ΔT) (K)	258
Rayleigh number $\left(Ra = \frac{g\beta\Delta T l^3}{\nu\alpha_\ell} \right)$	3×10^{11}

6.3.3 Model Assumptions

- (1). Condensation occurring inside the tube is a film condensation and hence the tube is at a constant saturation temperature ($T_s = 558$ K) corresponding to the saturated steam pressure ($P_s = 7$ MPa).
- (2). Fluid is Newtonian and incompressible. However, Boussinesq approximation was assumed to be valid which means the temperature differences produced the force due to buoyancy and resulted into flows
- (3). Fluid properties are constant except in the formulation of buoyancy term.
- (4). The correlation for interstitial site density developed by Kurul and Podowski (1991) was assumed to hold true for pool boiling.
- (5). The Ranz and Marshall (1952) model has been used for the estimation of heat transfer coefficient for vapor formation in the bulk.

6.3.4 Method of solution

In the present work, 3D CFD simulations have been performed under unsteady conditions. The first order implicit scheme was used for the time discretization of all unsteady terms. QUICK spatial discretization scheme was used for modeling the convective terms and central differencing scheme for diffusive terms. All the discretized equations were solved in a segregated manner with the PISO (Pressure Implicit with Splitting of Operators) algorithm. Further, the solutions were considered to be fully converged when the sum of scaled residuals was below 10^{-5} .

Table 6.4: Details of experimental situations of various authors

Author	Tank Shape	Fluid	Ra	Tank dimensions (m)	Tube dimensions (m)
Kang (2013)	Vertical	Water	10^{10}	$L = 0.95$, $B = 1.3$ m, $H = 0.25$	$d = 0.051$, $h = 0.3$
Ganguli et al. (2010)	Vertical	Water	10^{13}	$L = 0.3$, $D = 0.3$	$d = 0.02$, $H = 0.3$

6.3.5 Model Validation

In order to check the capability of the present CFD simulations for the prediction of bubble sliding motion and heat transfer, experimental data from Kang (2013) and Ganguli et al. (2010) have been used. Kang (2013) performed experiments to study nucleate pool boiling heat transfer inside a water tank consisting of a horizontal ($\alpha = 90^\circ$) heated tube. The details of the experimental set up are given in Table 6.4. Two phase transient CFD simulations using mixture model have been performed with the help of commercial CFD software Fluent 6.3 (Didio, 1992). In both, experiments and CFD simulations, it was found that the heat transfer rate decreases with an increase in the azimuthal angle (θ). The comparison in Fig 6.1 shows that the CFD simulation exactly predicts the locations of maximum ($\theta_{max} = 45^\circ$) and minimum ($\theta_{min} = 180^\circ$) heat transfer coefficients. The enhanced liquid convection and reduced bubble coalescence at $\theta = 45^\circ$ results in maximum heat transfer. As the azimuthal angle increases ($\theta > 90^\circ$), the bubble arriving from the bottom ($\theta = 0^\circ$) starts to depart from the surface due to buoyancy and the intensity of liquid agitation decreases. The CFD simulations over predict (10%) the heat transfer in the region $45^\circ \leq \theta \leq 150^\circ$ and under predict (13%) it in the region $150^\circ \leq \theta \leq 180^\circ$. Ganguli et al. (2010) have performed experiments to study two phase natural convection in a cylindrical water tank (0.02 m^3) with a centrally heated vertical ($\alpha = 0^\circ$) tube. The details of the experimental set up are given in Table 6.4. The contribution of various heat transfer mechanisms such as natural convection, quenching and evaporation have been studied by the authors. The transient heat flux distribution shown in Fig 6.2 indicates that the evaporative heat flux contributes 2-3%, quenching heat flux contributes 8-10% and the major heat transfer contribution (85-90%) is through convective heat flux. Thus, the CFD model is able to predict the heat flux distribution with a maximum deviation of 20% from the experimental values. The accuracy of the CFD results can be improved further by (1) using more complex multiphase models such as Eulerian model (Section 6.3.1.1.3) along with DNS (2) better correlations for calculating interstitial site density, bubble generation frequency and bubble departure diameter.

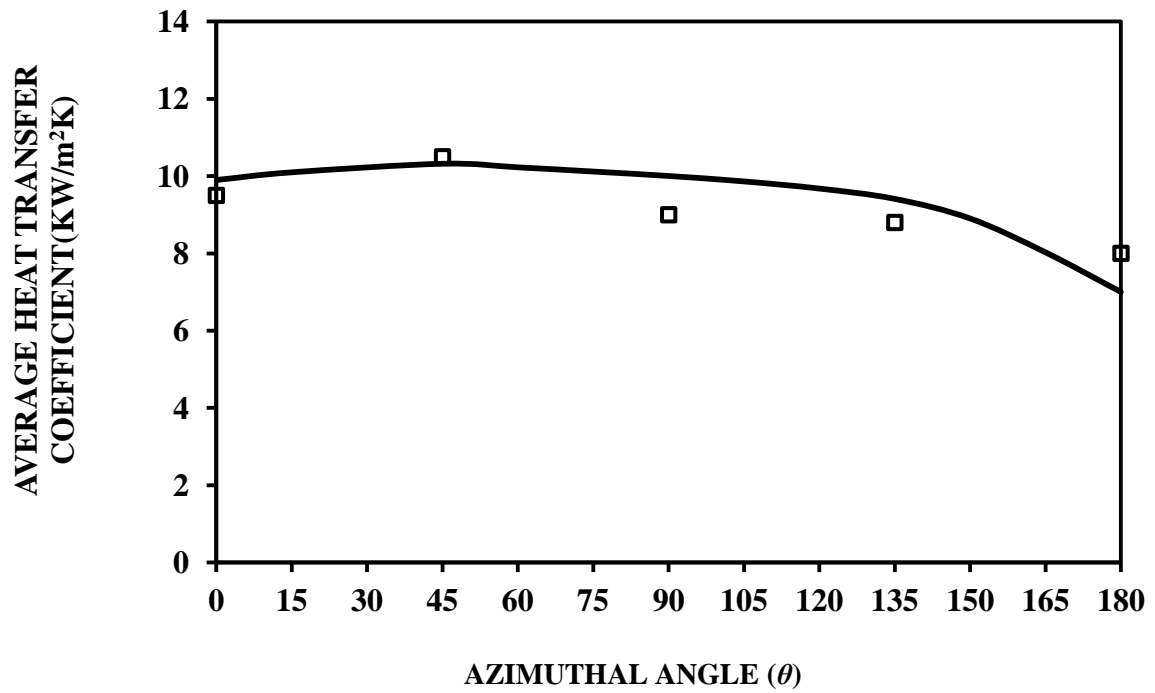


Fig 6.1: Comparison of CFD model and experimental data for azimuthal (θ) variation of average heat transfer coefficient for Kang, 2013; Experimental value (□) and CFD (—)

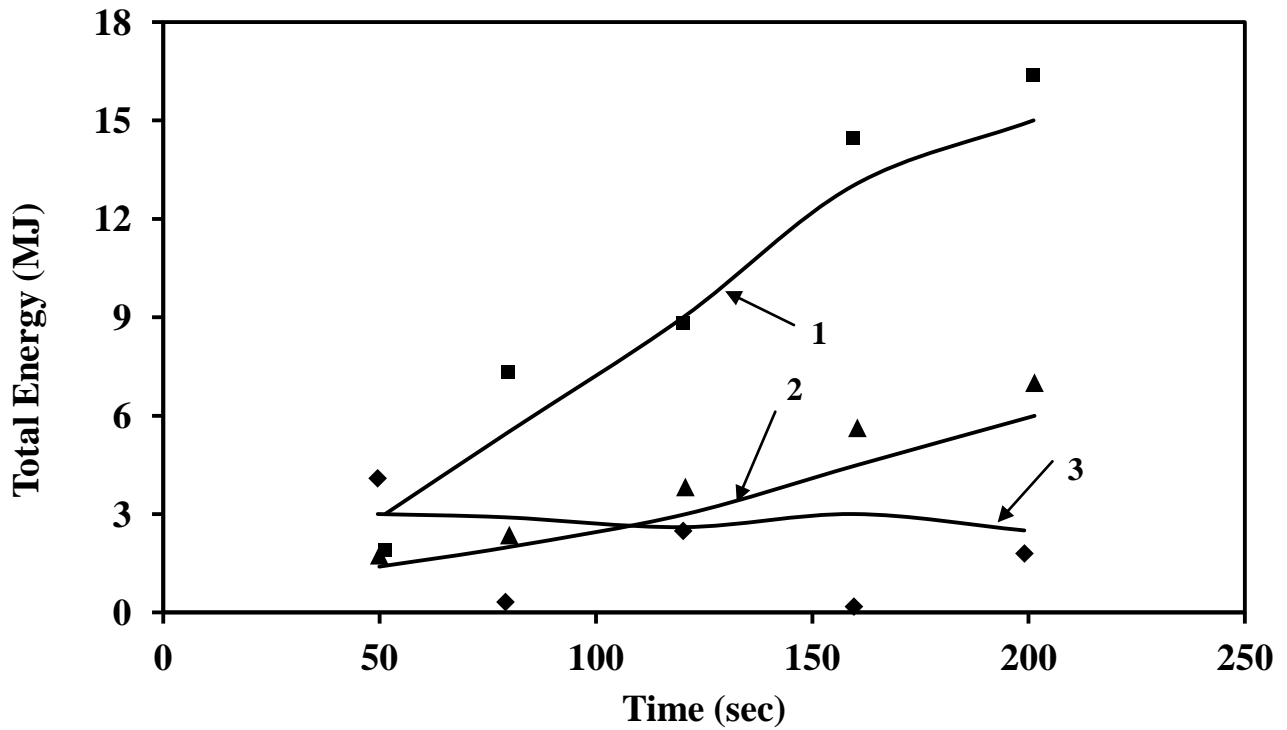
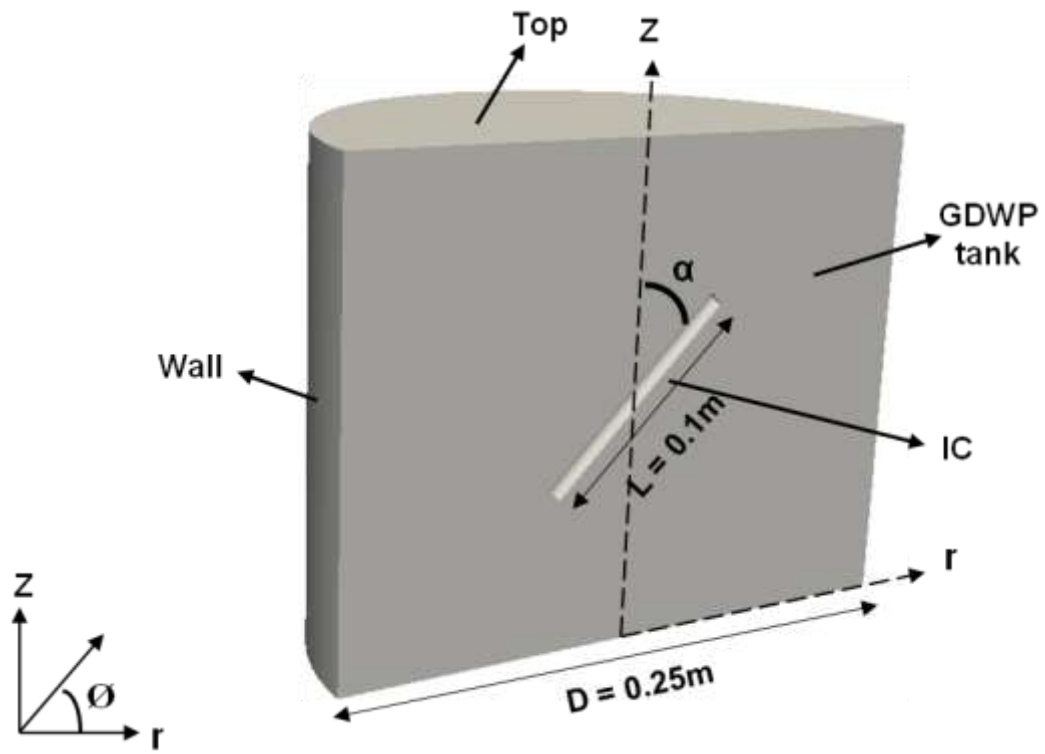
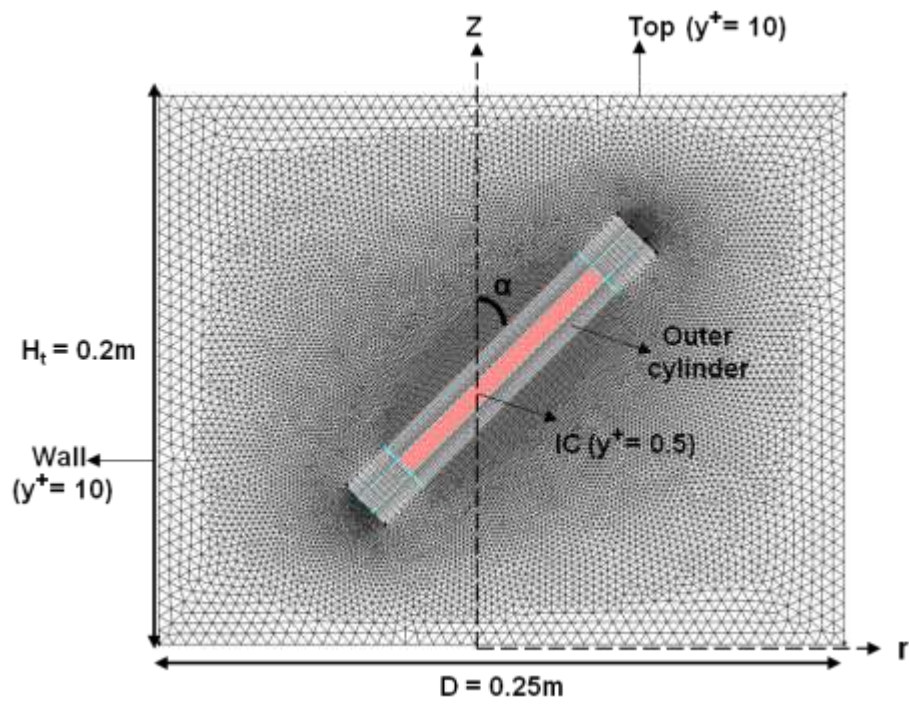


Fig 6.2: Comparison of present CFD model and experimental data of Ganguli et al. (2010) to study transient heat flux distribution. Experimental value (1) Natural Convection (■); (2) Quenching (▲); (3) Evaporation (●), CFD (—)



(A)



(B)

Fig 6.3: (A) Schematic of pilot scale GDWP with single inclined IC tube and (B) Grid generation

6.4 Results and discussions

The overall objective of the present work is to design an efficient and economical IC for the PDHRS which satisfies the design criterion of achieving 50% heat decay in less than 100s and the maximum possible mitigation of temperature stratification. The effect of inclination of condenser tubes on the flow field and the bubble sliding motion over inclined tubes for seven inclination angles ($\alpha = 0^\circ, 15^\circ, 30^\circ, 45^\circ, 60^\circ, 75^\circ, 90^\circ$) have been studied. Further, the effect of these fields on mixing and thermal stratification inside GDWP has been investigated. Initially, such an analysis was performed for a pilot scale GDWP (10 lit) and the optimum results were tested for the large scale GDWP ($\sim 10000\text{m}^3$).

Table 6.5: Design details of pilot scale and large scale GDWP and Isolation condenser (ICs)

System	Tank dimensions (m)	IC Tube dimensions (m)	Header dimensions (m)
Pilot scale GDWP	$D=0.25, H=0.2m$	$d=0.0071, h=0.1m$	
Large scale GDWP	$OD=50, ID=12, H_T=5, \phi = -22.5^\circ \text{ to } 22.5^\circ$	$No. \text{ of tubes } = 40$ $D_t = 0.4m, \text{ pitch } = 0.726m,$ $\alpha = 75^\circ,$ $\phi = -11.25^\circ \text{ to } 11.25^\circ$	$D_h = 0.6m, L_h = 14.5m$

6.4.1 Effect of inclination of IC tube for pilot scale GDWP

6.4.1.1 Geometry and Boundary conditions

In this section, two phase mixing and thermal stratification phenomenon has been studied inside a pilot scale GDWP (10 liters, Fig 6.3A) provided with a heating tube (IC) at centre. The detailed dimensions of pilot scale GDWP and heating tube are given in Table 6.5. The inclination angle (α) of the tube with respect to vertical axis (z) was varied in the range 0° to 90° ($\alpha = 0^\circ, 15^\circ, 30^\circ, 45^\circ, 60^\circ, 75^\circ, 90^\circ$) by considering tube centre as a point, located 0.1m from the bottom. The details of the boundary conditions for pilot scale GDWP are given in Table 6.6. The sidewalls, the bottom of the tank, were considered as adiabatic with no slip boundary condition. A constant temperature ($T_w = 558 \text{ K}$) boundary condition was specified on the surfaces of the IC tube. This value corresponds to

Table 6.6: Details of the boundary conditions for pilot scale GDWP:

Zone	Boundary Conditions	
	Temperature	Velocity
IC	$T=558\text{k}$	No slip $(u_r = u_\phi = u_z = 0)$
Top	Adiabatic $(\partial T / \partial z = 0)$	Free slip $\left(\frac{\partial u_r}{\partial z} = \frac{\partial u_\phi}{\partial z} = 0, u_z = 0 \right)$
Walls	Adiabatic $(\partial T / \partial r = 0)$	No slip $(u_r = u_\phi = u_z = 0)$

the saturation temperature of steam at 7 MPa pressure. Water in the open cylindrical tank can have motion in the radial as well as in tangential direction at the free water surface. However, water does not escape the surface (except in the form of water vapor). Therefore, the boundary conditions at the top liquid surface are as follow:

$$\frac{\partial u_r}{\partial z} = \frac{\partial u_\phi}{\partial z} = 0 \text{ and } u_z = 0 \quad (6.31)$$

At $\phi = 0^\circ$, symmetry plane is considered having boundary conditions as follows:

$$\frac{\partial u_r}{\partial \phi} = \frac{\partial u_\phi}{\partial \phi} = \frac{\partial u_z}{\partial \phi} = 0 \quad (6.32)$$

All the three terms in Eq (6.32) represent symmetry. Secondly, the condition of $u_z = 0$ at $z = 0.2\text{m}$ and at all r and θ permits the description of “no escape of water (in the liquid form) from the top surface”. In a real life situation, as the time progresses, vapor is generated in the system, which escapes into the atmosphere thereby decreasing the liquid level. However, the liquid phase does not leave the domain. Therefore, in the present work the "opening or degassing" boundary condition was implemented by creating a small "domain" near the top free surface of the GDWP tank.

6.4.1.2 Grid independence

The grid sensitivity analysis for pilot scale GDWP has been performed at three tube inclination angles ($\alpha = 0^\circ, 45^\circ, 90^\circ$). For instance, three different grids were selected: (1) 0.3M (2) 0.6M and (3) 0.8M for the case of inclination angle ($\alpha = 45^\circ$). The open source software Gmsh 2.9 (Remacle et al., 2012) has been used for geometry and mesh generation. In natural convection systems, higher

gradient of velocity as well as temperature are present near the heat source (IC tube) region. Further, it results in onset of nucleate boiling near the tube. Accordingly, in the present work, an artificial cylindrical volume ($l=0.14\text{m}$, $d=20\text{mm}$) shown in Fig 6.3B was created enclosing the IC tube. The non-uniform hexahedral grid consisting of dense meshing was employed in this cylindrical volume which was finer close to the boundary layer of the IC tube. 30 nodes were assigned along the circumference of 7mm IC tube and 15 rows which begin with the first row of 0.01mm ($y^+ = 0.5$) and growth factor of 1.1, from the concentrated grids around the IC tube. 100 nodes were assigned along the 0.1m length of IC tube. Away from this volume surrounding the IC tube (Fig 6.3B), tetrahedral mesh of uniform grid size (5mm) was employed. Grid independence study has been executed by comparing the axial temperature and velocity at $t = 8\text{s}$ for three grid densities (0.3M, 0.6M, 0.8M). The peaks in axial temperature (Fig 6.4A) and velocity (Fig 6.4B) profile shows the onset of nucleate boiling near the IC tube. The non-uniform temperature and velocity distribution along the length of the tube indicates the occurrence of boiling at different locations along the tube. All the chosen grids predict the temperature and mean flow patterns effectively. Minor differences (less than 1%) were observed between 0.6M and 0.8M cells as shown in Figs 6.4A and 6.4B (lines 2 and 3) in terms of temperature and velocities. Therefore, for all the simulations in the present work, 0.6M cells have been used for pilot scale assembly.

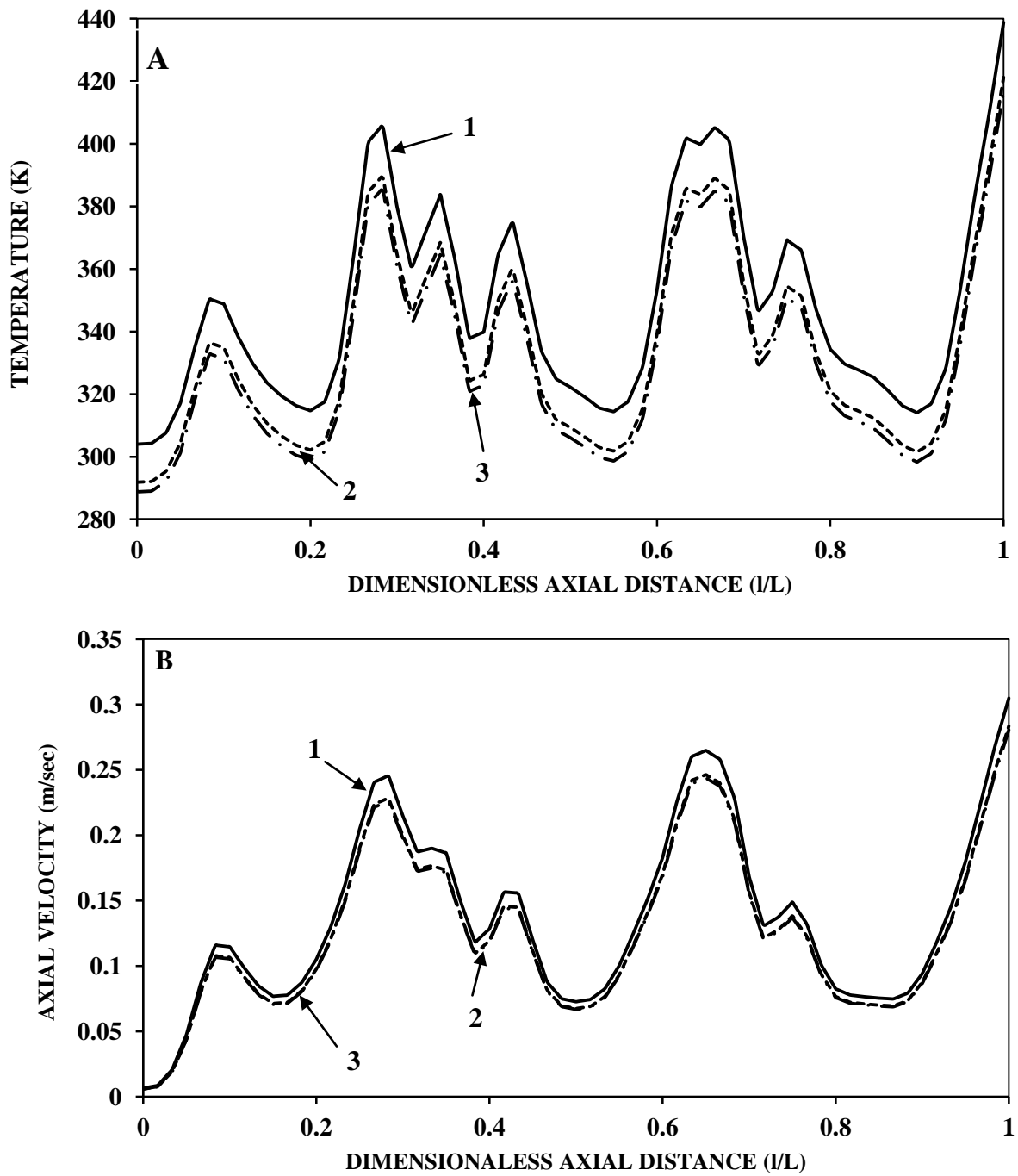


Fig 6.4: Effect of grid size for inclined heat source ($\alpha = 45^\circ$): Variation in (A) Axial temperature and (B) Axial velocity at 1mm away from the heat source at $t = 8s$ for different grid sizes (1) 0.3M; (2) 0.6M; (3) 0.8M.

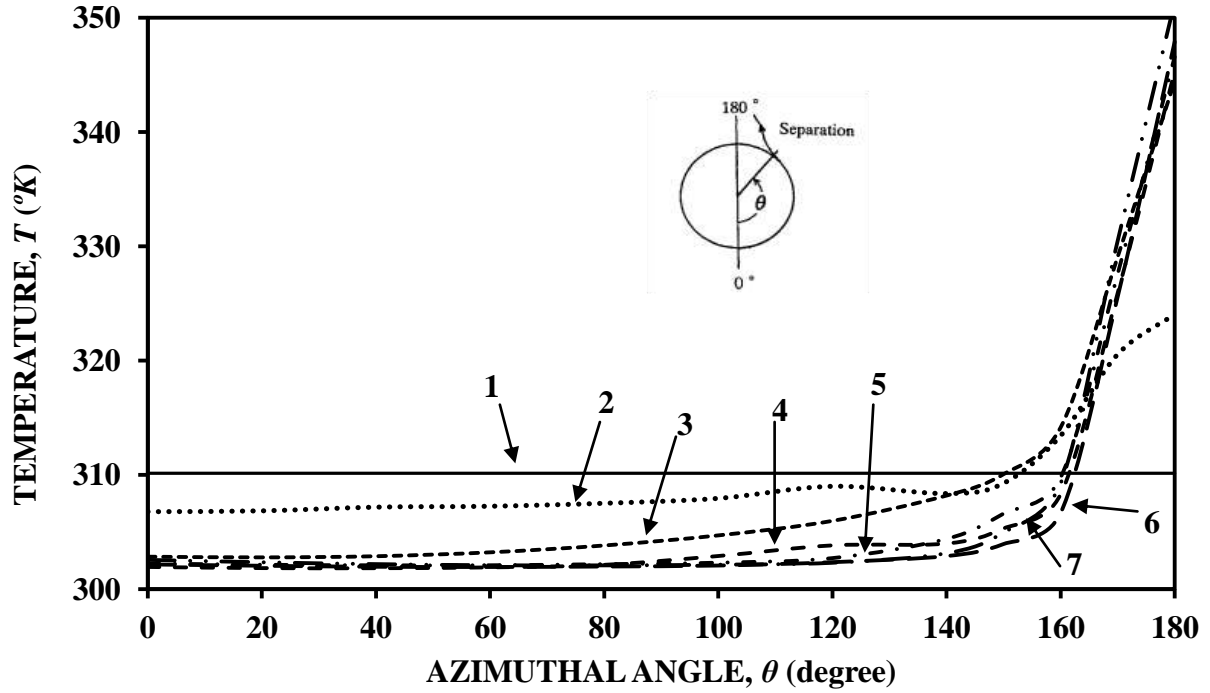


Fig 6.5: Azimuthal variation of fluid temperature at 1mm away from the tube at $t=10s$ for different inclination angle (1) $\alpha=0^\circ$; (2) $\alpha=15^\circ$; (3) $\alpha=30^\circ$; (4) $\alpha=45^\circ$; (5) $\alpha=60^\circ$; (6) $\alpha=75^\circ$; (7) $\alpha=90^\circ$

6.4.1.3 Azimuthal Variation of Temperature and Vapor fraction

The azimuthal ($0^\circ \leq \theta \leq 180^\circ$) variation of fluid temperature at 1mm away from the IC tube for different inclination angles ($\alpha = 0^\circ, 15^\circ, 30^\circ, 45^\circ, 60^\circ, 75^\circ, 90^\circ$) is shown in Fig 6.5. When the tube was vertical ($\alpha = 0^\circ$), the temperature and vapor fraction (ϵ_G) can be seen (Fig 6.5 and Fig 6.6A) to be uniform along the azimuthal (θ) direction. For the vertical heated tube ($\alpha = 0^\circ$), the buoyancy force due to density difference acts in the vertical direction. Hence, the bubbles all around the tube tend to slide along the surface and parallel to the axis of the tube. As a result, there is a nominal variation in azimuthal temperature (case (1) in Fig 6.5) for vertical heated tube. When the tube is inclined ($\alpha > 0^\circ$), the temperature and vapor fraction (ϵ_G) (Fig 6.6) can be seen to be minimum at the bottom ($\theta = 0^\circ$) and maximum at the top ($\theta = 180^\circ$) of the tube. A very sharp increase (14%) in temperature has been observed in the region ($160^\circ \leq \theta \leq 180^\circ$) whereas nominal temperature variation in the region ($0^\circ \leq \theta \leq 160^\circ$). The bubbles from the bottom of the tube tend to slide along the tube surface (azimuthal direction) due to buoyancy force acting in the vertical direction. The

bubbles accelerate in the region ($0^\circ \leq \theta \leq 90^\circ$) due to favorable pressure gradient ($\frac{\partial P}{\partial \theta} < 0$) and decelerate in the region ($90^\circ \leq \theta \leq 160^\circ$) due to adverse pressure gradient ($\frac{\partial P}{\partial \theta} > 0$). The bubbles separate from the tube surface at $\theta_{sep} = 160^\circ$ (Fig 6.5) and results in (a) creating a low pressure as well as (b) increasing the fluid temperature in the region ($160^\circ \leq \theta \leq 180^\circ$) and (c) formation of big bubble cluster (having vapor fraction in the range 0.7- 0.8 as shown by red color in Fig 6.6) after the point of separation. The pressure gradient in the region ($160^\circ \leq \theta \leq 180^\circ$) generates a primary flow which drives the bubbles along the tube length and results in an increase in the axial velocity (Fig 6.7C) as the bubble travels upstream. As the angle of inclination (α) increases, the primary flow

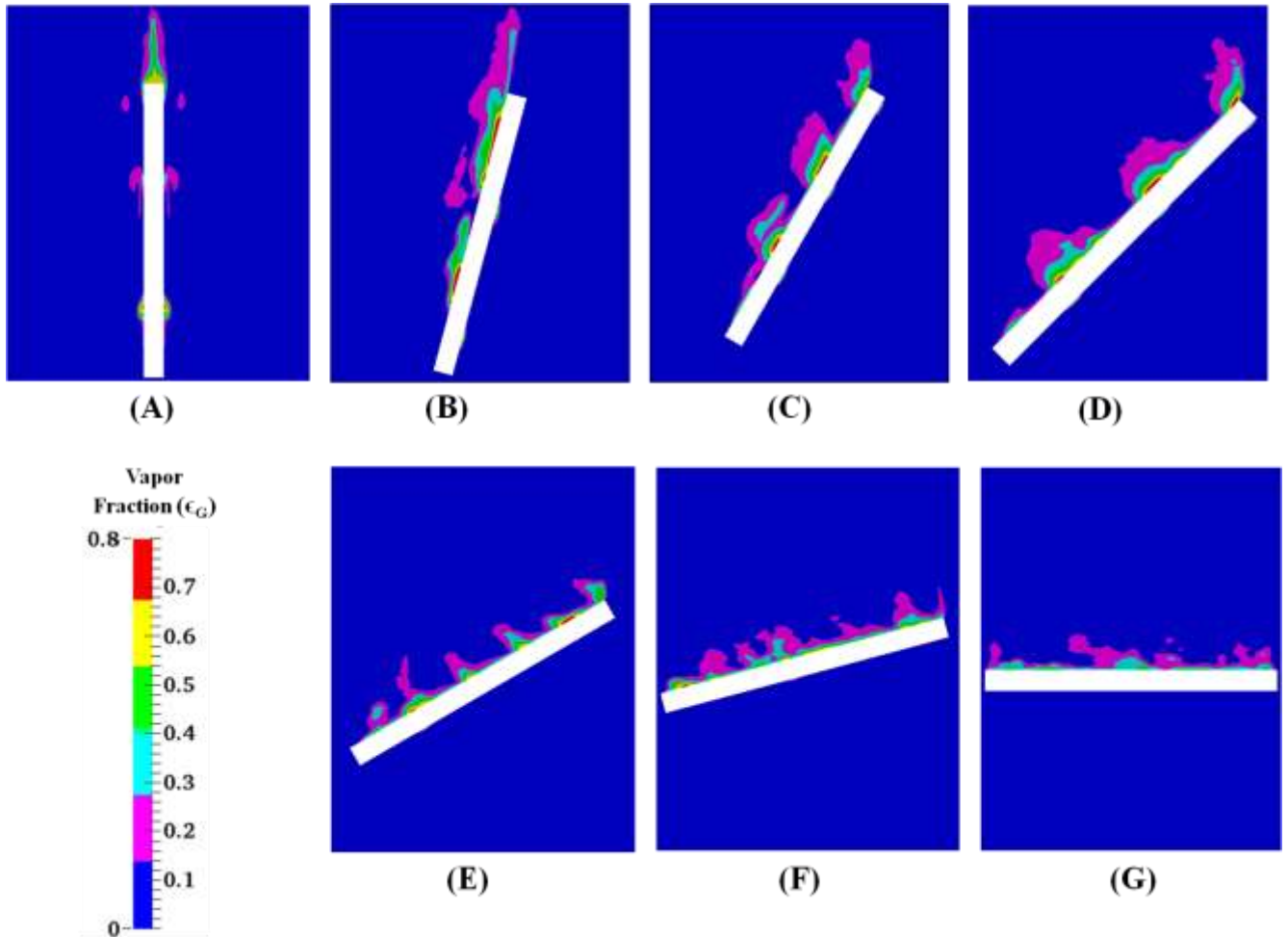
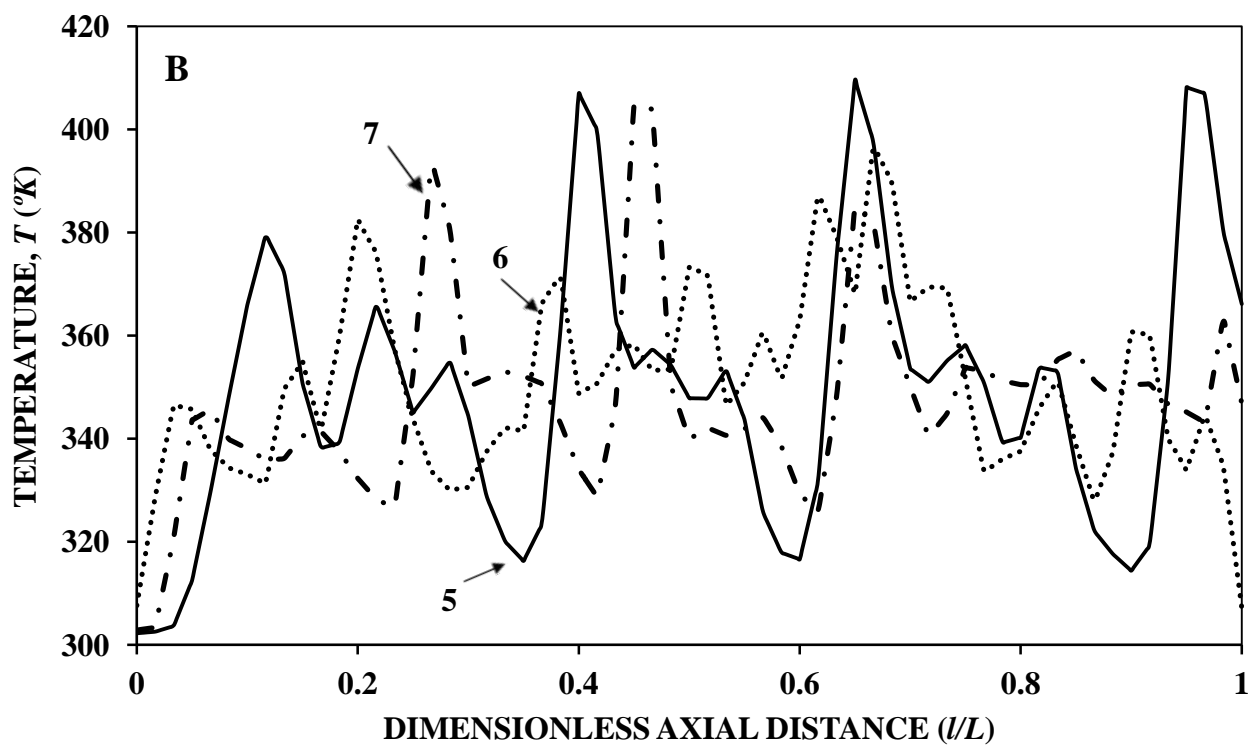
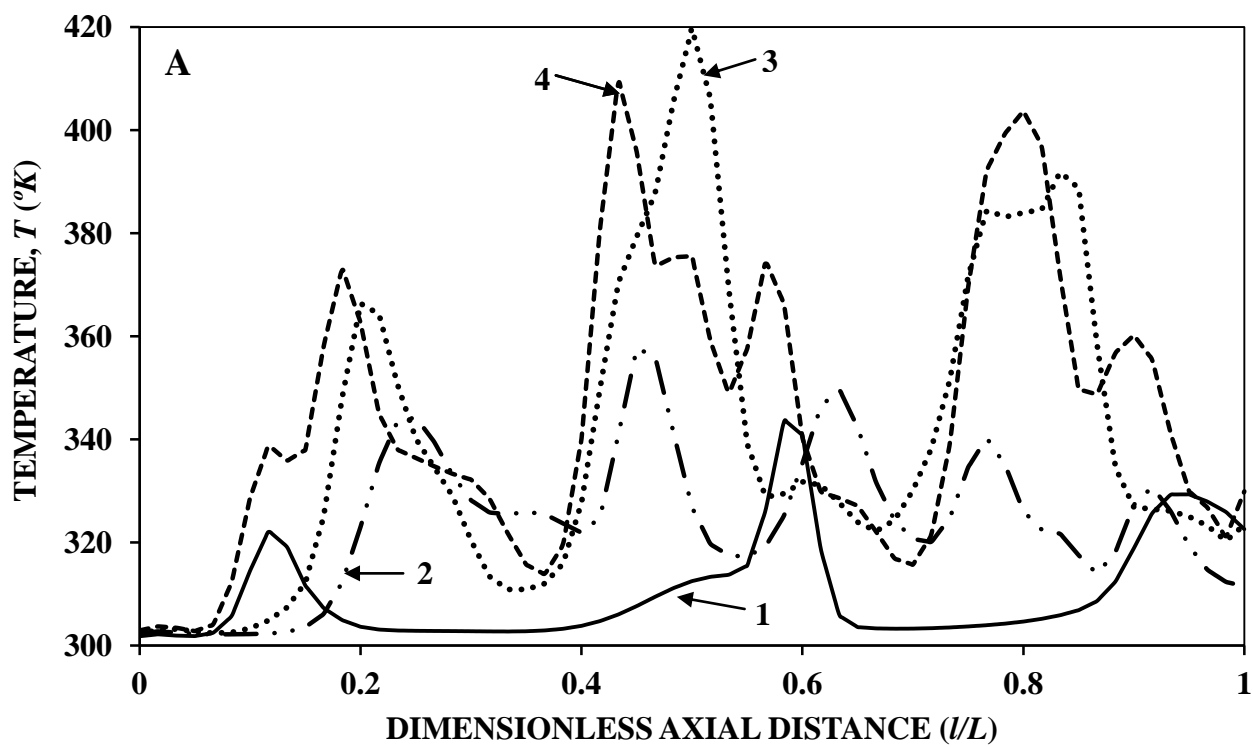


Fig 6.6: Vapor Fraction Contours for different inclination angles at $t=10s$ along symmetry plane:
 (A) $\alpha= 0^\circ$; (B) $\alpha= 15^\circ$; (C) $\alpha= 30^\circ$; (D) $\alpha= 45^\circ$; (E) $\alpha= 60^\circ$; (F) $\alpha= 75^\circ$; (F) $\alpha= 90^\circ$



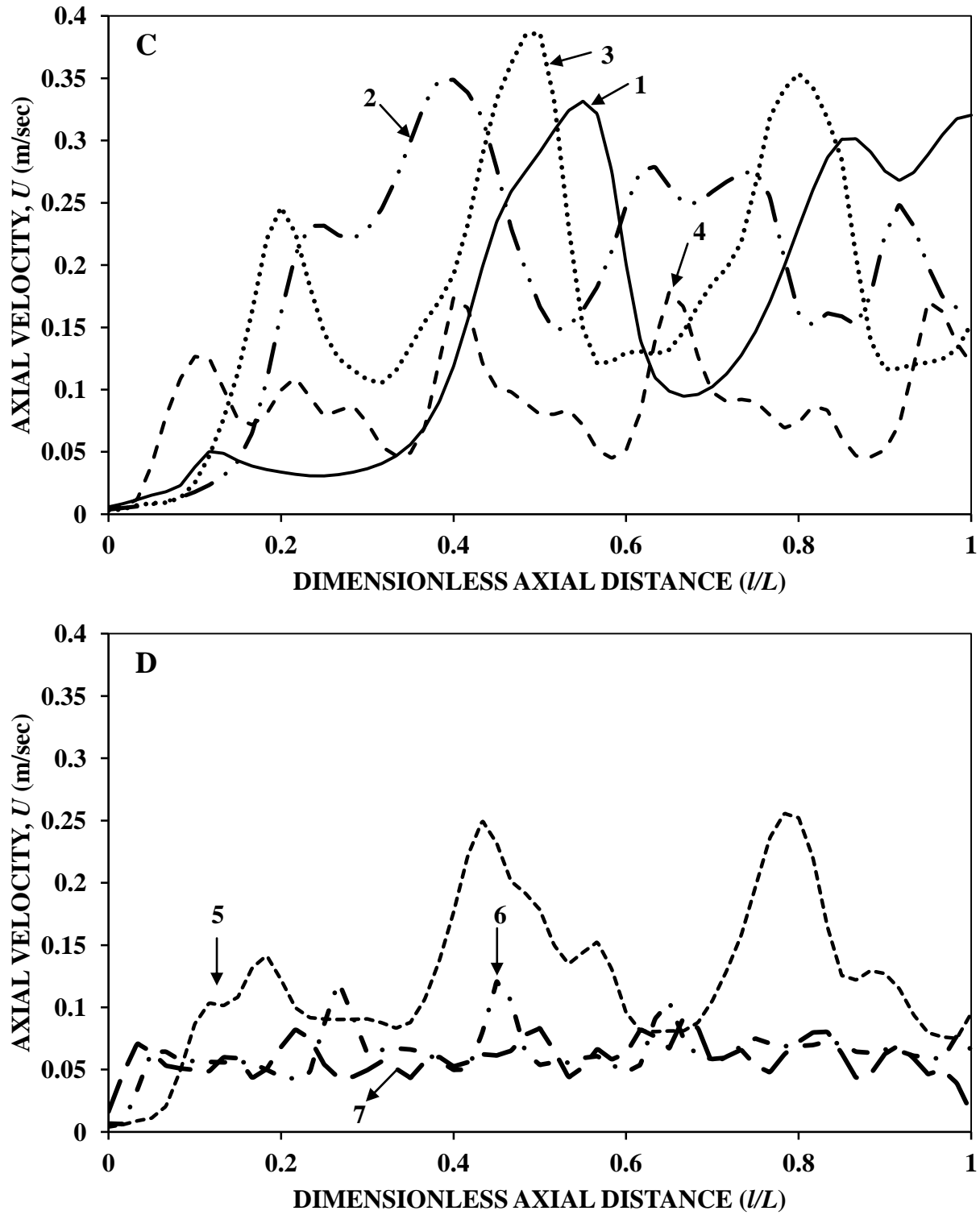


Fig 6.7: Effect of inclination of IC tube on (A) and (B) Axial temperature and (C) and (D) Axial velocity at $t=10$ s and 1mm away from the tube for different inclination angles;
(1) $\alpha=0^\circ$; (2) $\alpha=15^\circ$; (3) $\alpha=30^\circ$; (4) $\alpha=45^\circ$; (5) $\alpha=60^\circ$; (6) $\alpha=75^\circ$; (7) $\alpha=90^\circ$

(along the tube length due to pressure gradient) decreases and the secondary flow (along vertical direction due to buoyancy forces) become stronger. Further, it enhances the bubble sliding motion at the tube bottom and prevents the bubble sliding motion at the top of the tube. This behavior is in accordance with the experimental observation of (Sateesh et al., 2009). The increase in bubble sliding length at the bottom of the tube results in enhanced heat transfer. Further, it results in a decrease in the fluid temperature. For the horizontal heated tube ($\alpha = 90^\circ$), there is no primary flow and the secondary flow due to buoyancy forces acts completely perpendicular to the tube. The stronger secondary flow provides sufficient kinetic energy to overcome the adverse pressure gradient near the tube periphery and results in delay in flow separation. Hence, minimum fluid temperature is found for the horizontal heated tube.

6.4.1.4 Flow patterns associated with bubble sliding motion

The vapor fraction contours obtained from the CFD simulations at seven different inclination angles at $t = 10\text{s}$ are shown in Fig 6.6. For vertical heated tube ($\alpha = 0^\circ$), due to large temperature gradient ($\Delta T = 258\text{K}$) in the vicinity of heat source, the fluid adjacent to the heat source gets heated becomes lighter and rises. As the hot fluid rises along the tube length, the fluid temperature continues to increase because of continuous addition of enthalpy from the heated tube. The bubble forms in a superheated liquid adjacent to the heated tube. The temperature and velocity peaks near the heated tube for case (1) in Fig 6.7A and Fig 6.7C further confirms the bubble formation near the heated tube. The bubbles slide along the tube surface (Fig 6.6A) for some distance before departing away from the tube. The sliding motion of the bubble results in enhanced liquid convection as well as enhanced turbulence (eddy conduction). These enhancements are accompanied by enhancements in the rates of heat transfer from the tube. Fig 6.6A shows that the bubble formation along the tube length is not continuous and uniform. For vertical heated tube ($\alpha = 0^\circ$), the onset of boiling occurs at $l/L = 0.15$. The temperature peak at $l/L = 0.15$ for case (1) in Fig 6.7A, further confirms this behavior. The bubble slides along the tube for some distance before departing away from the tube. During the

bubble sliding motion, there is a continuous growth of the vapor bubble due to evaporation of liquid layer underneath the bubble which further results in increase in vapor fraction. As the bubble departs the cold liquid from the neighboring areas rushes in to take its place and results in enhanced heat transfer from the tube surface. Further, it results in decrease in fluid temperature ($0.15 < l/L < 0.4$). As the fluid travel further downstream ($0.4 < l/L < 0.6$), the fluid temperature increases again and reaches saturation temperature. Further, it results in vapor formation at $l/L = 0.6$. At the top of the heated tube, the fluid from all around the tube mix with each other and form a turbulent plume which results in enhancement in velocity and turbulent kinetic energy. The increase in inclination angle (α) results in decrease in formation of big bubble cluster (having vapor fraction (ϵ_G) in the range 0.7-0.8 shown in Fig 6.6) and bubble sliding motion at the top of the tube. The decrease in bubble sliding motion at the top, further results in decrease in fluid axial velocity (Fig 6.7C).

6.4.1.5 Transient bubble formation over inclined tube

The vapor fraction profile in Fig 6.8 (perpendicular to the tube) shows the transient behavior of bubble growth and fluid flow associated with it for an inclined ($\alpha = 60^\circ$) heated tube. Bubble growth occur in three steps (1) the bubble forms ($t = 0.45s$) in a superheated liquid adjacent to the tube surface (2) the bubble grows at a rate close to that of bubble radius (3) the bubble, after having reached a maximum radius, recedes till a neck forms ($t = 0.5s$) and the bubble starts to depart ($t = 0.55s$) from the surface. During the growth period ($0.45s < t < 0.55s$), the bubble pushes the liquid at its periphery in the outward direction. Immediately after the detachment, the lower surface of the bubble deforms (mushroom shaped) and liquid is entrained in the wake of the detaching and rising bubble. Following the bubble departure, colder liquid from the neighboring areas comes in contact with the tube surface and gets heated during the delay time, at the end of which another bubble is nucleated from the tube. Further, it results in enhanced heat transfer from the tube. The new bubble grows for some time (growth period) and then departs from the tube surface and the process is repeated. A bubble column is thus formed by bubbles successively rising from a nucleating center.

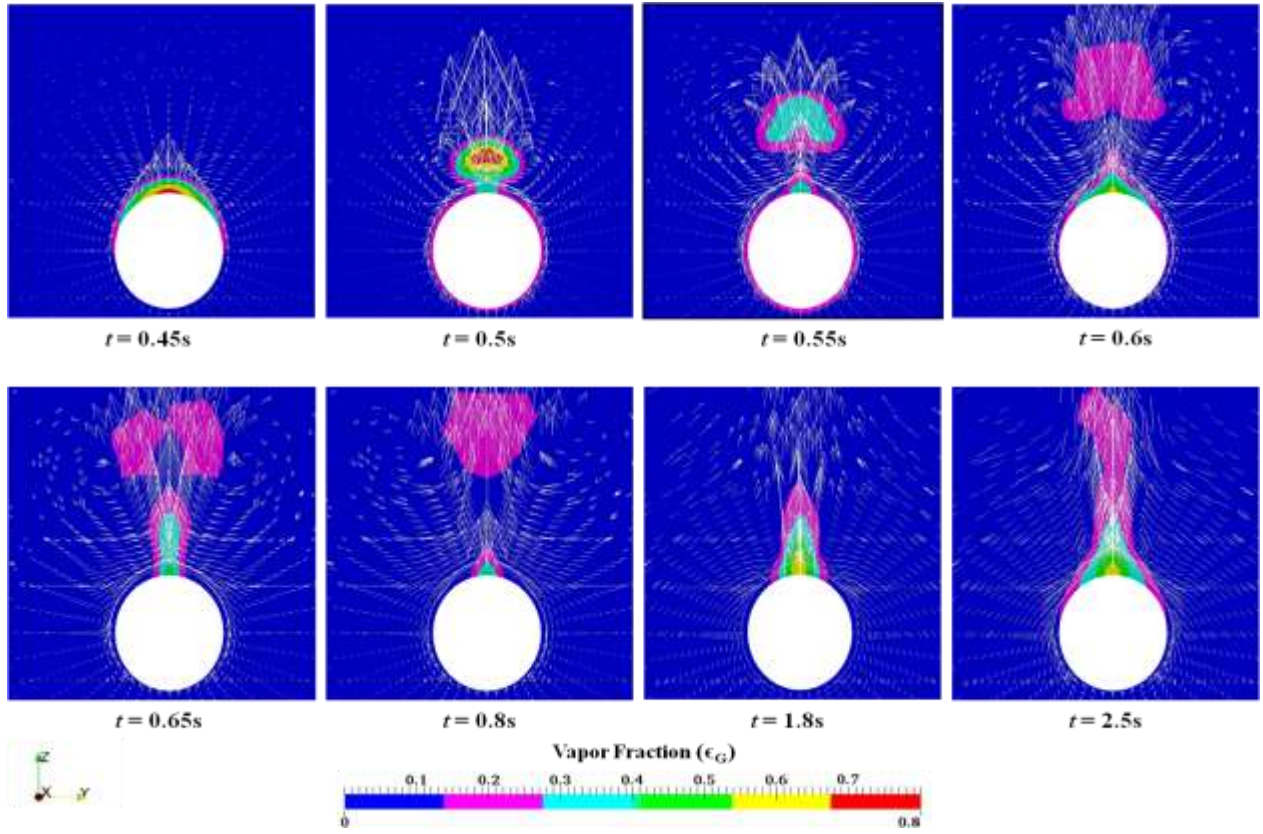


Fig 6.8: Transient vapor fraction contour and fluid flow perpendicular to the tube for inclined ($\alpha = 60^\circ$) tube

As the time progresses ($t > 0.65s$), the spacing between rising bubbles decreases so that bubble interacts with its predecessor and form a continuous vapor column ($t = 2.5s$).

The vapor fraction contours in Fig 6.9 shows the transient behavior of bubble formation and bubble sliding motion along the tube length. Initially (at $t = 0.45s$), at the top of the tube, there is a uniform thin vapor film along the tube length. This behavior was because of bubble separation near the tube top due to adverse pressure gradient. As the time progresses (at $t > 0.45s$), the bubble starts to depart from the tube surface and results into a decrease in the vapor fraction near the tube. After departure, the bubble rises in the vertical direction and vapor fraction decreases due to sub cooled liquid surrounding the bubble. At $t = 1.1 s$, the convective flow starts to develop near the heated tube. The bubble departs from the tube surface near the bottom of the tube and results in a decrease in the vapor fraction at that location. As the time progresses ($t > 1.1 s$), the bubble slides along the tube

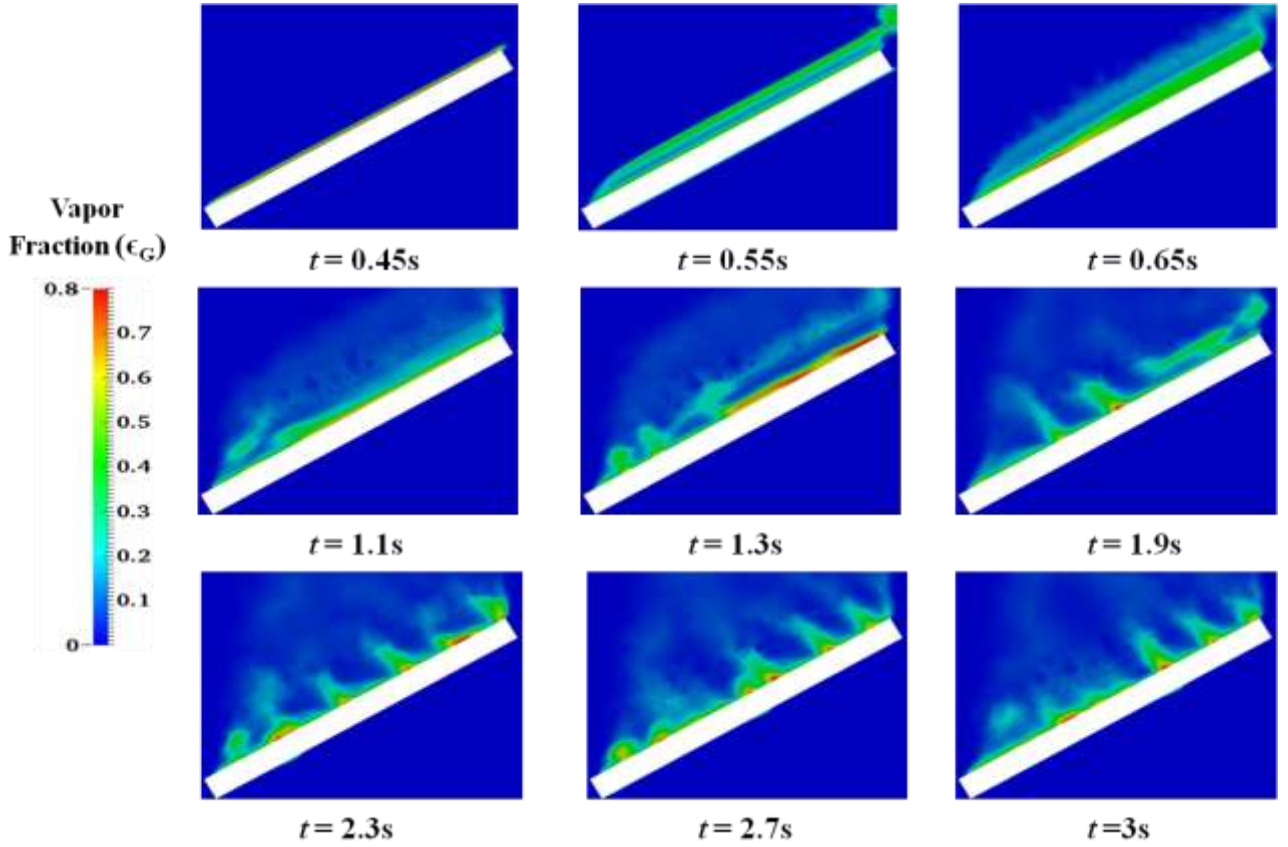


Fig 6.9: Transient vapor formation along the tube length for inclined ($\alpha = 60^\circ$) tube at symmetry plane

length from bottom to top. The bubble sliding motion results in enhanced liquid convection and discrete vapor formation along the tube length.

6.4.1.6 Fluid flow near the upward and downward face of the heated tube

The vapor fraction (ϵ_G) contour in Fig 6.6 shows that the vapor fraction at the top ($\theta = 180^\circ$) of the heated tube was higher than that at the bottom ($\theta = 0^\circ$). As the angle of inclination ($\alpha > 0^\circ$) of IC tube increases, the temperature of the fluid near the IC top ($\theta = 180^\circ$) (Fig 6.7A) increases whereas the temperature near the IC bottom ($\theta = 0^\circ$) decreases. This behavior is due to the increase in bubble sliding length at the bottom of the tube and a decrease in the bubble sliding length at the tube top. As the bubble slides along the tube, it agitates the surrounding liquid, disrupts the thermal boundary layer along the tube surface and contributes to enhanced heat transfer. Further, it results in a decrease in fluid temperature. In addition, the bubble sliding motion enhances the turbulent natural

convection. As the angle of inclination ($\alpha > 0^\circ$) of IC tube increases, the pressure gradient which drives the flow (primary) along the tube length becomes weaker whereas the buoyancy force which drives the flow (secondary) in the vertical direction becomes stronger. The stronger secondary flow results in an increase in the bubble sliding length at the bottom of the tube and prevents the bubble sliding motion near the tube top. Further, it results in enhanced heat transfer at the bottom of the tube and reduced heat transfer at the tube top. Cornwell and Einarsson (1990); Sateesh et al. (2009) have also reported similar behavior of higher heat transfer coefficient at the tube bottom and lower heat transfer coefficient at the tube top. In addition to the reduced sliding length, the stronger secondary flow also prevents the formation of big bubble cluster [having vapor fraction (ϵ_G) in the range 0.7-0.8 shown in Fig 6.6] at the top of the tube.

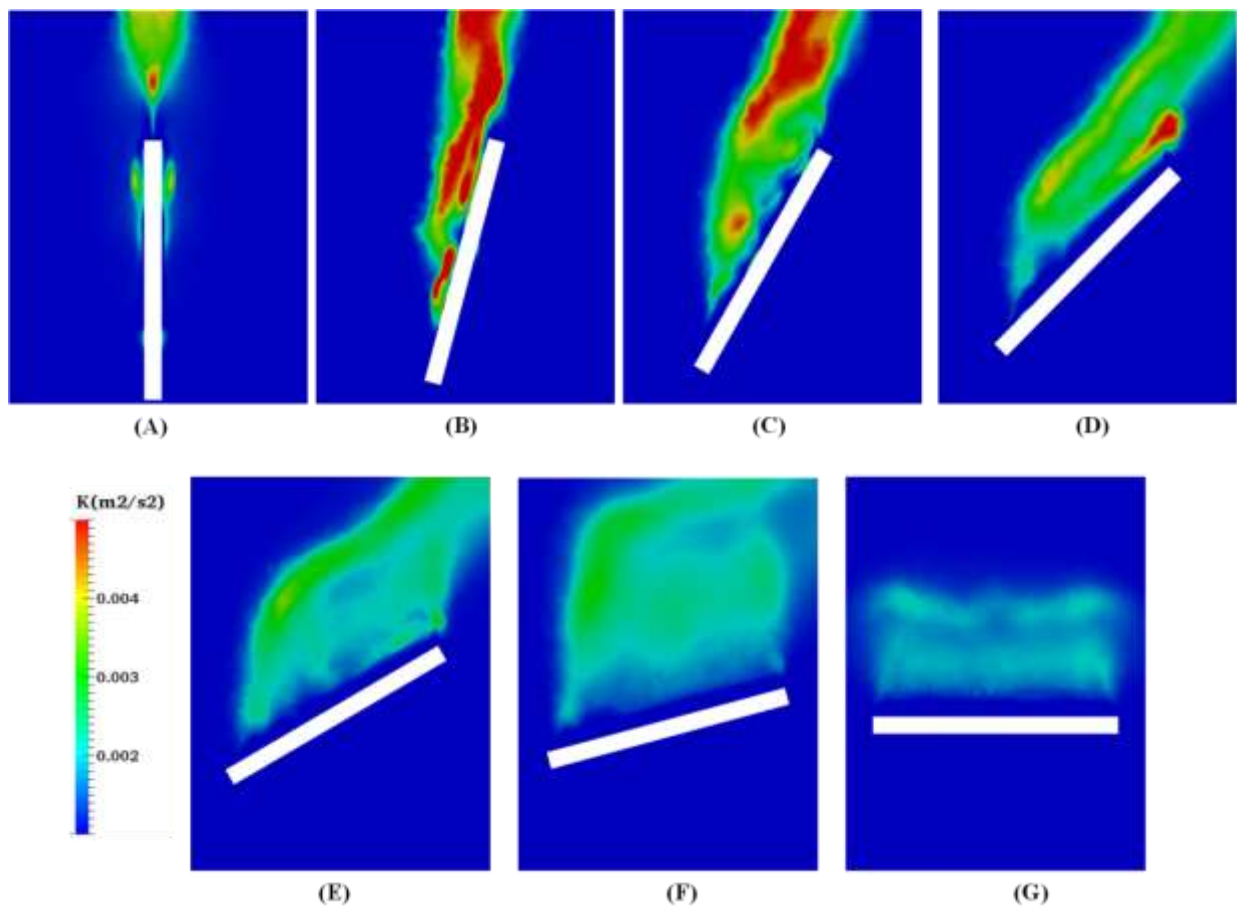


Fig 6.10: Turbulent kinetic energy contours for different inclination angles at $t=10s$ along symmetry plane : (A) $\alpha=0^\circ$; (B) $\alpha=15^\circ$; (C) $\alpha=30^\circ$; (D) $\alpha=45^\circ$; (E) $\alpha=60^\circ$; (F) $\alpha=75^\circ$; (G) $\alpha=90^\circ$

6.4.1.7 Turbulent kinetic energy (k) contour

The turbulent kinetic energy (k) decreases with an increase in the inclination angle (α) as shown in Fig 6.10. It is due to a decrease in the axial velocity (Fig 6.7C) with an increase in the inclination angle. The laminar-turbulent transition along the tube length can also be seen clearly in Fig 6.10. The value of turbulent kinetic energy (k) was almost zero before the transition point, and it reaches a high value just after the transition point. For $\alpha = 15^\circ, 30^\circ, 45^\circ, 60^\circ, 75^\circ, 90^\circ$, the k contour shows that, in the vicinity of heated tube, the value of k was almost zero implying no turbulence. This particular trend in k profile shows that the fluid flow around the tube was 2D and laminar at the beginning. As the fluid travels from bottom ($\theta = 0^\circ$) to the top ($\theta = 180^\circ$), the buoyant plume from both sides of the tube come together and interacts with each other at some distance away from the top of the tube. The interaction between the buoyant plumes results in large velocity fluctuations. Further, it also results in enhanced turbulence. It was also observed that, for smaller inclination angles, the turbulence was very high and concentrated mainly in a small region near the top of the tube. As the angle of inclination (α) increases, the turbulence was diffused away from the heated tube. This behavior is due to the fact that with an increase in the inclination angle (α), the buoyant force becomes stronger and drives the fluid away from the tube.

6.4.1.8 Transient heat transfer

The transient heat transfer behavior in Fig 6.11A shows that the heat transfer rate was maximum at the beginning ($t = 0$ s) because of large ΔT and then it decreases very sharply for few seconds till evaporation starts at the tube surface. The average total heat transfer coefficient (h_{tot}) was calculated as follows:

$$Q_{tot} = Q_{nat} + Q_{eva} + Q_{que} = \dot{m}_L C_p \overline{\Delta T}_{w,t} + \dot{m}_G \lambda \quad (6.33)$$

$$\overline{\Delta T}_{w,t} = \overline{T}_{w,t} - T_{w,t=0} \quad (6.34)$$

$$\overline{T}_{w,t} = \frac{\iiint_{r,\theta,z}^{R,\theta,Z} T_{w,t} dr d\theta dz}{\iiint_{r,\theta,z}^{R,\theta,Z} dr d\theta dz} \quad (6.35)$$

$$Q_{tot} = h_{tot} A \overline{\Delta T}_{s,t}$$

$$\overline{\Delta T}_{s,t} = T_{s,t} - \bar{T}_{w,t} \quad (6.36)$$

$$\bar{T}_{s,t} = \frac{\iint_{L,\theta}^{L,\theta} T_{s,t} dld\theta}{\iint_{L,\theta}^{L,\theta} dld\theta} \quad (6.37)$$

$h_{tot} = \frac{Q_{tot}}{A \overline{\Delta T}_{s,t}}$, where h_{tot} has been calculated at different time intervals. During the transient ($0 < t < 5s$) (Fig 6.11A) the heat transfer behavior has been divided into three domains: conduction ($0 < t < 0.2s$), evaporation ($0.2s < t < 2s$) and quenching period ($2s < t < 5s$). Initially, the fluid is at rest. Hence, heat transfer occurs by conduction only. The decay in HTC is very steep in the conduction period ($0 < t < 0.2s$). The total heat transfer coefficient in this period was found to be independent of inclination angle (α). As the time progresses ($t > 0.2s$), the temperature of the fluid in the vicinity of the heated tube exceeds saturation temperature and results in vapor formation (Fig 6.11B). This period ($0.2s < t < 2s$) is known as evaporation period because the dominant mode of heat transfer is by vapor formation. The evaporation slows down the decay rate (Fig 6.11B). The total heat transfer coefficient in the evaporation period shows fluctuations with time. This behavior is attributable to the rate of vapor formation which was not uniform and shows oscillations with time. Further, as the time progresses ($t > 2s$), the convective flow starts to develop near the heated tube (IC) due to bubble sliding motion and heat transfer becomes increasingly dominated by bubble induced liquid convection. This period is known as quenching period and found to be the longest period. The heat transfer due to enhanced liquid convection caused by sliding bubbles was found to be more than that due to evaporation of the liquid layer underneath the bubbles in the evaporation period. The enhanced convection ($2s < t < 5s$) further slows down the decay of heat transfer. The total heat transfer coefficient was found to be dependent on inclination angle (α) in the quenching period. The total heat transfer was found to be maximum for $\alpha = 75^\circ$ and minimum for $\alpha = 30^\circ$. The heat transfer through the inclined tube depends upon three key parameters (1) bubble sliding motion along the

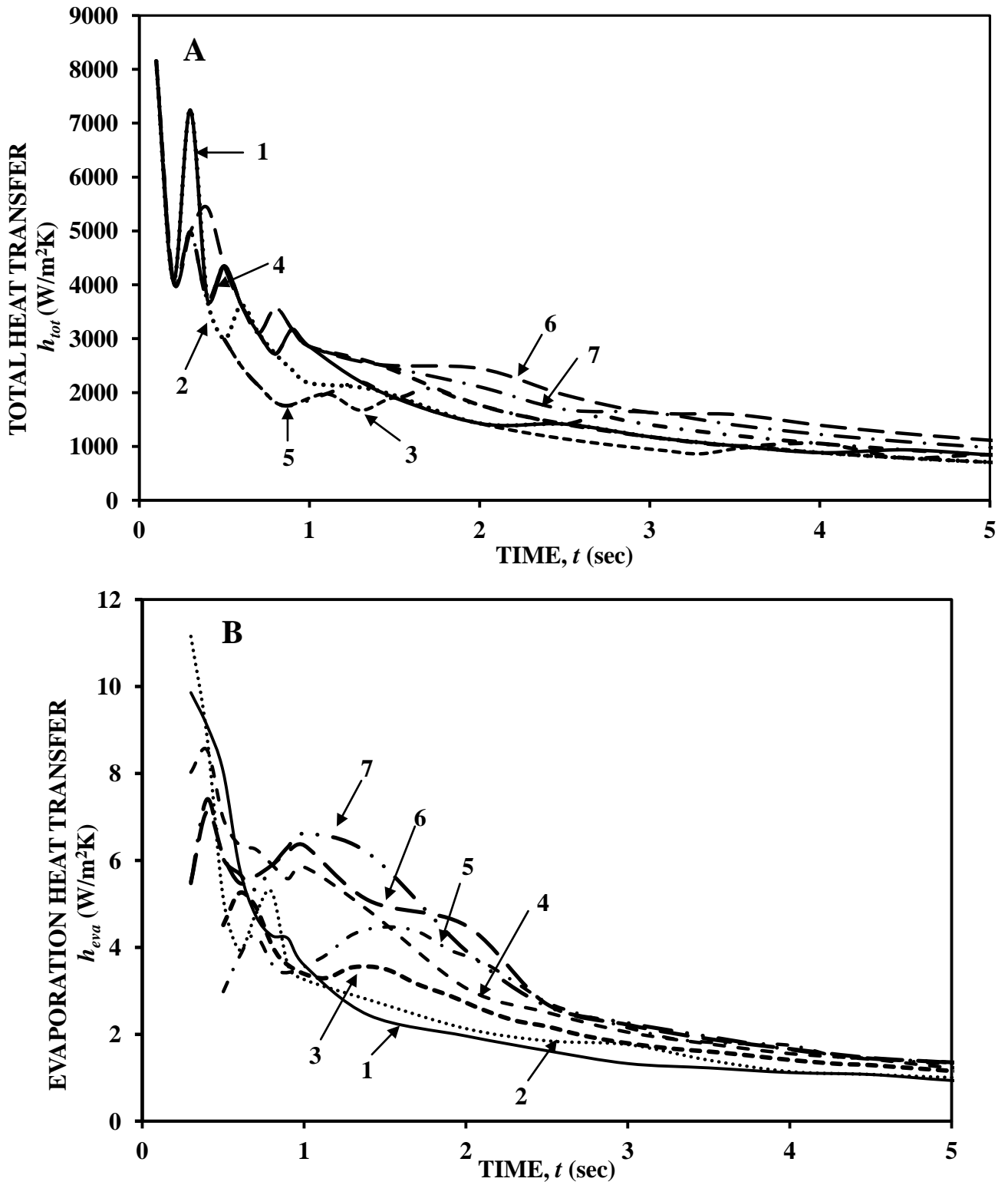


Fig 6.11: Transient variation of (A) Total heat transfer coefficient (h_{avg}) (B) Evaporation heat transfer coefficient (h_{eva}) with time for different inclination angles;
 (1) $\alpha = 0^\circ$; (2) $\alpha = 15^\circ$; (3) $\alpha = 30^\circ$; (4) $\alpha = 45^\circ$; (5) $\alpha = 60^\circ$; (6) $\alpha = 75^\circ$; (7) $\alpha = 90^\circ$

circumference of the tube (2) bubble sliding motion along the tube length (3) bubble detachment frequency. The bubble sliding motion along the tube length depends upon the pressure gradient near the tube top whereas the bubble sliding motion perpendicular (circumference) to the tube depends upon the buoyancy forces due to density gradient. It was observed that with an increase in the inclination angle (α), the bubble sliding motion along the tube length decreases whereas the bubble sliding motion perpendicular to the tube increases due to the increase in buoyant flow. The bubble detachment frequency also increases with an increase in the inclination angle (α) due to forces acting perpendicular to the tube. For $\alpha = 75^\circ$, the buoyant force overcome the pressure gradient near the tube top and results in enhancement in bubble sliding motion perpendicular to the tube. The enhanced liquid convection due to bubble sliding motion further results in enhanced bubble detachment frequency for $\alpha = 75^\circ$. On the other hand, the bubble sliding motion (perpendicular to the tube) as well as bubble detachment frequency was found to be minimum for $\alpha = 30^\circ$. The combined effect of enhanced bubble sliding motion as well as bubble detachment frequency results in maximum total heat transfer coefficient for the inclination angle $\alpha = 75^\circ$.

6.4.1.9 Quantification of Thermal Stratification

The procedure to calculate thermal stratification number was described in great detail in Section 3.5.1.3 of Chapter 3. In the present case, the simulation was carried up to $t = 10$ s and the stratification number was found to have a value of 0.76 (Fig 6.12) for the vertical heated tube ($\alpha = 0^\circ$). The stratification number first decreases with an increase in the inclination angle till $\alpha = 15^\circ$ and then it reaches a maximum value at $\alpha = 30^\circ$. For $\alpha > 30^\circ$, the stratification number decreases again with increase in inclination angle till it reaches a minimum value at $\alpha = 75^\circ$. This behavior is very much similar to the behavior in transient heat transfer coefficient in Section 6.4.1.8. The total heat transfer coefficient is found to be maximum for $\alpha = 75^\circ$ and minimum for $\alpha = 30^\circ$. This behavior is due to the interaction between primary and secondary flow. The primary flow results in enhancement in bubble sliding motion at the top whereas the secondary flow results in larger sliding distance from

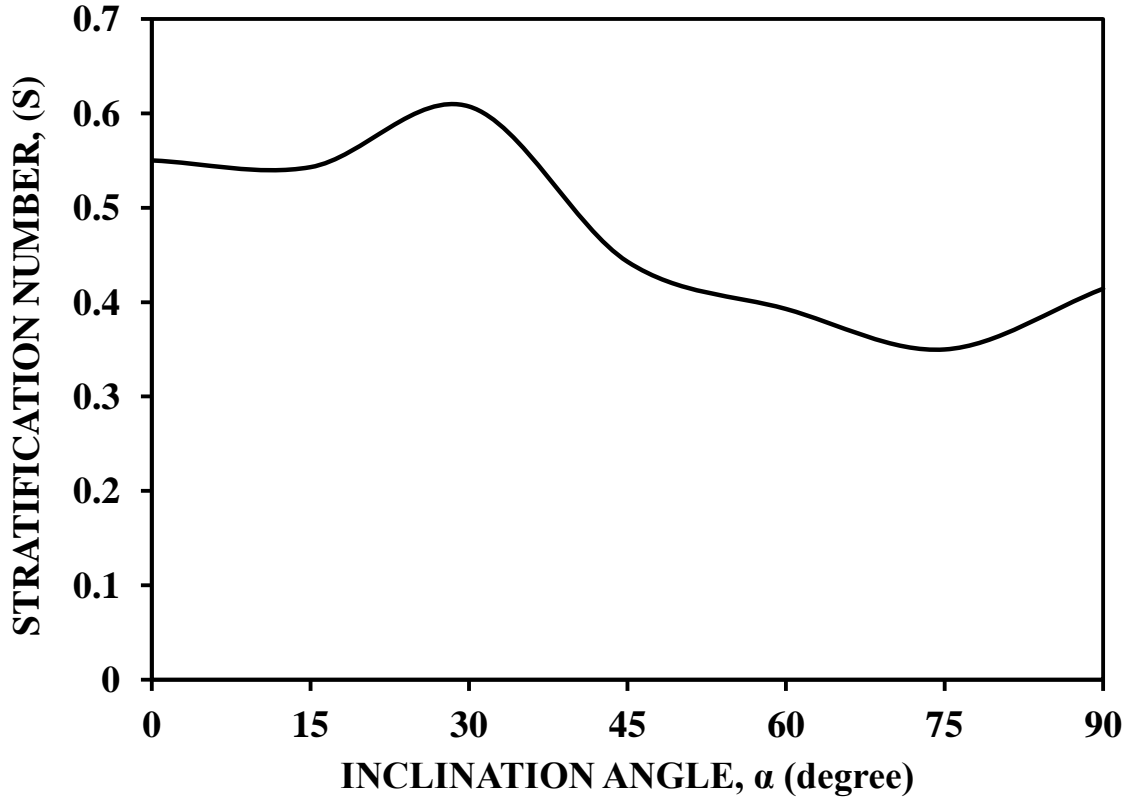


Fig 6.12: Effect of inclination of IC tube on thermal stratification (S) at $t = 10s$

the bottom of the tube till the separation point. As angle of inclination (α) increases, the secondary flow increases and primary flow decreases. The increase in bubble sliding motion from the bottom more than offsets the decrease in bubble sliding motion at the top and results in minimum stratification number ($S = 0.35$) and maximum total heat transfer coefficient for inclination angle $\alpha = 75^\circ$. The minimum stratification number at $\alpha = 75^\circ$ indicates excellent thermal mixing.

6.4.2 Condensation heat transfer over inclined tube

6.4.2.1 Analytical Model

The effect of inclination angle on two phase flow inside the IC has been studied using analytical model. The model is based on the work of Hassan and Jakob (1958); Fürst (1989); Fiedler and Auracher (2004). The detailed derivation of the analytical model is given in Appendix A at the end.

Fig 6.13B shows the distribution of condensate inside the tube inclined at an angle α ($\alpha = 90 - \beta$) w.r.t vertical direction. There are two distinct regions inside the tube (a) the condensate film

that drains at the circumference of the tube and (b) the condensate layer in the lowermost part of the tube. The height of this condensate layer is given by the angle ϕ^* (Fig 6.13B). The heat transfer (H) through the IC tube depends strongly on the condensate film thickness.

$$H = \left(\frac{\rho_1(\rho_1 - \rho_g)g\Delta h_v \lambda_1^3 \sin \alpha}{3\Delta T \eta_1 R} \frac{1}{\Psi} \right)^{1/4}$$

where Ψ is non-dimensional condensate film thickness given below:

$$\Psi = \frac{\rho_1(\rho_1 - \rho_g)g\Delta h_v \sin \alpha}{3\lambda_1 \Delta T \eta_1 R} \delta^4$$

The inclination angle has a strong effect on the condensate film thickness and hence condensation heat transfer. In case of vertical tube ($\alpha = 0^\circ$), the thickness of condensate film is uniform around the circumference of the tube and the thickness increases with increase in axial (z) position due to condensation. As a result, the average heat transfer is smallest for vertical tube ($\alpha = 0^\circ$). For higher inclination angle ($\alpha > 0^\circ$), the condensate film is no longer axisymmetric. The film thickness is very small in the upper region of the tube while a thicker stream of condensate drains in the lowermost part of the tube. The mean condensate film thickness decreases with increase in inclination angle ($\alpha > 0^\circ$) and therefore the mean heat transfer coefficient increases. In comparison to vertical tube ($\alpha = 0^\circ$), the film thickness does not decrease steadily with increase in axial location for inclined tube ($\alpha > 0^\circ$). The upper part of the tube reaches a limiting value that does not change in axial direction. Hence, the heat transfer decreases sharply for some distance and reaches a constant value after that axial position. At an inclination angle ($\alpha = 60^\circ$) this limiting value is established after the shortest distance in axial direction because of the shortest peripheral distance in direction of the gravitational force. The further slight decrease of the heat transfer coefficient at distances at which the limiting value of the film thickness is already reached is caused by the increase in height of the condensate layer at the lowermost point of the tube. At the largest inclination angle ($\alpha = 90^\circ$) the highest heat transfer coefficient is reached because at this inclination angle the peripheral

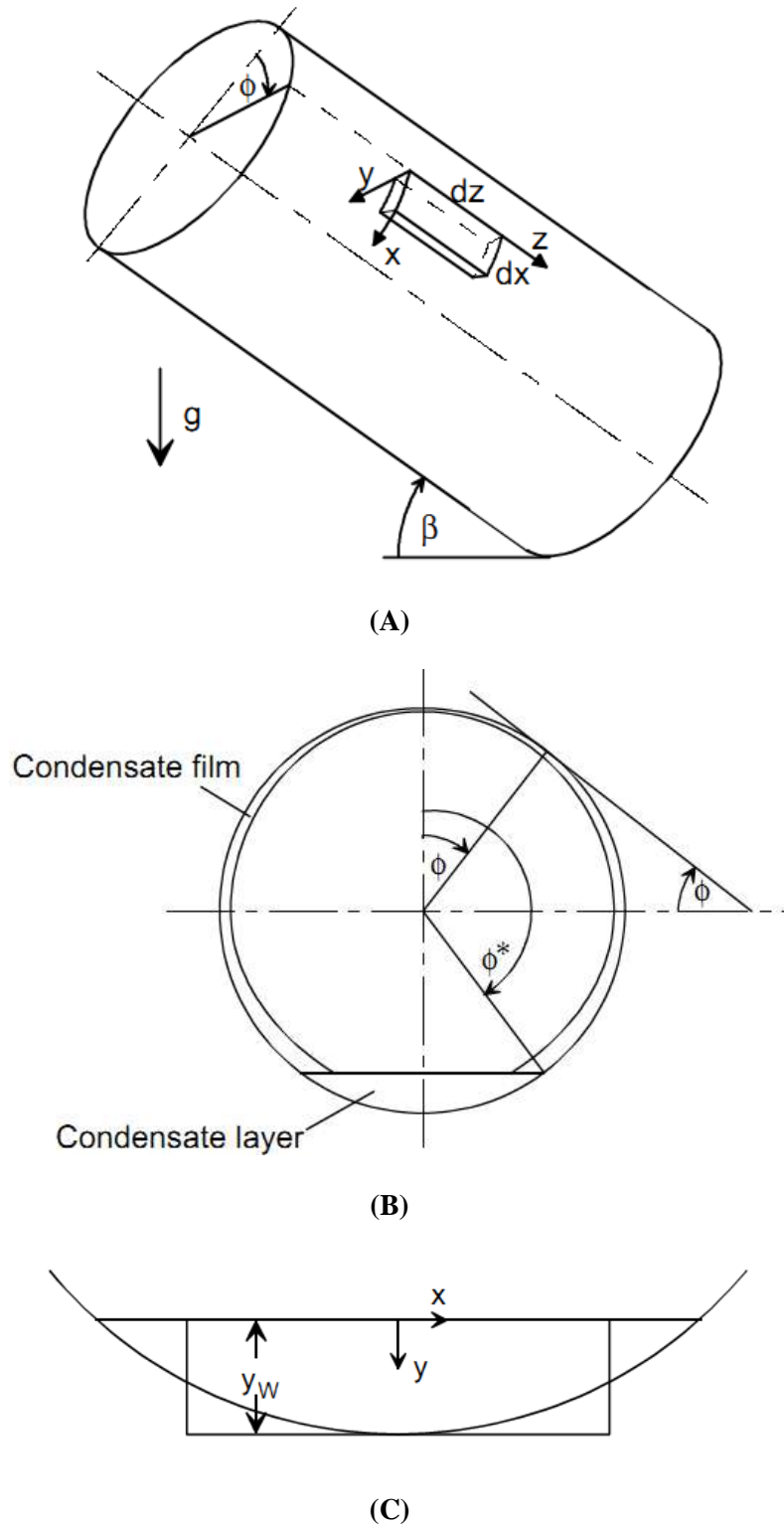


Fig 6.13: Modelling: (A) differential control volume of the condensate film inside the tube, (B) distribution of condensate inside the tube and (C) condensate layer at lowermost point of tube

distance in direction of the gravitational force is the shortest and therefore the film thickness is the smallest. But on the other hand at the largest inclination angle ($\alpha = 90^\circ$) the fraction of the gravitational force in axial direction, that causes the drainage of the condensate layer at the lowermost point of the tube, is smallest. This effect in turn deteriorates the heat transfer coefficient at small inclination angles.

6.4.2.2 Literature Survey on condensation inside inclined tubes

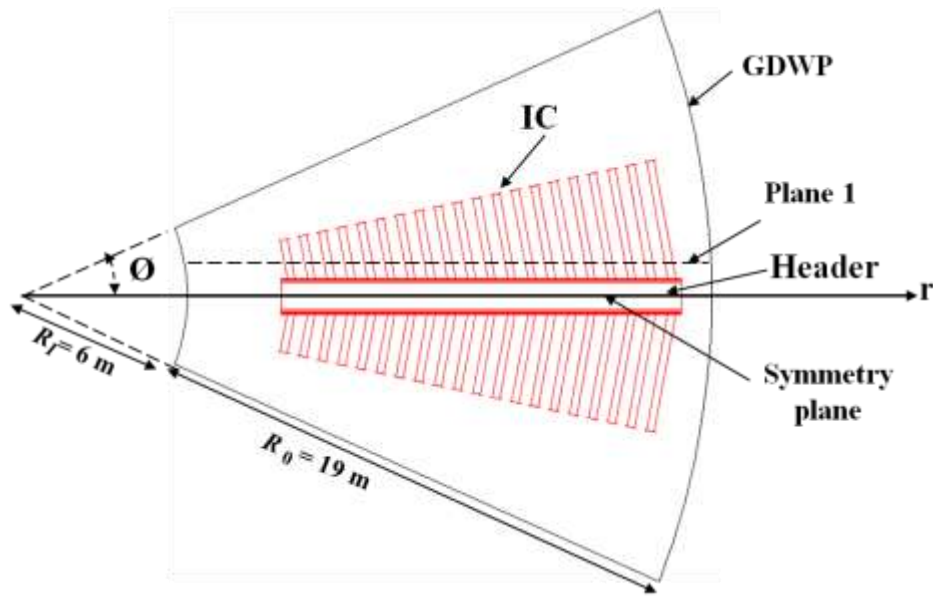
In the past, various researchers have studied the effect of condensation on heat transfer in inclined tubes. The summary of literature survey and the optimum inclination angle reported in literature is given in Table 6.7. Fiedler and Auracher (2004) have performed theoretical and experimental investigation of heat transfer, flooding point and film thickness during the reflux condensation of R134a in an inclined smooth tube ($d = 7.0$ mm and $l = 0.5$ m). The inclination angle was found to have significant effects on the heat transfer and flooding point. The optimum angle where the highest heat transfer occurred was found to be at ($\alpha = 50^\circ$). Klahm et al. (2010) performed experimental investigation of heat transfer during reflux condensation of the binary zeotropic mixture of R134a/R123 in a narrow tube ($d = 7$ mm and $l = 0.5$ m) and a rectangular channel ($d = 7.0$ mm and $l = 0.5$ m). The 20% enhanced heat transfer was observed for $\alpha = 45^\circ$ as compared with $\alpha = 0^\circ$.

Table 6.7: Summary of Literature survey on condensation heat transfer inside inclined tubes

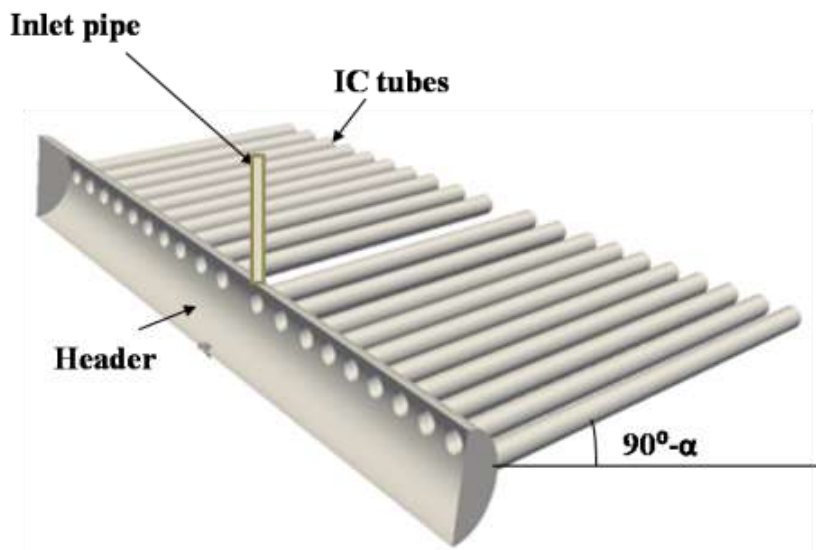
	Author	Working fluid	Optimum inclination angle (α)
1.	Fiedler and Auracher (2002, 2004)	R134a	50°
2.	Klahm et al. (2010)	Mixture of R134a/R123	45°
3.	Akhavan-Behabadi et al. (2007, 2011, 2012)	R134a	60°

Wang and Du (2000) performed theoretical and experimental investigation of film-wise condensation of steam inside copper pipes of inner diameter (1.94, 2.8, 3.95 and 4.98 mm) and mass flux ranged between $10 \text{ kg/m}^2\text{s}$ and $100 \text{ kg/m}^2\text{s}$ for. They concluded that gravity, unlike in larger tubes, had a

decreasing effect on flow condensation in small/mini tubes and that the inclination effect was accountable for stratifying the fluid and thinning the liquid film. No optimum inclination angle was reported. Akhavan-Behabadi et al. (2007, 2011, 2012) investigated both corrugated and microfin tubes in the condensation heat transfer of R134a for low mass fluxes for the whole range of inclination angle. Apart from the fact that the microfin and corrugated tubes had enhanced heat transfer, an optimum inclination angle of ($\alpha = 60^\circ$) was obtained.



(A)



(B)

Fig 6.14: (A) Schematic of the (A) top view of large scale GDWP and (B) Isolation condenser with inclined ($\alpha = 75^\circ$) IC tubes

6.4.3 Natural convection and heat transfer for new design of IC for real size GDWP

This section deals with the extension of the knowledge gained from the pilot scale in Section 6.4.1 to a real size GDWP ($\sim 10000\text{m}^3$) shown in Fig 6.14A.

6.4.3.1 Geometry and Boundary conditions

Based on the findings in Section 6.4.1, an improved design of IC (Fig 6.14B) has been proposed which consists of a cylindrical header ($D_h = 0.6\text{m}$) and a bundle of 40 inclined ($\alpha = 75^\circ$) tubes. The Section 6.4.2 shows the distribution of condensate inside the IC tube at various inclinations. There are two distinct regions (Fig 6.15) inside the IC header (a) the condensate film that drains at the circumference of the tube and (b) the condensate layer in the lowermost part of the tube. The presence of condensate inside the IC header provides resistance to the flow of steam to the IC tubes. The thickness of condensate layer is maximum at the lowermost part of the header. Hence, a great care has been taken while selecting the location of the IC tubes on the header surface. In order to prevent the resistance from the condensate film, the IC tubes are kept well above the maximum thickness of condensate layer at the bottom of the IC header. The detailed dimensions of large scale GDWP along with IC tubes are given in Table 6.5.

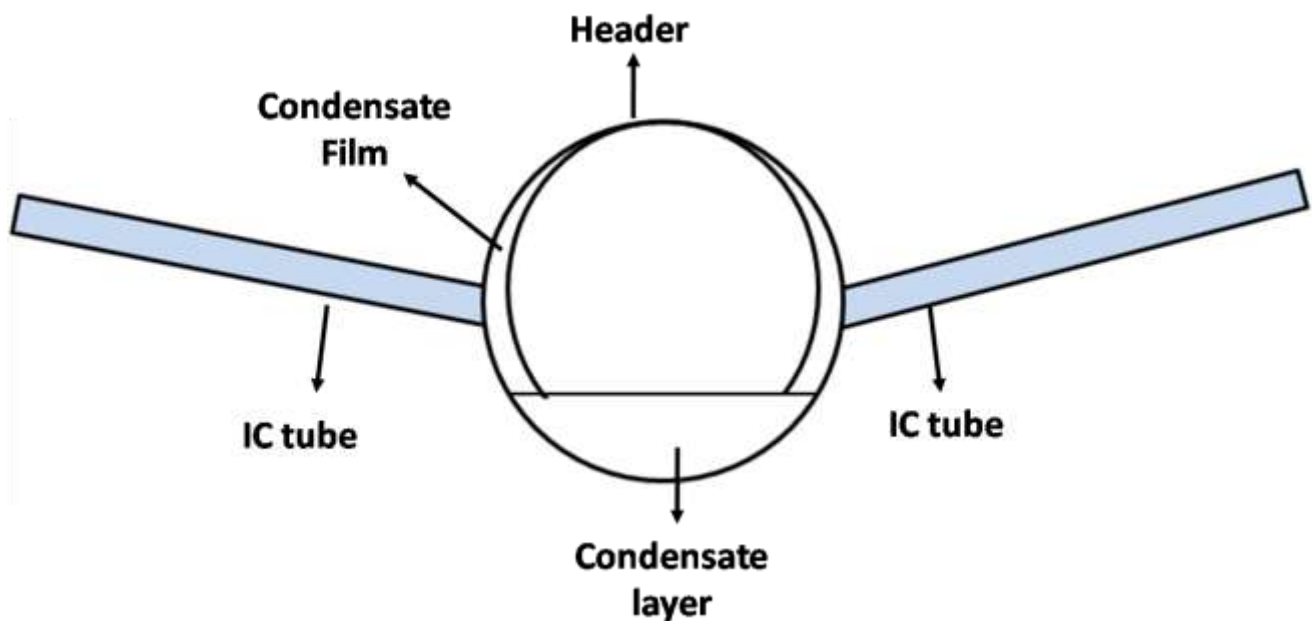


Fig 6.15: Distribution of condensate inside IC header for new IC design

The length of the IC tubes varies in radial direction (r) according to the availability of free water to provide uniform up and down flow throughout. In the tangential direction (\emptyset), the tubes were located at $-11.25 \leq \emptyset \leq 11.25^\circ$. The IC tubes are submerged so that the centerline of the steam header was at 0.5m ($z = 0.5\text{m}$) from the GDWP tank bottom ($z = 0$). Fig 6.14A shows the 1/8th sector ($-22.5 \leq \emptyset \leq 22.5^\circ$) of GDWP tank. The IC tubes are uniformly distributed inside GDWP to prevent non-uniform temperature distribution and hence thermal stratification. The comparison between the conventional IC design and new design of IC is given in Table 6.8. Due to the symmetry in tangential (\emptyset) direction, 1/16th sector ($0 \leq \emptyset \leq 22.5^\circ$) of GDWP has been considered for simulations. The details of the boundary conditions for the two phase CFD simulations of 1/16th sector of a real size GDWP ($\sim 10000\text{m}^3$) are given in Table 6.9.

Table 6.8: Comparison of new IC design and conventional IC design

	Design Parameters	Conventional IC	New IC Design
1.	IC tubes	Non-uniform distribution Number of tubes = 180 Diameter ($D = 0.05\text{ m}$) Length ($L = 1.6\text{ m}$) Pitch ($D_p = 0.1\text{ m}$)	Uniform distribution Number of tubes = 40 Diameter ($D = 0.2\text{ m}$) Length ($L_s = 1.3\text{ m}, L_h = 4\text{ m}, -11.25 \leq \emptyset \leq 11.25^\circ$) Pitch ($D_p = 0.2\text{ m}$)
2.	Submergence	Higher (2.5 m from bottom)	Lower (0.5 m from bottom)
3.	IC tube Inclination	Vertical ($\alpha = 0^\circ$)	Inclined ($\alpha = 75^\circ$)
4.	IC Header	Non-Uniform steam distribution Number of header = 2 Uniform ($D_1 = D_2 = 0.3\text{m}$) Length ($L = 2\text{ m}$)	Uniform steam distribution Number of header = 1 Converging ($D_1 = 0.8\text{ m}, D_2 = 0.6\text{ m}$) Length ($L = 14.5\text{ m}$)
5.	Inlet tube	Diameter ($D = 0.15\text{ m}$) Length ($L = 1.8\text{ m}$)	Diameter ($D = 0.2\text{ m}$) Length ($L = 0.5\text{ m}$)
6.	Perforated Baffle	None	12 x 2 x 0.5 m (L x W x H) Three types of holes ($D = 8, 20, 40\text{ mm}$)

Table 6.9: Details of the boundary conditions for large scale GDWP:

Zone	Temperature	Velocity
IC	$T=558\text{k}$	No slip ($u_r = u_\phi = u_z = 0$)
Header	$T=558\text{k}$	No slip ($u_r = u_\phi = u_z = 0$)
Top	Adiabatic ($\partial T/\partial z = 0$)	Free slip ($\frac{\partial u_r}{\partial z} = \frac{\partial u_\phi}{\partial z} = 0, u_z = 0$)
Walls	Adiabatic ($\partial T/\partial r = 0$)	No slip ($u_r = u_\phi = u_z = 0$)
Symmetry	($\partial T/\partial \phi = 0$)	$\frac{\partial u_r}{\partial \phi} = \frac{\partial u_\phi}{\partial \phi} = \frac{\partial u_z}{\partial \phi} = 0$

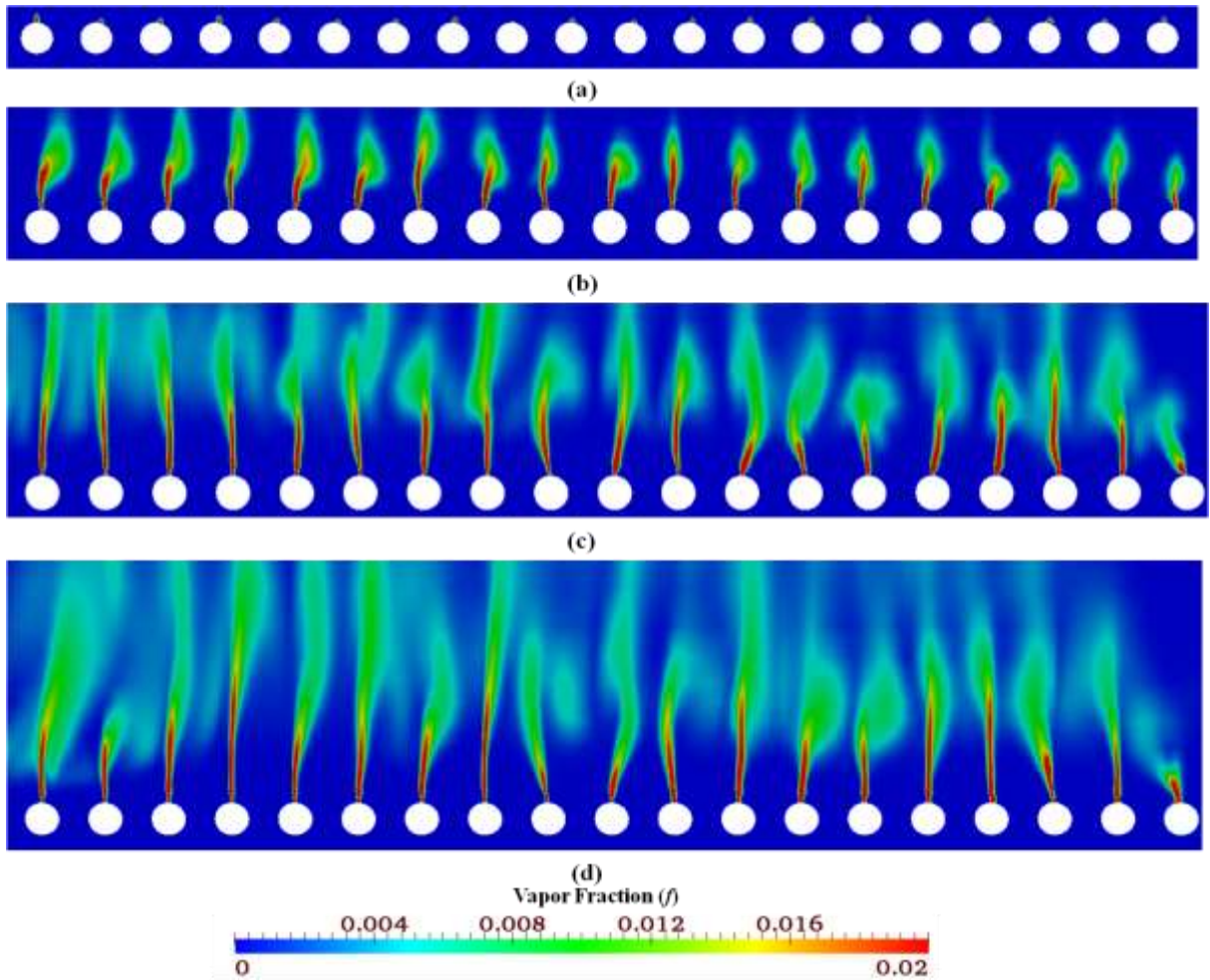


Fig 6.16: Transient variation of Vapor Fraction for spider shape IC along Plane 1: (a) $t = 40\text{s}$; (b) $t = 60\text{s}$; (c) $t = 80\text{s}$; (d) $t = 100\text{s}$

6.4.3.2 Vapor fraction Contours and Flow distribution

The vapor fraction contour in Fig 6.16 show the transient nature of flow as fluid travels in the vertical direction. The fluid inside the tank is highly sub cooled ($\Delta T_{sub} = 70K$) initially. Hence, for the initial period ($0 \leq t \leq 70s$) heat transfer occurs by single phase natural convection only. The fluid from the bottom of the tube slides along the tube surface towards the top of the tube. The flow was 2D and laminar at beginning. But near the top of the tube, the flow becomes separated and results in relatively high fluid temperature of the tube after the point of separation. As time progresses, the fluid temperature keeps on increasing and onset of nucleate boiling occurs on the tube surface when the fluid temperature exceeds the saturation temperature ($T_s = 373K$). The small vapor bubbles at time, $t = 80s$ at the top of the tube can be seen in Fig 6.16A indicating the onset of nucleate boiling. The vapor bubbles immediately condense due to sub cooled liquid surround the tube. As time progresses, the bubble generation around the tube increases and the vapor bubble travels some distance away from the tube before being condensed by the surrounding fluid. The vapor bubble motion results in enhanced convection surrounding the tube. As the fluid travels downstream, the buoyant plume form from both sides of the tube come together and interacts with each other near top of the tube. The plume interaction results in large velocity fluctuations. Further, it results in enhanced turbulence production and formation of eddies. The turbulent eddies results in enhanced mixing and lowering fluid temperature.

6.4.3.3 Interaction between the tubes

For the initial period ($0 \leq t \leq 50s$), the fluid flow around different tubes does not interact with each other. As a result, distinguishable flow pattern can be seen around the tube. As the time progresses ($t > 50s$), the convective flow around the tubes become intense. The hydrodynamic boundary layer of the individual tubes come closer and results in interaction between the tubes. Hence, the fluid flow and temperature distribution shows significant variation among all the tubes. Fluid flow is high near some of the tubes and results in enhanced heat transfer near those tubes.

Further, it results in lower fluid temperature amongst those tubes. The radial distribution of axial velocity profiles for $t = 60\text{s}$ are shown in Fig 6.17. The axial velocities are positive near the tubes and negative near the tank wall. The positive axial velocity indicates the upward flow due to rise of hot fluid near the tubes. The negative velocity near the tank wall indicates the downward flow to complete the material balance. As a result a natural circulation loop gets formed. Fig 6.17 also shows that the value of velocity and hence temperature are not symmetric for all the tubes. The axial velocities are very high for those tubes which are near the tank wall. Further, it results in enhanced heat transfer and lower fluid temperature near those tubes. This can be attributed to the availability of free water near those tubes which prevent the rise of fluid temperature. As we proceed in the radial

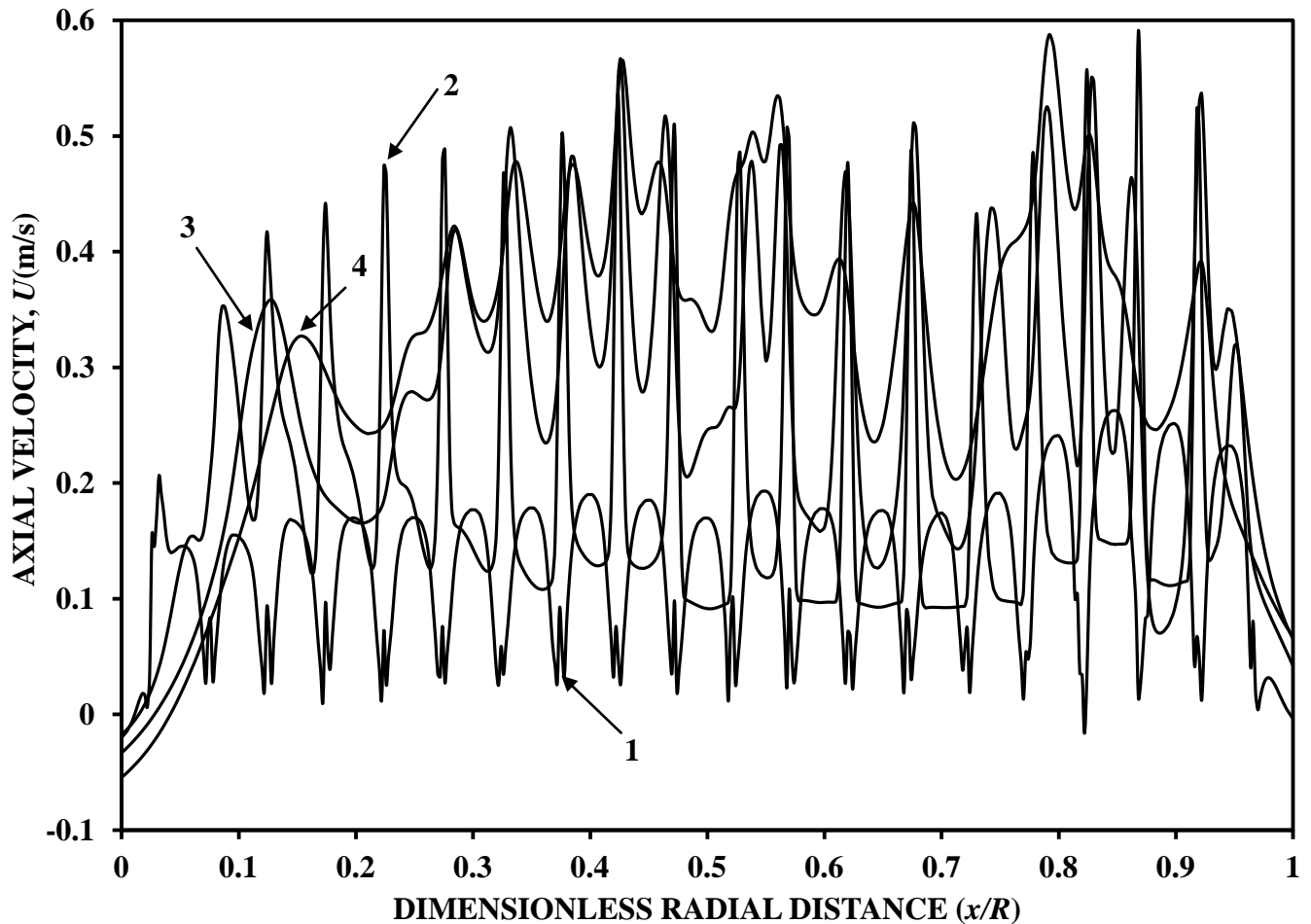


Fig 6.17: Radial distribution of Axial velocity at different axial locations (1) $z/H=0.24$, (2) $z/H=0.4$; (3) $z/H=0.6$; (4) $z/H=0.8$ at $t = 60\text{s}$ along plane 1 for new design of IC;

direction ($0 \leq x/R \leq 1$), the velocities increase initially for ($x/R < 0.15$) and then it decreases ($0.15 < x/R < 0.25$). The temperature peak present near ($x/R = 0.18$), further confirms lower fluid flow. After $x/R > 0.25$, velocity increases again till $x/R = 0.45$ and then again decreases. After $x/R > 0.45$, the velocities decrease again till $x/R = 0.75$. The temperature distribution also shows similar behavior. The high temperature is present near the low velocity region and low temperature near high velocity region. The axial velocity (Fig 6.17) first increases with an increase in the axial distance ($0 < z/H < 0.4$) and then decreases for ($0.4 < z/H < 0.6$). This behavior is due to the conversion of some mean kinetic energy into turbulent kinetic energy and results in decrease in axial velocity in the region ($0.4 < z/H < 0.6$). Further downstream ($0.6 < z/H < 0.8$), the axial velocity increases which implies that the mean flow feed on the turbulence and extract energy from the turbulent kinetic energy. On the other hand, the temperature decreases continuously with an increase in the axial distance ($0 < z/H < 0.8$).

6.4.3.4 Transient heat transfer

The transient heat transfer behavior in Fig 6.18A indicates that the heat transfer rate was maximum at the beginning ($t = 0s$) because of large $\Delta T = 258K$ and then it decreases very sharply for few seconds. The entire transient ($0 < t < 100s$) heat transfer behavior has been divided into three domains: conduction ($0 < t < 20s$), single phase convection ($20s < t < 80s$) and quenching ($80s < t < 100s$). Initially, the fluid is at rest. Hence, the heat transfer occurs mainly by conduction. The decay in HTC is very steep in the conduction period ($0 < t < 20s$). This is because, as the time progresses, the temperature of the fluid near the IC increases due to the heat transfer from the IC. As a result, the temperature difference (driving force) between the IC and the nearby fluid decreases which further results in decrease in heat transfer. As the time progresses, the convective flow starts to develop near the heated tube (IC) and heat transfer becomes increasingly dominated by convection. Since, the temperature of the fluid was lower than the saturation temperature ($T_s = 373K$), the bubble generation has not started. As a result, heat transfer is completely by single phase convection.

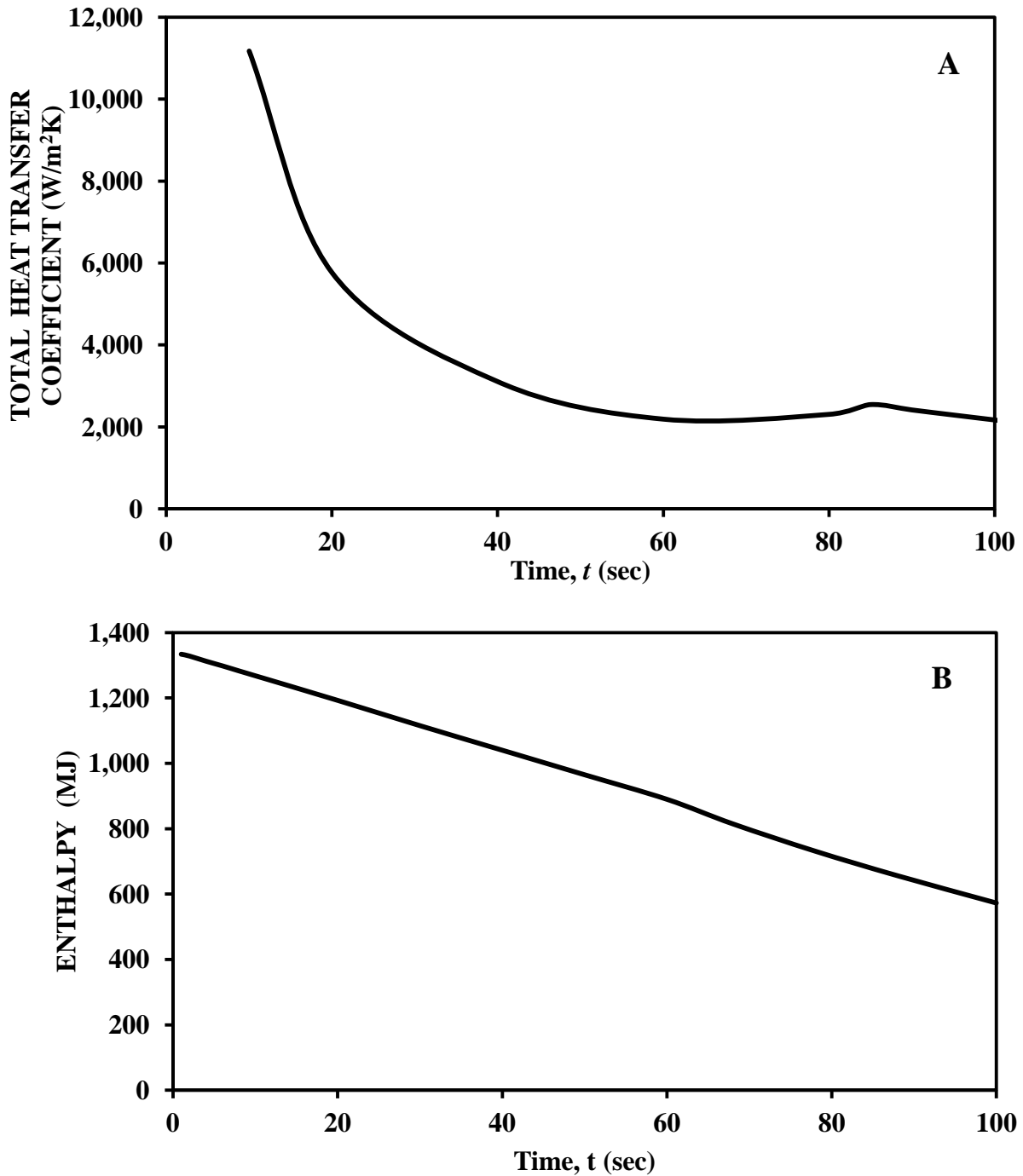


Fig 6.18: Transient variation of (A) Total heat transfer coefficient (h_{avg}) (B) Enthalpy decay for new design of IC

After ($t \geq 80$ s) the convective flow near the IC becomes very intense (large velocity gradients) due to bubble sliding motion around the tube and results into perturbations in the boundary layer. Further, it results in enhanced heat transfer. This period is known as two phase convection and characterized by intermittent disruption and growth of the boundary layer surrounding the IC tubes. The transient variation of enthalpy remains in the system has been shown in Fig 6.18B. The total amount of energy

to be removed by the system (GDWP) in 100s was calculated by integrating the decay heat power for 100s. The total energy comes out to be 1300MJ as shown in Fig 6.18B at $t = 0$ s. The decay rate of enthalpy, calculated using the pool side heat transfer coefficient, clearly indicates that the new design of IC is able to remove 56% of decay heat (1300 MJ to 570 MJ) in 100s. Hence, the new design of IC meets the design objective of 50% decay in 100s.

6.5 Closure

A set of numerical experiments have been performed using two phase boiling model for the better understanding of the bubble induced turbulent motion and heat transfer associated with it. The detailed CFD analysis of 3D temperature and flow distribution shows that enhanced liquid convection due to bubble sliding motion results in enhanced heat transfer and reduction in stratification number. The effect of inclination angle (α) of condenser tube on fluid flow and heat transfer associated with the bubble sliding motion has been studied for seven inclination angles. Based on the above studies, a new design of IC has been proposed for real size GDWP (10,000 m³).

The main conclusions are as follows:

- (1) The increase in inclination angle (α) of IC tube results in enhanced heat transfer. The heat transfer was found to be maximum for $\alpha = 75^\circ$ and minimum for $\alpha = 30^\circ$. The enhanced bubble sliding motion perpendicular to the tube as well as increase in bubble detachment frequency results in enhanced transfer at $\alpha = 75^\circ$. The enhanced transfer at $\alpha = 75^\circ$ ensures excellent thermal mixing and hence results in reduction in thermal stratification. The thermal stratification was found to be 0.35 for $\alpha = 75^\circ$.
- (2) The effect of inclination of IC tube on the fluid flow and temperature distribution at the top and bottom of the IC tube has been studied. The temperature at the top ($\theta = 180^\circ$) increases and bottom ($\theta = 0^\circ$) decreases with an increase in inclination angle (α) due to reduced bubble sliding motion at the top and enhanced bubble sliding motion at the bottom of the tube.
- (3) The new design of IC condenser is able to remove more than 50 per cent of decay heat in 100s.

CHAPTER 7

Conclusions and Recommendations for Future Work

7.1 Conclusions

In order to study turbulent natural convection and thermal stratification inside small and large water pools, a well validated three dimensional (3D) CFD code has been developed using the framework of open source CFD software OpenFOAM 2.2. The detailed CFD analysis of 3D temperature and flow distribution inside large size GDWP has been performed and thermal stratification has been quantified. In order to reduce the thermal stratification, various geometrical modifications have been incorporated on the design of isolation condenser. A new and improved design of isolation condenser (IC) for the PDHRS has been proposed based on the large set of numerical experiments. The new design of IC results in (a) enhanced heat transfer (b) mitigation of thermal stratification (c) efficient removal of decay heat in a stipulated time (50% decay in 100s)

The extensive CFD analysis performed in this thesis will improve upon the current understanding of (a) the effect of inclination (α) of condenser tubes on single phase natural convection and thermal stratification (b) the effect of longitudinal vortices on transient heat transfer (c) the mechanism of bubble formation over the inclined tubes (d) the relationship between the inclination (α) of condenser tube and the heat transfer associated with the bubble sliding motion (e) the transient heat transfer phenomena from sub cooled condition ($\Delta T_{sub} = 70^\circ\text{C}$) to boiling condition ($\Delta T_{sub} = 0^\circ\text{C}$) and to estimate the time required for the 50% decay (1300MJ to 650MJ) in 100s.

The main conclusions are summarized as follows:

1. The assessment of various turbulence models implies that SST $k-\omega$ model is capable of accurately predicting the near wall fluid flow and heat transfer. Hence, SST $k-\omega$ model can be used to study turbulent natural convection and thermal stratification inside small and large water pools.

2. The detailed CFD analysis of 3D temperature and flow distribution indicates GDWP indicates thermal stratification and poor mixing. The optimization in the design of IC by distribution and submergence of heat source results in enhanced mixing and reduction in stratification number by 33%.
3. A new concept of employing multiple draft tubes around IC is proposed in this thesis. Presence of appropriate size of draft tube at an optimum distance from the IC tubes results in additional driving force apart from buoyancy and results in reduction in stratification number by 46% and 40% for single and three draft tube design. In addition to this, it also reduces the size of hot dead zones near the top free surface.
4. The effect of inclination of condenser tubes on single phase natural convection and heat transfer has been studied. The relationship between inclination angle and thermal stratification phenomenon has been established. The thermal stratification phenomenon was found to be maximum at $\alpha = 15^\circ$ and minimum at $\alpha = 90^\circ$.
5. The steam mass distribution inside IC header and tube assembly was investigated. The uniform steam distribution inside the header and tube assembly of IC has been achieved. The maximum extent of non uniformity (ENU) was found to be 10 %.
6. The effect of local boiling on heat transfer inside GDWP for inclined IC tubes was studied. The major heat transfer mechanism was found to be liquid agitation caused by bubble sliding motion. The heat transfer coefficient was found to be maximum at $\alpha = 75^\circ$ and minimum at $\alpha = 30^\circ$.

7.2 Recommendations for Future Work

1. In order to obtain the best design of IC, transient 3D CFD simulation of the important heat transfer mechanisms must be studied in a coupled manner. The important heat transfer mechanisms are (a) condensation inside the condenser tubes; (b) conduction in the condensate film (c) conduction in the thickness of the IC tube (d) single phase natural convection and subcooled-boiling inside the GDWP.
2. Extensive validation of the single phase and two phase predictions of the used 3D CFD code are required. In view of this the future work should focus on the design of an experimental set up for the more accurate measurements of two phase flow parameters using advanced experimental techniques such as: laser Doppler anemometry (LDA), hot wire anemometry (HWA), particle image velocimetry (PIV). The high resolution (temporal as well as spatial) velocity time data obtained by these techniques should be explored to study the relationship between the near wall turbulent flow structures and heat transfer.
3. Further optimization in the design of IC to maximize the condensation heat transfer inside the IC tubes. The effect of various parameters can be studied such as (i) IC tube diameter, shape and inclination (ii) IC header diameter and shape (iii) corrugation inside the IC tubes for enhanced heat transfer.
4. An innovative design of PDHRS consists of both water and air as heat sinks. One of such design was proposed by Maio et al. 2012. The water has high heat transfer coefficient but it requires active systems to maintain a constant water level whereas air unlimited heat removal capacity but it requires a larger heat exchanger to compensate the lower heat transfer coefficient. This solution is based on a special IC submerged in a water pool designed so that when heat removal is requested, active systems are not required to maintain the water level; due to the special design, when the pool is empty, atmospheric air becomes the only heat sink. The special IC design allows to have a compact heat exchanger and to have a system

able to operate for unlimited period without external interventions. This innovative system provides an economic advantage as well as enhanced safety features.

5. The DNS simulation of two phase flow along with advanced phase change models. The detailed flow information obtained from DNS would be helpful (a) for the better understanding of bubble formation, bubble growth, bubble detachment, bubble induced turbulent motion and associated heat transfer (b) to modify the empirical constants and damping functions required by various RANS models.

Nomenclature

A	Heat transfer area (m^2)
A_i	Interfacial area (m^2)
B	Breadth of tank (m)
Bo	boiling number ($= q/Gh_{fg}$)
C_k	Mass fraction for phase k
C_p	specific heat of fluid (kJ m^{-2})
C_μ	constant
C_1	constant
C_2	constant
d	tube diameter (m)
D	Diameter of GDWP tank (m)
D_h	Header diameter (m)
D_t	Diameter of condenser tube (m)
D_s	mean Sauter bubble diameter
d_w	bubble departure diameter (m)
Δz	distance between each axial location for calculating stratification number
ΔT	temperature driving force (K)
ΔT_{sub}	degree of subcooling (K)
$\overline{\Delta T}_{w,t}$	Average rise in temperature of the pool after time t (K)
$\overline{\Delta T}_{s,t}$	Average temperature difference between tube surface and pool after time t (K)
$\langle \Delta T \rangle$	average temperature driving force (K)
$\langle \Delta T / \Delta z \rangle_{\text{max}}$	Average maximum temperature gradient (K)
ΔT_{sup}	wall super heat (K)
E_G	Enthalpy of vapor phase
E_L	Enthalpy of Liquid phase
F	External body force in momentum equation for VOF model
$F_{\text{lift},q}$	lift force
F_q	external body force
$F_{\text{td},q}$	turbulent dispersion force
$F_{\text{vm},q}$	virtual mass force
$F_{\text{wl},q}$	wall lubrication force

f	frequency of bubble departure (s^{-1})
f_{β}	constant
g	Acceleration due to gravity (ms^{-2})
G_b	generation of turbulence due to buoyancy ($m^4 s^{-1}$)
G_k	generation of turbulence kinetic energy due to mean velocity gradients ($kg.m^{-1}s^3$)
G_w	production of ω
h	height of liquid level in the GDWP tank (m)
Δh_v	specific enthalpy of vaporization, J/kg
h_{avg}	Average heat transfer coefficient (W/m^2K)
h_{pq}	volumetric heat transfer coefficient between the p^{th} phase and the q^{th} phase
h_q	specific enthalpy of the q^{th} phase
H	Height of heat source (m)
H_T	Height of the tank (m)
H	local heat transfer coefficient
H_{av}	mean heat transfer coefficient at each distance Z for an infinitesimal ring on the tube surface
$H_{av,total}$	mean heat transfer coefficient for the entire surface of the inclined tube
h_t	Tube length (m)
h_{tot}	average total heat transfer coefficient
ID	inner diameter of GDWP tank (m)
I_T	turbulent intensity (%)
j	axial locations for calculating stratification number
J	total number of nodes per lateral location in calculating stratification number (-)
Ja	Jakob number ($= \rho_l C_{pl}(T_{sat} - T_1)/\rho_g h_{fg}$)
k	turbulent kinetic energy ($m^2 s^{-2}$)
K	kinetic energy due to molecular motion ($m^2 s^{-2}$)
k_{eff}	effective thermal conductivity ($W m^{-1} K^{-1}$)
K_{pq}	momentum exchange coefficient
k_q	thermal conductivity of the q^{th} phase.
l	Characteristic length(m)
L	Length of tank (m)
L_h	Header length (m)
M	millions
\dot{M}	mass flow rate, kg/s

m_w	mass of water (kg)
M_w	Molecular weight (kg k/mol)
\dot{m}_G	mass flow rate of vapor phase (kg/s)
\dot{m}_L	mass flow rate of liquid phase (kg/s)
\dot{m}_{de}	Mass of gas leaving the system
\dot{m}_{GL}	mass source as in liquid phase continuity equation (kg m ⁻² s ⁻¹)
\dot{m}_{LG}	mass source as in gas phase continuity equation (kg m ⁻² s ⁻¹)
N_A	number of active site density (-)
NU_p	p th phase Nusselt number
OD	outer diameter of tank (m)
Pr	Prandtl number
P_s	Saturation pressure (Pa)
Q	Heat flux (KW/m ²)
q_E	evaporative heat flux (W m ⁻²)
q_N	natural convection heat flux (W m ⁻²)
q_q	quenching heat flux (W m ⁻²)
q_{tot}	total heat flux supplied at the tube wall (W m ⁻²)
\dot{Q}	total heat flow rate, W
Q_q	heat flux (W m ⁻²)
Q_{eva}	Energy transfer due to phase change (evaporation) (kJ/s)
Q_{nat}	Energy transfer due to sensible heat (kJ/s)
Q_{pa}	intensity of heat exchange between the p th and q th phases
Q_{que}	Energy transfer due to bubble induced convection (kJ/s)
Q_{tot}	Total energy accumulated in the system (kJ/s)
Ra	Rayleigh number $\left(g\beta\Delta T l^3 / \nu\alpha_\ell \right)$ (-)
ρ_{rq}	phase reference density (Kg/m ³)
R	radius, m
R_i	inner radius of GDWP tank (m)
R_o	outer radius of GDWP tank (m)
S	stratification number (-)
$ \bar{S} $	mean strain rate (s ⁻¹)
\bar{S}_{ij}	strain rate (s ⁻¹)
S_E	source term for energy equation
$S_{\in G}$	source term for mass transfer in volume fraction equation

S_{\emptyset}	source term in momentum equation in
t	Time (sec)
T	Fluid temperature (K)
ΔT	temperature difference, K
T^*	Temperature at tube surface (K)
T_s	Saturation temperature (k)
τ_p	bubble relaxation time
T_w	Heat source wall temperature (K)
T_G	temperature of gas (K)
T_j	temperature of j node for calculation of stratification number in (K)
T_{j+1}	temperature of $j + 1$ node for calculation of stratification number in (K)
T_L	temperature of liquid (K)
T_{max}	maximum temperature (K)
T_{min}	minimum temperature (K)
T_O	Operating temperature (K)
T_{rms}	root mean square temperature (K)
$T_{s,t}$	Tube surface temperature at time t
$\bar{T}_{s,t}$	Average tube surface temperature difference at time t (K)
$T_{w,t}$	Liquid pool temperature at time t
$\bar{T}_{w,t}$	Average rise in temperature of the pool after time t (K)
u	Velocity (m/sec)
u'	Turbulent velocity(m/sec)
u_m	mixture velocity ($m s^{-1}$)
u_{qp}	interphase velocity ($m s^{-1}$)
u_r	radial component velocity ($m s^{-1}$)
u_{\emptyset}	tangential component velocity ($m s^{-1}$)
u_z	vertical component velocity ($m s^{-1}$)
v_{dr}	drift velocity ($m s^{-1}$)
v_p	velocity of primary phase p ($m s^{-1}$)
v_{pq}	Relative velocity between phases ($m s^{-1}$)
v_q	velocity of secondary phase q ($m s^{-1}$)
V_{cell}	Cell volume in m^3
w	velocity, m/s
y^+	dimensionless distance from the wall (-)

z	any distance along the height of the rectangular tank (m)
Z	axial coordinate, dimensionless

Greek symbols

α	Inclination angle w.r.t vertical (z) axis (degrees)
α_1	constant
α_2	constant
α_{eff}	effective thermal diffusivity ($\text{m}^2 \text{s}^{-1}$)
α_l	Thermal diffusivity (m^2/s)
β	thermal expansion coefficient (K^{-1})
β_1	constant
β_2	constant
β_r	constant
β_{∞}^*	constant
Δ	constant
δ	film thickness (m)
ϵ_G	volume fraction of gas (-)
ϵ_k	volume fraction of phase k (-)
ϵ_L	volume fraction of liquid (-)
\mathcal{E}	turbulent energy dissipation rate per unit mass ($\text{m}^2 \text{s}^{-3}$)
η_1	dynamic viscosity, $\text{kg}/(\text{m s})$
λ	latent heat of vaporization (kJ kg^{-1})
\emptyset	Length of tank in tangential direction (degrees)
φ	contact angle
ν	kinematics viscosity ($\text{m}^2 \text{s}^{-1}$)
μ_{eff}	<i>effective</i> viscosity of fluid (Pa s)
ν_t	turbulent viscosity ($\text{m}^2 \text{s}^{-1}$)
$\Delta\rho$	density difference ($\rho_l - \rho_g$)
ρ_G	density of gaseous phase (kg/m^3)

ρ_L	density of liquid phase (kg/m ³)
σ	Surface tension
σ_L	density of water (kg m ⁻³)
σ_G	density of gas (kg m ⁻³)
$\sigma_{\omega 1}$	constant
σ_{ε}	constant
$\sigma_{\omega 2}$	constant
σ_{k1}	constant
σ_{k2}	constant
θ	Azimuthal angle (degree)
θ_{sep}	Angle of separation (degree)
ω	specific dissipation rate (s ⁻¹)
σ_{ε}	turbulent Prandtl number for energy dissipation rate (-)
σ_t	turbulent Prandtl number for kinetic energy (-)
ϕ	peripheral angle, °
ϕ^*	peripheral angle of condensate layer, °
χ_k	constant as in Table 1
Ψ	dimensionless film thickness

Subscript

b	buoyancy as in G_b
CL	condensate layer
CW	cooling water
eff	effective
g	gas
k	kinetic energy as in k
l	liquid
m	mean
max	maximum
min	minimum
W	wall

Abbreviation

AFM	algebraic flux model
CFD	Computational Fluid Dynamics
DFM	differential flux model
DNS	Direct Numerical Simulation
GDWP	Gravity Driven Water Pool
GGDH	generalized gradient diffusion hypothesis
HT	Heat Transfer
<i>HTA</i>	Heat Transfer Area
HTC	Heat Transfer Coefficient
IC	Isolation Condenser
<i>MHT</i>	Main Heat Transport
PDHRS	Passive Decay Heat Removal System
PISO	Pressure Implicit with Splitting of Operators
RSM	Reynolds Stress Model
SGDH	simple gradient diffusion hypothesis
SST	Shear Stress transport
$\nu_2 f$	Elliptic Relaxation Model
2D	Two dimensional
3D	Three dimensional

REFERENCES

- Addlesee, A.J., Cornwell, K., 1997. Liquid film thickness above a bubble rising under an inclined plate. *Transactions Inst. Chem. Eng.* 75, 663–667.
- Akhavan-Behabadi, M.A., Kumar, R., Mohseni, S.G., 2007. Condensation heat transfer of R134a inside a microfin tube with different tube inclinations. *Int. J. Heat Mass Transfer* 50, 4864–4871.
- Alzwayi, A.S., Paul, M.C., 2014. Transition of free convection flow inside an inclined parallel walled channel: Effects of inclination angle and width of the channel, *Int. J. Heat Mass transfer*, 68, 194-202.
- Arabi, M.A., Sarhan, A., 1984. Natural convection heat transfer from square cylinders, *Applied Scientific Research* 41, 93-104.
- Aszodi, A., Krepper, E., Prasser, H.M., 2000. Investigation of heating up and evaporation processes of fluids in storage tanks by experiments and by numerical simulation. *Proc. Second Int. Symp. Two Phase Flow Model. Exp. Pisa Proceeding* 1667–1674.
- Bhole, M.R., Joshi, J.B., Ramkrishna, D., 2008. CFD simulation of bubble columns incorporating population balance modeling, *Chem. Eng. Sci.* 63, 2267-2282.
- Bibeau, E.L., Salcudean, M., 1994. A study of bubble ebullition in forced convective subcooled nucleate boiling at low pressure. *Int. J. Heat Mass Transfer*, 37, 2245–2259
- Biertumpfel, R., Beer, H. 2003. Natural convection heat transfer increase at the laminar-turbulent transition in the presence of instationary longitudinal vortices, *Int. J. Heat Mass transfer*, 46, 3109-3117.
- Black, W.Z., Norris, J.K. 1975. The thermal structure of free convection turbulence from inclined isothermal surfaces and its influence on heat transfer, *Int. J. Heat Mass transfer*, 18, 43-50.
- Boetcher, K.S., Kulacki, F.A., Davidson, J.H. 2012. Use of a Shroud and Baffle to Improve Natural Convection to Immersed Heat Exchangers, *J. Solar Energy Eng.*, 134.
- Brackbill, J.U., Kothe, D.B. Zemach, C., 1992. A continuum method for modeling surface tension. *J. Comput. Phys.* 100, 335–354.

- Cebeci, T., Smith, A.M.O., 1974. Analysis of Turbulent Boundary Layers, Academic Press, New York.
- Chen, H.C., Patel, V.C., 1988. Near-wall turbulence models for complex flows including separation, AIAA J., 26, 641-648.
- Chien, K.Y., 1980. Predictions of channel and boundary layer flows with a low-Reynolds-number two-equation model of turbulence, AIAA, 80, 01-34.
- Chien, K.Y., 1982. Predictions of channel and boundary-layer flows with a low-Reynolds-number turbulence model, AIAA J., 20, 33-38.
- Choi, S.K., Kim, E.K., Kim, S.O., 2004. Computation of turbulent natural convection in a rectangular cavity with the $k-\epsilon-v_2-f$ model, Numer. Heat Transfer, Part B, 45, 159-179.
- Choi, S.K., Kim, S.O., 2012. Turbulence modeling of natural convection in enclosures: A review. J. Mech. Sci. Technol. 26, 283–297.
- Clift, Grace, Weber, 1978. Bubbles, drops, and particles. Technical Report. Academic Press.
- Cole, R., 1960. A photographic study of pool boiling in the region of the critical heat flux. AIChE J. 6, 533–542.
- Cooper, M.G., 1969. The microlayer and bubble growth in nucleate pool boiling, Int. J. Heat Mass Transfer, 12, 915–933
- Cooper, M.G., Lloyd, A.J.P., 1969. The microlayer in nucleate pool boiling, Int. J. Heat Mass Transfer 12, 895–913.
- Corcione, M., Habib, E., Campo, A. 2011. Natural convection from inclined plates to gases and liquids when both sides are uniformly heated at the same temperature, Int. J. thermal Sciences, 50, 1405-1416.
- Cornwell, K., Einarsson, J.G., 1990. Influence of Fluid Flow on Nucleate Boiling From a Tube. Exp. Heat Transf. 3, 101–116.
- Cornwell, K., Houston, S.D., 1994. Nucleate pool boiling on horizontal tubes: A convection-based correlation. Int. J. Heat Mass Transf. 37, 303–309.

- D. Khoeini, M.A. Akhavan-Behabadi, A. Saboonchi, Experimental study of condensation heat transfer of R134a flow in corrugated tubes with different inclinations, *Int. Commun. Heat Mass Transfer* 39 (2012) 138–143.
- D. Moalem Maron, S. Sideman, Condensation inside near horizontal tubes in co-current and counter-current flow, *Int. J. Heat Mass Transfer* 25 (1982) 1439–1444
- Didio, L., 1992. Fluent - User's guide. Comput. Secur. 11, 727.
- Fath, H.S., Judd, R.L., 1978. Influence of system pressure on microlayer evaporation heat transfer, *ASME J. Heat Transfer*, 100, 49–55.
- Fiedler, S., Auracher, H., 2002. Pressure drop during reflux condensation of R134a in a small diameter tube, in: *Proc. Int. Symp. Compact Heat Exchangers*, Grenoble, France, 369–373.
- Fiedler, S., Auracher, H., 2004. Experimental and theoretical investigation of reflux condensation in an inclined small diameter tube, *Int. J. Heat Mass Transfer*, 47, 4031–4043.
- Fiedler, S., 2003. Untersuchungen zur Rücklaufkondensation in einem engen geneigten Rohr, *Fortschr.-Ber. VDI, Reihe 3, Nr. 777*, VDI-Verlag, Düsseldorf.
- Fritz, W., 1935. Berechnung des Maximalvolumes von Dampfblasen, *Phys. Z.*, 36, 379.
- Fürst, J., 1989. Kondensation in geneigten ovalen Rohren, *Fortschr. Ber. VDI, Reihe 19, Nr. 36*, VDI-Verlag, Düsseldorf.
- Gandhi, M.S., Joshi, J.B., Vijayan, P.K., 2013a. Study of two phase thermal stratification in cylindrical vessels: CFD simulations and PIV measurements. *Chem. Eng. Sci.* 98, 125–151.
- Gandhi, M.S., Joshi, J.B., Vijayan, P.K., 2013b. Reduction in thermal stratification in two phase natural convection in rectangular tanks: CFD simulations and PIV measurements. *Chem. Eng. Sci.* 100, 300–325.
- Gandhi, M.S., Sathe, M.J., Joshi, J.B., Vijayan, P.K., 2011. Two phase natural convection: CFD simulations and PIV measurement, *Chem. Eng. Sci.*, 66, 3152–3171.
- Ganguli, A. A., Sathe, M. J., Pandit, A. B., Joshi, J. B. and Vijayan, P. K., 2010. Hydrodynamic and heat transfer characteristics of passive decay heart removal systems: cfd simulations and experimental measurements, *Chem. Eng. Sci.*, 65, 3457–3473.

- Genske, P., Stephan, K., 2006. Numerical simulation of heat transfer during growth of single vapor bubbles in nucleate boiling. *Int. J. Therm. Sci.* 45, 299–309.
- Graham, R.W., Hendricks, R.C., 1967. Assessment of convection and evaporation in nucleate boiling, NASA TN D-3943.
- Gray, D.D., Giorgini, A., 1976. The validity of the boussinesq approximation for liquids and gases. *Int. J. Heat Mass Transfer*, 19, 545-551.
- Gunn, D.J., 1978. Transfer of heat or mass to particles in fixed and fluidized beds. *Int. J. Heat Mass Transfer*. 21, 467–476
- Han, Y.M., Wang, R.Z., Dai, Y.J., 2009. Thermal stratification within the water tank. *Renew. Sustain. Energy Rev.* 13, 1014–1026.
- Hanjalic, K., 1994. Achievements and limitations in modeling and computation of buoyant turbulent flows and heat transfer. In: *Institution of Chemical Engineers Symposium Series*. 135.
- Hassan, K.E., Jakob, M., 1958. Laminar film condensation of pure saturated vapor on inclined circular cylinders, *J. Heat Transfer* 80, 887–894
- He, S., Kin, W.S., Bae, J.H., 2008. Assessment of performance of turbulence models in predicting supercritical pressure heat transfer in a vertical tube, *Int. J. Heat Mass Transfer*, 51, 4659-4675.
- Heindel, T.J., Ramadhyani, S., and Incropera, F.P., 1994. Assessment of turbulence models for natural convection in an enclosure, *Numer. Heat Transfer, Part B* 26, 147-172.
- Henkes, R.A.W.M., Hoogendoorn, C.J., 1989. Comparison of turbulence models for the natural convection boundary layer along a heated vertical plate, *Int. J. Heat Mass Transfer*, 32, 157-169.
- Henkes, R.A.W.M., Van Der Vlugt, F.F., Hoogendoorn, C.J., 1991. Natural-convection flow in a square cavity calculated with low-Reynolds-number turbulence models. *Int. J. Heat Mass Transf.* 34, 377–388.
- Hibiki, T., Ishii, M., 2000. One-group interfacial area transport of bubbly flows in vertical round tubes. *Int. J. Heat Mass Transf.* 43, 2711–2726.
- Hsu, Y.Y., Graham, R.W., 1976. *Transport Processes in Boiling and Two-phase Systems*, Hemisphere, Washington, DC.

- Hughmark, G.A., 1967. Mass and heat transfer from rigid spheres. *AICHE Journal*. 13, 1219–1221.
- Ishii, M., Kim, S., 2001. Micro four-sensor probe measurement of interfacial area transport for bubbly flow in round pipes. *Nuclear Engineering and Design*. 205, 123–131.
- Ivey, H.J., 1967. Relationships between bubble frequency, departure diameter and rise velocity in nucleate boiling, *Int. J. Heat Mass Transfer*, 10, 1023–1040
- Jones, W.P., Launder, B.E., 1972. The prediction of laminarization with a two-equation model of turbulence, *Int. J. Heat Mass Transfer*, 15, 301-314.
- Joshi, J. B., Pandit, A. B., Patel, S. B., Singhal, R. S., Bhide, G. K., Mariwala, K. V., Devidayal, B. A., Danao, S. P., Gudekar, A. S., and Shinde, Y. H.. 2012. Development of Efficient Designs of Cooking Systems. I. Experimental, *Ind. Engg. Chem. Res.*, 51, 1878-1896.
- Joshi, J.B., Tabib, M.V., Deshpande, S.S., Mathpati, C.S., 2009. Dynamics of flow structures and transport phenomena-1: experimental and numerical techniques for identification and energy content of flow structures, *Ind. Eng. Chem. Res.* 48, 8244–8284.
- Judd, R.L., 1999. The role of bubble waiting time in steady nucleate boiling, *ASME J. Heat Transfer*, 121, 852–855.
- Judd, R.L., Hwang, K.S., 1976. A comprehensive model for nucleate pool boiling heat transfer including microlayer evaporation, *ASME J. Heat Transfer*, 98, 623–629.
- Kang, M.G., 2002. Thermal mixing in a water tank during heating process. *Int. J. Heat Mass Transf.* 45, 4361–4366.
- Kang, M.G., 2003. Effects of tube inclination angle on nucleate pool boiling heat transfer. *Nucl. Eng. Des.* 220, 67–81.
- Kang, M.G., 2005. Local pool boiling coefficients on the outside surface of a horizontal tube. *J. Heat Transfer* 127, 949.
- Kang, M.G., 2013. Variation of local pool boiling heat transfer coefficient on 3degree inclined tube surface. *Nucl. Eng. Technol.* 45, 911–920.

- Kataoka, Y., Fukui, T., Amiy, A., Murase, M., Natioh, M., Sumid, I., 1990. Thermal-Hydraulic Characteristics and Heat Removal Capability of Containment Cooling System with External Water Wall, *J. Nucl. Sci. Tech.*, 27(9), 802-814.
- Kenneth, W., 1988. Generalized thermodynamic relationship. *Thermodynamics* (5th ed.). New York, NY: McGraw-Hill, Inc.
- Khan, Z., Joshi, J.B., 2015. Comparison of k-epsilon, RSM and LES models for the prediction of flow pattern in jet loop reactor, *Chem. Eng. Sci.*, 127, 323-333.
- Khoeini, D., Akhavan-Behabadi, M.A., Saboonchi, A., 2012. Experimental study of condensation heat transfer of R134a flow in corrugated tubes with different inclinations. *Int. Commun. Heat Mass Transfer* 39, 138–143.
- Kim, S., Wu, Q., Ishii, M., 1997. One-group interfacial area transport in vertical bubbly flow. *Int. J. Heat Mass Transf.* 41, 1103–1112.
- Kitamura, K., Kamiwa, F., Misumi, T. 1999. Heat transfer and fluid flow of natural convection around large horizontal cylinders, *Int. J. Heat Mass transfer*, 42, 4093-4106.
- Klahm, T., Auracher, H., Ziegler, F., 2010. Heat transfer during reflux condensation of R134a/R123 mixture in vertical and inclined narrow tubular and rectangular channels, *Int. J. Refrig.*, 33, 1319–1326.
- Kumar, M., Nayak, A.K., Jain, V., Vijayan P.K., 2007. Managing a prolonged station blackout condition in AHWR by passive means, *Nuclear Eng. and Tech.*, 45, 605-612.
- Kolasinski, K.W., 2012. *Surface science: Foundations of catalysis and nanoscience*, Third Edition. p. 203
- Kolev, N.I., 2005. *Multiphase Flow Dynamics 2: Thermal and mechanical interactions*. Springer, Berlin, Germany, 2nd edition.
- Komori, K., Kito, S., Nakamura, T., Inaguma, Y., Inagaki, T. 2001. Fluid flow and heat transfer in the transition process of natural convection over an inclined plate, *Heat Transfer Asian Research*, 30, 648-659.

- Krepper, E., Beyer, M., 2010. Experimental and numerical investigations of natural circulation phenomena in passive safety systems for decay heat removal in large pools. Nucl. Eng. Des. 240, 3170–3177.
- Krepper, E., Hicken, E.F., Jaegers, H., 2002. Investigation of natural convection in large pools, Int. J. Heat Fluid Flow 23, 359-365.
- Kulkarni, A.A., Joshi, J.B., Ravikumar, V., Kulkarni, B.D., 2001. Application of multi-resolution analysis for simultaneous measurement of gas and liquid velocities and fractional gas hold-up in bubble column using LDA, Chem. Eng. Sci. 56, 5037-5048.
- Kumaresan, T., Joshi, J.B., 2006. Effect of Impeller Design on the Flow Pattern and Mixing in Stirred Tanks. Chem. Eng. J., 115, 173-193.
- Kurul, N., Podowski, M.Z., 1991. On the modeling of multidimensional effects in boiling channels. Proc. 27th Natl. Heat Transf. Conf. Minneapolis, Minnesota, USA.
- Lai, Y.G., So, R.M.C., 1990a. On Near Wall Turbulent Flow Modeling,” J. Fluid Mech., 221, 641.
- Lai, Y.G., So, R.M.C., 1990b. Near Wall Modeling of Turbulent Heat Fluxes, Int. J. Heat Mass Transfer, 33, 1429.
- Lam, C.K.G., Brernhorst, K., 1981. A modified form of the k- ϵ model for predicting wall turbulence, J. Fluids Engg, 103, 456-460.
- Launder, B.E., 1989. Second-moment closure and its use in modeling turbulent industrial flows. International Journal for Numerical Methods in Fluids, 9, 963-985.
- Launder, B.E., 2007. Wall-function strategies for use in turbulent flow CFD. Comput. Model. Ind. Environ. Flows, Work. Macerata, Italy 1–18.
- Launder, B.E., Sharma, B.I., 1974. Application of the energy dissipation model of turbulence to the calculation of near spinning disc, Lett. in Heat and Mass Transfer, 1, 131-138.
- Launder, B.E., Spalding, D.B., 1972. Lectures in Mathematical Models of Turbulence; Academic Press: London.
- Lavieville , J., Quemerais, E., Mimouni, S., Boucker, M., Mechitoua , N., 2005. NEPTUNE CFD V1.0 Theory Manual". EDF.

- Lee, W.H., 1979. A pressure iteration scheme for two-phase modeling. Technical Report LA-UR 79-975.
- Lloyd, J.R., Sparrow, E.M. 1970. On the instability of natural convection flow on inclined plates, *J. Fluid Mech.*, 42, part3, 465-470.
- Maio, D.V.D., Navigilo, A., Giannetti, F., Manni, F., 2012. An innovative pool with a passive heat removal system. *Energy*, 45, 296-303.
- Manickam, S., Dhir, V., 2012. Holographic interferometric study of heat transfer to a sliding vapor bubble. *Int. J. Heat Mass Transf.* 55, 925–940.
- Manninen, M., Taivassalo, V., Kallio, S., 1996. "On the mixture model for multiphase flow". VTT Publications 288, Technical Research Centre of Finland.
- Maron, D.M., Sideman, S., 1982. Condensation inside near horizontal tubes in co-current and counter-current flow. *Int. J. Heat Mass Transfer* 25, 1439–1444.
- Mathpati, C.S., Tabib, M.V., Deshpande, S.S., Joshi, J.B., 2009. Dynamics of flow structures and transport phenomena-2: Relationship with design objectives and design optimization, *Ind. Eng. Chem. Res.* 48, 8285–8311.
- Medic, G., Durbin, P.A., 2002. Toward Improved prediction of heat transfer on turbine blades, *J. Turbomachinery*, 124, 187-192.
- Medic, G., Durbin, P.A., 2012. Turbulence modeling of natural convection in enclosures: A review,” *Journal of Mechanical Science and Technology*, 26 (1), 283-297.
- Menter, F.R., 1994. Two-equation eddy-viscosity turbulence model for engineering applications. *AIAA* 32, 1598–1605.
- Minocha, N., Joshi, J. B., Nayak, A. K., and Vijayan, P. K., 2015. Numerical investigation of three-dimensional natural circulation phenomenon in passive safety systems for decay heat removal in large pools. *Int. J. Heat Mass Transf.*, 81, 659-680.
- Mohseni, S.G., Akhavan-Behabadi, M.A., 2011. Visual study of flow patterns during condensation inside a microfin tube with different inclinations, *Int. Commun. Heat Mass Transfer*, 38, 1156–1161

- Morsi, S.A., Alexander, A. J., 1972. An Investigation of Particle Trajectories in Two-Phase Flow Systems. *J. Fluid Mech.* 55(2), 193–208.
- Nere, N. K., Patwardhan A. W. and Joshi J. B., 2003. Liquid Phase Mixing in Stirred Vessels: Turbulent Flow Regime. *Ind. Eng. Chem. Res.*, 42, 2661-2698.
- Nusselt, W., 1916. Die Oberflächenkondensation des Wasserdampfes the surface condensation of water. *Zetschr. Ver. Deutch. Ing.*, 60, pp.541-546, and pp. 568–578.
- Park, H., Choi, K.Y., Cho, S., Yi, S.J., Park, C.K., Chung, M.K., 2008. Experimental study on the natural circulation of a passive residual heat removal system for an integral reactor following a safety related event, *Ann. Nucl. Energy*, 35, 2249–2258.
- Patel, V.C., Rodi, W., Scheuerer, G., 1984. Turbulence Models for Near Wall and Low Reynolds Number Flows: A Review. *AIAA J.*, 23, 1308-1319.
- Qiu, D., Dhir, V.K., 2002. Experimental study of flow pattern and heat transfer associated with a bubble sliding on downward facing inclined surfaces. *Exp. Therm. Fluid Sci.* 26, 605–616.
- R. Wurfel, T. Kreutzer, W. Fratzscher, Turbulence transfer processes in a diabatic and condensing film flow in inclined tube, *Chem. Eng. Technol.* 26 (2003) 439–448.
- Ranade, V.V. and Joshi, J.B., 1990. Flow Generated by a Disc Turbine I: Experimental. *Trans. Instn. Chem. Engrs. (U.K.)-A: Chem. Eng. Res. Des.*, 68, 19-33.
- Ranade, V.V., Joshi, J.B. and Marathe, A.G., 1989. Flow Generated by Pitched Bladed Turbine Part II: Mathematical Modelling and Comparison with Experimental Data. *Chem. Eng. Commun.*, 81, 225-248.
- Ranz, W.E., Marshall, W.R., 1952. Evaporation from drops. *Chem. Eng. Prog.* 141-146.
- Reynolds, W.C., 1987. Fundamentals of Turbulence for Turbulence Modeling and Simulation. Lecture Notes for Von Karman Institute Agard. Report No. 755.
- Sateesh, G., Das, S.K., Balakrishnan, A.R., 2005. Analysis of pool boiling heat transfer: Effect of bubbles sliding on the heating surface. *Int. J. Heat Mass Transf.* 48, 1543–1553.
- Sateesh, G., Das, S.K., Balakrishnan, A.R., 2009. Experimental studies on the effect of tube inclination on nucleate pool boiling. *Heat Mass Transf.* 45, 1493–1502.

- Schiller, L., Naumann, Z., 1935Z. Ver. Deutsch. Ing. 77, 318.
- Shahinfar, S., Sattarzadeh, S.S., Fransson, J.H.F., Talamelli, A. 2012. Revival of Classical Vortex Generators Now for Transition Delay, Physical Review Letters, 109, 074501-5.
- Singhal, A.K., Li, H.Y., Athavale, M.M., Jiang, Y., 2001. Mathematical basis and validation of the full cavitation model. ASME FEDSM'01. New Orleans, Louisiana.
- Sparrow, E.M., Husar, R.B. 1969. Longitudinal vortices in natural convection flow on inclined plates. J. Fluid Mech., 37, part 2, 251-285.
- Speziale, C.G., Xu, X.H., 1996. Towards the development of second-order closure models for non-equilibrium turbulent flows, Int. J. Heat Fluid Flow, 17, 238-244.
- Stephan, K., 1992. Heat Transfer in Condensation and Boiling, Springer, New York.
- Takamasa, T., Tomiyama, A., 1999. Three-dimensional gas-Liquid two-phase bubbly flow in a C-shaped tube. Ninth International Topical Meeting on Nuclear Reactor Thermal Hydraulics (NURETH-9). San Francisco, CA.
- Takamori, K., Fujii, T., Kataoka, Y., Murase, M., 1994. Experimental Analysis on Mitigation of Thermal Stratification in the Suppression Pool of a Water Wall Type Passive Containment Cooling System, J. Nucl. Sci. Tech., 31(7) 735-744.
- Thakre, S.S., Joshi, J.B., 2000. CFD modeling of heat transfer in turbulent pipe flows, AIChE, 46, 1798-1811.
- Thorat, B.N., Shevade, A.V., Bhilegaonkar, K.R., Agalave, R.H., Parasu Veera, U., Thakre, S.S., Pandit, A.B., Sawant, S.B., Joshi, J.B., 1998. Effect of sparger design and height to diameter ratio on gas hold-up in bubble column reactors, Trans. Instn. Chem. Engrs.-A: Chem. Eng. Res. Des. 76, 823-834.
- Tomiyama, A., 1998. Struggle with computational bubble dynamics. Third International Conference on Multiphase Flow, Lyon, France. June 8-12.
- Tu, J.Y., 1999. The influence of bubble size on void fraction distribution in subcooled flow boiling at low pressure, Int. Commun. Heat Mass Transfer, 26, 607-616.

- Tu, J.Y., Yeoh, G.H., 2002. On numerical modelling of low-pressure subcooled boiling flows, *Int. J. Heat Mass Transfer*, 45, 1197-1209
- Unal, H.C., 1976. Maximum bubble diameter, maximum bubble growth time and bubble growth rate, *Int. J. Heat Mass Transfer*, 19, 643–649.
- Verma, P.K., Nayak, A.K., Jain, V., Vijayan, P.K., Vaze, K.K., 2013. Suppression of thermal stratification in gravity driven water pool of an advanced reactor using shrouds, *Ann. Nucl. Energy*, 58, 221–227.
- Victor, H., Valle, M.D., Kenning, D.B.R., 1985. Subcooled flowboiling at high heat flux, *Int. J. Heat Mass Transfer*, 28, 1907–1920.
- Vusse, J.G., 1962. A new model for the stirred tank reactor, *Chem. Eng. Sci.*, 17, 507–521.
- Wei, J.J., Yu, B., Wang, H.S., Tao, W.Q. 2002. Numerical study of simultaneous natural convection heat transfer from both surfaces of a uniformly heated thin plate with arbitrary inclination, *Heat Mass transfer*, 38, 309-317.
- Wang, B.X., Du, X.Z., 2000. Study on laminar film wise condensation for vapour in an inclined small/mini-diameter tube. *Int. J. Heat Mass Transfer*, 43, 1859–1868.
- Zeitoun, O., Shoukri, M., 1997. Axial void fraction profile in low pressure subcooled flow boiling, *Int. J. Heat Mass Transfer*, 40, 867-879
- Zeitoun, O., Shoukri, M., 1996. Bubble behavior and mean diameter in subcooled flow boiling, *ASME J. Heat Transfer*, 118, 110–116.
- Zuercher, E.J., Jacobs, J.W., Chen, C.F. 1998. Experimental study of the stability of boundary-layer flow along a heated inclined plate, *J. Fluid Mech.*, 367, 1–25.

APPENDIX A

1. Analytical model for two phase flow inside the condenser tube

1.1 Condensate film flow at the circumference of the tube

The following simplifying assumptions are made:

- The vapour is pure and saturated.
- The condensate film is smooth and laminar.
- The shear stress on the condensate film caused by the vapour is negligible
- The pressure drop of the vapour is negligible. Hence the temperature at the interface is uniform and equal to the saturation temperature.
- The temperature at the inner tube wall is uniform and constant.
- The velocity distribution at any point in the condensate film is the same as that in a fully developed film flowing on a plane tangential to the surface at that point. Consequently the curvature of the tube wall is neglected.
- The film thickness is small compared to the tube diameter.
- The latent heat liberated by the condensing vapour is transferred by heat conduction across the condensate film. The convective heat transfer is neglected.
- The physical properties of the condensate are constant.

Assuming a steady-state flow, the forces exerted by the shear stresses are in equilibrium with gravity. The following differential equations for the velocity components in x- and z-direction are obtained from a balance of forces acting on a differential control volume of the condensate film (Fig. 6.13A) according to the classical Nusselt film condensation theory:

$$\eta_1 \frac{\partial^2 w_x}{\partial y^2} + (\rho_1 - \rho_g) g \sin \phi \cos \beta = 0, \quad \dots(1)$$

$$\eta_1 \frac{\partial^2 w_z}{\partial y^2} + (\rho_1 - \rho_g) g \sin \beta = 0. \quad \dots(2)$$

The boundary conditions are as follows:

$$y = 0: \quad w_x = w_z = 0 \quad \dots(3)$$

$$y = \delta: \quad \frac{\partial w_x}{\partial y} = \frac{\partial w_z}{\partial y} = 0 \quad \dots(4)$$

An integration yields the velocity components in x- and z-direction:

$$w_x = \frac{(\rho_1 - \rho_g) g \sin \phi \cos \beta}{\eta_1} \left(\delta y - \frac{y^2}{2} \right), \quad \dots(5)$$

$$w_z = \frac{(\rho_1 - \rho_g) g \sin \beta}{\eta_1} \left(\delta y - \frac{y^2}{2} \right). \quad \dots(6)$$

The mean velocities are obtained by an integration across the film thickness:

$$w_{m,x} = \frac{1}{\delta} \int_0^\delta w_x dy = \frac{(\rho_1 - \rho_g)g \sin \phi \cos \beta}{3\eta_1} \delta^2, \quad \dots(7)$$

$$w_{m,z} = \frac{1}{\delta} \int_0^\delta w_z dy = \frac{(\rho_1 - \rho_g)g \sin \beta}{3\eta_1} \delta^2. \quad \dots(8)$$

The mass flow rate in x- and z-direction can be expressed as follows:

$$\dot{M}_x = w_{m,x} \rho_1 \delta dz, \quad \dots(9)$$

$$\dot{M}_z = w_{m,z} \rho_1 \delta dx. \quad \dots(10)$$

By formation of the condensate mass flow rate \dot{M} the heat flow rate

$$d\dot{Q} = \Delta h_v d\dot{M} \quad \dots(11)$$

is liberated. According to the assumptions made above this heat flow rate is transferred by pure heat conduction across the condensate film. Thus the heat flow rate transferred in a surface element $dx dz$ is

$$d\dot{Q} = \frac{\lambda_1}{\delta} \Delta T dx dz \quad \dots(12)$$

From Eqs. (11) and (12) follows:

$$\Delta h_v d\dot{M} = \frac{\lambda_1}{\delta} \Delta T dx dz \quad \dots(13)$$

The vapour condensing on a surface element causes an increase of the condensate mass flow rate in circumferential direction (x-direction) as well as in axial direction (z-direction).

Therefore Eq. (13) can be written as

$$\Delta h_v \left(\frac{\partial \dot{M}_x}{\partial x} dx + \frac{\partial \dot{M}_z}{\partial z} dz \right) = \frac{\lambda_1}{\delta} \Delta T dx dz \quad \dots(14)$$

By combining Eqs. (7)-(10) with Eq. (14) the following partial differential equation for the local film thickness $\delta(\phi, z)$ is obtained (with $dx = R d\phi$):

$$\delta^2 \cos \phi \cos \beta + 3\delta^3 \cos \beta \sin \phi \frac{\partial \delta}{\partial \phi} + 3\delta^3 R \sin \beta \frac{\partial \delta}{\partial z} = \frac{3\lambda_1 \Delta T \eta_1 R}{\rho_1 (\rho_1 - \rho_g) g \Delta h_v} \quad \dots(15)$$

Eq. (15) is also applicable to the cases ‘‘vertical tube’’ and ‘‘horizontal tube’’: substituting $\beta = \pi/2$ in Eq. (15) reduces it to that for condensation on a vertical plate that is in case of $\delta \ll d$ also valid for vertical tubes (Nusselt (1916)). By substituting $\beta = 0$ in Eq. (15) the partial differential equation for condensation at the outside of a horizontal tube is obtained (Nusselt (1916)).

With the abbreviations

$$\Psi = \frac{\rho_1 (\rho_1 - \rho_g) g \Delta h_v \cos \beta}{3\lambda_1 \Delta T \eta_1 R} \delta^4 \quad \dots(16)$$

and

$$Z = \frac{z}{R \tan \beta} \quad \dots(17)$$

Eq. (15) becomes

$$\frac{\partial \psi}{\partial Z} + \sin \phi \frac{\partial \psi}{\partial \phi} = \frac{4}{3}(1 - \Psi \cos \phi). \quad \dots(18)$$

Two boundary conditions are required to obtain the solution of Eq. (18). At the top of the tube the film thickness equals zero:

$$Z = 0: \quad \Psi = 0. \quad \dots(19)$$

Due to symmetry of the condensate film the gradient of condensate film thickness at the uppermost point of the tube is zero along the entire length of the tube:

$$\phi = 0: \quad \frac{\partial \Psi}{\partial \phi} = 0 \quad \dots(20)$$

Eq. (18) was solved numerically using finite differences (refer to Fiedler (2003)).

1.2. Condensate layer in the lowermost part of the tube

The condensate formed at the circumference of the tube accumulates in the lowermost part of the tube and drains gravity-controlled in z-direction. The following simplifying assumptions are made:

- The condensate layer is smooth and laminar.
- The shear stress on the condensate film caused by the vapour is negligible.
- The pressure drop of the vapour is negligible.
- Since the condensate layer is considerably thicker than the condensate film at the circumference of the tube the heat transferred through the condensate layer is neglected.
- The condensate layer is in stationary, developed flow.

Under these assumptions the simplified Navier–Stokes equation for the condensate layer is:

$$\eta_1 \left(\frac{\partial^2 w_{CL}}{\partial x^2} + \frac{\partial^2 w_{CL}}{\partial y^2} \right) + (\rho_1 - \rho_g)g \sin \beta = 0. \quad \dots(21)$$

Differing from the model for the condensate film flow at the circumference of the tube the origin of the coordinate system is now at the surface of the condensate layer (see Fig. 6.13c).

Assuming that the width of the condensate layer in the lowermost part of the tube is much bigger than its height the following relation applies:

$$\frac{\partial^2 w_{CL}}{\partial x^2} \ll \frac{\partial^2 w_{CL}}{\partial y^2} \quad \dots(22)$$

The velocity distribution in the condensate layer is calculated under the assumption that the condensate drains in a rectangular cross-section (see Fig. 6.13C). This simplification was also made by Fürst (1989) as well as by others (e.g. Moalem Maron and Sideman (1982)). Taking Eq. (22) into account Eq. (21) can be simplified:

$$\frac{\partial^2 w_{CL}}{\partial y^2} = - \frac{(\rho_1 - \rho_g)g \sin \beta}{\eta_1}. \quad \dots(23)$$

The following boundary conditions apply:

$$y = 0: \quad \frac{\partial w_{CL}}{\partial y} = 0. \quad \dots(24)$$

$$y = y_W: \quad w_{CL} = 0. \quad \dots(25)$$

The solution of Eq. (23) is:

$$w_{CL} = - \frac{(\rho_1 - \rho_g)g \sin \beta}{\eta_1} (y_W^2 - y^2). \quad \dots(26)$$

The mean velocity is obtained by integration across the height of the condensate layer:

$$w_{m,CL} = \frac{1}{\delta} \int_0^\delta w_{CL} dy = \frac{(\rho_1 - \rho_g)g \sin \beta}{3\eta_1} y_W^2. \quad \dots(27)$$

The mass flow rate of the condensate layer is

$$\dot{M}_{CL} = w_{m,CL} \rho_1 A_{CL}. \quad \dots(28)$$

The cross-sectional area A_{CL} of the condensate layer is related to the angle ϕ^* and the radius R :

$$A_{CL} = \frac{R^2}{2} (2 \cdot (180^\circ - \phi^*) - \sin(2 \cdot (180^\circ - \phi^*))). \quad \dots(29)$$

The mass flow rate of the condensate layer increases in axial direction due to condensation at the circumference of the tube. The increase per unit tube length follows from the flow rate of the draining condensate from the sides of the tube and can be calculated as (Fiedler (2003))

$$\frac{d\dot{M}_{CL}}{dz} = \frac{2\rho_1(\rho_1 - \rho_g)g \sin \phi^* \cos \beta \delta^3}{3\eta_1} \quad \dots(30)$$

Based on the calculated film thickness at the circumference of the tube (solution of Eq. (15)) and under consideration of Eqs. (28) and (29) the angle ϕ^* can be iteratively determined.

1.3. Heat transfer coefficient

From the values of ψ (solution of Eq. (18)) local values of the heat transfer coefficient can be obtained. Under the assumptions made the local heat transfer coefficient is

$$H = \frac{\lambda_1}{\delta} \quad \dots(31)$$

By rearranging Eq. (16) to δ and inserting it into Eq. (31) one obtains:

$$H = \left(\frac{\rho_1(\rho_1 - \rho_g)g\Delta h_v \lambda_1^3 \cos \beta}{3\Delta T \eta_1 R} \frac{1}{\Psi} \right)^{1/4} \quad \dots(32)$$

Also, β is defined in terms of inclination w.r.t vertical α as:

$$\beta = 90 - \alpha \quad \dots(33)$$

Substituting for angle β from Eq. (33) in Eq. (32):

$$H = \left(\frac{\rho_1(\rho_1 - \rho_g)g\Delta h_v \lambda_1^3 \sin \alpha}{3\Delta T \eta_1 R} \frac{1}{\Psi} \right)^{1/4} \quad \dots(34)$$

From the local heat transfer coefficients a mean heat transfer coefficient can be calculated at each distance z for an infinitesimal ring on the tube surface:

$$H_{av} = \frac{1}{\pi} \int_0^{\phi^*} H d\phi. \quad \dots(35)$$

The local heat transfer coefficients are integrated only up to the angle ϕ^* because the heat transferred through the condensate layer is assumed to be negligible.

The mean heat transfer coefficient for the entire surface of the inclined tube can be obtained from

$$H_{av,total} = \frac{1}{L} \int_0^L H_{av} dz. \quad \dots(36)$$

List of Publications arising from the thesis

Journal

1. “Numerical investigation of three-dimensional natural circulation phenomenon in passive safety systems for decay heat removal in large pools.”, Minocha N., Joshi J. B., Nayak A. K., Vijayan P. K., *International Journal of Heat and Mass Transfer*, 2015, 81, 659-680.
2. “3D CFD Simulation of passive decay heat removal system under boiling conditions: role of bubble sliding motion on inclined heated tubes.”, Minocha N., Joshi J. B., Nayak A. K., Vijayan P. K., *Chemical Engineering Science*, 2016, 145, 245-265.
3. “3D CFD simulation to study the effect of angle of inclination of condenser tube on natural convection and thermal stratification in a passive decay heat removal system.”, Minocha N., Joshi J. B., Nayak A. K., Vijayan P. K., *Nuclear Engineering and Design*, 2016, 305, 582-603.

Conferences

1. “3D CFD Simulation of passive decay heat removal system under boiling conditions: role of bubble sliding motion on inclined heated tubes.”, Minocha N., Joshi J. B., Nayak A. K., Vijayan P. K., *12th International Conference on Gas-Liquid and Gas-Liquid-Solid Reactor Engineering (GLS 12)-2015*. June’ 28-July’ 1, 2015. Columbia University, New-York
2. “3D CFD simulation to study natural circulation phenomenon in Passive Safety Systems for decay heat removal in large pools.”, Minocha N., Joshi J. B., Nayak A. K., Vijayan P. K., *Fluid Mechanics and Fluid Power-2014*. December’2014. Kanpur, India.
3. “Numerical investigation of multidimensional natural circulation phenomenon in Passive Safety Systems for decay heat removal in large pools.” Minocha N., Joshi J. B., Nayak A. K., Vijayan P. K., *New Horizons in Nuclear Thermal Hydraulics and Safety*. January’2014. Mumbai, India.
4. “Numerical investigation of multidimensional natural circulation phenomenon in Passive Safety Systems for decay heat removal in large pools.” Minocha N., Joshi J. B., Nayak A. K., Vijayan P. K., *New Horizons in Nuclear Thermal Hydraulics and Safety*. January’2014. Mumbai, India.